

# **Field correlations in Coulomb gases**

Callum Gray

University College London

Thesis submitted toward the degree of

Doctor of Philosophy

8th February 2019



# **Declaration**

I, Callum John Gray, confirm that the work presented in this thesis is my own. Where information has been derived from other sources, I confirm that this has been indicated in the thesis.



# Abstract

The Coulomb gas is a ubiquitous concept not just in physics but in many other fields of science, including chemistry, biology and engineering.

In this thesis I make use the concept of the “generalised” Coulomb gas, which extends the concept of the “traditional” Coulomb gas by allowing more general solutions to Gauss’ law without changing its fundamental thermodynamic properties. The generalised Coulomb gas was first introduced by Maggs and collaborators, who used it to develop a fast local simulation algorithm for Coulombic systems by taking advantage of the fact that the thermodynamics are unchanged. Further studies were conducted by Faulkner, who studied the generalised Coulomb gas not just for its intrinsic interest but also in the context of the XY model of magnetism, which maps to a 2D generalised Coulomb gas.

I perform numerical studies of the generalised Coulomb gas, paying particular attention to the calculation of its field correlations; surprisingly, these have not been supplied before in the literature. These correlations can be separated into Helmholtz-decomposed components in order to extract the correlations of the traditional Coulomb gas, which are contained within those of the generalised system.

I calculate field correlations in the 2D generalised Coulomb gas in the grand canonical ensemble in all regions of its phase diagram, which was given by Lee and Teitel and includes two Berezinskii-Kosterlitz-Thouless transitions, a first-order gas-solid transition and an Ising solid-liquid transition.

I also perform analogous simulations of the harmonic XY model of magnetism, following the work of Faulkner, and show that it is the generalised Coulomb gas rather than the traditional one which provides a natural description of the emergent Coulomb physics therein.

Lastly, I show preliminary simulations of the 2D canonical and 3D grand canonical generalised lattice Coulomb gases on the square and simple cubic lattices respectively, and suggest further work, including the possibility of performing simulations on the diamond lattice in order to make closer contact with spin ice physics.



# Impact statement

The work presented in this thesis touches on the theory of correlation functions, neutron scattering and “pinch point” features; as well as the theory of emergent Coulomb physics. Neutron scattering is a very-widely used experimental tool for the probing of correlation functions in real systems, and so furthering the understanding of field correlations and how neutron scattering data relates to those correlations is of considerable real-world utility, in addition to the intrinsic academic interest. The theory of emergent Coulombic behaviour is also relevant to experimental systems in physics, for example artificial spin ices, which are a very active area of current research interest.

This work provides increased understanding of all these areas, particularly in the observation of pinch point scattering and its interpretation in terms of emergent Coulomb phases. In addition the work is expected to provide impact via publication in academic journals.

Therefore this work will particularly benefit scholars in many labs around the world who are studying artificial spin ice arrays via X-ray or neutron scattering, or more generally Coulomb phases in diverse systems.



# Acknowledgements

First and foremost my thanks go to my supervisors for the last four years, Steve Bramwell and Peter Holdsworth. It goes without saying that without them I could not have completed this project, and I am immensely grateful for all of their guidance and support over the last four years.

Steve's understanding of spin ices, correlation functions and neutron scattering, as well as his clear and patient explanations of many relevant concepts, were invaluable throughout my studies. Likewise, Peter's approach to breaking down the tough theoretical problems involved in this work was extremely helpful, particularly when it came to the details of the computational implementation, lattice Green's functions and Helmholtz decompositions; I am also very thankful for all his help in getting me down to ENS Lyon to visit. I am grateful also to have had the chance through Steve and Peter to travel to several conferences and summer schools over the course of my PhD, which have all been great experiences and very useful scientifically.

My thanks also go to Michael Faulkner and Vojtech Kaiser, who both took the time to provide me with their code as well as their insights into the physics of Coulomb gases, the XY model and spin ices, which were all very helpful over the course of my project.

I would like to thank UCL, ENS Lyon and the EPSRC for the funding which made this project possible, as well as particular thanks to Tommaso Roscilde for extra funding at the end of the project.

I am grateful to all my friends at UCL, who have made the last four years so much more enjoyable: special thanks to Kane, Jack Baker, and Shereif; Francesco and Giulia; Stephen, Louis, and Katie; and particular thanks to Jack Poulton, who has been a great friend throughout my PhD.

My thanks also to all my friends outside UCL, of whom there are many, but in particular: to my flatmates at Rutland Gardens for making the last chunk of thesis writing so much less stressful; to the whole Frome/Bristol/etc. crew, especially Paula, Char, Roo, Dutton, Jack Humphrey, Cam, Théo, and Aimae; and to Cecile, Ross, Amy, Scott, and Jack Kennedy, who have all put up with my

## *Acknowledgements*

descent into madness for so many years now.

Finally, to my family, without whom I could never have got here in the first place: Mum and Tony; Angie; Kelly and Rick; Kim; Nanna and Grandad; Niall, Daisy, Ella, and Evan; Liam; and most importantly to my dad. I could not have managed this without you, and I'm grateful for all of your help. I love you all.

# Contents

<b>Declaration</b>	ii
<b>Abstract</b>	iii
<b>Impact statement</b>	iv
<b>Acknowledgements</b>	v
<b>Glossary</b>	xxvi
<b>Acronyms</b>	xxxii
<b>Symbols</b>	xxxiv
<b>1. Introduction</b>	1
1.1. Coulomb's law . . . . .	1
1.2. Coulomb gases: the “traditional” and the generalised . . . . .	3
1.3. Aims, objectives and thesis plan . . . . .	5
<b>2. Lattice electromagnetic theory</b>	8
2.1. Discrete differential operators . . . . .	8
2.2. Lattice Green's functions . . . . .	10
2.2.1. Two dimensions: square lattice . . . . .	11
2.2.2. Three dimensions: simple cubic lattice . . . . .	13
2.3. Partition function of a Coulomb gas in the Green's function representation . . . . .	13
2.3.1. The chemical potential . . . . .	16
<b>3. The generalised lattice Coulomb gas</b>	18
3.1. The auxiliary field . . . . .	19
3.2. The harmonic mode . . . . .	19
3.3. The partition function . . . . .	22
3.3.1. Core-energy constant . . . . .	23

## Contents

3.3.2. Expansion of the partition function . . . . .	23
3.4. Field updates . . . . .	25
3.4.1. Field link updates . . . . .	25
3.4.2. Rotational update . . . . .	26
3.4.3. Harmonic update . . . . .	27
3.5. Helmholtz-Hodge decomposition . . . . .	28
3.6. Choice of parameters . . . . .	32
<b>4. Lattice Coulomb gases and spin models</b>	<b>33</b>
4.1. XY-type models . . . . .	33
4.1.1. The 2d-XY model . . . . .	33
4.1.2. Charge deconfinement in the 2D Coulomb gas . . . . .	34
4.1.3. The Berezinskii-Kosterlitz-Thouless transition . . . . .	35
4.1.4. Villain model . . . . .	40
4.1.5. Harmonic XY model . . . . .	40
4.2. The harmonic XY model – Coulomb gas mapping . . . . .	41
4.2.1. The emergent electric field . . . . .	42
4.2.2. The HXY Hamiltonian and partition function in the Coulomb gas representation . . . . .	43
4.2.3. Simulation details for the HXY model . . . . .	45
4.3. Vertex models . . . . .	46
4.3.1. Sixteen-vertex model . . . . .	47
4.3.2. Six-vertex model . . . . .	48
4.3.3. Square ice model . . . . .	48
4.3.4. F model . . . . .	48
4.3.5. The Coulomb phase . . . . .	49
4.4. Spin ice . . . . .	50
4.4.1. Near-neighbour spin ice model . . . . .	52
4.4.2. Coarse-graining . . . . .	54
4.4.3. Dipolar spin ice . . . . .	55
4.4.4. Projective equivalence . . . . .	55
4.4.5. Dumbbell model . . . . .	57
4.5. Magnetic moment fragmentation . . . . .	58
4.6. Artificial spin ice . . . . .	59
<b>5. Correlation tensors and our models</b>	<b>63</b>
5.1. Correlation functions . . . . .	63

5.2.	Scattering experiments . . . . .	63
5.3.	Neutron scattering . . . . .	64
5.4.	Static approximation . . . . .	64
5.5.	Polarised neutron scattering . . . . .	65
5.6.	Scattering function and correlation functions . . . . .	67
5.7.	Propagation vectors . . . . .	67
5.8.	Geometric representations of tensors . . . . .	68
5.8.1.	Principal axes . . . . .	69
5.9.	Coulomb gas formulation . . . . .	70
5.10.	Our models . . . . .	73
<b>6.</b>	<b>Results for the 2D grand canonical Coulomb gas</b>	<b>75</b>
6.1.	Phase diagram . . . . .	75
6.2.	The BKT transition . . . . .	76
6.2.1.	Specific heats and susceptibilities . . . . .	77
6.2.2.	Correlations . . . . .	79
6.3.	Pinch points and bow ties . . . . .	97
6.3.1.	Correlation tensor . . . . .	98
6.3.2.	Neutron scattering . . . . .	98
6.3.3.	The origin of pinch point and bow tie scattering . . . . .	99
6.3.4.	The harmonic mode and $\mathbf{q} = \mathbf{0}$ . . . . .	100
6.3.5.	Pinch point rounding . . . . .	101
6.4.	First-order transition . . . . .	102
6.4.1.	Charge density . . . . .	104
6.4.2.	Correlations . . . . .	104
6.4.3.	Lorentzian fits . . . . .	117
6.4.4.	Discussion . . . . .	120
6.5.	High core-energy BKT and second-order transitions . . . . .	120
6.5.1.	Correlations . . . . .	123
6.5.2.	Lorentzian fits . . . . .	128
6.5.3.	Decreasing core-energy . . . . .	132
6.6.	Tricritical point . . . . .	135
6.7.	Discussion and conclusions . . . . .	139
6.7.1.	BKT transition at zero core-energy . . . . .	139
6.7.2.	First-order transition . . . . .	141
6.7.3.	High core-energy BKT and melting transitions . . . . .	142

## *Contents*

<b>7. Results for the HXY model</b>	<b>144</b>
7.1. Parameter choices . . . . .	144
7.2. Specific heats, susceptibilities and effective electric permittivity .	144
7.3. Spin-spin correlations . . . . .	146
7.4. Emergent field correlations . . . . .	148
7.4.1. $S^\perp(\mathbf{Q})$ functions . . . . .	151
7.4.2. Lorentzian fits . . . . .	153
7.4.3. Quadrics . . . . .	153
7.5. Discussion and conclusions . . . . .	157
<b>8. Results for the 2d canonical and 3d grand canonical Coulomb gases</b>	<b>158</b>
8.1. 2d canonical Coulomb gas . . . . .	158
8.1.1. Winding susceptibilities . . . . .	158
8.1.2. Specific heat . . . . .	159
8.1.3. Correlations . . . . .	160
8.1.4. Lorentzian fits . . . . .	167
8.2. 3d grand canonical Coulomb gas . . . . .	169
8.3. Discussion and conclusions . . . . .	174
<b>9. Conclusions</b>	<b>176</b>
9.1. Summary of main results . . . . .	176
9.2. Relation to more general systems . . . . .	178
9.3. Future work . . . . .	182
<b>A. Simulation details</b>	<b>192</b>
<b>B. Equivalence of Lorentzian forms</b>	<b>193</b>

# List of Figures

1.1. (Quasi-) neutron scattering plots for two different types of artificial spin ice, classical spin ice and the 2D Coulomb gas, showing common pinch point features in the correlations. . . . .	7
3.1. A general field link update in the Maggs-Rossetto model. The direction of the arrow signifies that we treat the flux as positive when it goes from site $\mathbf{x}$ to site $\mathbf{x} + a\mathbf{e}_\mu$ . We also require $ q_\alpha  \leq 1 \forall \alpha$ . . . . .	25
3.2. The four possible charge moves associated with a field link decrease in the Maggs-Rossetto model: positive charge moving “forwards”, negative charge moving “backwards”, dipole creation, dipole annihilation. A blank circle indicates an empty site. . . . .	26
3.3. A rotational update in the Maggs-Rossetto model. The flux is “rotated” around the plaquette by an amount $\Delta$ . Charge values for the sites $\alpha, \beta, \gamma, \delta$ are not shown here since they are irrelevant in this context; the rotational update does not affect the charge configuration. . . . .	27
3.4. A sampled field configuration of a 2D Coulomb gas in the canonical ensemble, with $L = 20$ , at $T = 0.1$ in the units used by Lee and Teitel [44]. Two bound pairs of charges are shown with positive and negative in red and blue respectively. . . . .	29
3.5. The irrotational component of the field shown above, found by solving the Poisson equation for the charge configuration using the lattice Green’s function 2.35. This component is then only the longitudinal one; we see divergence-full fields which emanate from positive charges and end on negative charges as we expect. . . . .	30

## List of Figures

3.6. The rotational component of the field shown above; found by subtracting 3.5 from 3.4. Charges are not shown since the rotational component does not arise from the charges. This is the divergence-free transverse component which is absent in the TLCG but present for emergent field representations of magnetic systems, such as the XY model, which will be discussed in more detail in Chap. 4. . . . .	31
4.1. Simulations of the magnetisations of the XY (open circles) and HXY (filled) models for $N = 10^4$ spins, from [6]. We see a long tail in the magnetisation due to the extremely slow approach to the thermodynamic limit. . . . .	38
4.2. The mapping between the lattice Coulomb gas and the HXY model. Coulomb gas sites are represented by unfilled circles and lattice electric fields by black arrows, as in Chap. 3; the spin-difference field of the HXY model is shown here as green arrows. The direction of the HXY spins shown here is arbitrary. . . . .	42
4.3. The mapping between spin rotations in the HXY model and the rotational update of the Maggs-Rossetto model. In the HXY model, the maximum rotation $\Delta_{\max}$ is necessarily $2\pi$ due to the modular symmetry; this restriction does not apply to the Maggs-Rossetto algorithm. . . . .	46
4.4. A spin update in the HXY model which corresponds to a charge hop in the Coulomb gas, reproduced from [32]. . . . .	46
4.5. The sixteen possible configurations of a single vertex of the square lattice, with $\mathbb{Z}_2$ spins. . . . .	47
4.6. The six ice-rule-obeying configurations of a single vertex of the square lattice. Several different ice-type models are obtainable by varying the energies of the $\epsilon_i$ in different ways. . . . .	48
4.7. The six allowed vertices with energy levels for the F model. . . . .	49
4.8. Pyrochlore lattice structure and example of smallest closed loop, reproduced from [61]. . . . .	52
4.9. Two possible states of a pair of tetrahedra in spin ice. The two-in-two-out ground state (left) becomes an excited state consisting of a pair of oppositely-charged defects (right) via the flipping of the spin connecting the two; depending on which model of spin ice we consider, these defects interact entropically, via a dipolar interaction or a Coulomb interaction. . . . .	53

4.10. Polarised neutron scattering plots for holmium titanate, from experiment and Monte Carlo simulation of the NNSI model respectively, showing only the spin-flip component of the scattering. . . . .	56
4.11. Comparison of the DSI and dumbbell models. From left to right are shown tetrahedra with zero, positive, negative, double positive and double negative charges; the top and bottom rows show their representations in the DSI and dumbbell models respectively. . . . .	57
4.12. Neutral, singly charged and doubly charged defects in the dumbbell model. For clarity, the dumbbells here are drawn with space between them; in reality the dumbbell model proceeds by assuming that the dumbbells meet exactly at the tetrahedral centres. . . . .	58
4.13. The four vertex types of the 16 vertex model, arranged by overall “charge” and magnetic moment. . . . .	60
4.14. Magnetic structure factors for different z-offsets $d$ , reproduced from [36]. We see the crossover from a Type-II dominated ordered state at zero offset to an ice-rule obeying state at $d = 100nm$ . . . . .	61
4.15. Magnetic structure factors for different disc diameters $D$ reproduced from direct observation of the discs, reproduced from [37]. Again, we see the crossover from a relatively ordered state with no disc to one with the six-vertex degeneracy of the square ice model.	62
5.1. Diagram showing the shape of two different examples of $S^{\alpha\beta}(\mathbf{q})$ tensor. The solid blue disk corresponds to regime 1 below (Coulomb phase); the translucent dark blue mesh to regime 2 (harmonic phase). Reproduced from [89]. . . . .	73
5.2. The two relevant Brillouin zones of the system used in this thesis. The charges and the diagonal components share the Brillouin zone shown in blue; the off-diagonal components have a larger, rotated Brillouin zone, since they have a smaller separation in direct space.	74
6.1. The $u - T$ (core-energy vs. temperature) phase diagram for the 2D grand canonical Coulomb gas, as originally probed in [44] using Monte Carlo simulation. . . . .	76

## List of Figures

6.2. Harmonic susceptibilities in the 2D grand canonical Coulomb gas, with core-energy $u = 0$ and system size $N = 64 \times 64$ , as a function of temperature. We can see that the winding component (blue) increases across the BKT transition whereas the polarisation component saturates and its associated susceptibility (green) goes to zero. . . . .	77
6.3. Specific heats in the 2D grand canonical Coulomb gas for core-energy $u = 0$ and system size $N = 64 \times 64$ . We see that the rotational component of the specific heat is constant, as expected for a freely fluctuating field, but there is a pronounced peak in the irrotational component at around $T = 0.3$ , above the BKT transition temperature. . . . .	78
6.4. The winding susceptibility $\chi_w$ calculated across the BKT transition with $u = 0$ . We see that the increase is sharper as the lattice size increases, but the asymptotic value does not change. . . . .	79
6.5. ( $T = 0.223 ; u = 0$ ). The total and rotational field-field correlation tensors $S^{\alpha\beta}(\mathbf{q})$ . This is slightly above the BKT transition temperature $T_{\text{BKT}} = 0.22$ . Top left, top right, bottom left and bottom right plots are $S^{xx}$ , $S^{xy}$ , $S^{yx}(= S^{xy})$ and $S^{yy}$ . . . . .	80
6.6. ( $T = 0.223 ; u = 0$ ). The irrotational correlation tensor for the same parameters as Figs. 6.5. By concentrating only on the longitudinal component of the field, we isolate the field correlations of a TLCG (the electrostatic correlations). . . . .	81
6.7. ( $T = 0.500 ; u = 0$ ). The correlation tensor of the total field. This is significantly above the BKT transition temperature $T_{\text{BKT}} = 0.22$ . We see that the intensities for the diagonal components are higher than in Fig. 6.5a, for example, and also that the function is flatter overall. The off-diagonal component is smaller in magnitude, also. . . . .	82
6.8. ( $T = 0.500 ; u = 0$ ). Rotational and irrotational tensors $S^{\alpha\beta}(\mathbf{q})$ , again significantly above $T_{\text{BKT}}$ . The longitudinal component (right) is rotated by $\pi/2$ compared to the rotational component (left) in Fig. 6.5b. . . . .	83
6.9. ( $T = 0.223$ and $T = 0.500 ; u = 0$ ). The rotational tensor $S_{\text{rot.}}^{\alpha\beta}(\mathbf{q})$ . The shape of the function is the same in both cases, but the intensities increase with temperature. . . . .	84

6.10. ( $T = 0.223 ; u = 0$ ). The trace $S^{xx} + S^{yy}$ for the total and rotational tensors respectively. The rotational component is flat except for the point at $\mathbf{q} = \mathbf{0}$ which corresponds to the harmonic mode; the total correlations also feature a small peak above the flat rotational background centred around the origin, which comes from the irrotational component. The similarity in intensity between the plots here indicates, again, that the correlations are dominated by the rotational component of the field at this temperature. . . . .	85
6.11. ( $T = 0.500 ; u = 0$ ). The trace $S^{xx} + S^{yy}$ for the total and irrotational tensors respectively. The total trace (left) is mostly very flat, with a small, broad peak centred at the origin; the irrotational component now also has a flat background with a central peak superimposed, as opposed to the flat background of the rotational component. . . . .	86
6.12. ( $T = 0.223 ; u = 0$ ). The neutron scattering function $S_{\text{total}}^{\perp}(\mathbf{Q})$ at $T \approx T_{\text{BKT}}$ , showing sharp pinch point features. The harmonic mode at $\mathbf{Q} = \mathbf{0}$ has vanishingly small intensity here. . . . .	87
6.13. ( $T = 0.275 ; u = 0$ ). $S_{\text{total}}^{\perp}(\mathbf{Q})$ above the BKT transition, displaying a finite intensity at $\mathbf{Q} = \mathbf{0}$ and a rounded pinch point, indicating the increased intensity in the longitudinal component. .	88
6.14. ( $T = 0.500 ; u = 0$ ). $S_{\text{total}}^{\perp}(\mathbf{Q})$ . At this very high temperature, the $\mathbf{Q} = \mathbf{0}$ point has double the intensity of any other $\mathbf{Q}$ , and the rest of the function becomes very flat, with only a $\approx 15\%$ difference between the highest and lowest intensities. This plot has the lower end of the scale explicitly set to zero in order to show the flatness of the function away from $\mathbf{Q} = \mathbf{0}$ . . . . .	89
6.15. ( $T = 0.223 ; u = 0$ ). The trace $S_{\text{irrot.}}^{\alpha\alpha}(\mathbf{Q})$ with the cut which I take for the Lorentzian fit shown as a white line. . . . .	91
6.16. ( $T = 0.223 ; u = 0$ ). The fit to a cut of the trace $S_{\text{irrot.}}^{\alpha\alpha}(\mathbf{Q})$ , showing that either Lorentzian on its own is insufficient to fit the data, and also that the flat background is required. . . . .	92
6.17. ( $T = 0.223 ; u = 0$ ). $S_{\text{irrot.}}^{\alpha\alpha}(\mathbf{Q})$ from fitted parameters (left), and simulation (right). The simulation result has a “cross” shape arising from the translational symmetry, whereas the fitting function has a continuous symmetry. The intensity across the chosen cut is quantitatively accurate, however. . . . .	93

## List of Figures

6.18. ( $T = 0.223 ; u = 0$ ). $S_{\text{irrot.}}^{\perp}(\mathbf{Q})$ from the fitted function using Eq. 6.6 (left), from the simulated trace $S_{\text{irrot.}}^{\alpha\alpha}(\mathbf{q})$ with Eq. 6.6 (centre), and directly from simulation (right). . . . .	93
6.19. ( $T = 0.223 ; u = 0$ ). $S_{\text{total}}^{\perp}(\mathbf{Q})$ from the fitted function using Eq. 6.6 (left), from the simulated trace $S_{\text{irrot.}}^{\alpha\alpha}(\mathbf{q})$ with Eq. 6.6 (centre), and directly from simulation (right). As with the irrotational component, we see that the fit reproduces the function well. . . . .	94
6.20. ( $T = 0.700 ; u = 0$ ). The fit to the cut of $S_{\text{irrot.}}^{\alpha\alpha}(\mathbf{Q})$ . Again, the flat background is necessary, but here the data is well-described by one Lorentzian. . . . .	95
6.21. ( $T = 0.700 ; u = 0$ ). $S_{\text{total}}^{\perp}(\mathbf{Q})$ from the fit (left), from the simulated trace with Eq. 6.6 (centre), and directly from simulation (right). . . . .	95
6.22. The correlation lengths $\xi_1, \xi_2$ , extracted from the fits to Eqs. 6.1, as a function of temperature. We can consider $\xi_1$ and $\xi_2$ as representing bound pairs and free vortices respectively. . . . .	96
6.23. The correlation lengths $\xi_1, \xi_2$ for systems of linear size $L = 32$ and 64. $\xi_1$ (which we interpret as a bound pair length) is shorter than the lattice spacing for all temperatures, but $\xi_2$ (which we identify with the Kosterlitz correlation length) shows a pronounced peak just above the BKT transition. . . . .	97
6.24. Diagram showing that $\mathbf{q}$ and $\mathbf{Q}$ are not parallel for non-zero $\mathbf{G}$ . BZB is the Brillouin zone boundary, shown as a dashed black line. . . . .	99
6.25. Neutron scattering pattern of the transverse (a) and longitudinal (b) components of the emergent field representation of the harmonic XY model at $T = 0.207$ , below the BKT transition temperature $T_{\text{BKT}} \approx 0.22$ . The transverse field configuration is entirely rotational, and the resulting neutron scattering pattern shows sharp pinch point features; the longitudinal is entirely irrotational and shows sharp bow ties. . . . .	100
6.26. The central Brillouin zone of the neutron scattering pattern for the 2D grand canonical GLCG, above and below the BKT transition. The evolution in intensity at $\mathbf{Q} = \mathbf{0}$ is clearly visible. Colourbars are not included here, since this is a qualitative example of the change in $\mathbf{Q} = \mathbf{0}$ , but it is important to note that the two are not on the same scale; the intensity at $\mathbf{Q} \neq \mathbf{0}$ remains relatively constant, while at $\mathbf{Q} = \mathbf{0}$ it increases by an order of magnitude. . . . .	101

6.27. Sharpness of pinch point in the total neutron scattering pattern, for the 2D GLCG across the BKT transition. We see that the sharp feature evident at $T = 1.3$ is replaced by a rounded feature at $T = 1.8$ . Again, colourbars are not included here since this is a qualitative example of the rounding. . . . .	102
6.28. Phase diagram 6.1 with the relevant $u, T$ parameters used in my simulations of the first-order transition highlighted with purple rectangles. The dashed purple line is a guide for the eye. . . . .	103
6.29. The average charge density of the 2D Coulomb gas on the square lattice, as a function of core-energy constant $u$ . The exact core-energy of the transition in the thermodynamic limit is displayed as a dashed line. . . . .	105
6.30. ( $T = 0.100$ ; $u = 0.200$ ). Correlation tensors $S_{\text{total}}^{\alpha\beta}$ and $S_{\text{rot.}}^{\alpha\beta}$ respectively, below the BKT and first-order transitions. We can see that the total correlations are completely dominated by the rotational component. . . . .	106
6.31. ( $T = 0.100$ ; $u = 0.392$ ). The correlation tensor for the irrotational component at $u = 0.392$ , almost precisely at the critical core-energy value $u_c = \pi/8 = 0.392699\dots$ in the thermodynamic limit. . . . .	107
6.32. ( $T = 0.100$ ; $u = 0.392, 0.400, 0.405, 0.410$ ). The trace of the irrotational correlation tensor at $T = 0.1$ as $u$ increases beyond the transition, showing the growing intensity of the peaks at the Brillouin zone corners. . . . .	108
6.33. ( $T = 0.100$ ; $u = 0.410$ ). The correlation tensor for the total field (left) and irrotational component (right) at $u = 0.410$ , showing that the total correlations are now dominated by the longitudinal component. . . . .	109
6.34. ( $T = 0.100$ ; $u = 0.400, 0.405, 0.410$ ). The quadric $\bar{S}_{\text{total}}^{\alpha\beta}(\pi, \pi)$ as the charge solid forms (a-c), with the corresponding $S^\perp(\mathbf{Q})$ plots (d-f). The plots for $u = 0.405, 0.410$ use a logscale for the intensity, since otherwise the peaks become invisible against the background. . . . .	110
6.35. ( $T = 0.100$ ; $u = 0.375$ ). $S^\perp(\mathbf{Q})$ . The core-energy here is below the critical value; despite its being finite, the total correlations are still those of the gas phase. . . . .	111

## List of Figures

6.36. ( $T = 0.100$ ; $u = 0.392$ ). $S^\perp(\mathbf{Q})$ . We are now essentially at $u = u_c = \pi/8$ ; the peaks associated with the solid phase are now beginning to be visible superimposed on the diffuse correlations of the gas phase. . . . .	112
6.37. ( $T = 0.100$ ; $u = 0.398, 0.400, 0.402, 0.404$ ). Four examples of $S_{\text{total}}^\perp(\mathbf{Q})$ around the critical core-energy value $u_c$ . We can clearly see the solid-gas coexistence, with the pinch point of the gas phase and the sharpening peaks of the solid phase; by $u = 0.404$ , the peaks are almost Bragg-like and the rotational correlations are invisible. . . . .	113
6.38. ( $T = 0.100$ ; $u = 0.410$ ). $S^\perp(\mathbf{Q})$ . The system is now completely ordered; the neutron scattering pattern shows extremely sharp peaks. The intensities are plotted on a log scale in order to make the plot legible. . . . .	114
6.39. ( $T = 0.100$ ; $u = 0.420$ ). An example of an irrotational field configuration for $L = 20$ . Here, the system is a fully ordered charge crystal; in general charge annihilations are possible, but the average charge density for these parameters is around 95%. . . . .	115
6.40. The parallel component of the scattering function of the electric field, displaying the same peaks and systematic absences as the perpendicular component of the scattering function for ASI experiments conducted in [37]. . . . .	117
6.41. ( $T = 0.100$ ; $u = 0.420$ ). $S_{\text{total}}^\perp(\mathbf{Q}) + S_{\text{total}}^{\parallel}(\mathbf{Q})$ . We see that the function displays peaks of identical intensity at the corner of each Brillouin zone: this function essentially corresponds to taking the trace of $S^{\alpha\beta}(\mathbf{q})$ , as shown in (for example) Fig. 6.32d. . . . .	118
6.42. The evolution of the peak in $S_{\text{total}}^\perp(\mathbf{Q}) + S_{\text{total}}^{\parallel}(\mathbf{Q})$ at $\mathbf{Q} = (\pi, \pi)$ as a function of $u$ . At higher core-energies it becomes necessary to use a log scale and the peaks shown here become invisible. . . . .	119
6.43. Phase diagram 6.1 with the relevant $u, T$ parameters used in my simulations of the high- $u$ transitions highlighted with purple rectangles. . . . .	120
6.44. The evolution of the $\mathbf{q} = \mathbf{0}$ point of $S_{\text{total}}^\perp$ across the high- $u$ BKT transition, for different system sizes. We see a sharp increase across the BKT transition followed by a slowing down above the Ising transition; the increase is sharper for the larger system size. . . . .	121

6.45. Average charge density of the Coulomb solid across the insulator-conductor BKT transition, showing a drop from $\approx 95\%$ below the BKT transition to around 0.7 at $T = 0.24$ , just above the Ising transition. . . . .	122
6.46. ( $T = 0.150$ ; $u = 0.500$ ). Correlation tensors $S_{\text{total}}^{\alpha\beta}$ and $S_{\text{irrot}}^{\alpha\beta}$ , respectively, in the insulating solid phase. As in Sec. 6.4, the correlations consist of Bragg peaks at the Brillouin zone corners consistent with the ordered charge crystal. . . . .	123
6.47. ( $T = 0.200$ ; $u = 0.500$ ). $S_{\text{total}}^{\alpha\beta}$ in the conducting solid phase. For reference, the value of the $\mathbf{q} = \mathbf{0}$ point here is around 0.75 – significantly higher than its value in the insulating phase, but still several orders of magnitude smaller than the peaks at the Brillouin zone corners. . . . .	124
6.48. ( $T = 0.220$ ; $u = 0.500$ ), the melting transition temperature. $S_{\text{total}}^{\alpha\beta}$ . The peaks arising from the longitudinal component are now significantly ( $\approx 50\%$ ) less intense than in Fig. 6.47, but still several orders of magnitude larger than the correlations of the transverse component, giving qualitatively similar overall correlations. . . . .	125
6.49. ( $T = 0.220, 0.300$ ; $u = 0.500$ ). $S_{\text{total}}^{\alpha\beta}$ . We can now see the peaks have a finite width instead of being Bragg-like, signifying the breakdown of crystal ordering. . . . .	126
6.50. ( $T = 0.600$ ; $u = 0.500$ ). The tensor $S_{\text{irrot}}^{\alpha\beta}(\mathbf{q})$ . We see diffuse features as in the zero- $u$ phase which are of nearly the same intensity as the peaks in the Brillouin zone corners which signal the high- $u$ phase. . . . .	127
6.51. ( $T = 0.600$ ; $u = 0.500, 0.000$ ). $S_{\text{irrot}}^{xx}$ . The diffuse features are qualitatively the same and have similar magnitudes, for example at $\mathbf{q} = \mathbf{0}$ ; the only qualitative differences being the peak at $(\pm\pi, 0)$ and a smaller, even less visible region of high intensity at $(\pm\pi, \pm\pi)$ . . . . .	128
6.52. ( $T = 0.300, 0.400, 0.500, 0.600$ ; $u = 0.500$ ). Four examples of $S_{\text{total}}^\perp(\mathbf{Q})$ in the conducting liquid phase as the temperature increases. We see the Bragg peaks which characterise the solid phase becoming more diffuse and Lorentzian and the intensities decreasing with temperature. . . . .	129
6.53. ( $T = 0.250, 0.300, 0.400, 0.600$ ; $u = 0.500$ ). Four examples of the peak at $(3\pi, 5\pi)$ in $S_{\text{total}}^\perp(\mathbf{Q})$ . We see the Lorentzians broadening and the peak height decreasing as the temperature increases. . . . .	130

## List of Figures

6.54. The Lorentzian peak at $(3\pi, 5\pi)$ across $4\pi \leq Q_y \leq 6\pi$ for a range of temperatures, showing that as the temperature increases so does the width of the peak. . . . .	131
6.55. Linear fit of $\kappa(T)$ , the temperature-dependent peak width. The fitted width is fairly well approximated by a linear function, as expected due to the critical exponent for the 2D Ising transition. . . . .	132
6.56. ( $T = 0.600$ ; $u = 0.400, 0.300, 0.200, 0.100$ ). $S_{\text{total}}^{\perp}(\mathbf{Q})$ in the conducting liquid phase as the core-energy decreases, moving back towards the flatter correlations of the zero core-energy phase. At $u = 0.1$ the function is almost completely flat; the corresponding plot has its lower bound explicitly set to zero since otherwise the function appears black everywhere. . . . .	134
6.57. ( $T = 0.600$ ; $u = 0.000, 0.100$ ). $S_{\text{total}}^{\alpha\beta}(\mathbf{q})$ . In both cases the diagonal components are very flat due to the high temperature, but the finite core energy has a qualitative effect: the (slightly) higher intensity band becomes the (slightly) lower intensity band and vice versa. . . . .	135
6.58. ( $T = 0.150$ ; $u = 0.380$ ). $S_{\text{total}}^{\alpha\beta}(\mathbf{q})$ . The peaks at $(\pm\pi, \pm\pi)$ resemble those of the crystal phase, but the intensities here are much lower, as is the charge density. . . . .	136
6.59. ( $T = 0.150$ ; $u = 0.380$ ). $S_{\text{total}}^{\perp}(\mathbf{Q})$ . Again, we see peaks qualitatively similar to those of the charge crystal phase, but more rounded and with lower intensity. . . . .	137
6.60. ( $T = 0.160$ ; $u = 0.360$ ). $S_{\text{total}}^{\alpha\beta}(\mathbf{q})$ . The diffuse correlations of the transverse-dominated, low- $u$ phases can be seen in dark purple with the peaks of the high- $u$ phase superimposed. . . . .	137
6.61. ( $T = 0.160$ ; $u = 0.360$ ). $S_{\text{total}}^{\perp}(\mathbf{Q})$ . The lower-intensity diffuse features seen in the $S^{\alpha\beta}(\mathbf{q})$ tensor do not survive here; the broad peaks of the high- $u$ phases dominate the neutron scattering function. . . . .	138
6.62. ( $T = 0.150$ ; $u = 0.410$ ). $S_{\text{total}}^{\alpha\beta}(\mathbf{q})$ . These parameters put us very close to the critical point but in the solid phase, and the correlations of the solid phase are all that we see in the tensor. . . . .	138
6.63. ( $T = 0.150$ ; $u = 0.410$ ). $S_{\text{total}}^{\perp}(\mathbf{Q})$ , again showing only the correlations from the solid phase. A log scale is used to make the peaks visible against the background. . . . .	139

6.64. Simulated neutron scattering plots of the Coulomb gas across the BKT transition, showing the increased intensity at $\mathbf{Q} = \mathbf{0}$ and the rounding of the pinch points. . . . .	140
6.65. Simulated neutron scattering plots of the Coulomb gas across the first-order transition, showing the emergence of sharp peaks indicating the onset of all-in-all-out order. The right-hand function is plotted to a log scale in order to make the peaks more visible. . . . .	141
6.66. Simulated neutron scattering plots of the Coulomb gas in the high core-energy conducting liquid phase. The sharp peaks of the insulating crystal phase become Lorentzian in shape with the Lorentzian width increasing linearly with temperature. . . . .	143
7.1. The specific heats of the total and Helmholtz-decomposed components of the HXY model as a function of temperature. . . . .	145
7.2. The winding susceptibility $\chi_w$ of the HXY model across the BKT transition, showing a qualitatively similar increase to that of the GLCG, but with a lower asymptotic value. . . . .	145
7.3. Winding susceptibilities of the HXY model and Coulomb gas for $L = 32$ and $64$ showing that the HXY result is always smaller than the GLCG result for a given temperature and lattice size. . . . .	146
7.4. $S_\theta^\perp(\mathbf{q})$ at $T = 1.300$ . A log scale is used in order to make the peaks visible against the background; the system is (quasi)-ordered at this low temperature. . . . .	147
7.5. $S_\theta^\perp(\mathbf{q})$ at $T = 2.500$ , with log scale no longer needed. The intensity of the peaks is about 1% of the intensity at $T = 1.3$ , as was shown in Fig. 7.4. . . . .	148
7.6. $T = 1.300$ . $S_{\text{total}}^{\alpha\beta}(\mathbf{q})$ and $S_{\text{irrot}}^{\alpha\beta}(\mathbf{q})$ respectively, below the BKT transition temperature $T_{BKT} = 1.35$ . The total correlations are completely dominated by the rotational component. As in Chap. 6, $S^{xx}, S^{xy}, S^{yx}, S^{yy}$ are shown in the top left, top right, bottom left and bottom right panels respectively. . . . .	149
7.7. $T = 1.800$ . $S_{\text{total}}^{\alpha\beta}(\mathbf{q})$ for the HXY model and Coulomb gas respectively, where the Coulomb gas figures were taken at $T = 1.8/2\pi$ and with $q = 1$ . The intensities are slightly higher for the GLCG than the HXY model; Ref. [32] attributes this difference to decreased charge mobility in the HXY model due to the constrained rotational field component. . . . .	150

## List of Figures

- 7.8.  $T = 1.800$ .  $S_{\text{irrot}}^{\alpha\beta}(\mathbf{q})$  and  $S_{\text{irrot}}^{\alpha\beta}(\mathbf{q})$  for the HXY model and Coulomb gas respectively. We see that the irrotational component has slightly higher intensities for the GLCG than the HXY model, for the same reason as discussed in the previous figure. . . . . 151
- 7.9. The neutron scattering function  $S_{\text{total}}^{\perp}(\mathbf{Q})$  for the HXY model across the BKT transition. We see the same phenomena as for the GLCG: the harmonic mode entering at becomes the highest-intensity point in the diagram and the increased longitudinal intensity acts to round off the pinch points. . . . . 152
- 7.10. The correlation lengths  $\xi_1, \xi_2$  for the HXY model and the Coulomb gas for  $L = 64$ , corrected to use the same units, showing good agreement. . . . . 154
- 7.11. The zero contour of the representation quadric at  $\mathbf{q} = (\pi, \pi)$  for  $\bar{S}_{\text{total}}^{\alpha\beta}$  as the BKT transition is crossed. We see that the eccentricity of the quadric decreases: at  $T = 1.3$  the quadric is a very thin ellipse and the transverse eigenvalue is an order of magnitude larger than the longitudinal one; at  $T = 2.5$  this is down to about 50% larger. At infinite temperature we would expect a perfect circle. . 155
- 7.12. The zero contour of the quadric at  $\mathbf{q} = (0, 0)$ , which is always a circle regardless of temperature. This is a reflection of the fact that the harmonic mode is both curl-free and divergence-free. . . . . 156
- 8.1. The phase diagram of the 2d canonical Coulomb gas on the square lattice, probed via Monte Carlo simulation, reproduced from [45]. Open symbols are for  $L = 16$ , filled symbols for  $L = 32$ . . . . . 159
- 8.2. The winding susceptibility  $\chi_w/\epsilon$  as a function of temperature for different values of  $n$ , for  $L = 64$ . The grand canonical BKT transition temperature in these units is  $T_{\text{BKT}}^{\text{gce}} = 0.22$ , and we see that for vanishingly low charge density  $\chi_w$  is small here well above  $T = 0.22$ , indicating that the dilute limit gives a higher BKT transition temperature. . . . . 160
- 8.3. The winding susceptibility  $\chi_w/\epsilon$  for higher values of  $n$  along with the grand canonical result for  $L = 64$ . We see that for higher charge densities the winding susceptibility is finite at lower temperature, consistent with a lowered BKT transition temperature. . . . . 161

8.4. Specific heat for values of $n$ above 32. For very low charge densities the specific heat is approximately 0.5 for all temperatures, as would be the case for a purely transverse field, indicating a very small longitudinal contribution. . . . .	162
8.5. ( $n = 2$ , $\rho = 0.0005$ , $T = 0.25$ ). The simulated neutron scattering function $S_{\text{total}}^{\perp}(\mathbf{Q})$ . This temperature is significantly higher than $T_{\text{BKT}}^{\text{gce}}$ but features sharp pinch points and zero harmonic mode, indicating the transverse-dominated phase below the transition. . . . .	163
8.6. The simulated neutron scattering function $S_{\text{total}}^{\perp}(\mathbf{Q})$ for lower and higher charge densities at the same temperature. The lower density (left) shows a small harmonic mode and sharp pinch points corresponding to the insulating phase, whereas the higher density (right) shows a large harmonic mode and rounded pinch points characteristic of the conducting phase. . . . .	164
8.7. ( $n = 512$ , $\rho = 0.125$ , $T = 0.191$ ). The simulated neutron scattering function $S_{\text{total}}^{\perp}(\mathbf{Q})$ . We see the diffuse features of the transverse-dominated phase but with broad peaks superimposed which imply the presence of the solid phase: therefore, we take these correlations as suggestive of phase coexistence, as would be expected for these parameters from [45]. . . . .	165
8.8. ( $n = 512$ , $\rho = 0.125$ , $T = 0.318$ ). The simulated neutron scattering function $S_{\text{total}}^{\perp}(\mathbf{Q})$ . We now see very rounded pinch points and a strong signal at $\mathbf{Q} = \mathbf{0}$ : the system is in the conducting liquid phase, which is again consistent with the phase diagram. . . . .	166
8.9. The higher and lower correlation lengths of the canonical Coulomb gas as a function of temperature and charge density up to $n = 32$ ( $\rho = 0.008$ ). . . . .	167
8.10. The higher and lower correlation lengths of the canonical Coulomb gas as a function of temperature and charge density up to $n = 256$ ( $\rho = 0.125$ ). . . . .	168
8.11. ( $n = 512$ ; $\rho = 0.125$ ; $T = 0.191$ ). The longitudinal correlation function obtained via the trace of the scattering tensor $S_{\text{irrot}}^{\alpha\alpha}(\mathbf{q})$ . The broad areas of high intensity at $(\pm\pi, \pm\pi)$ are characteristic of the solid phase; the effect of this is essentially that the function can no longer be represented by a pair of Lorentzians. . . . .	169

## List of Figures

8.12. Phase diagram for the 3D grand canonical restricted primitive model on the simple cubic lattice, for the zero field case, reproduced from [95]. . . . .	170
8.13. ( $T = 0.25$ , $u = 0$ ). $S_{\text{total}}^{\perp}(Q_z = 0)$ . At this low temperature we again see a transverse dominated state with sharp pinch points. . . . .	171
8.14. ( $T = 0.500$ ; $u = 0.250, 0.500, 1.000$ ). Three examples of $S_{\text{total}}^{\perp}(Q_z = 0)$ with the core-energy increasing. At $u = 0.25$ we see the onset of Lorentzians associated with the solid phase, which disappear at $u = 0.5$ and then return at $u = 1.0$ ; it is unclear what causes this disappearance and reappearance. . . . .	172
8.15. ( $T = 0.750$ ; $u = 0, 0.250, 0.500, 1.000$ ). Four examples of $S_{\text{total}}^{\perp}(Q_z = 0)$ with the core-energy increasing. Again, we begin to see the superposition of correlations associated with the conducting liquid and solid phases. . . . .	173
8.16. $S_{\text{total}}^{\perp}(\mathbf{Q})$ for two different charge densities at the same temperature. On the left we see correlations which correspond to the insulating phase, on the right the correlations are those of the conducting phase. . . . .	174
8.17. Three examples of $S^{\perp}(Q_z = 0)$ for different values of $T$ and $u$ . We see correlations reminiscent of the low- $T$ , low- $u$ insulating gas phase, the low- $T$ , high- $u$ insulating solid phase and the high- $T$ , high- $u$ melted phase respectively. . . . .	175
9.1. The 2D grand canonical Coulomb gas phase diagram, with superimposed examples of the correlations of each phase. . . . .	179
9.2. Lorentzian fits to pinch points: to experimental data on the $(h, h, 2)$ pinch point of $\text{Ho}_2\text{Ti}_2\text{O}_7$ as a function of temperature, from [39] (left); to the longitudinal correlation function in my work (centre); and to simulations of ice-rule obeying configurations in artificial spin ice, from [36] (right). . . . .	180
9.3. Single crystal of $\text{D}_2\text{O}$ ice $I_h$ investigated via diffuse neutron scattering (right) and model calculation (left). Reproduced from [97]. . . . .	181

# List of Tables

4.1. Table of relevant properties of spin ice materials [58]. . . . .	51
-----------------------------------------------------------------------	----



# Glossary

## Artificial spin ice

An umbrella term for many kinds of engineered magnetic systems, generally constructed of nanoscale single-domain Ising-type ferromagnets, which were originally intended to realise the Lieb square ice model. 61, 101, 114, 140

## BKT transition

A phase transition of infinite order which was discovered by Berezinskii [1] and also by Kosterlitz & Thouless [2]. 4, 19, 35, 37, 39, 42, 51, 77, 78, 80, 82, 88, 92, 96, 100, 119, 121, 133, 138, 140, 143, 147, 156–158, *see XY model*

## Bow tie

A common feature found in neutron scattering data of antiferromagnets and ferroelectrics. Roughly the shape of a bow tie, they arise from the longitudinal component of the field. 94, 95, 174, *see pinch point & longitudinal*

## Canonical ensemble

A thermodynamic ensemble in which the temperature is allowed to vary. The relevant free energy is then the Helmholtz free energy  $F = U - TS$ . 3, 5, 6, 36, 157, *see grand canonical ensemble*

## Chemical potential

A property of a grand canonical system in thermodynamics which represents the cost of introducing particles to the system. For charged particles, we can consider the cost of introducing a pair of charges at infinity and bringing them into the system. In 2D, this operation is not well-defined, and we use the core-energy instead. 17, *see grand canonical ensemble & core-energy*

## Core-energy

A finite term which we add to the energy calculation of the 2D Coulomb gas in place of the chemical potential, which is not well-defined in the case of a

## Glossary

confining potential. [xx](#), [17](#), [63](#), [100](#), [104](#), [111](#), [117](#), [119](#), [121](#), [124](#), [125](#), [131](#), [133](#), [134](#), [137–140](#), [150](#), [169](#), see [chemical potential](#)

### Coulomb phase

A phase described by Henley [3] which occurs in many frustrated magnetic systems. There are three criteria: a directed flux on a lattice, an effective divergenceless constraint on an associated vector field, and no long-range order. This Coulomb phase then has an entirely transverse field representation. [51](#), [56](#), [63](#), [137](#), [152](#), [156](#), see [transverse & Helmholtz-Hodge decomposition](#)

### Coulomb's law

The law governing the interaction of two electrically charged particles (or magnetic monopoles). Its form is different depending on the dimension of the system. [1](#)

In 2D, the the Coulomb potential is logarithmic, and therefore confining: the energy cost of separating two particles increases with the distance. The BKT transition represents the point where the gain in entropy of allowing charges to be free overcomes this energy barrier. [2](#), see [BKT transition](#)

In 3D, the the Coulomb potential goes as  $1/r$ , and is therefore non-confining: the energy cost of separating two particles decreases with distance and goes to zero at infinity. This means that there is no BKT transition in 3D. [1](#)

### F model

A vertex model derived from the six-vertex model. The two configurations with zero overall moment are set at lower energy than those with an overall moment. This makes it the “opposite” model to the KDP model. Its ground state is doubly degenerate and displays antiferroelectric order, making it a common toy model for antiferroelectrics. Often called the Rys F model [4], it was also solved by Lieb [5], and also exhibits a BKT transition. [50](#), [62](#), [114](#), [140](#), see [KDP model & BKT transition](#)

### Frustration

Frustration refers to an inability to simultaneously minimise all local interaction energies in a system, often due to geometrical considerations or the imposition of a symmetry on the system. [5](#), [51](#)

**Generalised lattice Coulomb gas**

Coulomb system on a lattice with rotational field component allowed to be finite. 4, 6, 19, 33, 82, 100, 143, 147, 156, 157, *see traditional lattice Coulomb gas & Helmholtz-Hodge decomposition*

**Grand canonical ensemble**

A thermodynamic ensemble in which the temperature and particle number are allowed to vary. The relevant potential is then the grand (or Landau) potential:  $\Phi = U - TS - \mu N$ . 3, 5, 6, 77, 138, 143, 157, *see canonical ensemble*

**Harmonic XY model**

An XY-type model introduced independently by Bramwell & Holdsworth [6] and Vallat & Beck [7]. It is found by expanding the cosine potential of the XY model up to the squared term and introducing an onsite variable  $n_{ij}$ , representing vortices, which keeps the spin difference between  $[-\pi, \pi]$  everywhere. It also exhibits a BKT transition. 5, 39, 42, 47, 143, 148, 150, 157, *see XY model & BKT transition*

**Helmholtz-Hodge decomposition**

A decomposition which can be performed on an arbitrary vector field  $\mathbf{F}$  by splitting it into divergence-full, divergence-free and harmonic terms. 19, 26, 29, 43, 52, 77, 78, 81, 84, 86, 137, 147, 156, 174

**Ice model**

A type of vertex model in which an effective divergenceless constraint is placed on the vertex. The original example is that of water ice, in which each oxygen atom has two hydrogens to which it is covalently bonded and two to which it is hydrogen bonded. 50, *see vertex model*

**Irrational (field component)**

The divergence-full component of a vector field. 20, 88, 92, 95, *see longitudinal*

**KDP model**

A vertex model derived from the six-vertex model. The four configurations with an overall moment are set at lower energy than those without an overall

## Glossary

moment. This gives a four-fold degenerate ground state with ferroelectric order, making it a common toy model for ferroelectrics. 51, *see F model*

### **Longitudinal (field component)**

The longitudinal field component is the field given by  $\mathbf{q} \times \mathbf{E}(\mathbf{q}) = 0$ . This corresponds to the divergence-full component of the field in direct space. xv, 31, 52, 80, 81, 86, 87, 90, 92, 103, 115, 121, 124, *see transverse & Helmholtz-Hodge decomposition*

### **Maggs-Rossetto algorithm**

An algorithm for simulation of Coulombic systems developed by Maggs and collaborators [8], which uses a rotational auxiliary field in order to reduce computational complexity. In this case the auxiliary field is used simply as a tool, rather than an object of study. xvi, 9, 19, 20, 26, 29, 47, *see Helmholtz-Hodge decomposition*

### **Pinch point**

A common feature found in neutron scattering data of emergent Coulomb systems. Roughly the shape of an hourglass, they arise from the transverse component of the field. xx, 77, 88, 89, 92, 94–96, 111, 125, 137, 138, 150, 156, 173, 174, *see bow tie & transverse*

### **Rotational (field component)**

The divergence-free component of a vector field. 20, 88, 92, 95, *see transverse*

### **Six-vertex model**

A vertex model derived from the sixteen-vertex model, where the only allowed configurations have two arrows pointing in and two pointing out. There are six such configurations, four with an overall moment and two without; by grouping them and assigning energies to them we can construct three different statistical mechanics models. 50, 62, *see square ice (Lieb) model, F model & KDP model*

### **Sixteen-vertex model**

A vertex model for  $\mathbb{Z}_2$  (Ising-like) spins on the square lattice on the square lattice. There are  $2^4 = 16$  possible configurations of one vertex, hence the name. By allowing or disallowing some vertices and assigning energies to

the different configurations, we can recover multiple well-known statistical mechanics models. 49, 61, *see* six-vertex model

### **Spin ice**

A group of rare-earth pyrochlores with formula  $X_2Y_2O_7$ , e.g. holmium titanate. Their comparatively weak (ferromagnetic) exchange interactions and strong magnetic moments combine with the pyrochlore geometry to make them highly frustrated systems, exhibiting a Coulomb phase and providing a magnetic analogue of the water ice problem studied by Bernal & Fowler [9] and Pauling [10], among others. 5, 52, 53, 87, 91, 118, 137

### **Square ice (Lieb) model**

The six-vertex model with the energy of all six vertex configurations set to zero. This gives an exact degeneracy which mimics the two-in-two-out degeneracy of ice models. Exactly solved by Lieb [11]. 50, 62, *see* square ice (Lieb) model, F model & KDP model

### **Traditional lattice Coulomb gas**

Coulomb system on a lattice with rotational field component equal to zero (electrostatic case). 4, 5, 82, *see* generalised lattice Coulomb gas & Helmholtz-Hodge decomposition

### **Transverse (field component)**

The transverse field component is the field given by  $\mathbf{q} \cdot \mathbf{E}(\mathbf{q}) = 0$ . This corresponds to the divergence-free component of the field in direct space. xv, 32, 52, 80, 81, 87, 103, 114, 115, 124, 137, 169, *see* longitudinal & Helmholtz-Hodge decomposition

### **Vertex model**

A type of statistical mechanics model in which the energies correspond to states of the vertices, rather than the edges. 48, 61

### **Villain model**

An XY-type model introduced by Villain [12]. It is very similar to the harmonic XY model but the  $n_{ij}$  variables are independently sampled and hence cannot be treated as vortices. 41, 42, *see* harmonic XY model

## Glossary

### **XY model**

A well-known theoretical model in statistical physics, condensed matter and magnetism. It consists of  $U(1)$  spins on a square lattice which interact via a cosine potential. 4, 35, 37, 39, 41, 42, 51, 87, 91, 124, 146, 156, *see BKT transition*

# Acronyms

## ASI

Artificial spin ice. 61

## BKT

Berezinskii-Kosterlitz-Thouless (transition). 36

## CE

Canonical ensemble. 157

## DSI

Dipolar spin ice. 53, 56–58

## GCE

Grand canonical ensemble. 77

## GLCG

Generalised lattice Coulomb gas. 19, 23, 24, 26, 61, 63, 84, 114, 118, 138, 148, 150, 152, 156

## HXY

Harmonic XY. 33, 35, 39, 42, 143, 152, 156

## LGF

Lattice Green’s function. 11

## MR

Maggs-Rossetto. 19

## NNSI

Near-neighbour spin ice. 53, 54, 57, 58

*Acronyms*

**TLCG**

Tradditional lattice Coulomb gas. [xv](#), [32](#), [82](#)

# Symbols

$\chi_{\bar{\mathbf{E}}}$

Harmonic susceptibility.

$\chi_p$

Harmonic polarisation susceptibility.

$\chi_w$

Winding susceptibility.

$\epsilon_0$

Permittivity of free space.

$\epsilon$

Permittivity ( $= \epsilon_0 \epsilon_r$ ).

$\epsilon_r$

Relative permittivity.

$\mathbf{G}$

Reciprocal lattice vector.

$\mu$

Chemical potential.

$\mu_0$

Permeability of free space.

$\mu_B$

Bohr magneton.

## Symbols

$q$

Charge value.

$\mathbf{Q}$

Neutron wavevector.

$\mathbf{q}$

Sample wavevector.

$S^{\alpha\beta}(\mathbf{q})$

Correlation tensor.

$S^\perp(\mathbf{Q})$

Neutron scattering function.

$u$

Core-energy.

$x_l$

# 1. Introduction

## 1.1. Coulomb's law

Since this thesis will focus on field correlations in Coulomb gases, it is natural to begin with the derivation of [Coulomb's law](#).

The standard way to do this is to begin with an electric field which is the gradient of a scalar potential:

$$\mathbf{E} = -\nabla\phi(\mathbf{r}) \quad (1.1)$$

and then use Gauss' law

$$\nabla \cdot \mathbf{E} = \frac{\rho(\mathbf{r})}{\epsilon_0} \quad (1.2)$$

to arrive at Poisson's equation (in vacuum):

$$\nabla^2\phi(\mathbf{r}) = -\rho(\mathbf{r})/\epsilon_0 \quad (1.3)$$

In general, we can solve this by the method of Green's functions. Our Green's function in the [3D](#) case is defined by

$$\nabla^2G(\mathbf{r}, \mathbf{r}') = -\delta^3(\mathbf{r} - \mathbf{r}') \quad (1.4)$$

We start by considering the integral

$$\int_V \nabla^2G(\mathbf{r}, \mathbf{r}')dV = \int_V \delta^3(\mathbf{r} - \mathbf{r}')dV = 1 \quad (1.5)$$

where  $\mathbf{r}'$  must be inside the region  $V$  for the integration of the delta function. By the divergence theorem,

$$\int_V \nabla^2G(\mathbf{r}, \mathbf{r}')dV = \int_S \nabla G(\mathbf{r}, \mathbf{r}') \cdot \hat{\mathbf{n}}dS \quad (1.6)$$

where  $\hat{\mathbf{n}}$  is the outward unit normal to  $S$  at any point. The problem is spherically

## 1. Introduction

symmetric, precluding any dependence on  $\theta$  or  $\phi$ , so we have  $G(\mathbf{r}, \mathbf{r}') = G(\mathbf{r} - \mathbf{r}') = G(r)$ ; the surface integral is then

$$\int_S \nabla G(\mathbf{r}, \mathbf{r}') \cdot \hat{\mathbf{n}} dS = \int_S \frac{dG}{dr} \hat{\mathbf{r}} \cdot \hat{\mathbf{n}} r^2 \sin \theta d\theta d\phi \quad (1.7)$$

$$= 4\pi r^2 \left. \frac{dG}{dr} \right|_{r=R} = 1 \quad (1.8)$$

where  $R$  is the radius of the surface  $S$ . We then trivially have

$$\frac{dG}{dr} = \frac{1}{4\pi r^2} \quad (1.9)$$

$$G(r) = \frac{-1}{4\pi r} + C \quad (1.10)$$

We fix the constant by requiring that  $G(\infty) = 0$ , so that  $C = 0$ . To obtain the potential for a specific system we need to know the charge distribution: for the example of a single point charge of magnitude  $q$  at the origin, the charge distribution is simply

$$\rho(\mathbf{r}) = q\delta^3(\mathbf{r}) \quad (1.11)$$

and following the above procedure gives us the potential at a distance  $r$ ,

$$\phi(r) = \frac{q}{4\pi\epsilon_0 r} \quad (1.12)$$

In 2D the derivation is very similar: we use the divergence theorem in the same way but we now have

$$\int_S \nabla G(\mathbf{r}, \mathbf{r}') \cdot \hat{\mathbf{n}} dS = \int_C \frac{dG}{dr} \hat{\mathbf{r}} \cdot \hat{\mathbf{n}} r d\theta \quad (1.13)$$

$$= 2\pi r \left. \frac{dG}{dr} \right|_{r=R} = 1 \quad (1.14)$$

where our surface integral is now simply a line integral  $\int_0^{2\pi} d\theta$  at constant radius  $R$ . Following the same procedure we find

$$\frac{dG}{dr} = \frac{1}{2\pi r} \quad (1.15)$$

$$G(r) = \frac{-1}{2\pi} \ln r + C \quad (1.16)$$

In 2D we obviously cannot use the same boundary condition as 3D since the 2D Coulomb potential diverges for  $r \rightarrow \infty$ ; instead we choose  $G(1) = 0$ , which

has the desired effect of setting the constant  $C$  to zero.

In both cases, then, we begin with the gradient of a scalar potential, but in fact there is a more general class of solutions to Gauss’ law, which I will refer to in this thesis as “generalised” Coulomb gases: a description of both the “traditional” Coulomb gas and its generalised counterpart follow.

## 1.2. Coulomb gases: the “traditional” and the generalised

A Coulomb gas is simply a gas of electric charges interacting via the Coulomb law presented above, which rather general definition encompasses an extremely broad range of experimental applications. The main difficulty in studying Coulomb gases arises from the Coulomb interaction itself, which is long-ranged and hence exhibits very different dynamics and statistical mechanics than would be found in an ideal gas, where the only interaction is a short-ranged hard-core repulsion. Methods of studying ideal gases then need to be extended or adapted in order to better capture the physics of the Coulomb gas.

The first discovered examples of Coulomb gases were electrolytes. Examples of electrolytes and related problems in which electrostatic correlations become important appear everywhere from biophysics and soft matter [13, 14] to plasma physics [15], with reviews in [16] among others. Arrhenius [17] was the first to understand that molecules dissociate into separate ions into solution, and that those ions obey the same laws which describe gases. The first theory to take into account the non-ideality of the Coulomb gas was that of Debye and Hückel [18, 19], who proposed that each ion is surrounded by an atmosphere of opposite charge, so that the effective potential decays exponentially over some characteristic length. Debye-Hückel theory was then extended by Bjerrum [20], who corrected it to include neutral pairs bound by the Coulomb interaction, and many further corrections also exist which are beyond the scope of this work to discuss; further detail can be found in [21, 22] among many others.

One simple model which captures the general properties of the Coulomb gas is the restricted primitive model (RPM), which consists of equal and opposite charges with the same ionic diameter  $a$  which interact via the Coulomb law and hard-core repulsion. The RPM can easily be studied in the canonical and grand canonical ensembles, in the continuum or on a lattice, and there exists an extensive literature on the subject; for an introduction see for example [23].

## 1. Introduction

However, electrolyte theory and the restricted primitive model only consider the “traditional” solutions to Gauss’ law, where the electric field is the gradient of some scalar potential; I will refer to such a model as the **traditional lattice Coulomb gas**. As mentioned above, this is not the most general solution: Gauss’ law only relates the divergence of the field to the charge density, and as such we can add any term to the electric field whose divergence is zero. Hence, any field which can be expressed as

$$\mathbf{E}(\mathbf{x}) = -\nabla\phi + \nabla \times \mathbf{Q} + \bar{\mathbf{E}} \quad (1.17)$$

for some arbitrary vector field  $\mathbf{Q}$  and some constant vector  $\bar{\mathbf{E}}$ , is also trivially a solution to Gauss’ law, since the divergence of a curl is identically zero. A Coulomb gas with an associated electric field of this form could be described as a “**generalised lattice Coulomb gas**”; any reference to Coulomb gases in this thesis will refer to a generalised Coulomb gas unless explicitly stated otherwise. I will refer to the component  $\nabla \times \mathbf{Q}$  as the rotational component of the field and the component  $\bar{\mathbf{E}}$  as the harmonic component.

This fact was first noted by Maggs and collaborators [8], who called the  $\nabla \times \mathbf{Q}$  term the “auxiliary” field and used it to develop a fast and local simulation algorithm for Coulombic systems, which will be used throughout this thesis. This is possible because, as will be shown in Chap. 3, the partition function of this generalised system factorises: the rotational component  $\nabla \times \mathbf{Q}$  is statistically independent of the others, and hence the thermodynamics and phase diagram of the system is identical to that of the traditional Coulomb gas. Maggs and collaborators used the rotational component of the field as a simple simulation tool and discarded it, since its thermodynamics are identical to that of the traditional Coulomb gas, but in fact it can be a real object, and an object of interest in and of itself.

For example, it is well known that the 2D Coulomb gas on the square lattice maps to the **2d-XY model** of magnetism [1, 2, 7, 12, 24, 25] and exhibits the celebrated **Berezinskii-Kosterlitz-Thouless (BKT)** transition in the form of a charge unbinding transition first noted by Salzberg and Prager [26]. The XY model of magnetism is well-studied not just for its remarkable statistical mechanics but also for its wide-ranging experimental relevance: thin films of superfluids [27, 28], Bose-Einstein condensates [29], superconducting Josephson junctions [30] and many others have been shown to be described by the XY model. Recent work by Faulkner [31, 32] has shown that the emergent electric field generated by the

mapping from the XY model is in fact that of a generalised Coulomb gas: the low-temperature critical phase of the XY model, which consists of quasi-long-range order arising from spin wave excitations, maps to an entirely rotational electric field and hence provides a prominent example of the utility of the generalised Coulomb gas.

Further examples of generalised Coulomb gases can also be found in the field of frustrated magnetism, in systems such as spin ices [33–35] and artificial spin ices [36–38]. Here, the Coulomb physics arises from the so-called “Coulomb phase” [3]: frustrated magnetic systems often have hard constraints which take the form of divergence-free conditions on some coarse-grained vector field, and this gives a free energy for that field identical to that of an electric field in the absence of charges. Excitations out of this phase then correspond to divergences in the field, and we find a superposition of divergence-full and divergence-free components, just as we do in the generalised Coulomb gas.

In the case of [spin ice](#), for example, the coarse-grained vector field is the magnetisation: in the ground state we have the constraint  $\nabla \cdot \mathbf{M} = 0$ , and excitations out of the ground state correspond to divergences in the magnetisation which can be shown to (approximately) interact via the Coulomb law. Hence, the generalised Coulomb gas provides an approximation to the physics of spin ice as well.

In this thesis, I aim to extend the work of Faulkner by studying the field correlations of the generalised Coulomb gas on the square lattice in both the [canonical ensemble](#) and [grand canonical ensemble](#), as well as the simple cubic lattice in the [grand canonical ensemble](#), and the [harmonic XY model](#) model of magnetism. It should be noted that studying the correlations of the generalised Coulomb gas also gives us the correlations that would be found in a [traditional lattice Coulomb gas](#) “for free”: by decomposing the system into each of the different components given in Eq. 1.17, we can study the correlations of the traditional Coulomb gas as well as the generalised one.

### 1.3. Aims, objectives and thesis plan

Given all of the above, it seems surprising that relatively little attention has been paid to the field correlations of the Coulomb gas in the physics literature. In this thesis, I aim to show that the similarities between the disparate systems mentioned above can be expressed clearly and naturally by adopting a lattice electric-field description of the Coulomb gas and studying its correlations.

Fig. 1.1 shows four examples of (quasi-) neutron scattering plots in different

## 1. Introduction

Coulombic systems: two experimentally derived examples of magnetic structure factors in artificial spin ice, one experimental structure factor of the spin ice material dysprosium titanate, and a simulated field correlation function using a neutron form factor, from my simulations of a generalised Coulomb gas on the square lattice.

The main aim of this thesis is to investigate the 2D grand canonical **generalised lattice Coulomb gas**, paying particular attention to the field correlations, in every region of its phase diagram. I will also study the harmonic XY model in order to provide a concrete example of Coulombic physics in a magnetic system, and will also present results on the 2D **canonical** Coulomb gas and the 3D **grand canonical** Coulomb gas. Chapters 2 and 3 present the theory of **generalised lattice Coulomb gases** which will be used extensively in this work. Chapters 4 and 5 introduce spin models which can be related to the Coulomb gas, including the 2D-XY and harmonic XY models, spin ices and artificial spin ices, as well as presenting the theory of correlation functions and neutron scattering. Chapters 6, 7 and 8 present my results for the 2D **grand canonical** generalised lattice **Coulomb gas**, the harmonic XY model and the 2D **canonical**/3D **grand canonical** Coulomb gases respectively.

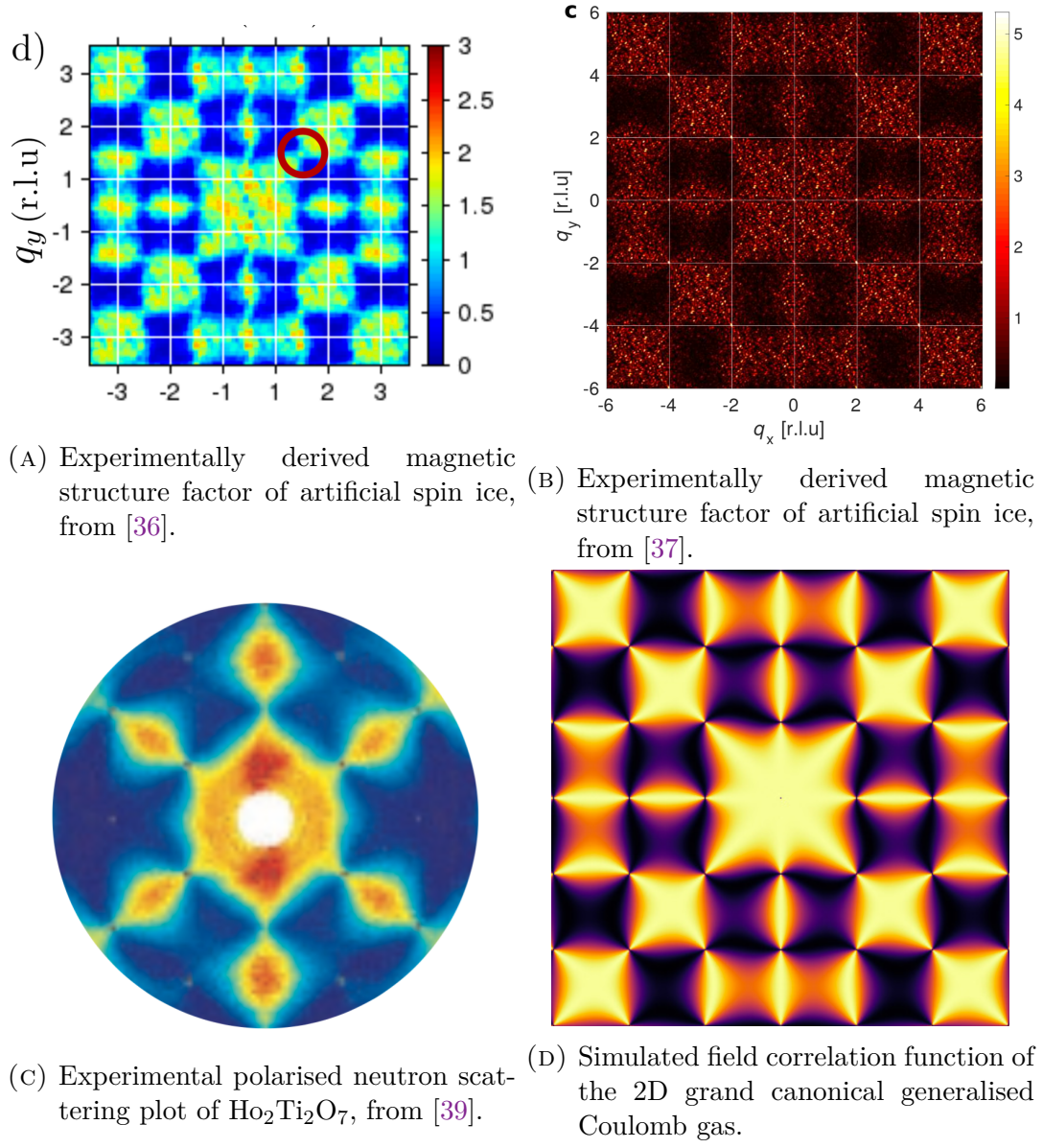


FIGURE 1.1.: (Quasi-) neutron scattering plots for two different types of artificial spin ice, classical spin ice and the 2D Coulomb gas, showing common pinch point features in the correlations.



## 2. Lattice electromagnetic theory

Standard electromagnetic theory assumes a continuous space over which fields and operators are defined, but it is entirely possible to re-derive all of Maxwell's equations along with the Poynting theorem, etc. in a discrete space as well [40]. Such a formulation is inherently useful for simulations, since it is usually necessary to discretise space when working on computational problems. Additionally, this approach obviously lends itself quite naturally to electromagnetic problems which are inherently discrete, such as in XY-type models or spin ices, as will be discussed in Chap. 4. I reproduce the beginning of the derivation of fields, operators and electromagnetic theory up to the definition of a lattice Laplacian; for complete derivations of basic theorems of vector calculus and Maxwell's equations, see Chew [40]. Further information can be also be found, along with a two-dimensional implementation of the [Maggs-Rossetto algorithm](#), in the thesis of Michael Faulkner [31].

### 2.1. Discrete differential operators

Before proceeding to the derivations of Maxwell's equations, it is first necessary to rigorously define discrete vector operators, which in turn require a well-defined discrete derivative. We can do this by defining either a forward or backward difference operator:

$$f'_{n+\frac{1}{2}} = \tilde{\partial}_x f_n = \frac{1}{\Delta_x} [f_{n+1} - f_n] \quad (2.1)$$

$$f'_{n-\frac{1}{2}} = \hat{\partial}_x f_n = \frac{1}{\Delta_x} [f_n - f_{n-1}] \quad (2.2)$$

where  $f_n = f(n\Delta_x)$ ,  $\Delta_x$  is the mesh size, and  $\tilde{\partial}$  and  $\hat{\partial}$  are the forward- and backward-difference analogues of the partial derivative  $\partial$ . The quantities  $f'_{n\pm\frac{1}{2}}$  given by applying the forward or backward difference operators are defined at half-grid points  $n + \frac{1}{2}$  and  $n - \frac{1}{2}$  respectively. Expanding on this, we can define a

## 2. Lattice electromagnetic theory

discrete forward or backward gradient operator in 3D as follows:

$$\tilde{\nabla}f(x, y, z) = \tilde{\partial}_x f(x, y, z) \mathbf{e}_x + \tilde{\partial}_y f(x, y, z) \mathbf{e}_y + \tilde{\partial}_z f(x, y, z) \mathbf{e}_z \quad (2.3)$$

$$= \left[ \frac{1}{\Delta_x} (f(x+1, y, z) - f(x, y, z)) \right] \mathbf{e}_x \quad (2.4)$$

$$+ \left[ \frac{1}{\Delta_y} (f(x, y+1, z) - f(x, y, z)) \right] \mathbf{e}_y$$

$$+ \left[ \frac{1}{\Delta_z} (f(x, y, z+1) - f(x, y, z)) \right] \mathbf{e}_z$$

and

$$\hat{\nabla}f(x, y, z) = \hat{\partial}_x f(x, y, z) \mathbf{e}_x + \hat{\partial}_y f(x, y, z) \mathbf{e}_y + \hat{\partial}_z f(x, y, z) \mathbf{e}_z \quad (2.5)$$

$$= \left[ \frac{1}{\Delta_x} (f(x, y, z) - f(x-1, y, z)) \right] \mathbf{e}_x \quad (2.6)$$

$$+ \left[ \frac{1}{\Delta_y} (f(x, y, z) - f(x, y-1, z)) \right] \mathbf{e}_y$$

$$+ \left[ \frac{1}{\Delta_z} (f(x, y, z) - f(x, y, z-1)) \right] \mathbf{e}_z$$

Note that following the definition of the difference operators above, the components of this discrete gradient are defined at different half-grid points: the x-component is defined at the point  $(x \pm \frac{1}{2}, y, z)$  for a forward or backward gradient respectively, and analogously for the other components. I will use the notation  $\tilde{\partial}_\mu f = \tilde{F}_\mu$ , with the vector  $(F_x, F_y, F_z) \equiv \mathbf{F}$ ; using parentheses to denote the point at which a given component is defined, we can write Eq. 2.5 as

$$\tilde{\nabla}f(x, y, z) = \tilde{\partial}_x f(x, y, z) \mathbf{e}_x + \tilde{\partial}_y f(x, y, z) \mathbf{e}_y + \tilde{\partial}_z f(x, y, z) \mathbf{e}_z \quad (2.7)$$

$$= \tilde{F}_x(x + \frac{1}{2}, y, z) \mathbf{e}_x + \tilde{F}_x(x, y + \frac{1}{2}, z) \mathbf{e}_y + \tilde{F}_x(x, y, z + \frac{1}{2}) \mathbf{e}_z \quad (2.8)$$

$$= \sum_{\mu \in \{x, y, z\}} \tilde{\mathbf{F}}(\mathbf{x} + \frac{a}{2} \mathbf{e}_\mu) \quad (2.9)$$

We can then use the example of the vector field defined by Eq. 2.9 to define the discrete divergence and curl operators. For example, the backward divergence of the field  $\tilde{\mathbf{F}}$  is defined as

$$\hat{\nabla} \cdot \tilde{\mathbf{F}} = \hat{\partial}_x \tilde{F}_x + \hat{\partial}_y \tilde{F}_y + \hat{\partial}_z \tilde{F}_z = \sum_{\mu \in \{x, y, z\}} \hat{\partial}_\mu \tilde{\mathbf{F}}(\mathbf{x} + \frac{a}{2} \mathbf{e}_\mu) \quad (2.10)$$

with the quantity  $\hat{\nabla} \cdot \tilde{\mathbf{F}}$  being equal to the flux through the faces of a cuboid with

dimensions  $(\Delta_x, \Delta_y, \Delta_z)$  centred on  $(x, y, z)$ . The discrete curl is equal to

$$\tilde{\nabla} \times \tilde{\mathbf{F}} = (\tilde{\partial}_y \tilde{F}_z - \tilde{\partial}_z \tilde{F}_y) \mathbf{e}_x \quad (2.11)$$

$$+ (\tilde{\partial}_z \tilde{F}_x - \tilde{\partial}_x \tilde{F}_z) \mathbf{e}_y \quad (2.12)$$

$$+ (\tilde{\partial}_x \tilde{F}_y - \tilde{\partial}_y \tilde{F}_x) \mathbf{e}_z$$

$$\Rightarrow (\tilde{\nabla} \times \tilde{\mathbf{F}})_i = \sum_{j,k,l \in \{x,y,z\}} \delta_{ij} \epsilon_{jkl} \tilde{\partial}_k \tilde{F}_l$$

Finally we can define a discrete Laplacian using these operators:

$$\hat{\nabla} \cdot \tilde{\nabla} f(x, y, z) = \hat{\partial}_x \tilde{\partial}_x f(x, y, z) + \hat{\partial}_y \tilde{\partial}_y f(x, y, z) + \hat{\partial}_z \tilde{\partial}_z f(x, y, z) \quad (2.13)$$

It should also be noted that  $\hat{\nabla} \cdot \tilde{\nabla} f(x, y, z) \equiv \tilde{\nabla} \cdot \hat{\nabla} f(x, y, z)$ , since the partial derivatives commute. For brevity,  $\hat{\nabla} \cdot \tilde{\nabla} f(x, y, z)$  will be referred to as  $\nabla^2 f(x, y, z)$  henceforth, but this is only strictly true in the limit  $\Delta_\mu \rightarrow 0$  for  $\mu \in [x, y, z]$ .

As mentioned above, we can use the discretised vector operators to reproduce the standard theorems and formulas of vector calculus, along with Maxwell's equations

$$\tilde{\nabla} \times \tilde{\mathbf{E}} = -\tilde{\partial}_t \hat{\mathbf{B}} \quad (2.14)$$

$$\hat{\nabla} \times \hat{\mathbf{H}} = \hat{\partial}_t \tilde{\mathbf{D}} + \tilde{\mathbf{J}} \quad (2.15)$$

$$\tilde{\nabla} \cdot \hat{\mathbf{B}} = 0 \quad (2.16)$$

$$\hat{\nabla} \cdot \tilde{\mathbf{D}} = \rho \quad (2.17)$$

and Poisson's equation

$$\hat{\nabla} \cdot \tilde{\nabla} \phi(\mathbf{x}) = -\frac{\rho(\mathbf{x})}{\epsilon_0} \quad (2.18)$$

It is Poisson's equation that we need to solve to find the initial divergence-full field configuration. I do this by deriving the relevant [Lattice Green's function \(LGF\)](#).

## 2.2. Lattice Green's functions

Once we have derived the familiar formulae of electromagnetism using a lattice field description, we can derive the Green's function for our lattice and use it to solve Poisson's equation. For a given differential operator  $\mathcal{L}$  the Green's function

## 2. Lattice electromagnetic theory

$G(\mathbf{x}, \mathbf{x}')$  is the function which satisfies

$$\mathcal{L}G(\mathbf{x}, \mathbf{x}') = \delta^d(\mathbf{x} - \mathbf{x}') \quad (2.19)$$

in  $d$  dimensions, so that

$$\mathcal{L}f(\mathbf{x}) = \int G(\mathbf{x}, \mathbf{x}') f(\mathbf{x}') d\mathbf{x}' \quad (2.20)$$

An analogous result follows for a discrete function, with the integral replaced by a sum and the continuum Green's function replaced by a Green's function which depends on the lattice. Lattice Green's functions are available for a range of lattices [41]; here I derive the Green's functions for the square and simple cubic cases.

### 2.2.1. Two dimensions: square lattice

We start with the discrete version of Poisson's equation, which we can write as:

$$\sum_{\mathbf{x}_\mu \in \text{NN}_x} [\phi(\mathbf{x}) - \phi(\mathbf{x}_\mu)] = \frac{q}{\epsilon_0} \sum_{\mathbf{x}' \in D} m(\mathbf{x}') \delta_{\mathbf{x}\mathbf{x}'} \quad (2.21)$$

We can define  $\phi(\mathbf{x})$  as

$$\phi(\mathbf{x}) = \frac{q}{\epsilon_0} \sum_{\mathbf{x}' \in D} G(\mathbf{x}, \mathbf{x}') m(\mathbf{x}') \quad (2.22)$$

and combine both of these expressions to get

$$\frac{q}{\epsilon_0} \sum_{\mathbf{x}_\mu \in \text{NN}_x} \sum_{\mathbf{x}' \in D} \sum_{\mu \in \{x,y\}} [2G(\mathbf{x}, \mathbf{x}') - G(\mathbf{x} - a\mathbf{e}_\mu, \mathbf{x}') - G(\mathbf{x} + a\mathbf{e}_\mu, \mathbf{x}')] m(\mathbf{x}') \quad (2.23)$$

Combining these we can write

$$\delta_{\mathbf{x}\mathbf{x}'} = \sum_{\mu \in \{x,y\}} [2G(\mathbf{x}, \mathbf{x}') - G(\mathbf{x} - a\mathbf{e}_\mu, \mathbf{x}') - G(\mathbf{x} + a\mathbf{e}_\mu, \mathbf{x}')] \quad (2.24)$$

but we also have identically that

$$\delta_{\mathbf{x}\mathbf{x}'} = \frac{1}{N} \sum_{\mathbf{k} \in B} e^{i\mathbf{k} \cdot (\mathbf{x} - \mathbf{x}')} \quad (2.25)$$

where

$$\sum_{\mathbf{k} \in B} = \prod_{\mu \in \{x,y\}} \sum_{k_\mu \in B_\mu} \text{ and } B_\mu \in \{0, \pm \frac{2\pi}{N_\mu a}, \pm \frac{4\pi}{N_\mu a}, \dots, \frac{N_\mu}{2} \frac{2\pi}{n_\mu a}\}. \quad (2.26)$$

Hence, we can write

$$\sum_{\mathbf{k} \in B} e^{i\mathbf{k} \cdot (\mathbf{x} - \mathbf{x}')} = N \sum_{\mu \in \{x,y\}} [2G(\mathbf{x}, \mathbf{x}') - G(\mathbf{x} - a\mathbf{e}_\mu, \mathbf{x}') - G(\mathbf{x} + a\mathbf{e}_\mu, \mathbf{x}')]. \quad (2.27)$$

By definition, we can express the Green's function in Fourier space as

$$\tilde{G}_{\mathbf{x}'}(\mathbf{k}) = \sum_{\mathbf{x} \in D} e^{-i\mathbf{k} \cdot \mathbf{x}} G(\mathbf{x}, \mathbf{x}') \quad (2.28)$$

and then transforming back to direct space we find

$$G(\mathbf{x}, \mathbf{x}') = \frac{1}{N} \sum_{\mathbf{k} \in B} e^{i\mathbf{k} \cdot \mathbf{x}} \tilde{G}_{\mathbf{x}'}(\mathbf{k}) \quad (2.29)$$

$$G(\mathbf{x} + a\mathbf{e}_\mu, \mathbf{x}') = \frac{1}{N} \sum_{\mathbf{k} \in B} e^{i\mathbf{k} \cdot (\mathbf{x} + a\mathbf{e}_\mu)} \tilde{G}_{\mathbf{x}'}(\mathbf{k}) \quad (2.30)$$

$$= \frac{1}{N} \sum_{\mathbf{k} \in B} e^{ik_\mu a} e^{i\mathbf{k} \cdot \mathbf{x}} \tilde{G}_{\mathbf{x}'}(\mathbf{k}) \quad (2.31)$$

$$(2.32)$$

Combining all this, we have

$$\sum_{\mathbf{k} \in B} e^{i\mathbf{k} \cdot (\mathbf{x} - \mathbf{x}')} = \sum_{\mathbf{k} \in B} e^{i\mathbf{k} \cdot \mathbf{x}} (4 - e^{ik_x a} - e^{-ik_x a} - e^{ik_y a} - e^{-ik_y a}) \tilde{G}_{\mathbf{x}'}(\mathbf{k}) \quad (2.33)$$

which leads to

$$\tilde{G}_{\mathbf{x}'}(\mathbf{k}) = \frac{e^{-i\mathbf{k} \cdot \mathbf{x}'}}{2(2 - \cos(k_x a) - \cos(k_y a))} \quad \forall \mathbf{k} \neq \mathbf{0} \quad (2.34)$$

We can then transform back to direct space to end up with

$$G(\mathbf{x}, \mathbf{x}') = \frac{1}{2N} \sum_{k_\mu \in B} \frac{e^{i\mathbf{k} \cdot (\mathbf{x} - \mathbf{x}')}}{2 - \cos(k_x a) - \cos(k_y a)} \quad \forall \mathbf{k} \neq \mathbf{0} \quad (2.35)$$

### 2.2.2. Three dimensions: simple cubic lattice

For the simple cubic lattice in 3D, the derivation proceeds identically to the above, with the obvious difference that we now have  $\mu \in \{x, y, z\}$  for each quantity summed over Cartesian components. The derivation diverges at Eq. 2.33 above, where we instead find

$$\sum_{\mathbf{k} \in B} e^{i\mathbf{k} \cdot (\mathbf{x} - \mathbf{x}')} = \sum_{\mathbf{k} \in B} e^{i\mathbf{k} \cdot \mathbf{x}} (6 - e^{ik_x a} - e^{-ik_x a} - e^{ik_y a} - e^{-ik_y a} - e^{ik_z a} - e^{-ik_z a}) \tilde{G}_{\mathbf{x}'}(\mathbf{k}) \quad (2.36)$$

Following the same procedure, we finally find for the simple cubic lattice Green's function

$$G_{sc}(\mathbf{x}, \mathbf{x}') = \frac{1}{2N} \sum_{k_\mu \in B} \frac{e^{i\mathbf{k} \cdot (\mathbf{x} - \mathbf{x}')}}{3 - \cos(k_x a) - \cos(k_y a) - \cos(k_z a)} \quad \forall \mathbf{k} \neq \mathbf{0} \quad (2.37)$$

with  $\mathbf{k}$  and  $\mathbf{B}$  again defined analogously to the 2D case.

## 2.3. Partition function of a Coulomb gas in the Green's function representation

We can now formulate the partition function of a Coulombic system using the Green's functions presented above. The derivation here is identical for the two- and three-dimensional cases. We start by writing the total energy of the system in the electric-field representation, i.e. the energy of the fields:

$$U_{\text{Field}} = \frac{\epsilon_0}{2} \sum_{\mathbf{x}} |\mathbf{E}(\mathbf{x})|^2 \quad (2.38)$$

We could then simply write the partition function for the Coulomb gas as

$$Z_{\text{Coulomb}}^0 = \sum_{\{\rho(\mathbf{x})\}} \int \mathcal{D}\mathbf{E} \prod_{\mathbf{x}} \left[ \delta^d \left( \hat{\nabla} \cdot \mathbf{E}(\mathbf{x}) - \frac{\rho(\mathbf{x})}{\epsilon_0} \right) \right] \times \exp \left( -\frac{\beta \epsilon_0}{2} \sum_{\mathbf{x}} |\mathbf{E}(\mathbf{x})|^2 \right) \quad (2.39)$$

This formulation is technically correct, but it is also possible to decompose the field energy in order to separate out some of the complexity in the final term. We start by noting that in addition to Poisson's equation we also have Gauss' law for electrostatics:

### 2.3. Partition function of a Coulomb gas in the Green's function representation

$$\hat{\nabla} \cdot \tilde{\nabla} \phi(\mathbf{x}) = \nabla^2 \phi(\mathbf{x}) = \frac{-\rho(\mathbf{x})}{\epsilon_0} \quad (2.40)$$

for which the simplest electrostatic solution can be written

$$\mathbf{E}(\mathbf{x}) = -\tilde{\nabla} \phi \quad (2.41)$$

so that we satisfy Gauss' law:

$$\hat{\nabla} \cdot \mathbf{E} = \frac{\rho(\mathbf{x})}{\epsilon_0} \quad (2.42)$$

It is also generally possible to add a harmonic term which I will term  $\bar{\mathbf{E}}$ . This is some constant vector which we name harmonic since it trivially satisfies Laplace's equation  $\nabla^2 \bar{\mathbf{E}} = 0$ , and hence both its divergence and its curl will be zero. Adding such a term gives us

$$\mathbf{E}(\mathbf{x}) = -\tilde{\nabla} \phi + \bar{\mathbf{E}} \quad (2.43)$$

for a general electrostatic solution to the Poisson equation.

We can then write [31]

$$U_{\text{Field}} = \frac{\epsilon_0}{2} \sum_{\mathbf{x}} |\mathbf{E}(\mathbf{x})|^2 \quad (2.44)$$

$$U_{\text{Field}} = \frac{\epsilon_0}{2} \sum_{\mathbf{x}} \left| -\tilde{\nabla} \phi(\mathbf{x}) + \bar{\mathbf{E}} \right|^2 \quad (2.45)$$

$$= \frac{\epsilon_0}{2} \sum_{\mathbf{x}} \left| -\tilde{\nabla} \phi(\mathbf{x}) \right|^2 + \epsilon_0 \sum_{\mathbf{x}} -\tilde{\nabla} \phi(\mathbf{x}) \cdot \bar{\mathbf{E}} + \frac{\epsilon_0 N}{2} |\bar{\mathbf{E}}|^2 \quad (2.46)$$

Now we note that the coupling between the potential and harmonic terms is zero because the harmonic term factors out of the sum, and the sum of the non-harmonic components is zero by definition. In the following I omit arguments ( $\mathbf{x}$ ) from the potentials  $\phi$  for brevity. Also, we can use the vector calculus identity  $\nabla \cdot (\phi \tilde{\nabla} \phi) = \phi \nabla^2 \phi + \tilde{\nabla} \phi \cdot \tilde{\nabla} \phi$  to rewrite the first term in the last line above:

$$U_{\text{Field}} = \frac{\epsilon_0}{2} \sum_{\mathbf{x}} \left( \nabla \cdot (\phi \tilde{\nabla} \phi) - \phi \nabla^2 \phi \right) + \frac{\epsilon_0 N}{2} |\bar{\mathbf{E}}|^2 \quad (2.47)$$

The first term in the bracket here is zero for systems with periodic boundaries or in the thermodynamic limit, since it equates to a surface term which must vanish. Next we use the principle of superposition to rewrite the first term again,

## 2. Lattice electromagnetic theory

by considering the potential due to each individual charge:

$$U_{\text{Field}} = -\frac{\epsilon_0}{2} \sum_{\mathbf{x}} \phi \nabla^2 \phi + \frac{\epsilon_0 N}{2} |\bar{\mathbf{E}}|^2 \quad (2.48)$$

$$= -\frac{\epsilon_0}{2} \sum_{\mathbf{x}} \sum_{i,j=1}^{n_q} \phi_i \nabla^2 \phi_j + \frac{\epsilon_0 N}{2} |\bar{\mathbf{E}}|^2 \quad (2.49)$$

Next, we use the identities that

$$\nabla^2 G(\mathbf{x}, \mathbf{x}') = -\delta_{\mathbf{x}, \mathbf{x}'}; \quad G(\mathbf{x}, \mathbf{x}_i) = \frac{q_i}{\epsilon_0} \phi_i \quad (2.50)$$

which follow simply from the definition of the Green's function, in order to rewrite the first term yet again:

$$U_{\text{Field}} = -\frac{\epsilon_0}{2} \sum_{\mathbf{x}} \sum_{i,j=1}^{n_q} \phi_i \nabla^2 \phi_j + \frac{\epsilon_0 N}{2} |\bar{\mathbf{E}}|^2 \quad (2.51)$$

$$= -\frac{\epsilon_0}{2} \sum_{\mathbf{x}} \sum_{i,j=1}^{n_q} \frac{q_i}{\epsilon_0} G(\mathbf{x}, \mathbf{x}_i) \nabla^2 \frac{q_j}{\epsilon_0} G(\mathbf{x}, \mathbf{x}_j) + \frac{\epsilon_0 N}{2} |\bar{\mathbf{E}}|^2 \quad (2.52)$$

$$= -\frac{\epsilon_0}{2} \sum_{\mathbf{x}} \sum_{i,j=1}^{n_q} \frac{q_i}{\epsilon_0} G(\mathbf{x}, \mathbf{x}_i) \frac{q_j}{\epsilon_0} \delta_{\mathbf{x}, \mathbf{x}_j} + \frac{\epsilon_0 N}{2} |\bar{\mathbf{E}}|^2 \quad (2.53)$$

$$= \frac{\epsilon_0}{2} \sum_{i,j=1}^{n_q} \frac{q_i}{\epsilon_0} G(\mathbf{x}_j, \mathbf{x}_i) \frac{q_j}{\epsilon_0} + \frac{\epsilon_0 N}{2} |\bar{\mathbf{E}}|^2 \quad (2.54)$$

$$= \frac{1}{2\epsilon_0} \sum_{i,j=1}^{n_q} q_i G(\mathbf{x}_i, \mathbf{x}_j) q_j + \frac{\epsilon_0 N}{2} |\bar{\mathbf{E}}|^2 \quad (2.55)$$

Our final step is to separate the terms where  $\mathbf{x}_i = \mathbf{x}_j$ , which correspond to self-energy terms, from the interaction terms where  $\mathbf{x}_i \neq \mathbf{x}_j$ :

$$U_{\text{Field}} = \frac{1}{2\epsilon_0} \sum_{i,j=1}^{n_q} q_i G(\mathbf{x}_i, \mathbf{x}_j) q_j + \frac{\epsilon_0 N}{2} |\bar{\mathbf{E}}|^2 \quad (2.56)$$

$$= \frac{G(\mathbf{x}, \mathbf{x})}{2\epsilon_0} \sum_i q_i^2 + \sum_{i \neq j} q_i G(\mathbf{x}_i, \mathbf{x}_j) q_j + \frac{\epsilon_0 N}{2} |\bar{\mathbf{E}}|^2 \quad (2.57)$$

and lastly we note the possibility of multivalued charges: this is taken care of in principle by allowing the  $q_i$  to take different values, but for clarity we rewrite the

### 2.3. Partition function of a Coulomb gas in the Green's function representation

first term as

$$U_{\text{Field}} = \frac{G(\mathbf{0})}{2\epsilon_0} \sum_{z \in \mathbb{N}} n_z z^2 q_0^2 + \frac{1}{2\epsilon_0} \sum_{i \neq j} q_i G(\mathbf{x}_i, \mathbf{x}_j) q_j + \frac{\epsilon_0 N}{2} |\bar{\mathbf{E}}|^2 \quad (2.58)$$

where  $z$  is then the magnitude of the charge in units of the fundamental charge  $q_0$ , and we write  $G(\mathbf{0}) \equiv G(\mathbf{x}, \mathbf{x})$  for brevity, since the Green's function depends only on distance. We can use this to write an expression for the chemical potential of the Coulomb gas.

#### 2.3.1. The chemical potential

In general we can think of the **chemical potential** as being a combination of the self-energy of a pair of charged particles being introduced to the system along with a **core-energy** term, which we are free to tune: in this way, there is a cost to introducing a neutral pair of particles to the system which we are free to probe despite depending in part on their intrinsic self-energies.

We can add this core-energy constant analogously to the first term of Eq. 2.61:

$$U_{\text{Core}} = \frac{G(\mathbf{x}, \mathbf{x})}{2\epsilon_0} \sum_{z \in \mathbb{N}} n_z u_z z^2 q_0^2 \quad (2.59)$$

where  $u_z$  is the core-energy constant for a charge of species  $z$ . This constant may be set to zero, to effectively remove the penalty for introducing new charges to the system, to some finite value, or to infinity, which effectively prevents a charge of species  $z$  being generated.

Lastly we define a chemical potential as the sum of the first term in Eq. 2.61 and Eq. 2.59

$$\mu_z = - \left( \frac{G(\mathbf{0})}{\epsilon_0} + u_z \right) n_z z^2 q_0^2 \quad (2.60)$$

and add the quantity  $U_{\text{Core}}$  to  $U_{\text{Field}}$  to give us

$$U_{\text{total}} = - \sum_{z \in \mathbb{N}} \mu_z n_z + \sum_{i \neq j} q_i G(\mathbf{x}_i, \mathbf{x}_j) q_j + \frac{\epsilon_0 N}{2} |\bar{\mathbf{E}}|^2 \quad (2.61)$$

We can then rewrite the partition function of the Coulomb gas in the grand

## 2. Lattice electromagnetic theory

canonical ensemble in terms of the Green's function as

$$Z_{\text{Coul}} = \sum_{\{\rho(\mathbf{x})\}} \int \mathcal{D}\mathbf{E} \prod_{\mathbf{x}} \left[ \delta^d \left( \hat{\nabla} \cdot \mathbf{E}(\mathbf{x}) - \frac{\rho(\mathbf{x})}{\epsilon_0} \right) \right] \\ \times \exp \left( -\frac{\beta G(\mathbf{0})}{2\epsilon_0} \sum_{z \in \mathbb{N}} n_z z^2 q_0^2 \right) \exp \left( -\frac{\beta}{2\epsilon_0} \sum_{i \neq j} q_i G(\mathbf{x}_i, \mathbf{x}_j) q_j \right) \quad (2.62)$$

$$\times \exp \left( -\frac{\beta \epsilon_0 N}{2} |\bar{\mathbf{E}}|^2 \right) \exp (-\beta U_{\text{Core}}) \quad (2.63)$$

It should be noted that as a consequence of defining the core-energy in this way, we can express the phase diagram of the grand canonical Coulomb gas in terms of  $u$  vs.  $T$ , rather than the continuum  $\mu$  vs.  $T$ .

# 3. The generalised lattice Coulomb gas

The construction of the [generalised lattice Coulomb gas \(GLCG\)](#) starts by considering the solutions to Poisson's equation: here, we consider solutions to the discrete version derived in the previous chapter. The derivations presented in this chapter follow on from work by Michael Faulkner [31, 42], who first applied this formalism and the [Maggs-Rossetto \(MR\)](#) simulation algorithm [8] (discussed below) to the square lattice to investigate the [BKT transition](#).

In the previous chapter we used Eq. 2.43 as a general electrostatic solution to Gauss' law

$$\mathbf{E}(\mathbf{x}) = -\nabla\phi + \bar{\mathbf{E}} \quad (3.1)$$

to derive a separated partition function for the Coulomb gas.

Thus far, we have done nothing out of the ordinary except for restricting the fields to lie on the lattice: solving the Poisson equation in this way is central to (to take one example among many) the particle mesh Ewald method [43], variations of which are used widely in numerical simulations of charged systems. However, as noted in Chap. 1, the expression Eq. 2.43 can be extended further: we can construct the most general possible solution by noting that the divergence of a curl is identically zero. Hence, we can always add a term of the form  $\nabla \times \mathbf{Q}$  without violating Gauss' law (or, equivalently, Poisson's equation). We then have for the most general possible solution of Gauss' law

$$\mathbf{E}(\mathbf{x}) = -\nabla\phi + \nabla \times \mathbf{Q} + \bar{\mathbf{E}} \quad (3.2)$$

This description of the electric field as the sum of a divergence-full, divergence-free and harmonic term is an example of a [Helmholtz-Hodge decomposition](#), which will be discussed in more detail below.

### 3.1. The auxiliary field

The second term in Eq. 3.2 is a general divergence-free term which carries all of the rotational degrees of freedom of the field. For a purely electrostatic problem, the lowest-energy configuration of the field is purely **irrotational**, i.e.  $\nabla \times \mathbf{Q} = 0$  everywhere. In a true electrodynamic problem, however, there is also a magnetic field. Here, we deal with a problem analogous to electrodynamics, where we have both **irrotational** and **rotational** components, but in the absence of a magnetic field. As mentioned in Chap. 1, when considering other systems which admit Coulomb phases or which map to Coulomb gases, we can also have a combination of the two components; this will be relevant in Chapter 7, as well as in any discussion of magnetic fields in spin ices, where we also find a combination of the two.

It is important to note that while the vector potential  $\mathbf{Q}$  is freely fluctuating, the auxiliary field itself is not: the divergence-free constraint means that the field  $\nabla \times \mathbf{Q}$  is not a freely fluctuating Gaussian field. This point will be revisited in Chapter 5 in the context of correlation functions and in Chapter 4 in the context of spin systems.

It is also worth pointing out that in this system the **irrotational** and **rotational** fields are not directly coupled. This fact results in the factorisation of the partition function, making them thermodynamically independent, and hence is what drives the **Maggs-Rossetto algorithm**. However, in other systems the two components can be directly related in some way. For example, in spin ices, pairs of monopole defects correspond to the **irrotational** component of the field, but their creation is only possible by breaking up loops of spins in the **rotational**, zero-monopole ground state, and hence fluctuations in the two components are coupled non-trivially.

### 3.2. The harmonic mode

The harmonic term included in the full solution to Gauss' law becomes very important when dealing with systems with periodic boundaries in particular. Before exploring the role of the harmonic mode in more depth, however, it is useful to properly characterise it and decompose it into two parts. We can write the harmonic mode as a sum of a polarisation term and a winding term, which represents the winding of charges all the way around the system in any direction with periodic boundaries. One way to do this is to consider an origin,  $\mathbf{r} = \mathbf{0}$ , and rewrite the sum in terms of overlapping pairs in order to use Gauss' law:

$$\begin{aligned}
 \bar{E}_x &= \frac{a^2}{L^2} \sum_{\mathbf{x}} E_x(\mathbf{x} + \frac{a}{2} \mathbf{e}_x) \\
 &= \frac{a}{L^2} \sum_{y=0}^{L-a} \left[ a \left( E_x(\frac{a}{2}, y) - E_x(a + \frac{a}{2}, y) \right) \right. \\
 &\quad + 2a \left( E_x(a + \frac{a}{2}, y) - E_x(2a + \frac{a}{2}, y) \right) + \dots \\
 &\quad + (L-1)a \left( E_x((L-2)a + \frac{a}{2}, y) - E_x((L-1)a + \frac{a}{2}, y) \right) \\
 &\quad + La \left( E_x(L - \frac{a}{2}, y) - E_x(\frac{a}{2}, y) \right) \\
 &\quad \left. - La \left( E_x(\frac{a}{2}, y) \right) \right] \tag{3.3}
 \end{aligned}$$

where the second term in the second to last line comes from the periodic boundaries. It is obvious that the final pair of terms cancel; elsewhere, the second term in each bracket partially cancels with the first term in the next to give us back the original expression.

This expansion can be rearranged to give us

$$\bar{E}_x = \frac{a^2}{L^2} \sum_{\mathbf{x}} E_x(\mathbf{x} + \frac{a}{2} \mathbf{e}_x) \tag{3.4}$$

$$= \frac{a}{L^2} \sum_{x=0}^{L-a} (x+a) \sum_{y=0}^{L-a} \left( E_x(x + \frac{a}{2}, y) - E_x(x + \frac{3a}{2}, y) \right) + \frac{a}{L} \sum_{y=0}^{L-a} E_x(\frac{a}{2}, y) \tag{3.5}$$

The first sum over  $y$  in the second line here is equivalent to  $-\tilde{\nabla} \cdot \mathbf{E}(\mathbf{x})$  in the  $x$ -direction. By Gauss' law, we equate this to  $\rho(\mathbf{x})/\epsilon_0$ , and by shifting the sums we obtain

$$\bar{E}_x = -\frac{a^2}{\epsilon_0 L^2} \sum_{x=a}^L x \sum_{y=a}^L \rho(\mathbf{x}) + \frac{a}{L} \sum_{y=a}^L E_x(\frac{a}{2}, y) \tag{3.6}$$

The same procedure can be followed for the  $y$ -component, and we eventually obtain

$$\bar{\mathbf{E}} = -\frac{a^2}{\epsilon_0 L^2} \sum_{\mathbf{x} \in D} \mathbf{x} \rho(\mathbf{x}) + \frac{a}{L} \sum_{\mathbf{x} \in D} E_x(\frac{a}{2}, y) + E_y(x, \frac{a}{2}). \tag{3.7}$$

where the equivalent follows easily in 3D.

We then define a winding vector  $\mathbf{w}_0 = \epsilon_0 a \sum_{\mathbf{x} \in D} (E_x(a/2, y) + E_y(x, a/2))/q$  as an origin-dependent measure of the winding number of the system. We also note that the first term in the above is the origin-dependent polarisation of the system

### 3. The generalised lattice Coulomb gas

$\mathbf{P} = \sum_{\mathbf{x} \in D} \mathbf{x} \rho(\mathbf{x})/N$ , and so we have

$$\bar{\mathbf{E}} = -\frac{a^2}{\epsilon_0} \mathbf{P} + \frac{q}{\epsilon_0 L} \mathbf{w}_0 \quad (3.8)$$

The above origin-dependent decomposition of the harmonic mode is instructive but not ideal in practice, since the choice of origin is arbitrary and changing the origin can lead to field quanta being exchanged between the two terms. A more useful way to decompose the harmonic mode is to note that one charge winding around the system  $n$  times, in the same direction, corresponds to adding

$$\bar{E}_\mu \rightarrow \bar{E}_\mu + L \frac{q}{L^d \epsilon_0} n \quad (3.9)$$

to the harmonic mode overall in  $d$  dimensions, regardless of the origin; we can see this from the fact that a single charge hop adds  $\frac{q}{L^d \epsilon_0}$  to the harmonic mode in the direction in which it hops. This results in a change in the grand canonical energy of

$$\Delta U = \frac{\epsilon a^d}{2} \sum_{\mathbf{x} \in D} \left| E_\mu \left( \mathbf{x} + \frac{a}{2} \mathbf{e}_\mu \right) + \frac{q}{L^{d-1} \epsilon} w \right|^2 - \left| E_\mu \left( \mathbf{x} + \frac{a}{2} \mathbf{e}_\mu \right) \right|^2 \quad (3.10)$$

$$= \frac{\epsilon a^d}{2} \sum_{\mathbf{x} \in D} |E_\mu|^2 + \left| \frac{q}{L^{d-1} \epsilon} w \right|^2 + 2E_\mu \left( \frac{qw}{L^{d-1} \epsilon} \right) - |E_\mu|^2 \quad (3.11)$$

$$= \frac{\epsilon a^d}{2} \sum_{\mathbf{x} \in D} \frac{q^2}{L^{2(d-1)} \epsilon^2} + 2E_\mu \left( \frac{qw}{L^{d-1} \epsilon} \right) \quad (3.12)$$

$$= \frac{\epsilon a^d}{2} \left[ L^d \left( \frac{q^2}{L^{2(d-1)} \epsilon^2} \right) + 2L^d \bar{E}_\mu \left( \frac{qw}{L^{d-1} \epsilon} \right) \right] \quad (3.13)$$

$$= \frac{\epsilon a^d}{2} \left[ \left( \frac{L^{2-d} q^2}{\epsilon^2} \right) + 2\bar{E}_\mu \left( \frac{qLw}{\epsilon} \right) \right] \quad (3.14)$$

$$= a^d \left[ \left( \frac{L^{2-d} q^2}{2\epsilon} \right) + 2\bar{E}_\mu \left( \frac{qLw}{2} \right) \right] \quad (3.15)$$

$$= qLa^d \left[ \frac{L^{1-d} q}{2\epsilon} + w\bar{E}_\mu \right] \quad (3.16)$$

$$(3.17)$$

Setting  $a = 1$  this gives us, finally, a grand canonical energy change of

$$qL \left( \frac{q}{2L\epsilon} \pm \bar{E}_\mu \right) \quad (3.18)$$

in 2D and

$$qL \left( \frac{q}{2L^2\epsilon} \pm \bar{E}_\mu \right) \quad (3.19)$$

in 3D.

Since the energy is proportional to the field squared, it is true that the lowest-energy harmonic mode which describes an arbitrary charge configuration lies between

$$\left( -\frac{q}{2L^{d-1}\epsilon}, \frac{q}{2L^{d-1}\epsilon} \right]. \quad (3.20)$$

and hence we can construct an origin-independent decomposition of the harmonic mode:

$$\bar{\mathbf{E}} = \bar{\mathbf{E}}_p + \bar{\mathbf{E}}_w \quad (3.21)$$

where

$$\bar{\mathbf{E}}_p \in \left( -\frac{q}{2L^{d-1}\epsilon}, \frac{q}{2L^{d-1}\epsilon} \right] \quad \text{and} \quad \bar{\mathbf{E}}_w = \frac{q}{L^{d-1}\epsilon} \mathbf{w} \quad (3.22)$$

and  $\mathbf{w}$  is an integer-valued winding vector. The components of  $\mathbf{w}$  are chosen so that  $\bar{\mathbf{E}}_p$  satisfies Eq. 3.22; this is achieved in simulation by applying modular arithmetic to the total calculated  $\bar{\mathbf{E}}$ . The BKT transition then corresponds to the regime where non-zero values of  $\mathbf{w}$  are allowed; at temperatures  $T \approx T_{BKT}$  any windings greater than 1 are heavily suppressed, but at  $T \rightarrow \infty$  the values of the components of  $\mathbf{w}$  are unbounded from above in the GLCG. Allowing different values of  $\mathbf{w}$  then corresponds to allowing topological sector fluctuations. These topological sector fluctuations and the associated winding susceptibility provide a strong signature of the BKT transition, as studied in detail by Faulkner [31, 42].

We can then finally define the associated susceptibilities as

$$\chi_{\mathbf{E}} = \beta\epsilon L^d \left( \langle \bar{\mathbf{E}}^2 \rangle - \langle \bar{\mathbf{E}} \rangle^2 \right) \quad (3.23)$$

$$\chi_{\bar{\mathbf{E}}_p} = \beta\epsilon L^d \left( \langle \bar{\mathbf{E}}_p^2 \rangle - \langle \bar{\mathbf{E}}_p \rangle^2 \right) \quad (3.24)$$

$$\chi_{\bar{\mathbf{E}}_w} = \beta\epsilon L^d \left( \langle \bar{\mathbf{E}}_w^2 \rangle - \langle \bar{\mathbf{E}}_w \rangle^2 \right) \quad (3.25)$$

Note that I will also define  $\chi_p \equiv \chi_{\bar{\mathbf{E}}_p}$   $\chi_w \equiv \chi_{\bar{\mathbf{E}}_w}$  for readability.

### 3.3. The partition function

Using the constraints above for the field, we can now write the partition function of the GLCG as follows:

### 3. The generalised lattice Coulomb gas

$$\begin{aligned}
Z = & \sum_{\{\rho(\mathbf{x}) \in X\}} \sum_{\mathbf{w}_0 \in \mathbb{Z}^2} \int \mathcal{D}\mathbf{E} \prod_{\mathbf{x} \in D} \left[ \delta^d \left( \hat{\nabla} \cdot \mathbf{E}(\mathbf{x}) - \frac{\rho(\mathbf{x})}{\epsilon_0} \right) \right] \\
& \times \delta^d \left( \sum_{\mathbf{x} \in D} \mathbf{E}(\mathbf{x}) + \left( \frac{N}{\epsilon_0} \mathbf{P} - \frac{Nq}{L\epsilon_0 a^d} \mathbf{w}_0 \right) \right) \\
& \times \exp \left( -\frac{\beta \epsilon_0 a^d}{2} \sum_{\mathbf{x} \in D} |\mathbf{E}(\mathbf{x})|^2 \right) \exp(-\beta U_{\text{Core}}) \quad (3.26)
\end{aligned}$$

where  $X = \frac{q\mathbb{Z}}{a^d}$  is the set of all possible charge values.

The first two terms here represent the imposition of Gauss' law and the definition of the harmonic mode of the field; the third is the energy of the system, and the final term  $\exp(-\beta U_{\text{Core}})$  corresponds to the core-energy constants of the system.

#### 3.3.1. Core-energy constant

The core-energy constants will be important when probing the phase diagram of the 2D Coulomb gas. As defined in the previous chapter, we have a core-energy term

$$U_{\text{Core}} = \sum_{z \in \mathbb{N}} n_z u_z z^2 q^2 \quad (3.27)$$

which represents the intrinsic cost of adding a pair of charges to the system and can be directly related to a chemical potential in a continuum system.

$u_z$ , then, is a parameter we can tune in order to change the chemical potential of each charge species of the system. In principle  $u_z$  can be finite  $\forall z$ ; this thesis focuses on the case where  $u_{z>1} = \infty$ , meaning we restrict ourselves to single-valued charges and vary only the parameter  $u_1 \equiv u$ . This is because the two-dimensional spin models which map to the 2D Coulomb gas also have single-valued charges only. In the case of the 2D Coulomb gas there is a first-order transition at a critical value of  $u$ : this will be seen in Chapter 6, where I investigate the behaviour and correlations of the GLCG across the transition.

#### 3.3.2. Expansion of the partition function

The term  $\exp \left( -\frac{\beta \epsilon_0 a^d}{2} \sum_{\mathbf{x} \in D} |\mathbf{E}(\mathbf{x})|^2 \right)$  can be expanded by considering the decoupling of the rotational component from the total field

$$\tilde{\mathbf{E}}(\mathbf{x}) = \mathbf{E}(\mathbf{x}) + \nabla\phi(\mathbf{x}) \quad (3.28)$$

and noting that cross terms in the energy  $\sum_{\mathbf{x} \in D} |\mathbf{E}(x)|^2$  vanish [31], so that

$$\frac{a^d \epsilon_0}{2} \sum_{\mathbf{x} \in D} |\mathbf{E}(\mathbf{x})|^2 = \frac{a^d \epsilon_0}{2} \sum_{\mathbf{x} \in D} \left( |\tilde{\mathbf{E}}(\mathbf{x})|^2 + |\nabla\phi(\mathbf{x})|^2 \right) + \frac{L^d \epsilon_0}{2} |\bar{\mathbf{E}}|^2 \quad (3.29)$$

We can also separate out the field in the delta-function constraints: firstly, by separating out the Poisson component of the field from the other two. The delta function which imposes Gauss' law can be rewritten as

$$\delta^d \left( \hat{\nabla} \cdot \mathbf{E}(\mathbf{x}) - \frac{\rho(\mathbf{x})}{\epsilon_0} \right) = \delta^d \left( \nabla^2 \phi(\mathbf{x}) + \frac{\rho(\mathbf{x})}{\epsilon_0} \right) \delta^d (\hat{\nabla} \cdot \tilde{\mathbf{E}}(\mathbf{x})) \quad (3.30)$$

since the rotational component is divergence-free by definition.

The delta function which imposes the definition of the harmonic mode can be removed by noting that we already have a sum over  $\rho(\mathbf{x}) \in X$ ; by defining in turn  $Y = \frac{X}{\epsilon_0} = \frac{q\mathbb{Z}}{a^d \epsilon_0}$  we can write

$$Z = \sum_{\{\nabla^2 \phi(\mathbf{x}) \in Y\}} \exp \left( -\frac{\beta \epsilon_0 a^d}{2} \sum_{\mathbf{x} \in D} |\tilde{\nabla}\phi(\mathbf{x})|^2 \right) \sum_{\mathbf{w}_0 \in \mathbb{Z}^2} \int \mathcal{D}\mathbf{e} \prod_{\mathbf{x} \in D} \left[ \delta^d \left( \hat{\nabla} \cdot \mathbf{e}(\mathbf{x}) \right) \right] \\ \times \delta^d \left( \sum_{\mathbf{x} \in D} \mathbf{e}(\mathbf{x}) + \left( \frac{N}{\epsilon_0} \mathbf{P} - \frac{Nq}{L \epsilon_0 a^d} \mathbf{w}_0 \right) \right) \exp \left( -\frac{\beta \epsilon_0 a^d}{2} \sum_{\mathbf{x} \in D} |\mathbf{e}(\mathbf{x})|^2 \right) \exp(-\beta U_{\text{Core}}) \quad (3.31)$$

and finally, by defining  $\tilde{\mathbf{e}}(\mathbf{x}) := \mathbf{e}(\mathbf{x}) - \bar{\mathbf{E}}$ , we can separate the rotational and harmonic terms to end up with

$$Z = \sum_{\{\nabla^2 \phi(\mathbf{x}) \in Y\}} \exp \left( -\frac{\beta \epsilon_0 a^d}{2} \sum_{\mathbf{x} \in D} |\tilde{\nabla}\phi(\mathbf{x})|^2 \right) \\ \times \sum_{\mathbf{w}_0 \in \mathbb{Z}^2} \exp \left( -\frac{\beta}{2\epsilon_0} |L^{d-1} \mathbf{P} - q \mathbf{w}_0|^2 \right) \exp(-\beta U_{\text{Core}}) \\ \times \int \mathcal{D}\tilde{\mathbf{e}} \prod_{\mathbf{x} \in D} \left[ \delta^d \left( \hat{\nabla} \cdot \tilde{\mathbf{e}}(\mathbf{x}) \right) \right] \delta^d \left( \sum_{\mathbf{x} \in D} \tilde{\mathbf{e}}(\mathbf{x}) \right) \exp \left( -\frac{\beta \epsilon_0 a^d}{2} \sum_{\mathbf{x} \in D} |\tilde{\mathbf{e}}(\mathbf{x})|^2 \right) \quad (3.32)$$

This formulation shows us the utility of the model: the partition function fac-

### 3. The generalised lattice Coulomb gas

torises completely into the Helmholtz-Hodge-decomposed components of the field, and hence are statistically independent of one another. We can use this fact to construct a local and  $O(N)$  algorithm for simulation of lattice electromagnetic problems, as described below.

## 3.4. Field updates

In order to perform simulations of the GLCG we turn to a result by Maggs and Rossetto [8] which describes a local algorithm for fast simulation of lattice Coulomb systems, using the lattice electric field description developed above. The Maggs-Rossetto algorithm consists of three Monte Carlo updates for the electric fields: individual field link updates, rotational updates and harmonic updates.

### 3.4.1. Field link updates

The first Monte Carlo update is the simplest one: updating the flux on a single field link. As described above, to reproduce the thermodynamics of Coulombic systems it is sufficient to ensure that Gauss' law is satisfied locally at all times. Hence, we only need to enforce Gauss' law at the two relevant vertices of the lattice; one way of doing this is to consider the flux on the link connecting the two vertices. By adding or subtracting one unit of  $q/\epsilon_0$  to the flux (depending on the current charge configuration at the two vertices) we can simulate charge creation, annihilation or movement. Since we restrict ourselves to a Coulomb gas of elementary charges, we include the constraint that the charge value on any given site must be  $\leq 1$ .

Associating the field links at  $(\mathbf{x} + \frac{a}{2}\mathbf{e}_\mu)$  with the lattice site  $(\mathbf{x})$ , a decrease in the field link at  $(\mathbf{x} + \frac{a}{2}\mathbf{e}_\mu)$  of  $q/\epsilon_0$  can then correspond to four different updates in the charge picture, depending on the current charge configuration at the two sites, as shown in Fig. 3.2:

1. A positive charge moving from  $(\mathbf{x})$  to  $(\mathbf{x} + a\mathbf{e}_\mu)$ .



FIGURE 3.1.: A general field link update in the Maggs-Rossetto model. The direction of the arrow signifies that we treat the flux as positive when it goes from site  $\mathbf{x}$  to site  $\mathbf{x}+a\mathbf{e}_\mu$ . We also require  $|q_\alpha| \leq 1 \forall \alpha$ .

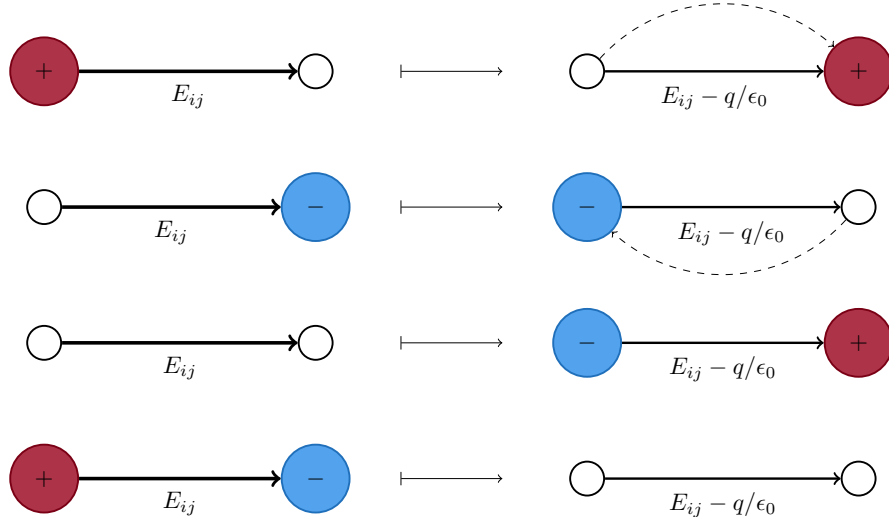


FIGURE 3.2.: The four possible charge moves associated with a field link decrease in the Maggs-Rossetto model: positive charge moving “forwards”, negative charge moving “backwards”, dipole creation, dipole annihilation. A blank circle indicates an empty site.

2. A negative charge moving in the opposite direction.
3. The creation of a dipole with the positive charge at  $(\mathbf{x} + a\mathbf{e}_\mu)$  and a negative charge at  $(\mathbf{x})$ .
4. The annihilation of a dipole with the opposite orientation; i.e. a positive charge at  $(\mathbf{x})$  and a negative charge at  $(\mathbf{x} + a\mathbf{e}_\mu)$ .

An increase in a field link corresponds to the same four charge moves with  $q \rightarrow -q$ .

### 3.4.2. Rotational update

The Monte Carlo update described above is sufficient to produce configurations which obey Gauss’ law, but the states produced through individual field link updates alone do not sample all degrees of freedom of the field.

To illustrate this, consider a charge moving around a square plaquette of the lattice: once it returns to its original site, a unit of flux  $q/\epsilon$  has been added to all four links of the plaquette. A single field link update represents a change in the divergence of flux around the two points, but the field resulting from these four moves is entirely rotational; the first update, then, can excite both rotational and irrotational degrees of freedom of the field.

### 3. The generalised lattice Coulomb gas

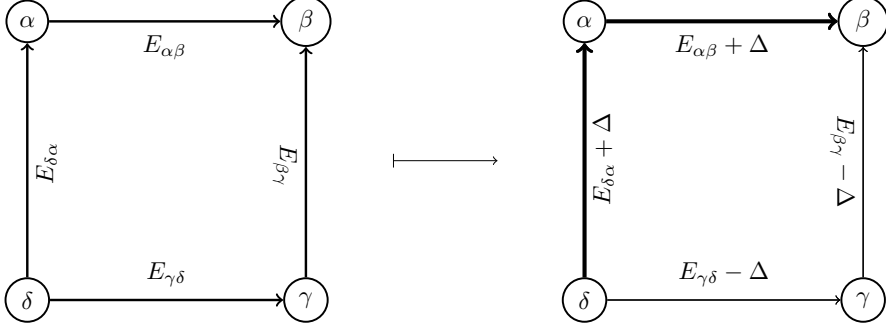


FIGURE 3.3.: A rotational update in the Maggs-Rossetto model. The flux is “rotated” around the plaquette by an amount  $\Delta$ . Charge values for the sites  $\alpha, \beta, \gamma, \delta$  are not shown here since they are irrelevant in this context; the rotational update does not affect the charge configuration.

However, the magnitude of each field link should be continuous (in particular, the field should be allowed to relax to lower-energy configurations), and this is impossible with the first update alone: the local field link update produces field configurations of higher energy than would be generated via solution of the Poisson equation at every time step. In order to integrate in between the degrees of freedom explored by the first update and allow the system to relax, it is necessary to also perform Monte Carlo updates on the rotational field. We do this by updating the field links around a single plaquette by an amount  $\Delta$  as shown in Fig. 3.3.  $\Delta$  is chosen at random from the interval  $[-\Delta_{\max}, \Delta_{\max}]$ .

Since the rotational field is continuous and there is no constraint on its magnitude, only its divergence,  $\Delta_{\max}$  is a tuneable parameter which we choose to keep the Monte Carlo acceptance rate within a reasonable window. In practice, it is acceptable to use  $\Delta_{\max} \approx T$  for a wide range of temperatures.

#### 3.4.3. Harmonic update

We can also perform a Monte Carlo update specifically on the harmonic field in order to allow the system to explore different topological sectors. In doing this we cannot simply propose a random change to the harmonic mode as with the second update, since the polarisation part  $\bar{\mathbf{E}}_p$  can be attributed to the charge configuration. Instead we propose a change to the winding number  $\mathbf{w}$  of the system, since an infinite number of fields with different  $\mathbf{w}$  describe the same charge configuration. In this way, we sample different topological sectors of the system: of course, the system can change its topological sector simply through the movement of charges via the first update, but an independent sampling of the winding mode

increases the efficiency of the simulation.

### 3.5. Helmholtz-Hodge decomposition

By using the expression for the Green's function given in 2.35 or 2.37 in 2D or 3D respectively, we can solve the Poisson equation for the charge configuration; from this we can calculate the irrotational component of the field  $-\nabla\phi$ . By subtracting this field from the total field, we can isolate the rotational component as well and calculate equilibrium properties like specific heats, as well as correlations, for each component separately. A sample configuration and its Helmholtz-Hodge decomposed components are shown below in Figs. 3.4, 3.5 and 3.6.

As mentioned above, the model described in this chapter was used by Maggs and collaborators as a tool for faster simulations of Coulombic systems, but its utility extends beyond that: it provides us with a clear and natural way to work with Helmholtz-Hodge-decomposed fields and investigate the two components. For a simple electrostatic problem this is unnecessary, since only the irrotational component is relevant, but in a more complex system, or when investigating the mapping between the Coulomb gas and spin systems, this separation of divergence-free and curl-free components becomes very useful conceptually.

Note also that the [Maggs-Rossetto algorithm](#) will in general produce different microscopic dynamics than a naive algorithm where we simply perform Ewald summation or solve Poisson's equation after each proposed move. However, since we have verified that the partition function of the Coulomb system is unchanged, we know that any quantity involving an ensemble average will also be unchanged; I use this property frequently in the calculation of field correlations in Chapters 6 – 8.

### 3. The generalised lattice Coulomb gas

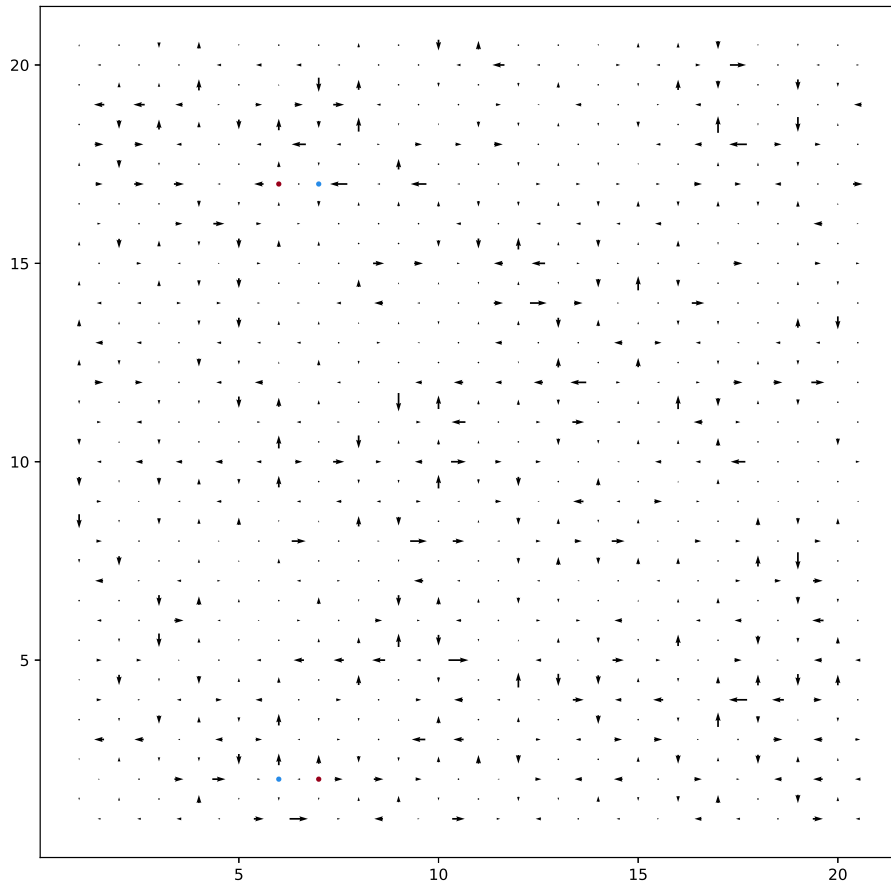


FIGURE 3.4.: A sampled field configuration of a 2D Coulomb gas in the canonical ensemble, with  $L = 20$ , at  $T = 0.1$  in the units used by Lee and Teitel [44]. Two bound pairs of charges are shown with positive and negative in red and blue respectively.

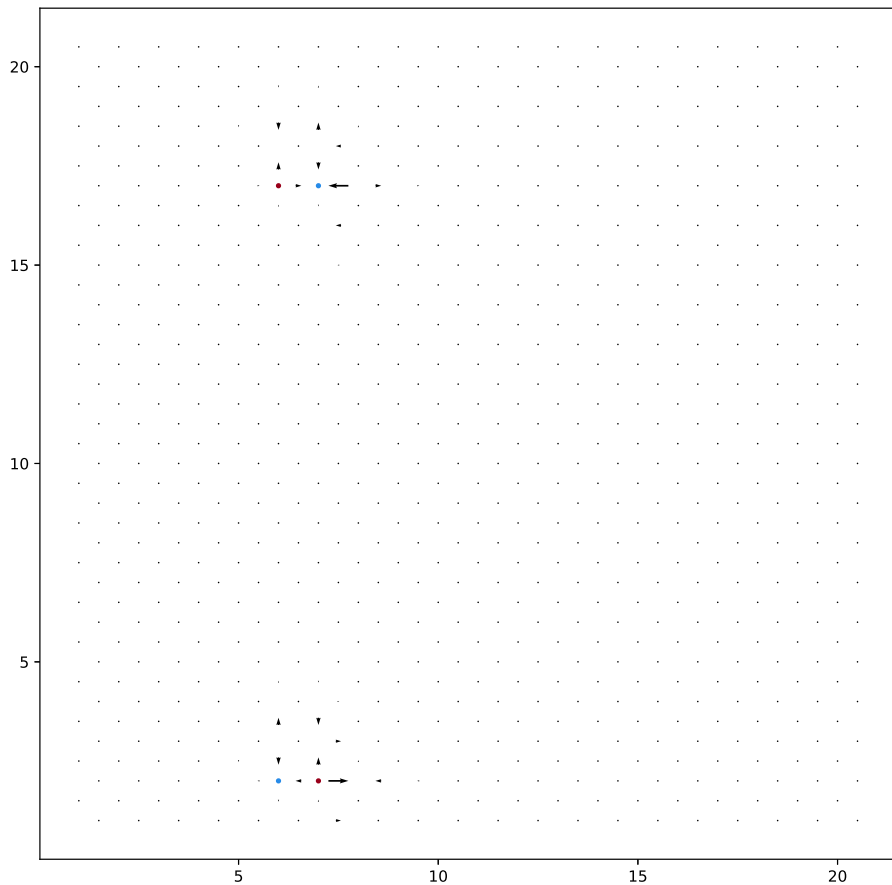


FIGURE 3.5.: The irrotational component of the field shown above, found by solving the Poisson equation for the charge configuration using the lattice Green's function 2.35. This component is then only the **longitudinal** one; we see divergence-full fields which emanate from positive charges and end on negative charges as we expect.

### 3. The generalised lattice Coulomb gas

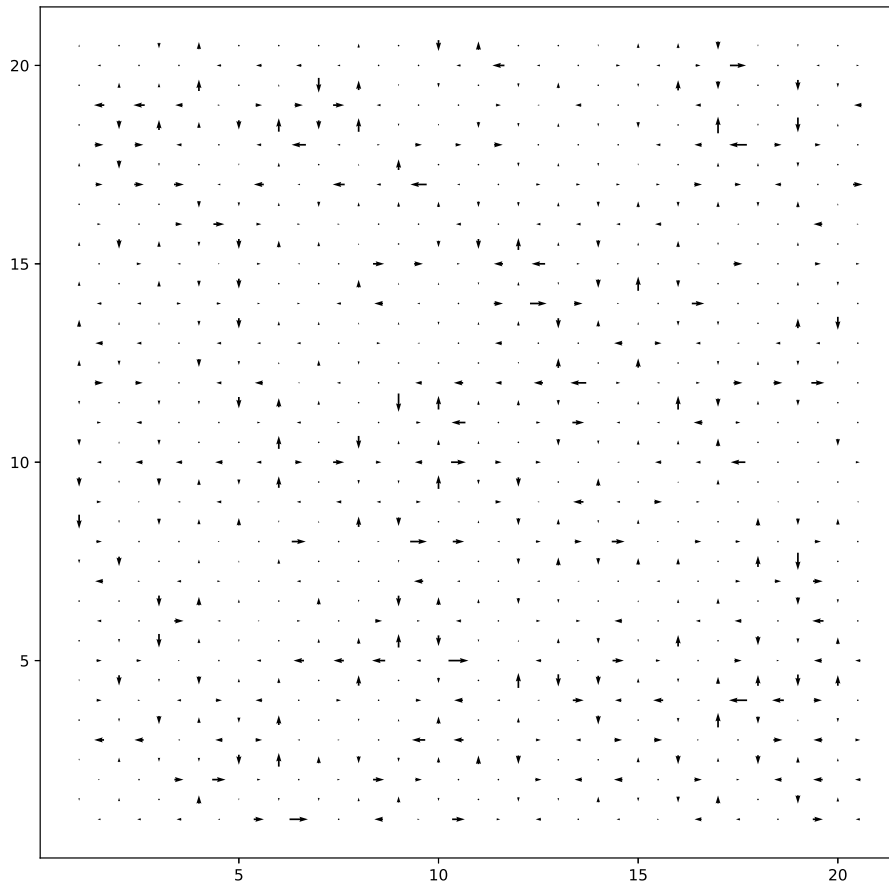


FIGURE 3.6.: The rotational component of the field shown above; found by subtracting 3.5 from 3.4. Charges are not shown since the rotational component does not arise from the charges. This is the divergence-free **transverse** component which is absent in the **TLCG** but present for emergent field representations of magnetic systems, such as the XY model, which will be discussed in more detail in Chap. 4.

### 3.6. Choice of parameters

The energy scale of the problem goes with  $q^2/\epsilon$ , as can be seen from the partition function of the Coulomb gas: we are free to choose both  $q$  and  $\epsilon$ . The  $2\pi$  modular symmetry of the XY and HXY models (discussed below in Chap. 4) give us  $q = 2\pi$ , and we are free in this case to set  $\epsilon = 1$ ; these are the units used in [31, 32] and in my simulations of the harmonic XY model, a model closely related to the 2d-XY model in magnetism. Briefly, the harmonic XY model results from taking an XY-type Hamiltonian

$$H_{\text{XY}} = -J \sum_{\langle i,j \rangle} \mathbf{S}_i \cdot \mathbf{S}_j = -J \sum_{\langle i,j \rangle} \cos(\theta_i - \theta_j) \quad (3.33)$$

and expanding the cosine to the squared term, then adding a modular variable between each pair of spins to ensure that the spin difference stays within  $[-\pi, \pi]$ . I will refer to this choice as “HXY” units.

Previous investigations of the 2D Coulomb gas [44, 45] have instead used  $q = 1, \epsilon = 1/2\pi$ , where the  $1/2\pi$  enters in Lee’s derivation of the Green’s function. I will refer to this choice of units as “Lee” units. In the interest of continuity I use Lee units in my simulations of the 2D generalised lattice Coulomb gas and for 3D simulations for continuity with the 2D results.



## 4. Lattice Coulomb gases and spin models

### 4.1. XY-type models

#### 4.1.1. The 2d-XY model

The [2d-XY model](#) (referred to hereafter simply as the [XY model](#)) is a spin model with Hamiltonian

$$H_{\text{XY}} = -J \sum_{\langle i,j \rangle} \mathbf{S}_i \cdot \mathbf{S}_j = -J \sum_{\langle i,j \rangle} \cos(\theta_i - \theta_j) \quad (4.1)$$

where the sum  $\langle i,j \rangle$  runs over nearest neighbours only,  $J$  is the coupling constant and  $\theta_i$  is the direction within the plane of the unit-length classical spin vector  $\mathbf{S}_i$ . The XY model then possesses both a global  $U(1)$  symmetry as well as a  $2\pi$ -modular symmetry from the cosine; any model with these symmetries can be described as an XY-type model.

Note that it is equally valid to discuss the set  $\{\mathbf{S}_i\}$  as a classical spin field  $\mathbf{S}(\mathbf{x})$  simply by denoting each lattice site by its position vector  $\mathbf{x}$  rather than an index  $i$ ; we will use the latter notation when describing lattice electric fields and spin-difference fields in the [Harmonic XY \(HXY\) model](#).

XY-type models have been a subject of intense interest for several decades now due to the rich statistical mechanics involved and the wide-ranging applicability of the model, which extends to various experimental systems including superfluids [27, 28] and superconducting Josephson junctions [30], among many others.

Despite the famous result of Mermin and Wagner [46] that there can be no long-range order in 2D systems with continuous symmetries and short-range interactions, XY-type models do display quasi-long-range order in their low-temperature phases, which are characterised by algebraically decaying correlations characteristic of criticality. They also display a phase transition, the celebrated [Berezinskii-Kosterlitz-Thouless \(BKT\) transition](#), from the low-temperature critical phase to

#### 4. Lattice Coulomb gases and spin models

a high-temperature paramagnetic one. This will be discussed further in Sec. 4.1.3; firstly, however, we note that the BKT transition was first noticed in the 2D Coulomb gas before the development of the XY model [26].

##### 4.1.2. Charge deconfinement in the 2D Coulomb gas

As derived in 1.16, the Coulomb potential in two dimensions is logarithmic: at low temperature charges are tightly bound together in neutral pairs, but at high temperature the charges are deconfined. This insulator-conductor phase transition was first noted by Salzberg and Prager [26], who gave the equation of state for a 2D Coulomb gas on the square lattice. They did so by transforming the 2D Coulomb gas partition function into the canonical ensemble and writing

$$Z_{\text{Coulomb}}^{SP} = \int \mathcal{D}\mathbf{x} \exp \left( \beta \sum_{i \neq j} \frac{q_i q_j}{4\pi\epsilon_0} \ln \left[ \frac{|\mathbf{x}_i - \mathbf{x}_j|}{r_0} \right] \right) \exp \left( -\frac{\beta\epsilon_0}{2} A |\bar{\mathbf{E}}|^2 \right) \quad (4.2)$$

where  $r_0$  is a UV cutoff for the particles and the measure

$$\int \mathcal{D}\mathbf{x} = \prod_i^N \left[ \int_{r_0}^L dx_i \int_{r_0}^L dy_i \right] \quad (4.3)$$

integrates over all  $N$  charges in the system.

By redefining the coordinate system to include the system size  $L$  and refactoring the partition function in terms of the new coordinates, it is possible to isolate the  $L$ -dependence of the partition function and obtain

$$Z_{\text{Coulomb}}^{SP} = L^{2N} L^{\beta \sum_{i \neq j} \frac{q_i q_j}{4\pi\epsilon_0}} Z_{\text{Coulomb}}; \quad (4.4)$$

$$Z_{\text{Coulomb}} = \int \mathcal{D}\mathbf{x}' \exp \left( \beta \sum_{i \neq j} \frac{q_i q_j}{4\pi\epsilon_0} \ln \left[ \frac{|\mathbf{x}'_i - \mathbf{x}'_j|}{r_0} \right] \right) \exp \left( -\frac{\beta\epsilon_0}{2} A |\bar{\mathbf{E}}|^2 \right) \quad (4.5)$$

where  $Z_{\text{Coulomb}}$  is the normalised partition function,  $\mathbf{x}' = \mathbf{x}/L$  and the measure

$$\int \bar{\mathcal{D}}\mathbf{x}' = \prod_i^N \left[ \int_{r_0/L}^1 dx'_i \int_{r_0/L}^1 dy'_i \right] \quad (4.6)$$

We then define  $A = L^2$  and note that  $\sum_{i \neq j} q_i q_j = -Nq^2$ ; using these, we can

express the (Helmholtz) free energy as

$$F^{SP} = -k_B T \ln \left( A^{N(1-\beta \frac{q^2}{8\pi\epsilon_0})} Z_{\text{Coulomb}} \right) \quad (4.7)$$

Salzberg and Prager then approximated by neglecting the L-dependence of the integrals in the measure  $Z_{\text{Coulomb}}$  (which corresponds to neglecting charge screening) and used the identity

$$p = -\frac{\partial F}{\partial A} \quad (4.8)$$

to arrive at the equation

$$p = 2nk_B T \left( 1 - \frac{q^2}{8\pi\epsilon_0 k_B T} \right) \quad (4.9)$$

where  $n$  is the density of charge pairs, i.e.  $N/A = 2n$ .

This equation tells us that at a specific temperature given by

$$T_c^{\text{ns}} = \frac{q^2}{8\pi\epsilon_0 k_B} \quad (4.10)$$

the pressure changes from negative (below  $T_c^{\text{ns}}$ ) to positive: in the low-temperature phase the charges are tightly bound, and this phase is characterised by negative pressure. As we shall see in Sec. 4.1.3, this transition is later identified as the BKT transition.

In Eq. 4.10, the subscript ns refers to the omission of screening considerations, which act to decrease the transition temperature. Upon adopting what I will subsequently refer to as the XY-type convention of  $q = 2\pi$ ,  $\epsilon_0 = k_B = 1$ , this temperature reduces to  $\pi/2$ , and the inclusion of screening considerations decreases this temperature to

$$T_{\text{BKT}} = 1.35 \quad (4.11)$$

### 4.1.3. The Berezinskii-Kosterlitz-Thouless transition

As mentioned above, the XY model was investigated by Berezinskii [1] as well as Kosterlitz and Thouless [2], who showed that it was physically analogous to the two-dimensional Coulomb gas. In moving from a system of electric charges to a magnetic system of spins, the charge deconfinement transition discovered by Salzberg and Prager becomes the BKT transition, which is often referred to simply as the KT transition in the literature. The algebraic correlations of the low-temperature critical phase are driven by spin-wave excitations; this phase also

#### 4. Lattice Coulomb gases and spin models

features tightly-bound topological defect pairs. These defect pairs are confined in the critical phase due to a diverging logarithmic free-energy barrier; above the transition temperature, however, entropic considerations bring the free-energy barrier down to a finite value, and the defect pairs are free to dissociate, leading to the paramagnetic high-temperature phase. This rather informal argument can be seen by considering the free energy and entropy of vortices: by expanding the cosine in Eq. 4.1 and moving to a continuum argument, we can rewrite the Hamiltonian as

$$H_{\text{HXY}} = -J \sum_{\langle i,j \rangle} \cos(\theta_i - \theta_j) \approx -\frac{J}{2} \sum_{\langle i,j \rangle} (\theta_i - \theta_j)^2 \quad (4.12)$$

$$\rightarrow \frac{J}{2} \int_a^L |\Delta\theta(\mathbf{r})|^2 d^2r \quad (4.13)$$

and then calculate the energy of a vortex as

$$E = \frac{J}{2} \int_a^L |\Delta\theta(\mathbf{r})|^2 d^2r \quad (4.14)$$

where  $a$  is some small cutoff representing the size of the vortex, which we introduce to avoid the singularity of  $\theta$  at  $\mathbf{r} = \mathbf{0}$ ; on the lattice, the natural choice for  $a$  is obviously the lattice constant.

Next, we note that for an XY system the integral around a vortex will be equal to  $2\pi m$  for some integer  $m$ , since the Hamiltonian encodes a  $2\pi$  modular symmetry. Hence, the integral Eq. 4.14 becomes

$$E = \pi J \ln \left( \frac{L}{a} \right) \quad (4.15)$$

which is the energy corresponding to a single free vortex.

Conversely, the entropy corresponding to a single free vortex is given by

$$S = k_B \ln \left( \frac{L^2}{a^2} \right) = 2k_B \ln \left( \frac{L}{a} \right) \quad (4.16)$$

because there are approximately  $(L/a)^2$  places in which to place a vortex.

By comparing Eqs. 4.15 and 4.16 we see that for  $T > \pi J / 2k_B$ , the free energy  $E - TS$  is negative and it is energetically favourable for a free vortex to exist. Below this temperature the entropic term “wins out” and free vortices are strongly

suppressed. By setting  $J = k_B = 1$  as above, we also recover the transition temperature  $T_{BKT}^{\text{ns}} = \pi/2$ .

We can also investigate the low-temperature behaviour of the **XY model** by disallowing vortices altogether and studying the spin-wave theory of the system.

### Spin-wave theory

The usual way to study the spin-wave fluctuations of the **XY model** is to perform the same expansion of the cosine as above and then extend the allowed values of  $\theta$  from  $[-\pi, \pi]$  to  $\pm\infty$ ; this has the effect of disallowing vortices.

We can define a magnetisation [47] as

$$M = \left\langle \left| \frac{1}{N} \sum_i \mathbf{S}_i \right| \right\rangle \quad (4.17)$$

where  $i$  runs over all spins in the lattice.

It can be shown that the magnetisation goes as

$$M = \left( \frac{1}{2N} \right)^{\frac{1}{8\pi K}} \quad (4.18)$$

where  $N$  is the number of spins and  $K = J/k_B T$  is the spin stiffness: this quantity approaches zero so slowly that in practice the thermodynamic limit is inaccessible for XY-type systems, especially in simulation. Taking  $K = 2/\pi$ , as in the original theory, gives  $1/8\pi K = 1/16$ , so that for example setting  $N = N_A$  gives a magnetisation of 0.0313, which is small but not vanishingly so; an XY magnet the size of Texas would have a measurable magnetisation [6]. Simulations of  $N = 10^4$  spins for the XY and **HXY** (discussed below) models are shown in Fig. 4.1; the unfilled circles correspond to the XY model and filled circles to the HXY. We see that there is indeed a measurable magnetisation at low temperature as predicted by the spin-wave theory. The two arrows denote the **BKT transition** temperatures for the **XY** and **HXY** models respectively.

### Effective spin stiffness and helicity modulus

When considering the thermodynamic limit (as is usual in the literature for XY systems) we can consider the vortex density as vanishingly small and the vortices themselves as essentially negligible. Below  $T_{BKT}$  it is possible to renormalise the vortices into an effective spin stiffness  $K_{\text{eff}}$ , which is closely related to the helicity modulus  $\Upsilon$  in the thermodynamic limit.

#### 4. Lattice Coulomb gases and spin models

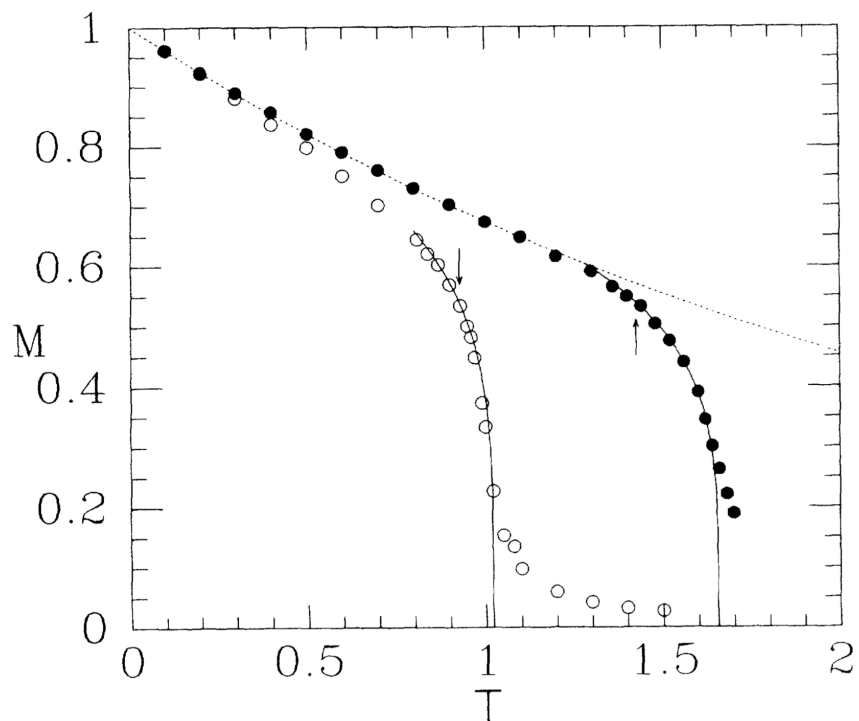


FIGURE 4.1.: Simulations of the magnetisations of the XY (open circles) and HXY (filled) models for  $N = 10^4$  spins, from [6]. We see a long tail in the magnetisation due to the extremely slow approach to the thermodynamic limit.

We can define a finite-size effective spin stiffness by replacing  $K = \beta J$  with  $K_{\text{eff}}$  in the spin-wave Hamiltonian, so that the partition function reads

$$Z_{\text{eff}}(L, T) = \int \mathcal{D}\theta \exp \left[ -\frac{K_{\text{eff}}(L, T)}{2} \sum_{\langle i,j \rangle} (\theta(\mathbf{x}_i) - \theta(\mathbf{x}_j))^2 \right] \quad (4.19)$$

Comparing this quantity with the corresponding XY Hamiltonian and partition function we see that  $K_{\text{eff}}$  has the effect of measuring the deviation of a system from purely spin-wave behaviour. In the thermodynamic limit we recover the spin stiffness defined above:

$$\lim_{L \rightarrow \infty} K_{\text{eff}}(L, T) = K(T) \quad (4.20)$$

Another quantity of interest is the helicity modulus  $\Upsilon$  which can be related to the spin stiffness by

$$K(T) = \beta \Upsilon(T); \quad (4.21)$$

this corresponds to adding a global twist to the spin system of size  $k_0 = 2\pi/L$ , and then taking the thermodynamic limit. It can also be defined as the second derivative of the free energy with respect to the spin twist, as the twist is taken to zero:

$$\Upsilon(T) = \frac{1}{N} \frac{\partial^2 F(T, k_0)}{\partial k_0^2} \Big|_{k_0 \rightarrow 0} \quad (4.22)$$

In the thermodynamic limit all XY systems are predicted to have a discontinuous jump in the spin stiffness, from  $2/\pi$  to zero; it follows that the same discontinuous jump should appear in the helicity modulus. For a finite size system, however, we expect to see a finite range over which the helicity modulus goes to zero: it has been shown that this is the case, and simulations have been performed on the fourth derivative of the free energy  $\Upsilon_4$  which are consistent with the jump being discontinuous in the thermodynamic limit [48].

Finally, it was shown by Kosterlitz and José et al. [24, 25] that the renormalised spin stiffness  $K_{RG}$  obeys the RG equation

$$K_{RG}^{-1} = K^{-1} + 4\pi^2 y^2 \int_{r_0}^{\infty} \frac{dr}{r_0} \left( \frac{r}{r_0} \right)^{3-2\pi K_{RG}} \quad (4.23)$$

where  $y = 4\pi K \tau^2$  and  $\tau$  is the renormalised lattice spacing. This equation is valid in the thermodynamic limit, for  $K_{RG} > 2/\pi$ ; for  $K_{RG} < 2/\pi$  the integral diverges.

The divergence of the integral as  $K_{RG}$  approaches  $2/\pi$  from above implies a discontinuous jump from  $2/\pi$  to zero, exactly as suggested by Minnhagen's finite

#### 4. Lattice Coulomb gases and spin models

size analysis of the spin stiffness [48].

Simulation and finite-size analysis of the XY model shows the renormalised temperature of the BKT transition in the 2d-XY model to be  $T_{\text{BKT}}^{\text{XY}} = 0.887$ ; similar analysis for the Villain model, which is discussed below, give the transition temperature  $T_{\text{BKT}}^{\text{Villain}} = 1.35$ . The HXY model, also discussed further below, is taken to have the same transition temperature as the Villain model.

##### 4.1.4. Villain model

The Villain model was introduced [12] to construct an analytically treatable partition function which mimicked the physics of the XY model. This is achieved by introducing a new set of variables which exist between the spins and impose the modular symmetry of the XY model. The partition function of the Villain model can be written

$$Z_{\text{Villain}} = \sum_{\{n_{ij} \in \mathbb{Z}\}} \int \bar{\mathcal{D}}\theta \exp \left[ -\frac{\beta J}{2} \sum_{\langle i,j \rangle} |\theta_i - \theta_j + 2\pi n_{ij}|^2 \right] \quad (4.24)$$

where once again the  $\langle i,j \rangle$  sum runs over nearest neighbours only and the functional integral  $\bar{\mathcal{D}}$  is defined as

$$\int \bar{\mathcal{D}}\theta = \prod_i \left[ \int_{-\pi}^{\pi} d\theta_i \right] \quad (4.25)$$

with the  $i$  in the product running over the entire lattice.

In the Villain model, as can be seen from 4.24, the set of  $n_{ij}$  are independently sampled and not dictated by the configuration of the spins  $\theta$ . This decouples the topological defects from the spin-difference field, unlike in the XY model; the topological defects of the Villain model are not then identifiable as vortices, as they are in the XY model, but the physics of the XY model and the BKT transition are still evident.

##### 4.1.5. Harmonic XY model

The harmonic XY model, or HXY model, is the simplest spin model which incorporates the modular symmetry of real spin systems while keeping the quadratic Hamiltonian of the Villain model, and was independently introduced by Vallat and Beck [7] and Bramwell and Holdsworth [6]. Essentially we do the same as in the first step of Eq. 4.13 above: we proceed by taking the XY Hamiltonian 4.1,

## 4.2. The harmonic XY model – Coulomb gas mapping

expanding the cosine and keeping only the squared term to leave an interaction of the form

$$H_{\text{HXY}} = -J \sum_{\langle i,j \rangle} (\theta_i - \theta_j + 2\pi n_{ij})^2 \quad (4.26)$$

where  $n_{ij}$  is an integer chosen to ensure that  $(\theta_i - \theta_j + 2\pi n_{ij}) \in (-\pi, \pi]$ . Hence, we avoid the sum over the  $n_{ij}$  variables which arises in 4.24; we then find that the topological defects are once again coupled to the spin differences at each site, and that they do (as in the XY model) correspond to vortices.

We can then define a modular spin-difference field: first, defining

$$\delta\theta_\mu \equiv \frac{1}{a} (\theta(\mathbf{x} + a\mathbf{e}_\mu) - \theta(\mathbf{x})) \quad (4.27)$$

for brevity, then by

$$\Delta\theta_\mu(\mathbf{x} + \frac{a}{2}\mathbf{e}_\mu) = \begin{cases} \delta\theta_\mu + 2\pi, & \text{for } \delta\theta_\mu \in [-2\pi, -\pi), \\ \delta\theta_\mu, & \text{for } \delta\theta_\mu \in [-\pi, +\pi], \\ \delta\theta_\mu - 2\pi, & \text{for } \delta\theta_\mu \in (+\pi, +2\pi] \end{cases} \quad (4.28)$$

It is clear that we can write the Hamiltonian in terms of the spin difference field as

$$H_{\text{HXY}} = -J \sum_{\mathbf{x}} |\Delta\theta(\mathbf{x})|^2 \quad (4.29)$$

We can also perform a Helmholtz decomposition on the spin-difference field: the topological defects in the HXY model are spin vortices, which are rotational and hence correspond to the divergence-free component of the total spin-difference field  $\Delta\theta$ , while spin-wave fluctuations correspond to the divergence-full component:

$$\Delta\theta = \Delta\theta_{\text{vortices}} + \Delta\theta_{\text{spin-wave}} = \Delta\theta_{\text{rot.}} + \Delta\theta_{\text{irrot.}} \quad (4.30)$$

## 4.2. The harmonic XY model – Coulomb gas mapping

So far we have introduced the harmonic XY model and stated both its relationship to the “full” XY model and the fact that it maps to the Coulomb gas; however, since my work includes simulations of the HXY model it is important here to discuss the details of that mapping, which is due to Faulkner et al. [32]. The microscopic details of moving between the harmonic XY model and the GLCG

#### 4. Lattice Coulomb gases and spin models

are outlined below.

##### 4.2.1. The emergent electric field

We begin by defining an electric field for the HXY model based on the definition of the modular spin-difference field  $\Delta\theta$ :

$$\mathbf{E}(\mathbf{x}) = J \begin{bmatrix} \Delta\theta_y(\mathbf{x} + \frac{a}{2}\mathbf{e}_x) \\ \Delta\theta_x(\mathbf{x} + \frac{a}{2}\mathbf{e}_y) \end{bmatrix} \quad (4.31)$$

where  $\mathbf{x}$  here denotes a site on the Coulomb gas lattice: this set of sites sit at the centres of plaquettes of the HXY lattice. An x-component of the spin-difference field then becomes a y-component of the emergent field. The mapping is shown schematically in Fig. 4.2.

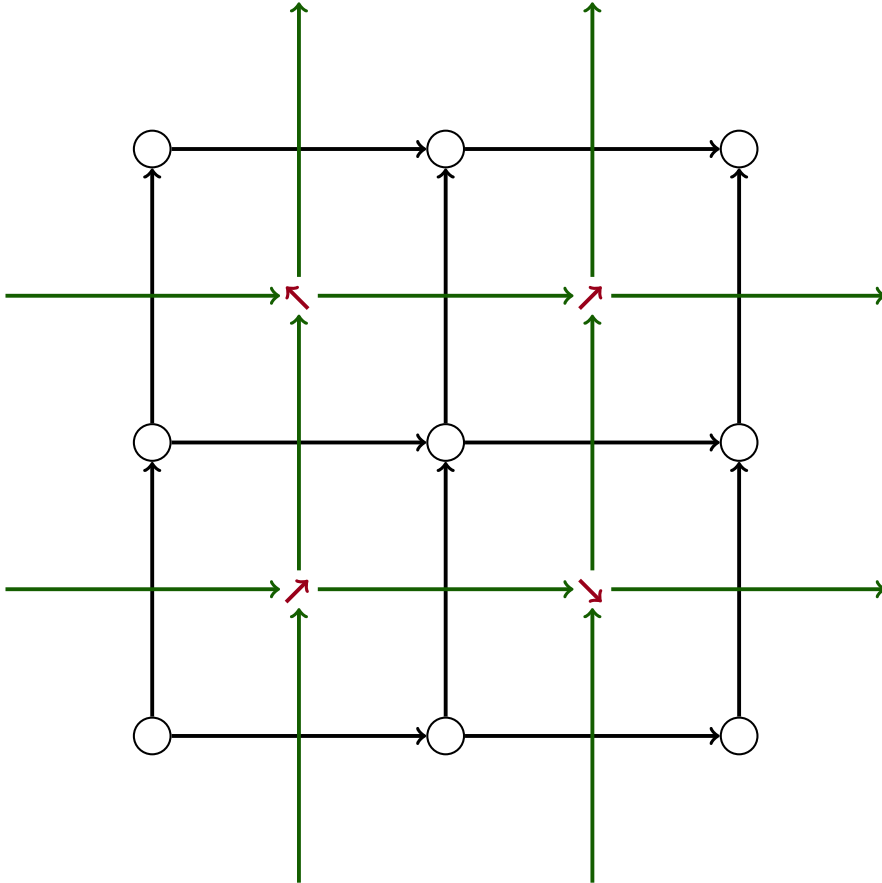


FIGURE 4.2.: The mapping between the lattice Coulomb gas and the HXY model. Coulomb gas sites are represented by unfilled circles and lattice electric fields by black arrows, as in Chap. 3; the spin-difference field of the HXY model is shown here as green arrows. The direction of the HXY spins shown here is arbitrary.

Next, we can consider the respective Helmholtz-Hodge decomposition of the Coulomb gas and HXY model: we see that the topological defects correspond to the divergence-full component of the field for the Coulomb gas, but the divergence-free component of the HXY model, and vice-versa:

$$\mathbf{E}_{\text{irrot.}}(\mathbf{x}) = -\tilde{\nabla}\phi(\mathbf{x}) + \bar{\mathbf{E}} = J \begin{bmatrix} \Delta\theta_{\text{rot.}}^y(\mathbf{x} + \frac{a}{2}\mathbf{e}_x) \\ \Delta\theta_{\text{rot.}}^x(\mathbf{x} + \frac{a}{2}\mathbf{e}_y) \end{bmatrix} \quad (4.32)$$

$$\mathbf{E}_{\text{rot.}}(\mathbf{x}) = \tilde{\mathbf{E}}(\mathbf{x}) = J \begin{bmatrix} \Delta\theta_{\text{irrot.}}^y(\mathbf{x} + \frac{a}{2}\mathbf{e}_x) \\ \Delta\theta_{\text{irrot.}}^x(\mathbf{x} + \frac{a}{2}\mathbf{e}_y) \end{bmatrix} \quad (4.33)$$

$$(4.34)$$

The rotational (vortex) component of the HXY spin-difference field then defines the irrotational component of an emergent electric field, and the irrotational (spin-wave) component defines the rotational component of the emergent electric field.

#### 4.2.2. The HXY Hamiltonian and partition function in the Coulomb gas representation

The emergent field defined in this way then obeys Gauss' law in the same way as described in Chap. 3, but with  $J = 1/\epsilon_0$ . We can also rewrite the Hamiltonian in terms of the emergent field components so that instead of  $|\Delta\theta|^2$  we have

$$H_{\text{HXY}} = -J \sum_{\mathbf{x}, \mathbf{x}'} \rho(\mathbf{x}) G(\mathbf{x}, \mathbf{x}') \rho(\mathbf{x}') + \sum_{\mathbf{x}} |\tilde{\mathbf{E}}(\mathbf{x})|^2 + \frac{qN\epsilon_0}{2} |\bar{\mathbf{E}}|^2 \quad (4.35)$$

which follows simply from replacing  $|\Delta\theta|^2 \rightarrow |\mathbf{E}(\mathbf{x})|^2$  and repeating the decomposition from Chap. 3.

The partition function can also be written analogously to Eq. 3.32 by separating the Helmholtz-decomposed components of the field: we arrive at

$$\begin{aligned} Z &= \left( \frac{a}{2\pi J} \right)^{2N} \int \mathcal{D}\tilde{\mathbf{E}} \exp \left[ -\frac{\beta a^2}{2J} \sum_{\mathbf{x}} |\tilde{\mathbf{E}}(\mathbf{x})|^2 \right] \\ &\quad \times \exp \left[ -\frac{\beta Ja^4}{2} \sum_{\mathbf{x}_i \neq \mathbf{x}_j} \rho(\mathbf{x}_i) G(\mathbf{x}_i, \mathbf{x}_j) \rho(\mathbf{x}_j) \right] \\ &\quad \times \exp \left[ -\frac{\beta L^2}{2J} |\bar{\mathbf{E}}_p + \frac{2\pi J}{L} \bar{\mathbf{E}}_w|^2 \right] \exp(+\beta\mu n) \end{aligned} \quad (4.36)$$

There is an important difference between Eqs. 3.26 and 4.36, however: the term

#### 4. Lattice Coulomb gases and spin models

representing the Coulombic component cannot be taken out of the integral over the rotational component. Here, by contrast, the functional integral is defined as

$$\int \mathcal{D}\tilde{\mathbf{E}} = \prod_{\mathbf{x}} \int_{\pi - \hat{E}_x}^{-\pi - \hat{E}_x} d\tilde{E}_x \prod_{\mathbf{x}} \int_{\pi - \hat{E}_y}^{-\pi - \hat{E}_y} d\tilde{E}_y \\ \times \sum_{\{\rho(\mathbf{x}) \in \{0, \pm q\}\}} \sum_{\tilde{\mathbf{E}}_w \in \mathbb{Z}^2} \delta \left( \sum_{\mathbf{x}} \rho(\mathbf{x}) \right) \delta \left( \sum_{\mathbf{x}} \tilde{\mathbf{E}}(\mathbf{x}) \right) \prod_{\mathbf{x}} \left[ \delta \left( \tilde{\nabla} \cdot \tilde{\mathbf{E}} \right) \right] \quad (4.37)$$

where  $\hat{\mathbf{E}}$  is the Coulombic component of the emergent electric field,  $q = 2\pi/a^2$  in the sum over  $\rho(\mathbf{x})$ , all  $\mathbf{E}, \hat{\mathbf{E}}, \tilde{\mathbf{E}}$  are the emergent electric field links with  $E_\mu$  centred at  $\mathbf{x} + a\mathbf{e}_\mu/2$  and the sums over  $\mathbf{x}$  run over the lattice of fields and charges, rather than the spin lattice. The first two terms are the integral over the rotational component, the third enforces overall charge neutrality and restricts the HXY model to single-valued charges only while allowing charge windings, and the final two terms enforce the divergenceless constraint on the rotational component.

We see in the first two terms that the Coulombic component enters the bound of the functional integral over the rotational component. This is because unlike in the generalised lattice Coulomb gas the phase space of the rotational field is limited by the  $[-\pi, \pi]$  bound on each spin difference, and hence the available configurations of the rotational component are dependent on the configuration of the irrotational component. Hence, the partition function does not factorise, and the two components are not statistically independent of each other, although it has been shown that they do energetically decouple [32].

We see that the periodicity of the spin-difference field has significant consequences for the physics of the HXY model, introducing several subtle differences from the Coulomb gas. Firstly, it means that the partition function cannot be separated into Coulombic and non-Coulombic components: this has consequences when considering the specific heat of the HXY model compared to a Coulomb gas. Because of the non-separability of the partition function, the rotational component of the emergent electric field is not freely fluctuating, as it is in the Coulomb gas. This represents a constraint on the rotational component which is not present in the Coulomb gas case, and which becomes important when considering the high-temperature specific heat of the HXY model.

At high temperature in 2D we expect from equipartition that the specific heat should be  $Nk_B$  for a general gas. In the case of a Coulomb gas with multi-valued charges, this would be the case; but for one with single charges only, the charge density at each site is bounded, and this places a constraint on the emergent elec-

tric field, removing one degree of freedom and giving a high-temperature specific heat asymptote of  $Nk_B/2$ . For the HXY model we have this additional constraint on the phase space of the rotational component arising from the periodicity of the spin-difference field, which removes the other degree of freedom and gives a high-temperature specific heat asymptote of 0.

When defining the harmonic mode susceptibilities of the HXY model we also have to be careful; the effective permittivity of the emergent electric field is not constant. This is again due to the periodicity of the components of the electric field, which again follows from the periodicity of the spin-difference field. The effective permittivity is defined as

$$(\epsilon_{\text{eff}}(L, T))^{-1} = \frac{J}{L^2} \sum_{\mathbf{x}} \sum_{n=1}^{\infty} (-1)^{n+1} \left\langle \cos \left[ \frac{na}{J} E_x(\mathbf{x}) \right] + \cos \left[ \frac{na}{J} E_y(\mathbf{x}) \right] \right\rangle \quad (4.38)$$

and the harmonic susceptibility as

$$\chi_{\bar{\mathbf{E}}} = \beta \epsilon_{\text{eff}}(L, T) L^2 \left( \langle \bar{\mathbf{E}}^2 \rangle - \langle \bar{\mathbf{E}} \rangle^2 \right) \quad (4.39)$$

We also expect that  $\chi_w^{\text{HXY}}(L, T) < \chi_w^{\text{CG}}(L, T)$  for a given system size and temperature, due to the coupling between the vortices and spin waves in the HXY model; this results in decreased mobility of the charges in the HXY model compared to the Coulomb gas, but does not affect the qualitative behaviour, as we will see in Chap. 7.

### 4.2.3. Simulation details for the HXY model

We can also define the microscopic dynamics of the [HXY model](#) in terms of the simulation method discussed in Chap. 3. The rotational update is unchanged: we add and subtract some unit of flux of the emergent electric field around a plaquette of the electric field lattice. This corresponds to a rotation of the HXY spin which sits at the centre of this plaquette, but without changing the vortex configuration. Such an update is shown in Fig. 4.3.

The field link update in the Coulomb gas is slightly more complicated in this context: it corresponds to a rotation of a spin in the HXY model, but one which takes a spin difference outside of  $[-\pi, \pi]$  and hence does change the vortex configuration.

Fig. 4.4 shows a spin rotation update in the HXY model which equates to a charge hop in the Coulomb gas. The central spin is rotated by an amount  $\pi/2 + \omega$ ,

#### 4. Lattice Coulomb gases and spin models

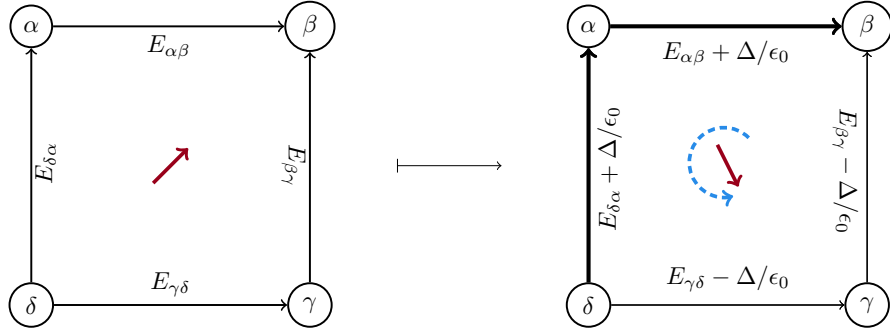


FIGURE 4.3.: The mapping between spin rotations in the HXY model and the rotational update of the Maggs-Rossetto model. In the HXY model, the maximum rotation  $\Delta_{\max}$  is necessarily  $2\pi$  due to the modular symmetry; this restriction does not apply to the Maggs-Rossetto algorithm.

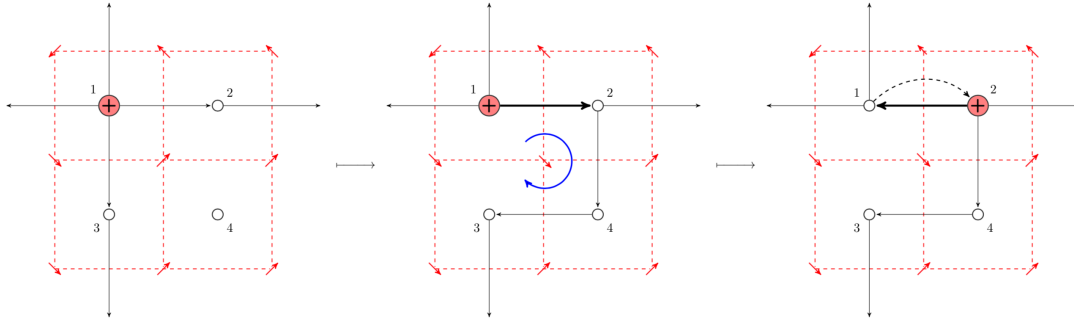


FIGURE 4.4.: A spin update in the HXY model which corresponds to a charge hop in the Coulomb gas, reproduced from [32].

where  $\omega$  is small and positive to ensure that the spin difference leaves the set  $[-\pi, \pi]$ . This means that the spin-difference field, and hence the corresponding field link of the emergent electric field, must be updated by subtracting  $2\pi J$ , which update is identical to a charge hop update in the Coulomb gas where a unit of flux  $q/\epsilon_0$  is added or subtracted. The spin rotation, which is equivalent to a rotational-field update, is then followed by a charge hop update.

### 4.3. Vertex models

**Vertex models** are a family of statistical physics models in which the energy levels (and hence Boltzmann weights) are associated with the configuration of a vertex. The vertices are connected by bonds (edges, if the vertices form a lattice), and the states of the bonds determine the energy associated with the vertex. This is fundamentally a different idea than (for example) the Ising model or other

nearest-neighbour models, where the energy of the system is solely determined by the states of the bonds themselves. In principle, it is possible to define a vertex model for whatever geometry we like, and to define an arbitrary number of configurations for any given vertex, but the models described in this section are all defined in 2D or 3D for regular lattices, with each bond having two possible states.

#### 4.3.1. Sixteen-vertex model

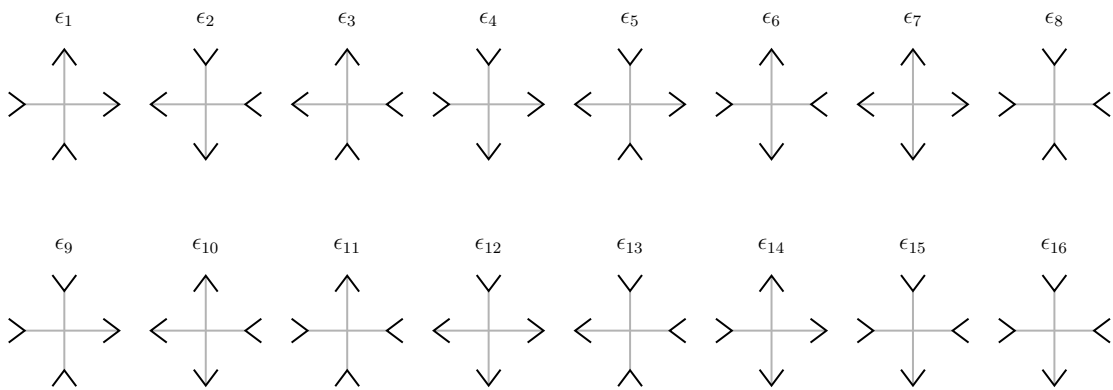


FIGURE 4.5.: The sixteen possible configurations of a single vertex of the square lattice, with  $\mathbb{Z}_2$  spins.

A vertex on the square lattice has a coordination number of 4 and hence four links to other vertices which surround it. By placing a “spin” (in this case, a classical Ising-type spin) on each of the links, and noting that each spin has two possible orientations, we see trivially that there are  $2^4 = 16$  possible configurations of a single vertex. Each configuration can, in principle, have a different statistical weight and correspond to a different energy.

In general, the [sixteen-vertex model](#) is not solvable analytically [49], but many other vertex models can be derived from it in different ways. One way of doing this is to assign different energies to vertex configurations based on some criteria. For example, by allowing all vertex configurations but assigning them different energies based on how many spins point in and how many point out, we can generate a simple model of spin ice materials, which will be discussed further below in Sec. 4.4. We can also assign some configurations an infinite energy, thereby disallowing them altogether and restricting the possible configurations of the vertex. By doing this, we can concern ourselves with vertex models which are more tractable but which also in some cases apply to real materials. One of the

## 4. Lattice Coulomb gases and spin models

simplest non-trivial models we can extract from the sixteen-vertex model is the six-vertex model, which serves as a toy model for water ice.

### 4.3.2. Six-vertex model

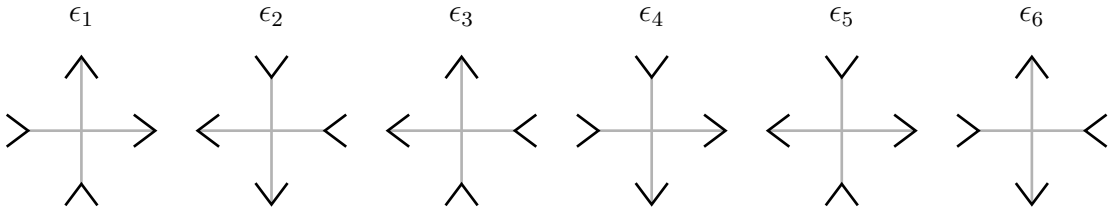


FIGURE 4.6.: The six ice-rule-obeying configurations of a single vertex of the square lattice. Several different ice-type models are obtainable by varying the energies of the  $\epsilon_i$  in different ways.

The [six-vertex model](#) is a starting point for three well-known statistical mechanics models, of which the square ice and F models are of particular interest here. To arrive at the six-vertex model we begin with the sixteen-vertex model and then add the constraint that exactly two spins must be pointing into the vertex, which disallows all but six possible configurations around any given vertex. We are free in principle to assign any energies we like to each vertex configuration, but in practice there are two groups of vertices shown: four with an overall magnetic moment and two without. In the absence of an external field, the energies of these groups should be degenerate, and this leaves us with three meaningful choices of energy levels, which correspond to the three models mentioned above.

### 4.3.3. Square ice model

The [square ice](#) is the prototypical [ice-type model](#) and was solved exactly by Lieb [11, 50]. In the square ice model we treat all six allowed configurations as exactly degenerate, i.e. set all  $\epsilon_i = 0$ : we then have a directed flux along links of a lattice along with a divergenceless condition, and the exact degeneracy means that the six-vertex model must also exhibit a Coulomb phase. Unlike in the spin ice models discussed below, however, the square ice model has no excited states, since any other vertex configuration with a higher energy is explicitly excluded.

### 4.3.4. F model

The Rys [F model](#) [4] is closely related to the six-vertex model, but instead of an exact degeneracy between the six vertex configurations, we assign each of the six

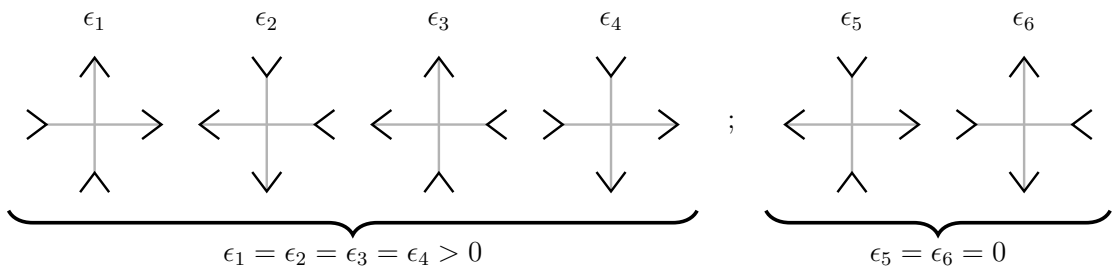


FIGURE 4.7.: The six allowed vertices with energy levels for the F model.

vertices to two different energy levels depending on their overall magnetic moment, as shown in Fig. 4.7. In this case, with the vertex configurations numbered as in 4.6, we set the four configurations with an overall magnetic moment to have some finite energy and the two with no overall moment to have zero energy, making it the ‘‘conjugate’’ model to the KDP model of ferroelectrics. This leaves us with two possible ground states which are identical up to a spin flip [51]; the ground state displays staggered, anti-ferroelectric order, and hence the model is also often referred to as the F model of anti-ferroelectrics.

The F model was also solved by Lieb [5], making it one of the few examples of an exactly solved non-trivial two-dimensional model. By duality arguments [52], it can be shown that the infinite-order phase transition admitted by the F model is exactly a BKT transition [53], with the high- and low-temperature regimes in the F model flipped compared to those in the XY model [54].

The F model is also relevant in the study of roughening transitions as shown by van Beijeren [55], since it is equivalent to the body-centred solid-on-solid (BCSOS) model.

#### 4.3.5. The Coulomb phase

We have now briefly outlined the theory of some well-known statistical mechanical vertex models and their physics, but there is another interesting class of system in which Coulombic physics can arise: we often see emergent Coulomb behaviour, or a ‘‘Coulomb phase’’, in frustrated magnetic systems. These are systems for which the global energy cannot be minimised by simultaneously minimising the energy at each point due to some local constraint. Such systems often end up with highly degenerate ground states separated from each other by large energy barriers. Henley [3] gives three conditions which are required for the presence of a Coulomb phase:

- A signed flux

#### 4. Lattice Coulomb gases and spin models

- A hard local constraint, e.g. that the divergence of some coarse-grained vector field  $\mathbf{P}(\mathbf{r})$  around a point be equal to zero
- No long-range order

Condition number 2 here leads to a free energy in terms of the vector field of

$$F_{\text{tot.}}(\{\mathbf{P}(\mathbf{x})\})/T = \text{const} + \int d^d \mathbf{r} K \frac{|\mathbf{P}(\mathbf{r})|^2}{2} \quad (4.40)$$

which is identical to the form of the free energy for an electric/magnetic field in the absence of charges/monopoles: hence the name “Coulomb phase”.

It should be noted that the Coulomb phase is then another example of the relevance of the [Helmholtz-Hodge decomposition](#) in physics: condition number 2 is precisely a divergence-free condition, and the associated vector field is an entirely [transverse](#) one. Excitations out of the Coulomb phase then correspond to a non-zero [longitudinal](#) component of the vector field.

One celebrated set of systems where the Coulomb phase takes a prominent role is that of the spin ices.

## 4.4. Spin ice

The compounds now referred to as [spin ices](#) are a family of rare-earth oxides with the general formula  $X_2Y_2O_7$ , where the rare-earth element  $X \in [Dy^{3+}, Ho^{3+}]$  and transition metal  $Y \in [Ti^{4+}, Zn^{4+}, Sn^{4+}]$ .  $Dy_2Ti_2O_7$  and  $Ho_2Ti_2O_7$  – dysprosium titanate and holmium titanate – are the two most closely studied, and are often referred to as DTO and HTO in the literature.

Holmium titanate was originally discovered during a systematic review of rare-earth titanate pyrochlores [33] as the first experimentally realisable geometrically frustrated ferromagnet. The pyrochlore lattice consists of corner-sharing tetrahedra and can be produced by placing atoms at  $(0, 0, 0), (\frac{a}{4}, \frac{a}{4}, 0), (\frac{a}{4}, 0, \frac{a}{4}), (0, \frac{a}{4}, \frac{a}{4})$  relative to each fcc lattice point, as shown in Fig. 4.8.

Dysprosium and holmium in particular have a crystal field environment which leads to a large magnetic moment [56] of  $\approx 10\mu_B$ . The lowest energy state is an Ising doublet with  $J_z = \pm J$ , which results in strong single-ion anisotropy along the local  $\langle 111 \rangle$  directions of the lattice [57]. In the case of pyrochlore materials, the  $\langle 111 \rangle$  axis connects each spin with the centres of the tetrahedra it sits on. The centre of each tetrahedron coincides with a lattice point on the diamond lattice, which is dual to the pyrochlore lattice and has a coordination number of 4.

The normalised directions of inward-pointing spins around a tetrahedron pointing down, e.g. the green tetrahedron in Fig. 4.9a, can then be written

$$\begin{aligned}\mathbf{s}_1 &= \frac{1}{\sqrt{3}}(+1, +1, +1); & \mathbf{s}_2 &= \frac{1}{\sqrt{3}}(-1, -1, +1) \\ \mathbf{s}_3 &= \frac{1}{\sqrt{3}}(-1, +1, -1); & \mathbf{s}_4 &= \frac{1}{\sqrt{3}}(+1, -1, -1)\end{aligned}\quad (4.41)$$

The overlap between any two spins is then  $\mathbf{s}_i \cdot \mathbf{s}_j = \pm \frac{1}{3}$ , with the positive sign if the spins both point inwards or both point outwards. However, the energy of the tetrahedron is minimised when exactly two spins are pointing in; it is therefore impossible to simultaneously minimise the energy on every bond, making the system highly geometrically frustrated.

The ferromagnetic interactions, crystal field environment and geometrical frustration in these systems combine to produce an emergent constraint around each vertex of the diamond lattice: the energy of a given diamond lattice point (which corresponds to a single tetrahedron of the pyrochlore lattice) is minimised when exactly two spins point towards it and the other two point away, leading to an extensively degenerate ground state with six possible configurations at each diamond lattice point. The ground state of a spin ice is then approximately an experimentally realisable example of the six-vertex model discussed above. However, unlike in the six-vertex model, spin ices have excited states with finite energy, which correspond to three-in-one-out/three-out-one-in or all-in-all-out vertex configurations, and it is these excited states which give us the rich Coulomb physics associated with these systems.

	$a_c$ [Å]	$D_{NN}$ [K]	$J_{NN}$ [K]	$U_C(a)$ [K]	$\nu_0$ [K]	$C_{\text{peak}}$ [ $\text{JK}^{-1}\text{mol}^{-1}_{\text{Ho, Dy}}$ ]	$T_{\text{peak}}$
$\text{Ho}_2\text{Sn}_2\text{O}_7$	10.37	2.17	-0.56	-2.83	-5.19	2.41	1.65
$\text{Ho}_2\text{Ti}_2\text{O}_7$	10.10	2.35	-0.63	-3.07	-5.57	2.61	1.75
$\text{Ho}_2\text{Ge}_2\text{O}_7$	9.90	2.50	-0.88	-3.27	-5.51	3.04	1.70
$\text{Dy}_2\text{Sn}_2\text{O}_7$	10.40	2.15	-0.99	-2.81	-4.27	2.65	1.20
$\text{Dy}_2\text{Ti}_2\text{O}_7$	10.10	2.35	-1.15	-3.07	-4.53	2.72	1.25
$\text{Dy}_2\text{Ge}_2\text{O}_7$	9.93	2.47	-1.80	-3.23	-3.58	3.17	0.828

TABLE 4.1.: Table of relevant properties of spin ice materials [58].

The simplest possible theoretical model for modelling spin ice physics is the sixteen-vertex model on the diamond lattice, which is normally referred to as the Near-neighbour spin ice (NNSI) model in the literature and will be discussed in more detail below. For NNSI, excitations are topological defects which interact only weakly via an entropic interaction. A more complicated theoretical model includes dipolar interactions, which are relatively strong in spin ices; the Dipolar spin ice (DSI) model mostly preserves the ground-state degeneracy [59], due to

#### 4. Lattice Coulomb gases and spin models

an inherent screening effect [60]. Further work on a related model, the dumbbell model [35], shows that the topological defects in DSI interact Coulombically and are deconfined (can be separated to infinity with finite energy cost); hence, we have dipolar excitations which fractionalise into magnetic monopoles.

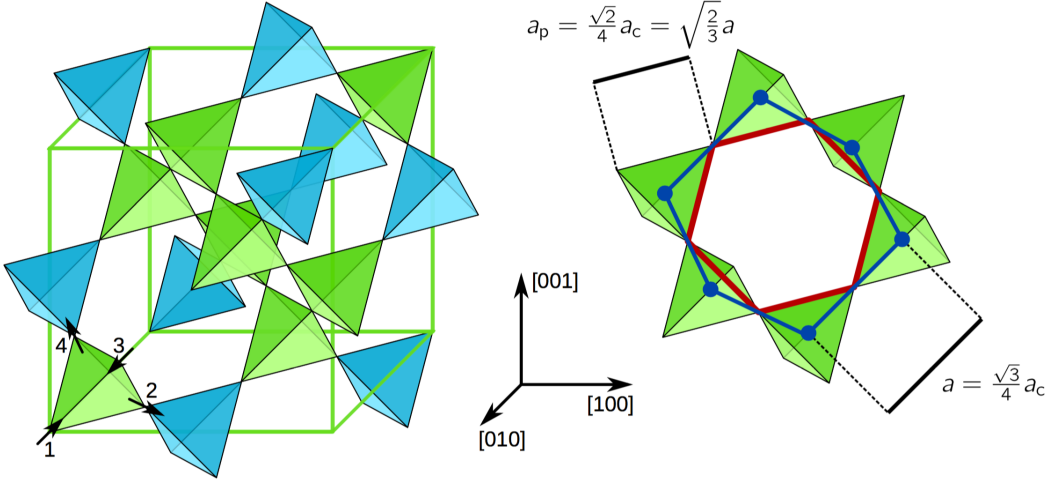


FIGURE 4.8.: Pyrochlore lattice structure and example of smallest closed loop, reproduced from [61].

We can think of the dumbbell model as describing a magnetic electrolyte, or “magnetolyte”, and can as such use concepts from electrolyte theory to characterise the behaviour of the magnetic monopole gas, including Debye-Hückel theory [62]. Previous work has also shown the presence of the second Wien effect in spin ice via simulations of AC field driving, with a sustained increase in free charge density matching that predicted by Onsager’s theory [61, 63].

Spin ice is a diverse and active area of research; for further information, reviews have been written by Castelnovo et al. [64] and Jaubert [65].

##### 4.4.1. Near-neighbour spin ice model

Near-neighbour spin ice is the simplest possible model for spin ices, but captures qualitative behaviour surprisingly well in many cases. Essentially, this is the Ising model with ferromagnetic interactions on the pyrochlore lattice, with the additional two-in-two-out constraint discussed above. Hence we have the standard

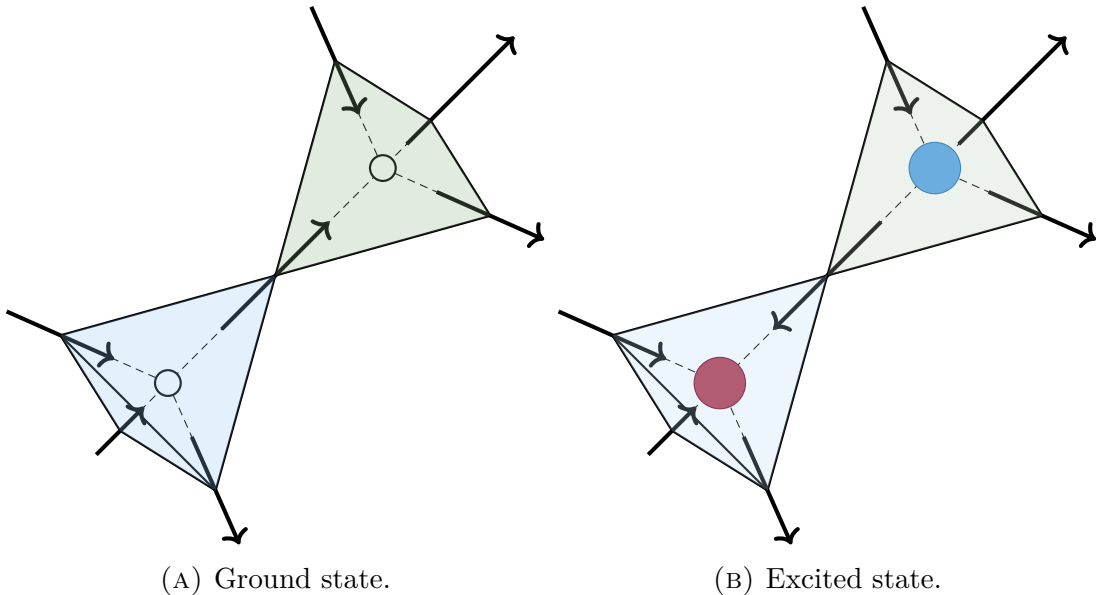


FIGURE 4.9.: Two possible states of a pair of tetrahedra in spin ice. The two-in-two-out ground state (left) becomes an excited state consisting of a pair of oppositely-charged defects (right) via the flipping of the spin connecting the two; depending on which model of spin ice we consider, these defects interact entropically, via a dipolar interaction or a Coulomb interaction.

Ising Hamiltonian

$$H = \sum_{i < j} J_{ij} \mathbf{s}_i \cdot \mathbf{s}_j \quad (4.42)$$

$$= J \sum_{i < j} \mathbf{s}_i \cdot \mathbf{s}_j \quad (4.43)$$

with  $J = -3.45$  K for DTO and  $-1.89$  K for HTO.

This Hamiltonian can be simplified by noting that outward spins correspond to up spins in one layer and down spins in the next, and that  $\mathbf{s}_i \cdot \mathbf{s}_j = \pm \frac{1}{3}$ , where the negative sign indicates one spin in and one spin out. In this way, we recover the Anderson antiferromagnetic pseudospin model [66].

The ground state properties of NNSI are also equivalent to those of the Pauling model of water ice [10], who gave an expression for the residual ground state entropy using an approximation based on the microstates of a single tetrahedron. The ice rules which govern the physics of this model were given by Bernal and Fowler [9]: in  $I_h$  water ice, the lowest energy state is reached when each oxygen ion is strongly bound to two protons and weakly bound to two others. For NNSI, the ice rules manifest as a “two-in two-out” constraint on each tetrahedron – two spins

#### 4. Lattice Coulomb gases and spin models

must point towards the centre of the tetrahedron, and two away. We note that there are six such configurations for each tetrahedron, out of a possible 16, and can give Pauling's result using this fact. There are  $N_s$  spins and  $N_t = \frac{1}{2}N_s$  tetrahedra, with each spin connecting two tetrahedra; the total number of configurations is then

$$\Omega = 2^{N_s} \left( \frac{6}{16} \right)^{N_t} = \left( 4 \frac{3}{8} \right)^{\frac{N_s}{2}} = \left( \frac{3}{2} \right)^{\frac{N_s}{2}} \quad (4.44)$$

so that the entropy per spin is

$$\frac{S_{g/s}}{N_s} = \frac{k_B \ln \Omega}{N_s} = \frac{1}{2} \ln \left( \frac{3}{2} \right) \quad (4.45)$$

The NNSI model makes exactly the same prediction as Pauling's result for water ice, since there are six exactly degenerate ice-rule obeying states out of sixteen total. The result is obviously an approximation, but comes surprisingly close to the real result; a series expansion by Nagle [67] gives a result 2% larger than Pauling's. Despite the NNSI model's qualitative utility, it is too simple to accurately describe the properties of the real-world materials DTO and HTO, and as such the **DSI** model was introduced.

##### 4.4.2. Coarse-graining

We can perform a coarse graining of the spins in the NNSI model in order to learn about the gauge structure of spin ice. We begin as normal by defining some volume  $V$  large enough to contain many spins, but still small compared to the system size, so that

$$\mathbf{M}(\mathbf{x}) = \sum_{\mathbf{x}} \frac{\mathbf{s}(\mathbf{x})}{V} \quad (4.46)$$

From the definitions of the spins, and the two-in-two out constraint discussed above, it becomes clear that in the absence of an external field the average sum of spins around a tetrahedron will be zero; there are two configurations with zero overall moment, two with a positive moment and two with a negative moment. We can see this also from noting that the system should be symmetric under  $\mathbf{M} \rightarrow -\mathbf{M}$  in the absence of applied field.

The constraint on the average magnetisation of a tetrahedron is, by definition, a divergence-free constraint:

$$\nabla \cdot \mathbf{M} = 0 \quad (4.47)$$

and so we have an example of the **Coulomb phase** in spin ice, and hence another

system where the Helmholtz decomposition is physically meaningful, since we can rewrite Eq. 4.47 as  $\mathbf{M} = \nabla \times \mathbf{Q}$  for some  $\mathbf{Q}$ .

### 4.4.3. Dipolar spin ice

As described above, the near-neighbour model gives a good qualitative description of the properties of spin ice. However, spin ices have relatively weak exchange interactions, since the electrons involved are deep in the shells of the rare-earth ions, and studying the relevant energy scales in more detail shows us that dipolar interactions in spin ice are of the same order of magnitude as the exchange. Because of this, dipolar interactions cannot be considered as a weak perturbation on the Hamiltonian and for quantitative accuracy it was necessary to introduce the dipolar spin ice model [34, 60, 68]

$$\mathcal{H} = -J \sum_{i>j} \mathbf{s}_i \cdot \mathbf{s}_j + D r_{nn}^3 \sum_{i>j} \frac{\mathbf{s}_i \cdot \mathbf{s}_j}{|\mathbf{r}_{ij}^3|} - \frac{3(\mathbf{s}_i \cdot \mathbf{r}_{ij})(\mathbf{s}_j \cdot \mathbf{r}_{ij})}{|\mathbf{r}_{ij}^5|} \quad (4.48)$$

Here the dipolar coupling  $D = \frac{\mu_0 \mu^2}{4\pi r_{nn}^3}$ , and the nearest neighbour dipolar interaction is  $D_{nn} = 5D/3$ . Likewise, the near-neighbour exchange coupling is actually  $J_{nn} = J/3$ , since the spins are not collinear.

The DSI model reproduces scattering data [34] and specific heats [60] very accurately, and also give good agreement with experimental measurements of Pauling's entropy [69]. It does however predict an ordered ground state at low temperature, which is not borne out by experiment.

### 4.4.4. Projective equivalence

It is interesting to note that most fundamental properties of spin ice are qualitatively captured by the simpler near-neighbour model, despite the lack of long-range dipolar interactions. The reason for this is that the NNSI model itself contains dipolar corrections; this was proved comprehensively by Isakov et al. [70], who named it the projective equivalence.

We can investigate the similarity between the NNSI and DSI ground state manifolds by Fourier transforming the respective Hamiltonians: for NNSI, we find a pair of degenerate flat bands and a pair of dispersive bands. Isakov et al. [70] then added a longitudinal projector, representing a model dipolar interaction, to the Hamiltonian and inspected the resulting spectrum. At  $T = 0$ , the physics is encoded entirely in the flat bands and hence the addition of a longitudinal component changes nothing. They show that the DSI Hamiltonian is proportional to

#### 4. Lattice Coulomb gases and spin models

their model projector at long distances and introduce a correction term which goes as  $O(r^{-5})$ . Combining all this, they show that including the long-range parts of the DSI Hamiltonian only weakly affects the ground states and entropy obtained using the NNSI Hamiltonian: the two models are equivalent under projection to the flat bands, hence “projective equivalence”. This equivalence is easier to see in the dumbbell model discussed below in Sec. 4.4.5, where the ground state corresponds to a vacuum and hence there is no longitudinal component by definition.

Fig. 4.10 shows an example of the projective equivalence: Fig. 4.10a shows experimental polarised neutron scattering result on  $\text{Ho}_2\text{Ti}_2\text{O}_7$  displaying pinch point features; Fig. 4.10b is taken from a simulation of the NNSI model with equivalent parameters, showing a qualitatively similar structure factor.

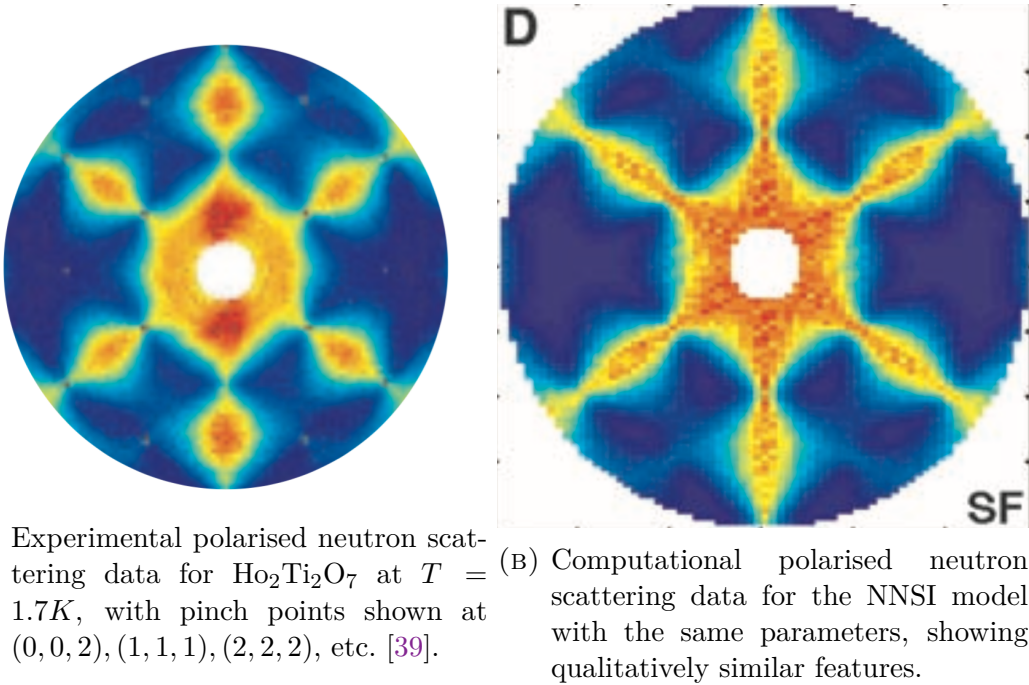


FIGURE 4.10.: Polarised neutron scattering plots for holmium titanate, from experiment and Monte Carlo simulation of the NNSI model respectively, showing only the spin-flip component of the scattering.

However, the projective equivalence only ensures screening of dipolar interactions in the ground state; once the system leaves the ice-rule obeying manifold of states, the associated defects once again have a dipolar interaction which contributes to the energy. The projective equivalence is another example of the relevance of the Helmholtz decomposition; the flat bands correspond to the divergence-free manifold of ice-rule obeying states at  $T = 0$ , and the dispersive bands correspond to the divergence-full component arising from the topological defects.

#### 4.4.5. Dumbbell model

Unlike in the **NNSI** model, defects in the **DSI** model possess a magnetic charge and interact Coulombically. Castelnovo et al.[35] and Ryzhkin [71] described this Coulomb gas of defects; Castelnovo et al. introduced the dumbbell model, transforming the DSI Hamiltonian into:

$$\mathcal{H} = -\nu_0 n_1 - 4\nu_0 n_2 + \frac{\mu_0 \mu^2}{\pi r_d^2} \sum_{i>j} \frac{q_i q_j}{|\mathbf{r}_{ij}|} \quad (4.49)$$

where  $\nu_0$  is the chemical potential associated with the creation of a single defect pair (i.e. the cost of flipping one spin in a 2-in-2-out tetrahedron),  $n_1$  is the population of single defects and  $n_2$  is the population of double defects. The final term in this Hamiltonian gives us a Coulombic interaction between magnetic charges  $Q_i$  and  $Q_j$ . We also note that  $\nu_0$  is obtained by requiring the energy of two neighbouring dipoles to match in the DSI and dumbbell models; we can therefore relate  $\nu_0$  to  $J_{NN}$  and  $D_{NN}$  via

$$\frac{\nu_0 q_m^2}{2} = \frac{4\nu_0 \mu^2}{2a_d^2} = 2J_{NN} + \frac{8}{3} \left(1 + \sqrt{\frac{2}{3}}\right) D_{NN} \quad (4.50)$$

The double defects represented by  $n_2$  have a charge of  $\pm 4\mu/a_d$  and therefore an associated chemical potential of  $4\nu_0$ .

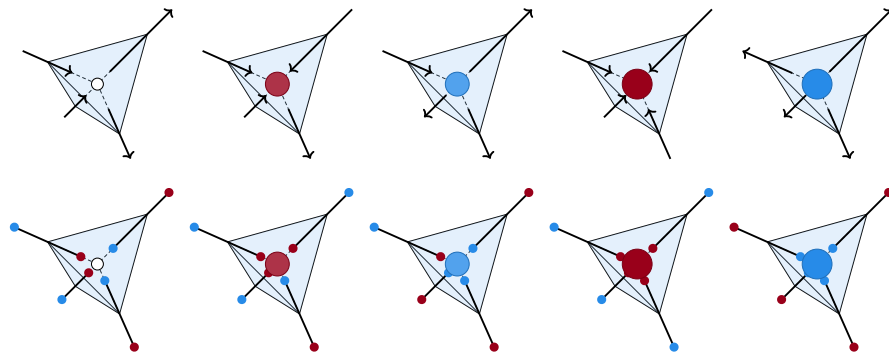


FIGURE 4.11.: Comparison of the DSI and dumbbell models. From left to right are shown tetrahedra with zero, positive, negative, double positive and double negative charges; the top and bottom rows show their representations in the DSI and dumbbell models respectively.

The transformation described by Castelnovo et al. works by imagining a “stretching” of the magnetic dipoles into dumbbells, consisting of equal and opposite magnetic charges. Both the dipoles and dumbbells are centred on pyrochlore lattice sites; the magnetic charges at either end of the dumbbell, however, are cleverly

#### 4. Lattice Coulomb gases and spin models

chosen to sit exactly on the vertices of the diamond lattice. As shown in Fig. 4.11, the four spins at each corner of a tetrahedron are then replaced by four magnetic charges which exactly coincide at the centre of the tetrahedron. The value of the charges is fixed at  $\pm\mu/a_d$ , where  $a_d$  is the diamond lattice near-neighbour distance, since we require the dipole moment of the spins to be preserved. A 3-in-1-out or 3-out-1-in defect then equates to an overall magnetic charge of  $Q_m = \pm 2\mu/a_d$  located at the centre of the tetrahedron, which we refer to as a positive or negative charge respectively. Fig. 4.12 shows examples of dumbbell configurations with zero, single and double charges respectively.

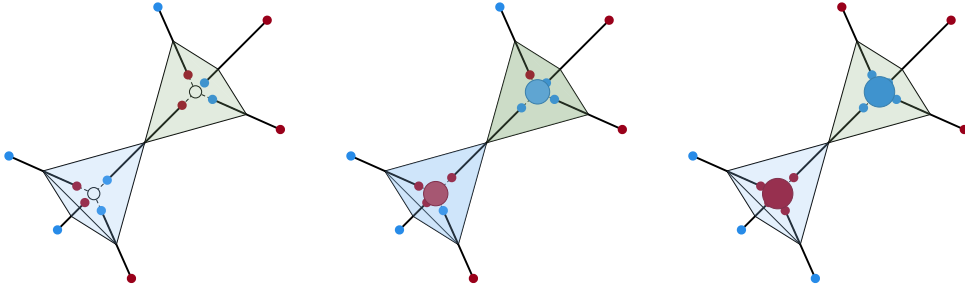


FIGURE 4.12.: Neutral, singly charged and doubly charged defects in the dumbbell model. For clarity, the dumbbells here are drawn with space between them; in reality the dumbbell model proceeds by assuming that the dumbbells meet exactly at the tetrahedral centres.

From Eq. 4.49 it is clear that the energy is minimised when the charge in each tetrahedron is zero – this constraint is exactly equal to the ice rule for spins discussed above, up to corrections of  $O(r^{-5})$  which can be neglected.

As shown in Eq. 4.49, we can consider the dumbbell model as a grand canonical Coulomb gas on the diamond lattice. Jaubert and Holdsworth [65] conducted coupled simulations of the DSI and dumbbell models in order to show rigorously that the mapping between the two is valid and that the chemical potential is a well-defined quantity. Since we can describe the dumbbell Hamiltonian as a grand canonical Coulomb gas, we can in turn use concepts from electrolyte theory to describe its behaviour.

## 4.5. Magnetic moment fragmentation

Magnetic moment fragmentation as seen in spin ice systems is an example of the wider phenomenon of fractionalisation, which arises in the fractional quantum Hall effect [72], one-dimensional solitons, and in graphene-like systems [73], among many other places. It has been a topic of intense interest in condensed matter and

statistical physics for many years and is much too broad a concept to be discussed in depth here.

In spin ice, however, fractionalisation arises essentially from a Helmholtz decomposition of the magnetic field, and so is directly relevant to the work presented in this thesis. To illustrate the idea we can return to Eq. 4.46.

The ice-rule obeying ground state is expressed as a divergence-free constraint in the coarse-grained picture; hence  $\mathbf{M}$  is entirely rotational in the absence of monopoles. Once the ice rule is broken, however, we have a divergence-full component which corresponds to the monopoles, and so we can write

$$\mathbf{M} = \mathbf{M}_m + \mathbf{M}_d = -\nabla\psi + \nabla \times \mathbf{Q} \quad (4.51)$$

where  $\mathbf{M}_m$  is the field due to monopoles,  $\mathbf{M}_d$  is the rotational dipolar field due to the spin network, and  $\mathbf{Q}$  is some arbitrary vector field as in the previous chapter.

The presence of a single monopole pair necessarily converts some of  $\mathbf{M}_d$  into  $\mathbf{M}_m$ , but not all of it. For example, for a three-out-one-in vertex (corresponding to a positive monopole) we can perform the Helmholtz decomposition by hand to find

$$\mathbf{M}_{ij} = \frac{m}{a} [1, 1, 1, -1] \quad (4.52)$$

$$= \frac{m}{a} \left[ \left( \frac{1}{2}, \frac{1}{2}, \frac{1}{2}, \frac{1}{2} \right) + \left( \frac{1}{2}, \frac{1}{2}, \frac{1}{2}, -\frac{3}{2} \right) \right] \quad (4.53)$$

$$(4.54)$$

where  $m$  is the magnetic moment strength; we see that the first term is divergence-full ( $\mathbf{M}_m$ ) and the second divergence-free ( $\mathbf{M}_d$ ).

In the spin ice case, a single monopole necessarily leaves some finite  $\mathbf{M}_d$ , whereas a double monopole is fully irrotational and  $\mathbf{M}_d = 0$ . This is different to the GLCG case where the rotational background is always present, because in spin ice the fields are of fixed length, but the underlying principle of Helmholtz decomposition is identical.

## 4.6. Artificial spin ice

Spin ices are excellent model systems for investigating frustrated magnetism and magnetic moment fragmentation, but there are a limited number of spin ice compounds and candidates which fit the models described above with varying degrees

#### 4. Lattice Coulomb gases and spin models

of success. In order to further investigate the same concepts in a more controlled way, there have been various efforts to reproduce the relevant physics by fabricating arrays of nanomagnets, which has led to the development of an entirely new field of study, both experimentally [74] and theoretically [75]. This interest is driven by the fact that it is possible to control the parameters of the fabricated system, e.g. the lattice constant and the effective exchange constant, and in this way to fundamentally change the physics of the system.

**Artificial spin ice (ASIs)** are constructed of single-domain, ferromagnetic islands with strong shape anisotropy, which results in a spin with Ising-like behaviour. The islands are arranged in such a way that the spins lie on the edges of a square lattice; the spins are taken to interact with their nearest-neighbours only. The analogy with spin ice and **vertex models** more generally is clear: at any given vertex of a square ice, there are sixteen possible configurations of the four Ising spins, so in principle we recover the **sixteen-vertex model** of Sec. 4.3.1.

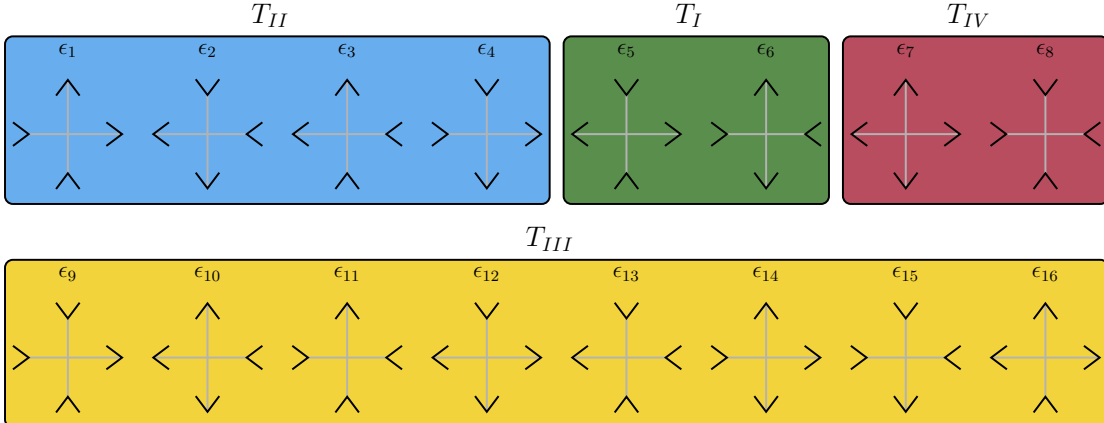


FIGURE 4.13.: The four vertex types of the 16 vertex model, arranged by overall “charge” and magnetic moment.

In practice, this lattice geometry places an immediate constraint on the energies of the four types of vertex, because the nearest-neighbour distances are anisotropic. A spin pointing in the x-direction is nearer to its neighbour in the x-direction than in the y-direction and vice-versa, meaning that the vertex energies are partitioned as in Fig. 4.13. The Type-I/Type-II degeneracy required for the **six-vertex model**/**square ice (Lieb) model** model is therefore broken and an artificial spin ice system produced with this geometry actually shows physics qualitatively similar to that of the **F model**, even though there are long-range interactions between dipoles.

Several experimental solution to this problem have been proposed: one approach

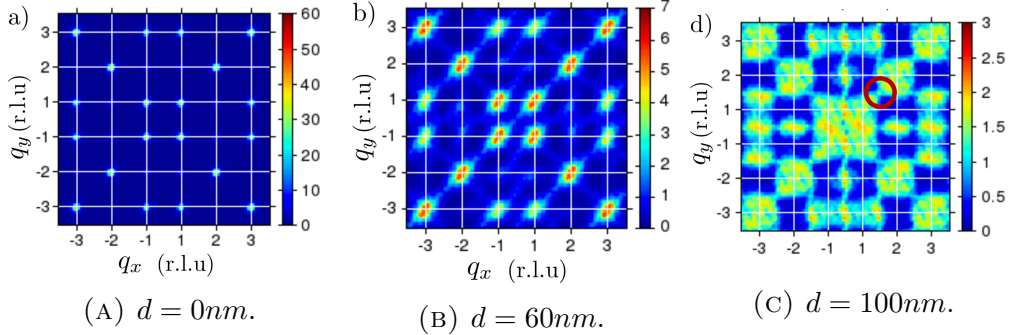


FIGURE 4.14.: Magnetic structure factors for different z-offsets  $d$ , reproduced from [36]. We see the crossover from a Type-II dominated ordered state at zero offset to an ice-rule obeying state at  $d = 100\text{nm}$ .

focuses on offsetting one sublattice in the z-direction [36, 76] in order to tune the respective coupling strengths. Fig. 4.14 shows three examples of magnetic structure factors for different z-offsets: Figs. 4.14a and 4.14b show peaks consistent with the ordering in the F model ground state, as will be discussed in Chap. 6, whereas Fig. 4.14c shows the diffuse features and pinch points associated with the ice-rule degeneracy.

Another approach is to introduce interaction modifiers, in the form of discs, at the vertices of the lattice. These modifiers behave as XY-like spins with different activation energies to the Ising-like spins on the edges; the different activation energies force the XY-like spins to be slaved to the Ising-like spins, and by varying the diameter  $D$  of the discs it is possible to tailor the strength and ratio of the interaction energies [37]. Fig. 4.15 shows two examples of magnetic structure factors, one with no XY-type disc and one averaged over seven individual structure factors with the disc diameter  $D = 150\text{nm}$ . We see that Fig. 4.15a has the broad peaks associated with the F model ground state, whereas Fig. 4.15b once again displays the features characteristic of a system obeying the ice rules.

The effect of either of these approaches is the same, and can be clearly seen from the magnetic structure factors: without tuning the interaction at all, we see the network of Type-I vertices which is the F model ground state. As the effective interaction strength is tuned towards isotropy, the antiferromagnetic order starts to break down and the peaks start to disappear. Type-I domains start to decrease in size and Type-II domains begin forming and increasing in size, until finally the two nearest-neighbour interaction strengths converge and the two vertex types are equally favourable. At this point, the system is highly disordered with Type-I and Type-II vertices equally likely, and the correlations start to show the diffuse

#### 4. Lattice Coulomb gases and spin models

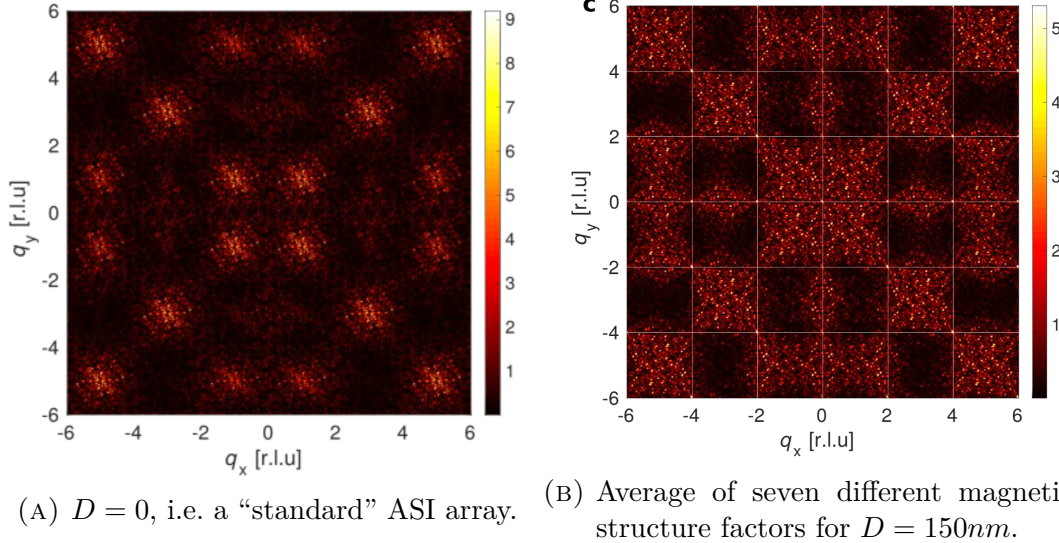


FIGURE 4.15.: Magnetic structure factors for different disc diameters  $D$  reproduced from direct observation of the discs, reproduced from [37]. Again, we see the crossover from a relatively ordered state with no disc to one with the six-vertex degeneracy of the square ice model.

features and pinch points associated with dipolar correlations and ice models.

A strikingly similar phenomenon to this can be observed in the [GLCG](#), as will be seen later in Sec. 6.4, where the staggered order emerges from a change in the [core-energy](#) constant of the system resulting in a charge crystal. This is reminiscent of the suggestion of Brooks-Bartlett et al. [77] that a change in the chemical potential of a spin ice could result in condensation of a monopole crystal accompanied by a [Coulomb phase](#) in the “leftover” magnetisation.

Additionally, the study of artificial spin ices is not limited to the square lattice: there has also been substantial recent work on “Shakti” lattices [78, 79] which use a combination of 4-fold, 3-fold and even 2-fold coordination [38]. These also map to the Coulomb gas via a mapping to the F model, discussed above in Sec. 4.3.4.

Next, I outline the basic ideas behind correlation functions and neutron scattering, since I will use these concepts extensively in my simulations of the Coulomb gas.

# 5. Correlation tensors and our models

## 5.1. Correlation functions

A correlation function is any response function which measures how some quantity of interest in a system is correlated with some other quantity. This extremely broad definition means that correlation functions are of extremely broad utility.

Scattering experiments give us information about correlation functions in the scattering system. For example, X-ray scattering gives information about electron-electron correlations, while spin-spin correlation functions are probed by neutron scattering experiments.

## 5.2. Scattering experiments

In general, a scattering experiment consists of perturbing some system using a probe of some kind: the probe has some incoming wavevector  $\mathbf{k}_i$  and is scattered by the system into some outgoing wavevector  $\mathbf{k}_f$ . By measuring the change in the momentum  $\mathbf{p} = \hbar\mathbf{k}$  of the probe we have the relationship

$$(\mathbf{p}_f - \mathbf{p}_i)/\hbar = \mathbf{k}_f - \mathbf{k}_i = \mathbf{Q} \quad (5.1)$$

where  $\mathbf{Q}$  is called the scattering vector.

We can also, in general, have a change in the energy of the probe; this corresponds to the case where  $|\mathbf{k}_i| \neq |\mathbf{k}_f|$ . In this case we can calculate the change in energy, which for a neutron is given by

$$\Delta E = E_f - E_i = \frac{\hbar^2}{2m} (|\mathbf{k}_f|^2 - |\mathbf{k}_i|^2) = \hbar\omega \quad (5.2)$$

the frequency  $\omega$  then tells us about the magnitude of the energy transfer. The two parameters  $\mathbf{Q}$  and  $\omega$  are the most important parameters in a neutron scattering

## 5. Correlation tensors and our models

experiment; for a photon we would instead find  $E = h\nu$  and so  $\mathbf{Q}$  and  $\nu$  would be the relevant parameters.

In this rest of this chapter I will discuss neutron scattering only, since neutron scattering is a natural choice for investigating properties of condensed matter systems, as explained below, and hence is useful in spin systems such as those mentioned in Chap. 4 which map to the Coulomb gas.

### 5.3. Neutron scattering

Neutrons (in particular thermal neutrons) make good probes for investigating both the nuclear and magnetic structure of a system for several reasons: firstly, the wavelength of thermal neutrons is of the same order as the separation of nuclei in condensed matter systems [80]. Also, and most importantly, the neutron possesses a magnetic moment but no electric charge: this allows it to couple to the spins of both nuclei and electrons. In what follows we will not be concerned with neutron scattering from nuclei since we study idealised systems with point charges.

We then consider that neutrons are scattered by a magnetic field  $\mathbf{B}$  which originates from the electron spins in the sample: neutron scattering shows us the Fourier-space representation of the field,  $\mathbf{B}(\mathbf{q})$ , which is related to the spin field in Fourier space  $\mathbf{S}(\mathbf{q})$ .

It can be shown [81] that the scattering is proportional to the two-spin correlation function of the system:

$$S^{\alpha\beta}(\mathbf{q}, \omega) = \frac{1}{2\pi} \sum_{\mathbf{x}} \int_{-\infty}^{+\infty} \exp[i\mathbf{q} \cdot \mathbf{x} - \omega t] \langle S^\alpha(\mathbf{0}, 0) S^\beta(\mathbf{x}, t) \rangle dt \quad (5.3)$$

where  $S^\alpha$  in the above represents the spin field; the quantity in  $\langle \dots \rangle$  is the Fourier transform of the two-spin correlation function and the brackets denote an ensemble average. The quantity  $S^{\alpha\beta}(\mathbf{q}, \omega)$  may be referred to as the “dynamic scattering function”.

### 5.4. Static approximation

For elastic neutron scattering, i.e. where energy transfer between the neutron and sample are negligible, the full (dynamic) scattering function will approach a delta function at the origin at  $\omega$  [82]. Hence, we can integrate over frequencies, giving

the “static approximation”:

$$S^{\alpha\beta}(\mathbf{q}) = \sum_{\mathbf{x}} \langle S^\alpha(\mathbf{0}, \omega = 0) S^\beta(\mathbf{x}, \omega = 0) \rangle \exp[i\mathbf{q} \cdot \mathbf{x}] \quad (5.4)$$

$$= \int_{-\infty}^{+\infty} S^{\alpha\beta}(\mathbf{q}, \omega) d\omega \quad (5.5)$$

The static scattering function  $S^{\alpha\beta}(\mathbf{q})$  is technically defined here for  $t = 0$  but in a real experiment (or the simulations performed for the Coulomb gas) the correlations are sampled at many different times; by doing so, we take an ergodic average, which by the ergodic theorem is equal to an ensemble average.

The correlation tensor given in Eq. 5.5 contains all the information about the instantaneous field correlations in the system, but is not a quantity which can be directly probed experimentally, for the simple reason that no probe can “see” all of the tensor at once.

## 5.5. Polarised neutron scattering

A neutron scattering experiment cannot provide us with the entire scattering function Eq. 5.5; we can only observe part of it. One fundamental limitation is due essentially to Gauss’ Law of magnetism:  $\nabla \cdot \mathbf{B} = 0$ . The Fourier transform of this equation is  $\mathbf{q} \cdot \mathbf{B}(\mathbf{q})$ , implying that the Fourier transform of the magnetic field inspected at any wavevector  $\mathbf{q}$  has no component along the direction  $\mathbf{q}$ . Hence, a neutron with wavevector  $\mathbf{Q}$  “sees” no spin component in the direction of  $\mathbf{Q}$ , and only sees the components *perpendicular* to the scattering vector. Mathematically, we can represent this projection with the expression  $(\delta_{\alpha\beta} - \hat{Q}_\alpha \hat{Q}_\beta)$ . There is also another factor which enters the formula for an experimental neutron scattering cross-section which arises from the fact that electrons in real materials are not point particles: the Wigner-Eckhart theorem tells us that the cloud of electron density around a real atom can be replaced, up to some factor, by a spin operator localised to a point. This extra factor is called a magnetic form factor and is specific to the atom or ion in question; detailed discussion of these is beyond the scope of this thesis.

Another feature of unpolarised neutron scattering is that it cannot distinguish between spin states. In order to separate the components of the tensor and remove the sum over  $\alpha$  and  $\beta$  in the previous equation, we can use polarisation analysis; this relies on the fact that scattering may flip the neutron spin or not, and that a neutron spin flip is necessarily accompanied by a spin flip in the sample. A

## 5. Correlation tensors and our models

simplified explanation follows in which I again ignore the effect of nuclear scattering, since the field correlations I study in this thesis do not have associated nuclei. There are two spin states  $(+, -)$  of a neutron and hence four potential cross sections  $U^{++}, U^{+-}, U^{-+}, U^{--}$ ; it can be shown [83] that they can be written

$$U_i^{ss'} = \langle s' | -p_i \mathbf{S}_i^\perp \cdot \boldsymbol{\sigma} | s \rangle \quad (5.6)$$

where  $p$  is the magnetic amplitude defined by

$$p = \frac{\gamma e^2}{2mc^2} gS f(\mathbf{q}) \quad (5.7)$$

the perpendicular component of the scattering tensor is given by

$$S^\perp(\mathbf{Q}) = (\delta_{\alpha\beta} - \hat{q}_\alpha \hat{q}_\beta) S^{\alpha\beta}(\mathbf{q}) \quad (5.8)$$

the  $\boldsymbol{\sigma}$  are the Pauli matrices,  $\gamma$  is the neutron magnetic moment,  $gS$  is the atomic moment and  $f(\mathbf{q})$  is the magnetic form factor. I use  $\mathbf{Q} = \mathbf{q} + \mathbf{G}$  where  $\mathbf{G}$  is a reciprocal lattice vector to denote the argument of the perpendicular component of the tensor, since  $S^{\alpha\beta}(\mathbf{q})$  is periodic in each Brillouin zone but  $S^\perp(\mathbf{Q})$  in general is not. We will see examples of this in Chapters 6 to 8.

Following through Eq. 5.6 we find for the four cross sections

$$U^{++} = -p S_z^\perp \quad (5.9)$$

$$U^{--} = +p S_z^\perp \quad (5.10)$$

$$U^{+-} = -p(S_x^\perp + iS_y^\perp) \quad (5.11)$$

$$U^{-+} = -p(S_x^\perp - iS_y^\perp) \quad (5.12)$$

where the directions  $x, y, z$  refer to the polarisation direction of the neutron. Hence, we see that by measuring the cross sections of spin-flipped neutrons and non-spin-flipped neutrons as a function of polarisation, the components of  $S^{\alpha\beta}(\mathbf{q})$  can be separated.

For example, paramagnetic and nuclear spin scattering give rise to spin-flip scattering, and may be distinguished by measuring spin-flip cross sections with the neutron polarisation first parallel and then perpendicular to the wavevector [84], since if the polarisation is parallel to the scattering wavevector all magnetic scattering must be spin-flip [83]. Polarisation analysis is a powerful technique and was used (for example) in Fig. 1.1c to isolate the in-plane component of the magnet-

isation.

## 5.6. Scattering function and correlation functions

We can also exploit the connection between susceptibilities and correlation functions to rewrite the scattering function in terms of the magnetisation of the system.

Defining a Fourier-transformed magnetisation field as

$$\mathbf{M}(\mathbf{q}) = \frac{1}{N} \sum_{\mathbf{x}} \mathbf{S}(\mathbf{x}) \exp [i\mathbf{q} \cdot \mathbf{x}] \quad (5.13)$$

we can rewrite  $S^{\alpha\beta}(\mathbf{q})$  as

$$S^{\alpha\beta}(\mathbf{q}) = \langle \mathbf{M}^\alpha(\mathbf{q}) \mathbf{M}^\beta(-\mathbf{q}) \rangle \quad (5.14)$$

Note that via the classical fluctuation-dissipation theorem, we have

$$S^{\alpha\beta}(\mathbf{q}) = \frac{\chi^{\alpha\beta}(\mathbf{q})T}{C} \quad (5.15)$$

with  $C$  the Curie constant.

## 5.7. Propagation vectors

One very appealing thing about neutron scattering experiments is the ability they give us to measure both nuclear and magnetic structures, but this can also present a difficulty: the two structures are not generally coincident. A powerful way of describing the magnetic structure with reference to the underlying nuclear structure is given by the language of propagation vectors [85]. Assuming that magnetic moments form a field

$$\boldsymbol{\mu}(\mathbf{x}) = \sum_{\mathbf{q}} \mathbf{m}(\mathbf{q}) \exp (-i\mathbf{q} \cdot \mathbf{x}) \quad (5.16)$$

where  $\mathbf{m}(\mathbf{q})$  is the Fourier component of the magnetic moment distribution associated with the wavevector  $\mathbf{q}$ .

Assuming that the magnetic moments are associated with magnetic atoms, the periodicity of the moments in real space is the same as that of the nuclear

## 5. Correlation tensors and our models

structure. Hence, the wavevectors  $\mathbf{q}$  can be chosen in the first Brillouin zone.

We then have as many magnetic peaks appearing in a neutron scattering experiment as there are distinct propagation vectors  $\mathbf{q}$  in Eq. 5.16; the peaks appear at wavevectors  $\mathbf{Q} = \mathbf{q} + \mathbf{G}$ .

As an example [86], if there is only one wavevector  $\mathbf{q}_0$  in this sum we have

$$\boldsymbol{\mu}(\mathbf{x}) = \mathbf{m}(\mathbf{q}_0) \exp(-i\mathbf{q}_0 \cdot \mathbf{x}) \quad (5.17)$$

If, for example,  $\mathbf{q}_0 = 2\pi(0, 0, 1/2)$  and  $\mathbf{m}(\mathbf{q}_0) = (0, 1, 0)$ , at  $\mathbf{x}_0 = (0, 0, 0)$  we have

$$\boldsymbol{\mu} = \mathbf{m}(\mathbf{q}_0) \exp(-i\mathbf{q}_0 \cdot \mathbf{x}_0) \quad (5.18)$$

$$= (0, 1, 0) \exp(-i(0, 0, \pi) \cdot (0, 0, 0)) = (0, 1, 0) \times 1 \quad (5.19)$$

$$= (0, 1, 0) \quad (5.20)$$

At  $\mathbf{x}_1 = (0, 0, 1)$  we have

$$\boldsymbol{\mu} = \mathbf{m}(\mathbf{q}_0) \exp(-i\mathbf{q}_0 \cdot \mathbf{x}_1) \quad (5.21)$$

$$= (0, 1, 0) \exp(-i(0, 0, \pi) \cdot (0, 0, 1)) = (0, 1, 0) \times -1 \quad (5.22)$$

$$= (0, -1, 0) \quad (5.23)$$

and we see that the exponential flips the sign of the resulting magnetic moment. Hence, the propagation vector  $\mathbf{q}_0 = 2\pi(0, 0, 1/2)$  corresponds to antiferromagnetic order in the  $c$  direction of the lattice.

In magnetic diffraction experiments these wavevectors are normally referred to using the letter  $\mathbf{k}$ ; I use  $\mathbf{q}$  here for consistency with notation elsewhere. In general, we can have systems where only one wavevector (referred to as single- $k$  structures) or multiple wavevectors (multi- $k$  structures) appear in this sum.

The wavevector or wavevectors chosen by the system arise because the system breaks some symmetry and condenses into some kind of magnetic order in order to minimise its energy; the details of the wavevectors depend on the details of the Hamiltonian.

## 5.8. Geometric representations of tensors

The static scattering function discussed previously is an example of a tensor: a geometrical object which transforms in specific ways under changes in coordinate

system. A full overview of the theory of tensors is far beyond the scope of this thesis, but there is a useful interpretation of a two- or three-dimensional tensor which can be useful in the context of visualisation of electromagnetic systems. Most of the following is due to Nye [87].

By considering the equation

$$A_{ij}x_i x_j = 1 \quad (5.24)$$

where  $A_{ij}$  are some coefficients and we use Einstein summation notation, we can write the equation out longhand as

$$\begin{aligned} & A_{11}x_1^2 + A_{12}x_1 x_2 + A_{13}x_1 x_3 + \\ & A_{21}x_2 x_1 + A_{22}x_2^2 + A_{23}x_2 x_3 + \\ & A_{31}x_3 x_1 + A_{32}x_3 x_2 + A_{33}x_3^2 = 1 \end{aligned} \quad (5.25)$$

from which, by assuming  $A_{ji} = A_{ij}$ , we can collect terms to obtain

$$A_{11}x_1^2 + A_{22}x_2^2 + A_{33}x_3^2 + 2A_{12}x_1 x_2 + 2A_{13}x_1 x_3 + 2A_{23}x_2 x_3 = 1 \quad (5.26)$$

which is the equation of a three-dimensional surface which may be an ellipsoid or hyperboloid.

It can be shown that the coefficients  $A_{ij}$  transform as components of a tensor under a change in coordinate system  $x_i \rightarrow x'_i$ . The surface formed by these coefficients are referred to as the representation quadric of the tensor  $\mathbf{A}$ .

This formulation is quite general: the only requirement is that  $\mathbf{A}$  be a symmetric tensor, which is often true in physics and indeed always true if the property described by a tensor is isotropic.

### 5.8.1. Principal axes

A fundamental result for quadrics tells us that so long as at least one of the  $A_{ii}$  diagonal terms is non-zero, we can rearrange the quadric into the special form [88]

$$A_{11}x_1^2 + A_{22}x_2^2 + A_{33}x_3^2 = 1 . \quad (5.27)$$

This form is obtained by using three particular, orthogonal directions in Eq. 5.24: these directions are called the principal axes of the tensor. For the case of a second-rank tensor, i.e. a physical quantity which can be written in matrix form, this op-

## 5. Correlation tensors and our models

eration is equivalent to diagonalisation of the matrix; the principal axes are then the eigenvectors and the diagonal terms  $A_{ii}$  are the corresponding eigenvalues.

Once the principal axes have been found, we can compare the expression Eq. 5.27 to the equation for a general conic section

$$\frac{x^2}{a^2} + \frac{y^2}{b^2} + \frac{z^2}{c^2} = 1 \quad (5.28)$$

we see that the elements  $A_{ii}$  correspond to the lengths of the axes in a conic surface. The important quantities are then  $1/\sqrt{A_{ii}}$ , and their signs determine what kind of surface is represented by the tensor: if all three are positive the representation quadric is an ellipsoid, and so on for all the possible combinations of sign.

It is important to note here that we can also define quadrics for inverse tensors also; in the magnetic case, for example, we normally define

$$M^\alpha = \chi^{\alpha\beta} H^\beta \quad (5.29)$$

but it is equally valid to write

$$H^\alpha = \bar{\chi}^{\alpha\beta} H^\beta \quad (5.30)$$

and define the quadric for the inverse tensor  $\bar{\chi}$ . Basic linear algebra tells us that the eigenvalues of the inverse tensor are the reciprocal of the eigenvalues of the direct tensor.

## 5.9. Coulomb gas formulation

All of the above has been written for a spin field, i.e. a field of fixed-length magnetic moments, since this is what is relevant in an neutron scattering experiment, but the assumption of fixed-magnitude fields is unnecessary.

In my work, we calculate the static scattering function for the electric field because the Coulomb gas maps to magnetic systems such as the XY model and spin ices/artificial spin ices. By calculating the scattering function for the electric field in the Coulomb gas and simulating a neutron scattering experiment from that, we gain insight into neutron scattering experiments on those magnetic systems.

We then have a static scattering function defined by

$$S^{\alpha\beta}(\mathbf{q}) = \langle E^\alpha(\mathbf{q}) E^\beta(-\mathbf{q}) \rangle \quad (5.31)$$

where

$$E^\alpha(\mathbf{q}) = \sum_{\mathbf{x} \in D} \exp \left[ -i \frac{2\pi}{La} \mathbf{q} \cdot \left( \mathbf{x} + \frac{a}{2} \mathbf{e}^\alpha \right) \right] E^\alpha(\mathbf{x}) \quad (5.32)$$

is the Fourier transform of the  $\alpha$  component of the field. As can be seen from Eq. 5.32, to Fourier transform the field correctly we have to take into account the offset of each component relative to the charge sites it sits between and the field components in the other directions.

It is also worth noting a useful identity: for real inputs, such as the electric fields in this problem, it is trivially true that

$$E^\alpha(-\mathbf{q}) = (E^\alpha(-\mathbf{q}))^* \quad (5.33)$$

since  $E^\alpha(\mathbf{x}) \in \mathbb{R} \forall \mathbf{x}$ , so the only effect of  $\mathbf{q} \rightarrow -\mathbf{q}$  is to conjugate the exponential term in Eq. 5.32.

Next, we consider the shape of the correlation tensor in the Coulomb gas formulation via the method outlined in the previous section. We find that for each value of  $\mathbf{q}$ , the tensor will have  $d$  eigenvectors and eigenvalues in  $d$  dimensions. The tensor will also be periodic in each Brillouin zone (for a Bravais lattice), since it respects the direct-space periodicity of the lattice. In the case of the eigenvectors, it is also important to note that one will always be longitudinal to  $\mathbf{q}$ , and the other (in 2D) or others (3D) transverse: the  $d - 1$  eigenvalues corresponding to the transverse eigenvectors should also be degenerate, assuming the system is isotropic. We denote the eigenvalue corresponding to the longitudinal eigenvector as  $\lambda_l$  and the transverse eigenvalue as  $\lambda_t$ .

It can be shown that in the Coulomb phase discussed in Chap. 4, one of the eigenvalues of the tensor [89] becomes very small compared to the others; the quadric is an infinitely thin disc in 3D or a needle in 2D. This is a consequence of the definition of the Coulomb phase: the zero-divergence condition, when Fourier transformed, becomes  $\mathbf{q} \cdot \mathbf{M}(\mathbf{q}) = 0$ , i.e. there is no component parallel to the coarse-grained vector field and  $\lambda_l \rightarrow 0$ . This leaves two degrees of freedom (in 3D) or one (in 2D), and the shape of the tensor is a disc or a needle respectively. In the paramagnetic phase, by contrast, all the eigenvalues are degenerate; we are free to pick one longitudinal and  $d - 1$  transverse eigenvectors, and the tensor is a circle or a sphere. The quadrics I plot in Chaps. 6–8 are all those of the inverse tensor for this reason: in the case of the direct tensor we have Eq. 5.34, where the

## 5. Correlation tensors and our models

longitudinal direction is arbitrarily labelled as  $x$ .

$$\frac{x^2}{\lambda_l^2} + \frac{(y^2 + z^2)}{\lambda_t^2} = 1 \quad (5.34)$$

In the Coulomb phase,  $\lambda_l \rightarrow 0$ , and it becomes difficult to perform the eigen-decomposition, since the determinant of the tensor goes to zero. By using the inverse tensor we reciprocate the eigenvalues and have instead one small and one large eigenvalue by Eq. 5.35.

$$x^2 \lambda_l^2 + (y^2 + z^2) \lambda_t^2 = 1 \quad (5.35)$$

which is equivalent to Eq. 5.34 but numerically more stable to decompose. Using the inverse tensor and Eq. 5.35 also means that the principal axes of the tensor are proportional to the square root of the correlation function; hence, using this form, we represent fluctuations in the field rather than “inverse fluctuations”.

Finally, we can identify three main regimes of interest in the eigenvalues  $\lambda_l$  and  $\lambda_t$ :

1.  $\lambda_l = 0; \lambda_t \neq 0$ : Needle (2D) or disk (3D). Coulomb phase, as discussed by Henley [3].
2.  $\lambda_l \neq 0; \lambda_t \neq 0; \lambda_l \neq \lambda_t$ : Ellipse (2D) or ellipsoid (3D). Harmonic phase.
3.  $\lambda_l \neq 0; \lambda_t \neq 0; \lambda_l = \lambda_t$ : Circle (2D) or sphere (3D). Paramagnet.

Examples of regimes 1 and 2 are shown in Fig. 5.1 [89].

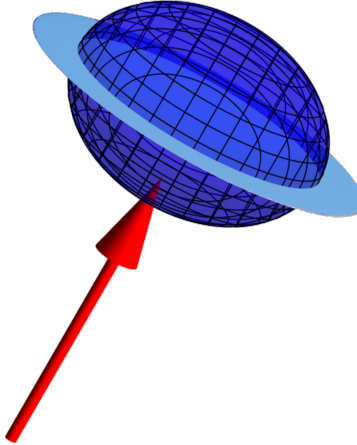


FIGURE 5.1.: Diagram showing the shape of two different examples of  $S^{\alpha\beta}(\mathbf{q})$  tensor. The solid blue disk corresponds to regime 1 below (Coulomb phase); the translucent dark blue mesh to regime 2 (harmonic phase). Reproduced from [89].

## 5.10. Our models

The models I use for simulation in this thesis are based on the square and simple cubic lattices, with fields constrained to lie along the lines connecting lattice points. This implies a bi(tri)partite field lattice of  $x, y, z$  components in two or three dimensions. As alluded to in Sec. 4.6, this arrangement necessarily leads to there being two different nearest-neighbour differences and Brillouin zone sizes: the Brillouin zone for the charges and for any single field component taken on its own are the same size, but the Brillouin zone for the off-diagonal components of the tensor is larger. We can see in Eq. 5.32 that the Fourier transform of the field must also take into account the different directional offsets of the field components.

The reciprocal vectors for the charge lattice and the diagonal field-field correlation terms are the standard reciprocal lattice vector for the square or simple cubic lattice vectors: in real space we have

$$(a, 0), (0, a) \quad \text{or} \quad (a, 0, 0), (0, a, 0), (0, 0, a) \quad (5.36)$$

which result in the familiar reciprocal lattice vectors of

$$\frac{2\pi}{a} [(a, 0), (0, a)] \quad \text{or} \quad \frac{2\pi}{a} [(a, 0, 0), (0, a, 0), (0, 0, a)] \quad (5.37)$$

## 5. Correlation tensors and our models

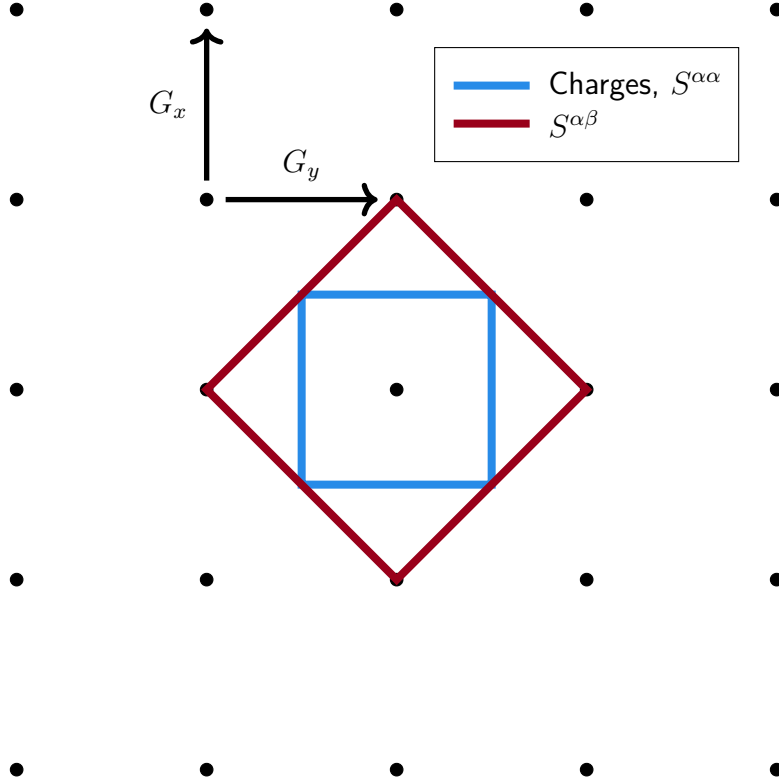


FIGURE 5.2.: The two relevant Brillouin zones of the system used in this thesis.

The charges and the diagonal components share the Brillouin zone shown in blue; the off-diagonal components have a larger, rotated Brillouin zone, since they have a smaller separation in direct space.

For the off-diagonal terms however we have real space vectors of

$$\frac{a}{2} [(\pm 1, \pm 1)] \quad \text{or} \quad \frac{a}{2} [(\pm 1, \pm 1, 0), (\pm 1, 0, \pm 1), (0, \pm 1, \pm 1)] \quad (5.38)$$

which leads to a larger Brillouin zone for the off-diagonal components of

$$\frac{2\sqrt{2}\pi}{a} [(1, 1), (1, 1)] \quad \text{or} \quad \frac{2\sqrt{2}\pi}{a} [(1, 1, 0), (0, 1, 1), (1, 0, 1)] \quad (5.39)$$

We see that the Brillouin zone is also rotated by  $\pi/4$  compared to that of the diagonal components. This results in the off-diagonal components of the correlation tensor having a different periodicity than the diagonal ones; we will see evidence of this in Chap. 6. A schematic is shown in Fig. 5.2.

# 6. Results for the 2D grand canonical Coulomb gas

In this chapter, we focus on the 2D Coulomb gas in the [grand canonical ensemble \(GCE\)](#) in every part of its phase diagram, including calculating the charge-charge correlations and the field-field correlations in direct and Fourier space. I calculate the scattering tensors  $S^{\alpha\beta}(\mathbf{q})$  for the total and [Helmholtz-Hodge-decomposed](#) components of the field and then take projections of the tensor parallel and perpendicular to  $\mathbf{q}$ : the latter corresponds to simulating a “neutron scattering” experiment on effective spins, but performed on electric fields.

In doing so, we also shed light on the nature of “[pinch points](#)” which appear in neutron scattering plots of spin ices and artificial spin ices, and suggest that the  $\mathbf{q} = \mathbf{0}$  point of the neutron scattering plot, which corresponds to the harmonic mode of the field, represents a useful signature of the [BKT transition](#) in systems with periodic boundary conditions.

Throughout the chapter some results particularly those quantities which characterise the transitions, will be presented for a range of lattice sizes from  $L = 16$  through  $L = 128$ . The plots of scattering functions are presented for  $L = 64$  since this lattice size offered the best balance of simulation speed, good statistics and resolution in the resulting plots.

## 6.1. Phase diagram

The 2D Coulomb gas in the [grand canonical ensemble](#) displays four distinct regions as well as a tricritical point [44, 45], as shown in Fig. 6.1.

I perform simulations across all four transitions as well as at and around the critical point, and find several signatures of the respective transitions in the resulting correlations. Across this chapter I use units  $q = 1, \epsilon_r = 2\pi$ ; the same units are used in Fig. 6.1.

## 6. Results for the 2D grand canonical Coulomb gas

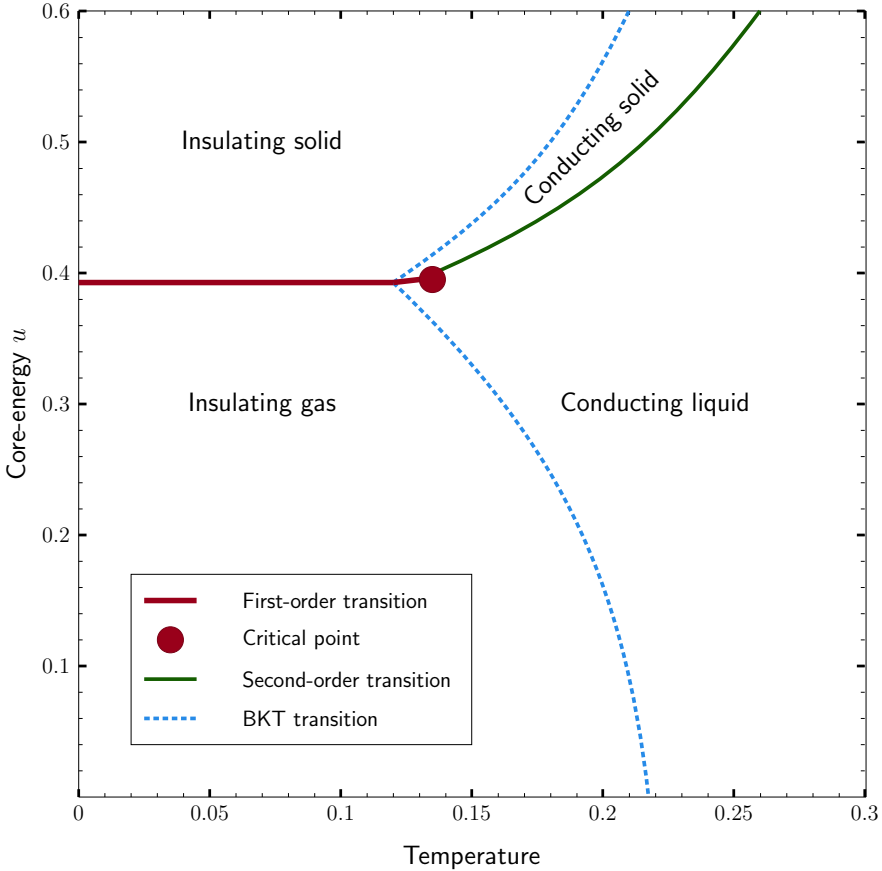


FIGURE 6.1.: The  $u - T$  (core-energy vs. temperature) phase diagram for the 2D grand canonical Coulomb gas, as originally probed in [44] using Monte Carlo simulation.

## 6.2. The BKT transition

In this section I present results of simulations of the “standard” BKT transition as described in Sec. 4.1.3, with the core-energy  $u$  equal to zero. The simulations reproduce the earlier result of Faulkner [31] concerning the evolution of the winding susceptibility through the transition, but also provide the accompanying field correlations. The results show that the  $\mathbf{Q} = \mathbf{0}$  point of the correlation function is another indicator of the transition, as expected, since it corresponds to the harmonic mode of the field.

We also use the analytical expressions for the Helmholtz-Hodge-decomposed correlations to fit the simulated correlation tensors, and use the fit results to extract effective Kosterlitz and bound-pair correlation lengths for the Coulomb gas across the BKT transition.

### 6.2.1. Specific heats and susceptibilities

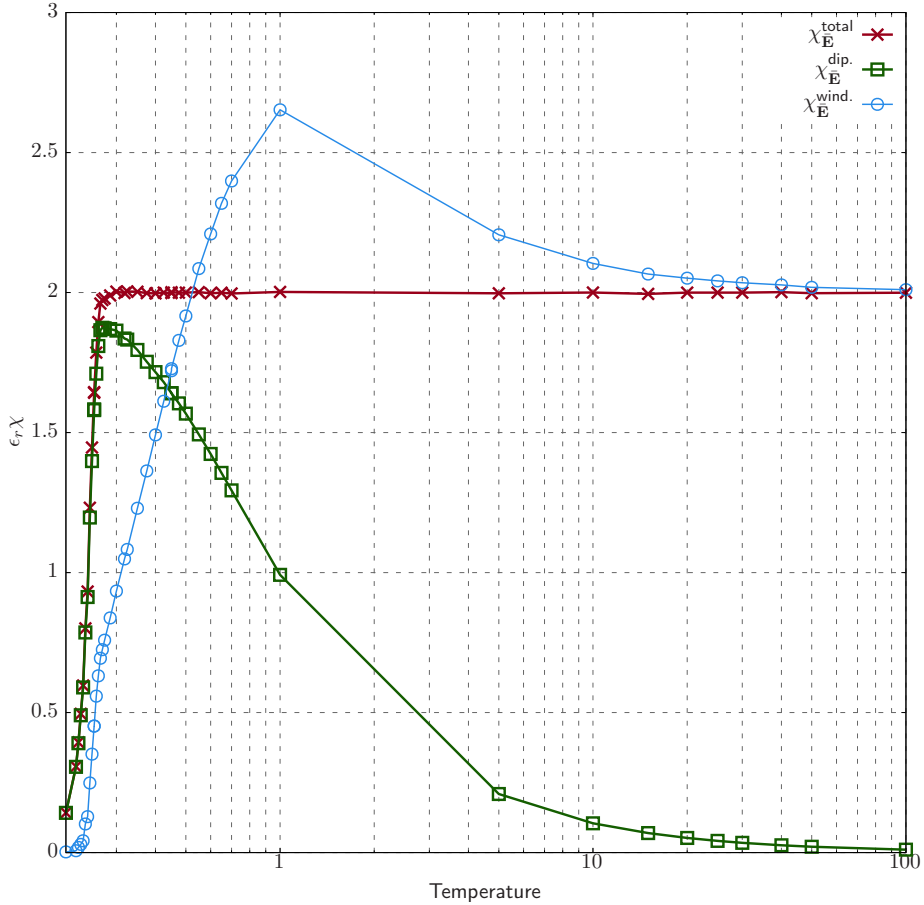


FIGURE 6.2.: Harmonic susceptibilities in the 2D grand canonical Coulomb gas, with core-energy  $u = 0$  and system size  $N = 64 \times 64$ , as a function of temperature. We can see that the winding component (blue) increases across the BKT transition whereas the polarisation component saturates and its associated susceptibility (green) goes to zero.

Fig. 6.2 shows the susceptibility of the harmonic mode of the Coulomb gas in the high-temperature limit, which was defined in Eq. 3.25. We find that the polarisation component of the harmonic mode saturates, as would be expected, since the charge density is bounded and we consider only single-valued charges; because of this the associated susceptibility goes to zero. By contrast, the winding number  $w$  is unbounded, since charges can continue winding around the torus indefinitely. This results in the winding component of the harmonic mode increasing linearly with temperature; the associated susceptibility is then a constant.

Fig. 6.3 shows that the specific heat of the rotational component is constant,

## 6. Results for the 2D grand canonical Coulomb gas

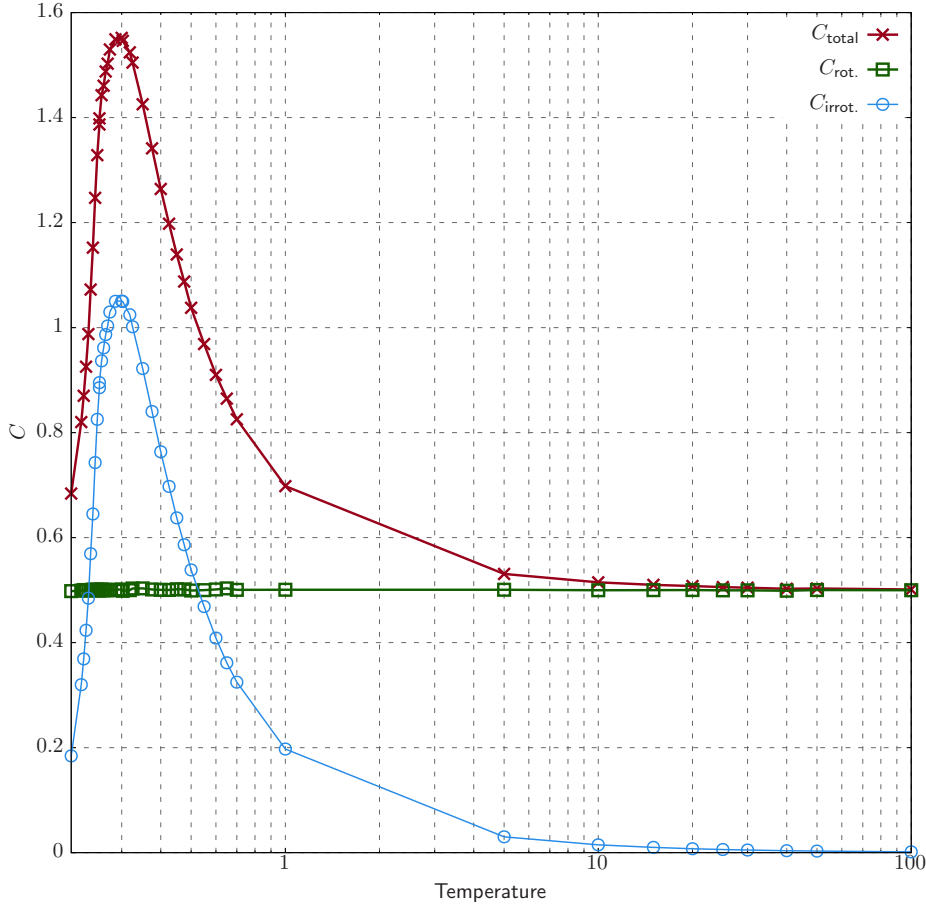


FIGURE 6.3.: Specific heats in the 2D grand canonical Coulomb gas for core-energy  $u = 0$  and system size  $N = 64 \times 64$ . We see that the rotational component of the specific heat is constant, as expected for a freely fluctuating field, but there is a pronounced peak in the irrotational component at around  $T = 0.3$ , above the BKT transition temperature.

as we would expect from a freely-fluctuating Gaussian field; the factor of  $\frac{1}{2}$  comes from the fact that there is only one **transverse** component in 2D. The specific heat of the **longitudinal** component goes to zero as the charge density reaches its asymptotic value of  $\frac{2}{3}$ .

Fig. 6.4 shows that the winding susceptibility Eq. 3.25 provides a clear signature of the **BKT transition** [31];  $\chi_w$  vanishes in the low-temperature critical phase but becomes finite above the transition. We can also see the expected system size dependence in Fig. 6.4, where the smaller systems have a slower increase in  $\chi_w$  across the transition. For example, at  $T = 0.25$ ,  $\chi_w(L = 128) \approx 0.6$  whereas  $\chi_w(L = 16) \approx 0.075$ . Above  $T_{\text{BKT}}$  the system size dependence vanishes;  $\chi_w(T = 0.35) \approx 1.2$  for all system sizes.

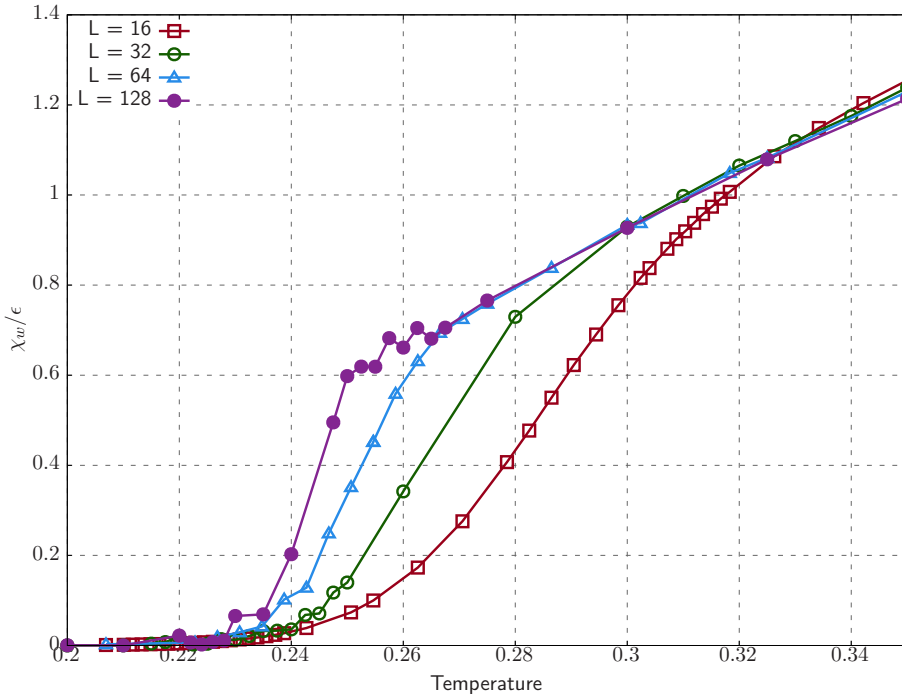


FIGURE 6.4.: The winding susceptibility  $\chi_w$  calculated across the BKT transition with  $u = 0$ . We see that the increase is sharper as the lattice size increases, but the asymptotic value does not change.

Now that the expected behaviour of these simple thermodynamic quantities has been verified across the transition, I turn to the investigation of correlation functions.

### 6.2.2. Correlations

The main quantities of interest are the field-field correlation tensors  $S^{\alpha\beta}(\mathbf{q})$  for the total and Helmholtz-Hodge-decomposed fields. Once these tensors are calculated we can use them to simulate (hypothetical) neutron scattering experiments on each part of the field using the mechanism described above in Chapter 5 and projecting out the component of the tensor parallel to the scattering vector, leaving only the transverse component  $S^\perp(\mathbf{Q})$ . In addition, it is possible to investigate what a model “longitudinal scattering” probe would show us by projecting out the perpendicular component. I calculate the field-field correlation tensors and the resulting neutron scattering plots across the transition and show that in the Helmholtz-Hodge-decomposed lattice electric-field description, the transition

## 6. Results for the 2D grand canonical Coulomb gas

is characterised by an increase in the irrotational correlations corresponding to charge unbinding.

Lastly I show that the  $\mathbf{q} = \mathbf{0}$  point of the  $S^\perp(\mathbf{Q})$  scattering function, which corresponds to the harmonic mode for a system with periodic boundaries, is a useful indicator of the unbinding which is the characteristic of the **BKT transition**. This  $\mathbf{q} = \mathbf{0}$  point will also be useful below when characterising the high- $u$  BKT and melting transitions.

### $S^{\alpha\beta}(\mathbf{q})$ tensors

The first thing I calculate is the field-field correlation tensor as derived above; this object contains all the information about the field correlations. There are obvious evolutions in the components of the tensor as we cross the BKT transition: first and foremost, we can see the  $\mathbf{q} = \mathbf{0}$  point increasing in the diagonal components of the tensor as the temperature increases. There are also interesting differences between the irrotational and rotational components of the Helmholtz-Hodge-decomposed tensor.

At low temperature,  $T \approx T_{\text{BKT}}$  and below, we see in Fig.6.5 that the total correlations are dominated by the rotational component.

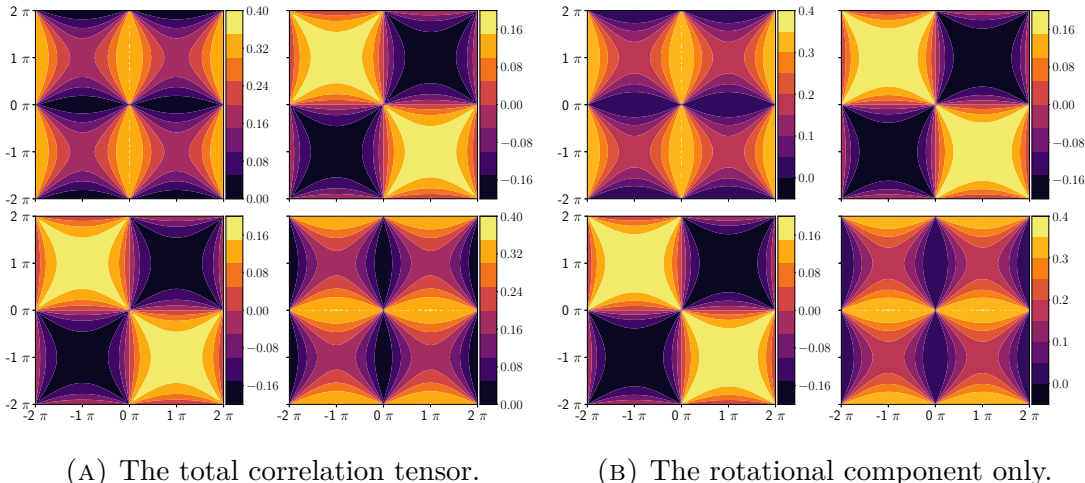


FIGURE 6.5.: ( $T = 0.223$ ;  $u = 0$ ). The total and rotational field-field correlation tensors  $S^{\alpha\beta}(\mathbf{q})$ . This is slightly above the BKT transition temperature  $T_{\text{BKT}} = 0.22$ . Top left, top right, bottom left and bottom right plots are  $S^{xx}$ ,  $S^{xy}$ ,  $S^{yx}$  ( $= S^{xy}$ ) and  $S^{yy}$ .

This of course implies that the intensity of the correlations for a **traditional lattice Coulomb gas (TLCG)** would be very small, which we can check by inspecting the irrotational component of the correlations of the **generalised lattice**

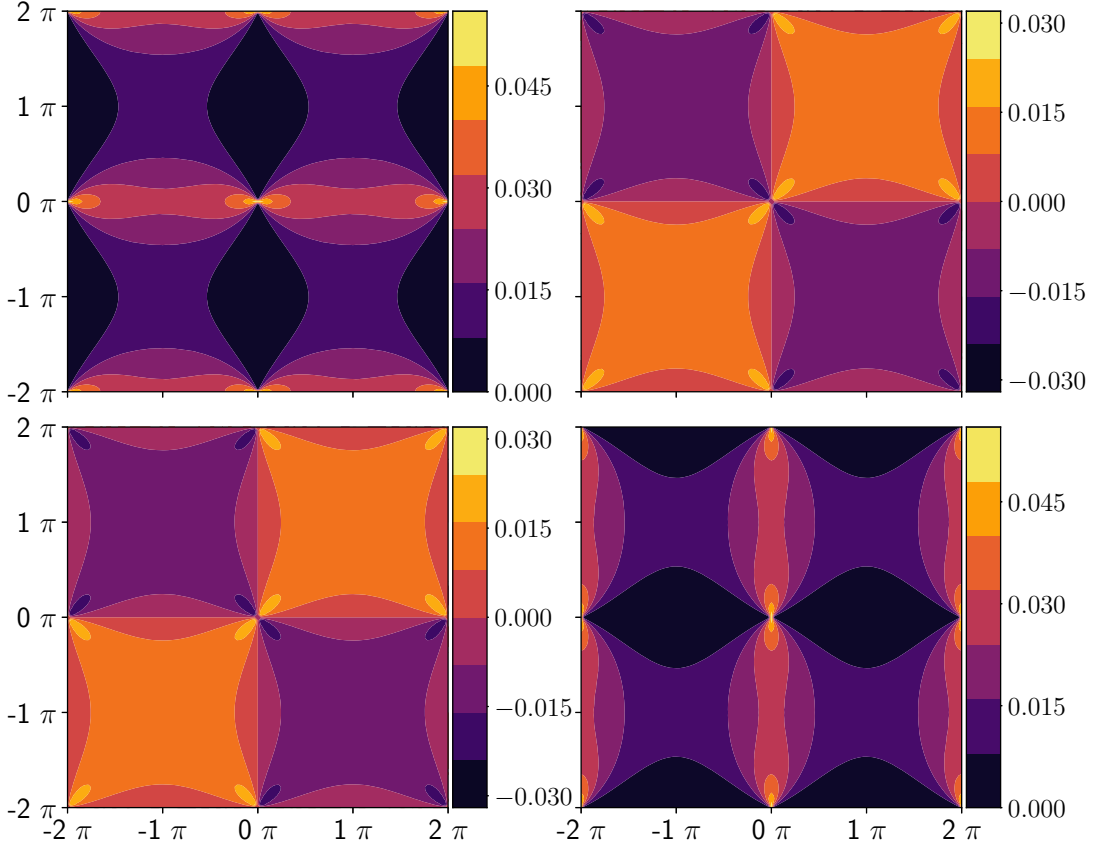


FIGURE 6.6.: ( $T = 0.223$  ;  $u = 0$ ). The irrotational correlation tensor for the same parameters as Figs. 6.5. By concentrating only on the longitudinal component of the field, we isolate the field correlations of a TLCG (the electrostatic correlations).

Coulomb gas, as shown in Fig. 6.6. We see when comparing Figs. 6.5a and 6.6 that the irrotational intensities are an order of magnitude smaller than the total; the total correlations are dominated by the rotational field, since charge windings are energetically suppressed.

As the temperature increases above  $T_{\text{BKT}}$  and the fraction of charges in the system becomes appreciable, we see the irrotational component increasing in magnitude, as will be seen in Fig. 6.8b. The contours on the diagonal components of the total tensor, shown in Fig. 6.7, belie the flatness of the overall function; there is a difference of  $\approx 20\%$  between the highest and lowest intensity points in the Brillouin zone. The off-diagonal component is also getting smaller and smaller, as shown by the index on the colour bar which shows a highest magnitude intensity of 0.05. This reflects that fact that at infinitely high temperature we would expect to see zero correlation between the different Cartesian components of the field, by

## 6. Results for the 2D grand canonical Coulomb gas

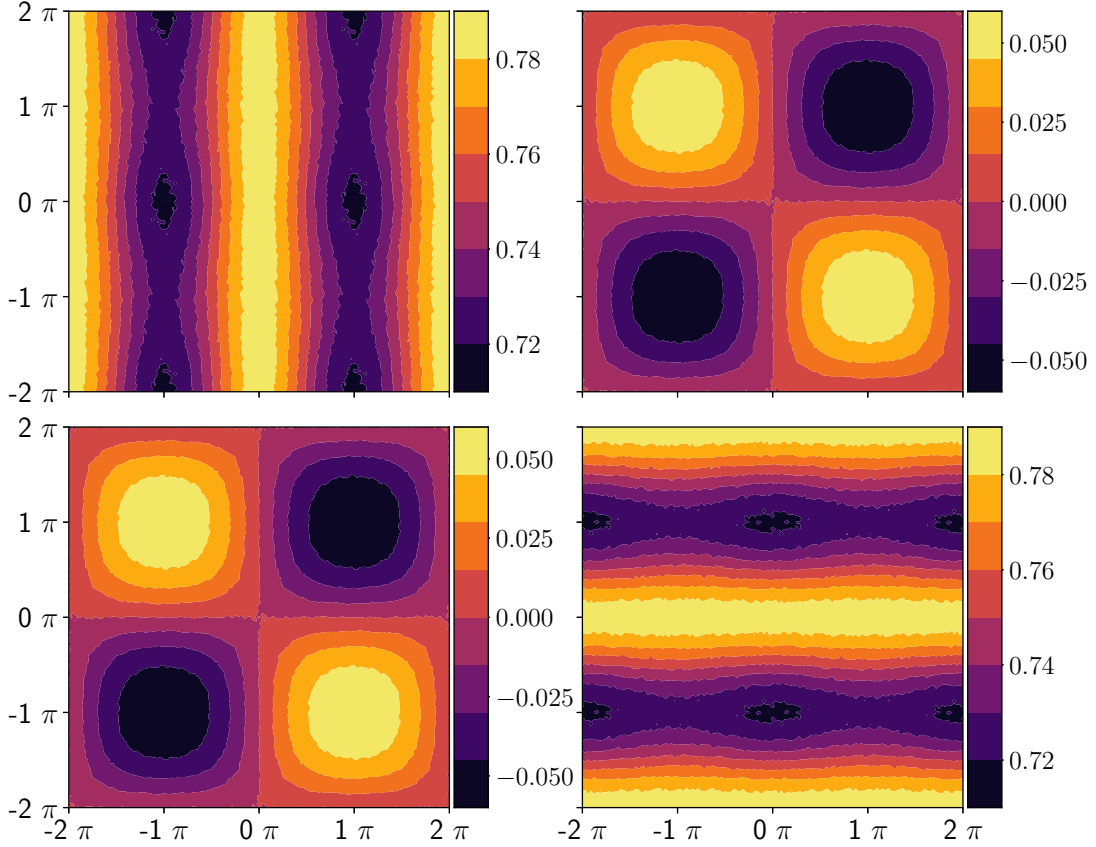


FIGURE 6.7.: ( $T = 0.500$ ;  $u = 0$ ). The correlation tensor of the total field. This is significantly above the BKT transition temperature  $T_{\text{BKT}} = 0.22$ . We see that the intensities for the diagonal components are higher than in Fig. 6.5a, for example, and also that the function is flatter overall. The off-diagonal component is smaller in magnitude, also.

equipartition.

Fig. 6.7 does not tell us the whole story, however. In order to analyse the correlations in more detail we can once again perform the [Helmholtz-Hodge decomposition](#) and inspect the correlations of the individual components.

Figs. 6.8a and 6.8b show us the transverse and longitudinal components respectively, making it clear that the two are now of comparable intensity, but rotated by  $\pi/2$  compared to each other. This is a reflection of the fact that in 2D a  $\pi/2$  rotation of the field will turn an entirely divergence-free field into a divergence-full one, and vice-versa. For a perfect [GLCG](#) at infinite temperature (or a paramagnet) we would expect the two components to be exactly equal and conjugate so that the total is perfectly flat; here, we find small differences between the two which give the overall shape of Fig. 6.7. We can also explain microscopically the form of the two tensors when considering them as transverse and longitudinal

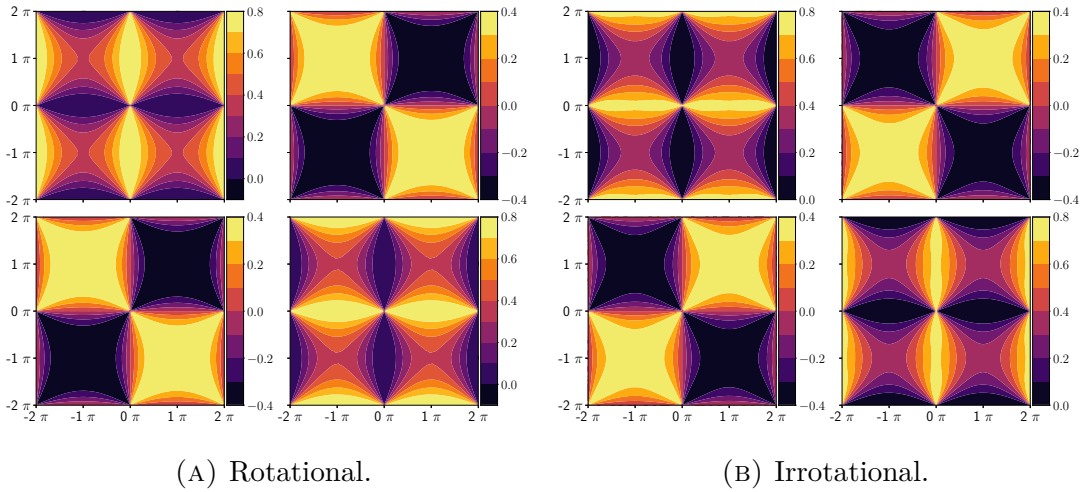


FIGURE 6.8.: ( $T = 0.500$  ;  $u = 0$ ). Rotational and irrotational tensors  $S^{\alpha\beta}(\mathbf{q})$ , again significantly above  $T_{\text{BKT}}$ . The longitudinal component (right) is rotated by  $\pi/2$  compared to the rotational component (left) in Fig. 6.5b.

components. Firstly, consider the  $xx$  component of the tensor (top right): when  $q_y = 0$  and  $q_x$  is finite, the transverse component to  $\mathbf{q}$  is in the y-direction, and hence we get a broad band of high intensity in the y-direction of the transverse component. By the same argument, when  $q_y = 0$  and  $q_x$  is finite, the longitudinal component to  $\mathbf{q}$  is in the x-direction, and we see a band of high intensity in that direction.

The off-diagonal component can be understood by considering the two components as divergence-free and divergence-full respectively. Considering the two field links around a single vertex, we have an overall divergence if the two have the same sign, whereas if the two links have opposite signs they will cancel out to some extent: hence, in the transverse component, we see a positive intensity where the two have opposite signs, whereas in the longitudinal component we see a positive intensity where the two components have the same sign.

We also see in Fig. 6.8 that the  $\mathbf{q} = \mathbf{0}$  point in the diagonal components of the irrotational tensor is now of equal intensity with the rest. This increase is due to the harmonic mode of the electric field which has now increased to its equipartition value.

It is important to emphasise that the change in the total field correlations between Figs. 6.5a and 6.7 results from the relative changes in magnitude of the two components: the rotational field increases in intensity roughly linearly with temperature, as we would expect from a freely-fluctuating field, while the irrotational and harmonic components increases as a result of the system passing

## 6. Results for the 2D grand canonical Coulomb gas

through the BKT transition. It is the sum of the three Helmholtz-Hodge-decomposed components which gives the overall change in the correlations. We can show this, for example, in the rotational component: Figs. 6.9a and 6.9b show us that the

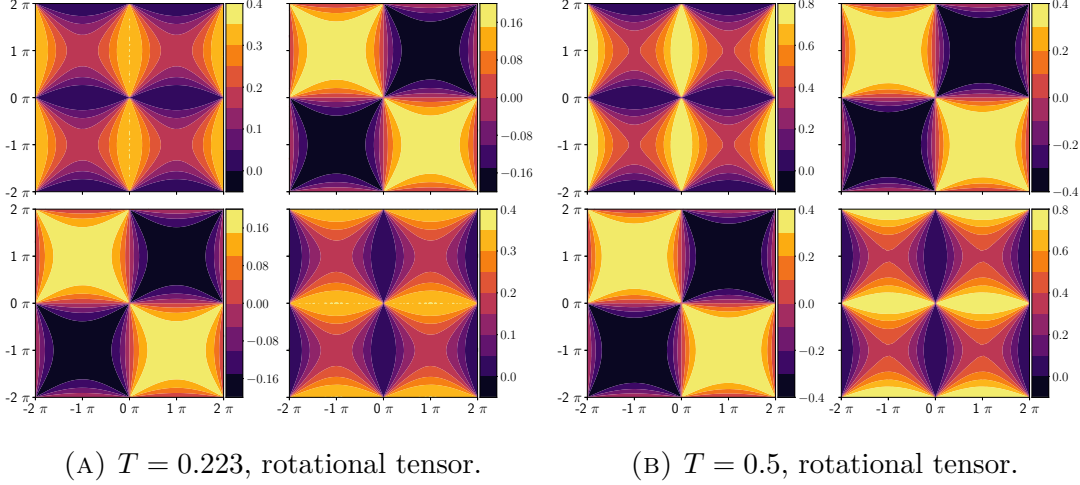


FIGURE 6.9.: ( $T = 0.223$  and  $T = 0.500$ ;  $u = 0$ ). The rotational tensor  $S_{\text{rot.}}^{\alpha\beta}(\mathbf{q})$ . The shape of the function is the same in both cases, but the intensities increase with temperature.

qualitative features evident in the rotational correlations do not change through the BKT transition, as we would expect from a freely-fluctuation Gaussian field with a constant constraint. It is only the average intensity which increases with temperature.

Another illuminating quantity is the trace of this correlation tensor as shown in Figs. 6.11 and 6.9. The trace of the irrotational component of the tensor is always equal to the longitudinal correlation function. We can see this by diagonalising the inverse tensor as described in Chap. 5 (or, in the quadric language, finding its principal axes): we find one zero eigenvalue and one finite eigenvalue, corresponding to the fact that there is only one longitudinal component of the field, and so the trace gives us the longitudinal correlation function in this case. However, the invariance of the trace under coordinate transformation is a standard result in linear algebra, and so we know that the trace of the tensor always gives us the longitudinal correlations, regardless of basis. I will use the trace to fit the tensors to the form given below in Eq. 6.1 [89, 90].

In Fig. 6.10, at  $T = 0.223$  we see that the trace of the total tensor is essentially flat, since it is dominated by the rotational component: the only points missing are at  $\mathbf{q} = \mathbf{0}, (\pm 2\pi, \pm 2\pi)$ , which correspond to the harmonic mode.

As discussed above, the rotational tensor stays qualitatively constant as the

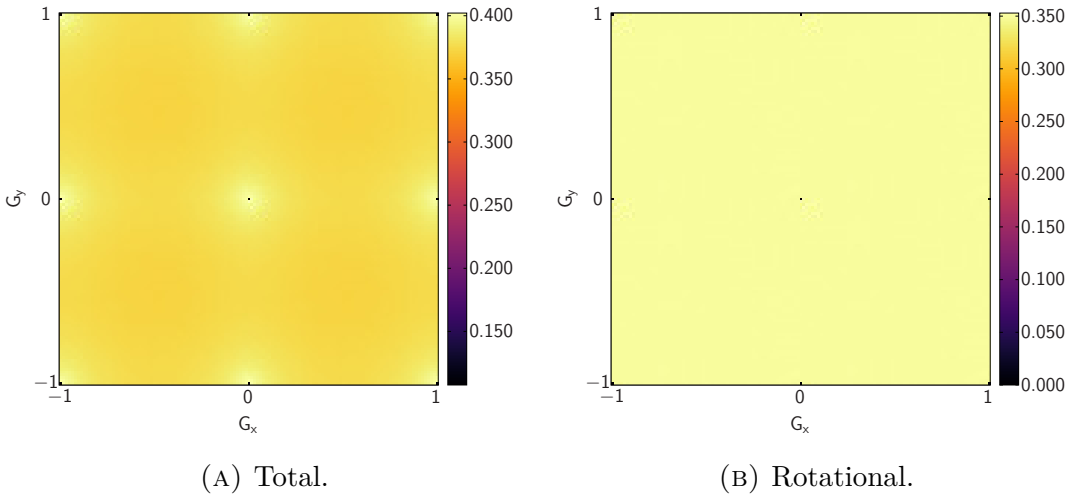


FIGURE 6.10.: ( $T = 0.223$  ;  $u = 0$ ). The trace  $S^{xx} + S^{yy}$  for the total and rotational tensors respectively. The rotational component is flat except for the point at  $\mathbf{q} = \mathbf{0}$  which corresponds to the harmonic mode; the total correlations also feature a small peak above the flat rotational background centred around the origin, which comes from the irrotational component. The similarity in intensity between the plots here indicates, again, that the correlations are dominated by the rotational component of the field at this temperature.

temperature changes, but the total correlations change: Fig. 6.11 shows that at the much higher temperature  $T = 0.5$  the total correlations are qualitatively different:

We see here that the total correlations now feature a large, broad peak around  $\mathbf{q} = \mathbf{0}$  and also that the function is much flatter overall, as noted above. On the right, the [longitudinal](#) correlation function is Lorentzian in shape, but now also has a background which is the “harmonic phase” of [89]; this function, when superposed onto the flat [transverse](#) function of similar magnitude, gives rise to the much broader peak seen in  $S_{\text{total}}^{\alpha\beta}$ .

### $S^\perp(\mathbf{Q})$ functions

As discussed above, the component of the tensor perpendicular to the scattering vector  $\mathbf{q}$  is all that is “seen” by a polarised neutron probe in a scattering experiment. For the case of a primitive electrolyte, this kind of scattering would be uninformative, since the neutron does not couple to the electric field; but when investigating magnetic systems such as [spin ices](#) or [XY models](#), neutron scattering is a very useful experimental tool. Hence, I simulate such an experiment for the

## 6. Results for the 2D grand canonical Coulomb gas

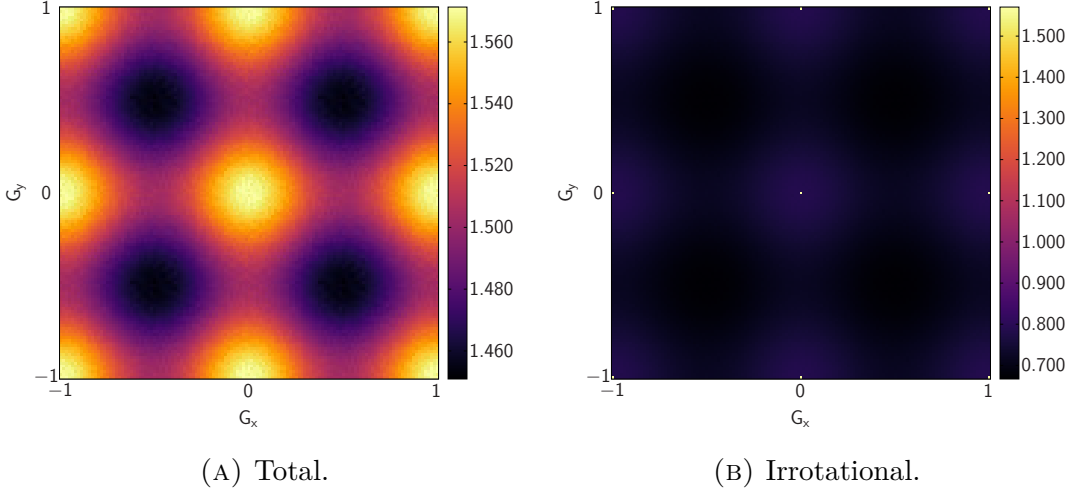


FIGURE 6.11.: ( $T = 0.500$  ;  $u = 0$ ). The trace  $S^{xx} + S^{yy}$  for the total and irrotational tensors respectively. The total trace (left) is mostly very flat, with a small, broad peak centred at the origin; the irrotational component now also has a flat background with a central peak superimposed, as opposed to the flat background of the rotational component.

Coulomb gas here, in order to make contact with spin ice and XY physics.

For the normal, zero- $u$  BKT transition, the  $S^\perp(\mathbf{Q})$  functions follow the same pattern as the full correlation tensors discussed in the previous section: at temperatures  $0 < T \lesssim T_{\text{BKT}}$ , the correlations are dominated by the **rotational** component, then for temperatures  $T > T_{\text{BKT}}$  we begin to see a qualitative change driven by the increasing intensity of the **irrotational** component and the evolution of the harmonic mode of the field.

A typical  $S^\perp$  function at  $T \approx T_{\text{BKT}}$  is shown in Fig. 6.12. We see the **pinch point** associated with dipolar correlations due to the divergence-free condition on the rotational field. The singularity at the centre of each pinch point is currently absent: the constraint  $\nabla \cdot \tilde{\mathbf{E}} = 0$  Fourier transforms to  $\mathbf{q} \cdot \tilde{\mathbf{E}} = 0$ , which is singular at a zone centre [91]. An alternative way of thinking of this is that each of the singularities is at a zone centre, and for any  $\mathbf{G}$  the intensity at the zone centre is controlled by the intensity of the  $\mathbf{q} = \mathbf{0}$  point, whose intensity is essentially zero at these temperatures due to charge confinement.

As the temperature increases the evolution of the harmonic mode at  $\mathbf{q} = \mathbf{0}$  becomes obvious, and this is reflected in the “filling in” of the pinch points. This is analogous to the breaking of the ice rules in spin ice, where a low-temperature ice-rule obeying state is entirely rotational (and hence singular at  $\mathbf{Q} = \mathbf{G}$ ) and it

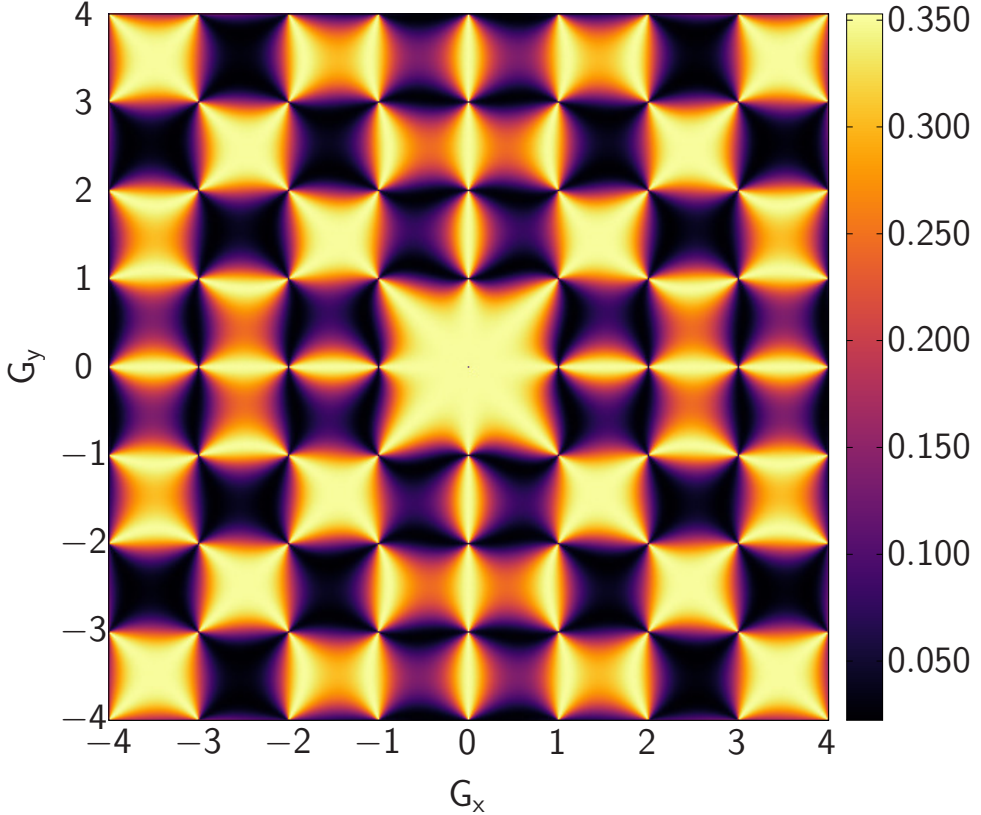


FIGURE 6.12.: ( $T = 0.223$  ;  $u = 0$ ). The neutron scattering function  $S_{\text{total}}^{\perp}(\mathbf{Q})$  at  $T \approx T_{\text{BKT}}$ , showing sharp pinch point features. The harmonic mode at  $\mathbf{Q} = \mathbf{0}$  has vanishingly small intensity here.

is the creation of monopole pairs which gives the pinch point a finite width.

Fig. 6.13 shows us that the  $\mathbf{Q} = \mathbf{0}$  point becomes the highest intensity point in the function; asymptotically it reaches twice the intensity of any other  $\mathbf{Q}$ . This is because the sum  $(\delta_{\alpha\beta} - \hat{Q}_\alpha \hat{Q}_\beta) S^{\alpha\beta}(\mathbf{q})$  at  $\mathbf{Q} = \mathbf{0}$  is simply equivalent to the trace of the tensor. Also in Fig. 6.13, the sharp **pinch point** observed at the lower temperature in Fig. 6.12 are noticeably broadened, as predicted: at this temperature the irrotational correlations are of the same order of magnitude as the rotational ones, and the sum of the two components give us a pinch point of finite width. The broadening then corresponds to the unbinding of defects, as shown in neutron scattering experiments on spin ices [39].

As the temperature increases further we see the pinch points continue to broaden and the rotational background increases in intensity, which has the effect of making the function flatter: this reflects the (very slow) onset of paramagnetism discussed in Sec. 4.1.1. Fig. 6.14 shows this quite clearly for  $T \approx 2.5T_{\text{BKT}}$ ; apart from the

## 6. Results for the 2D grand canonical Coulomb gas

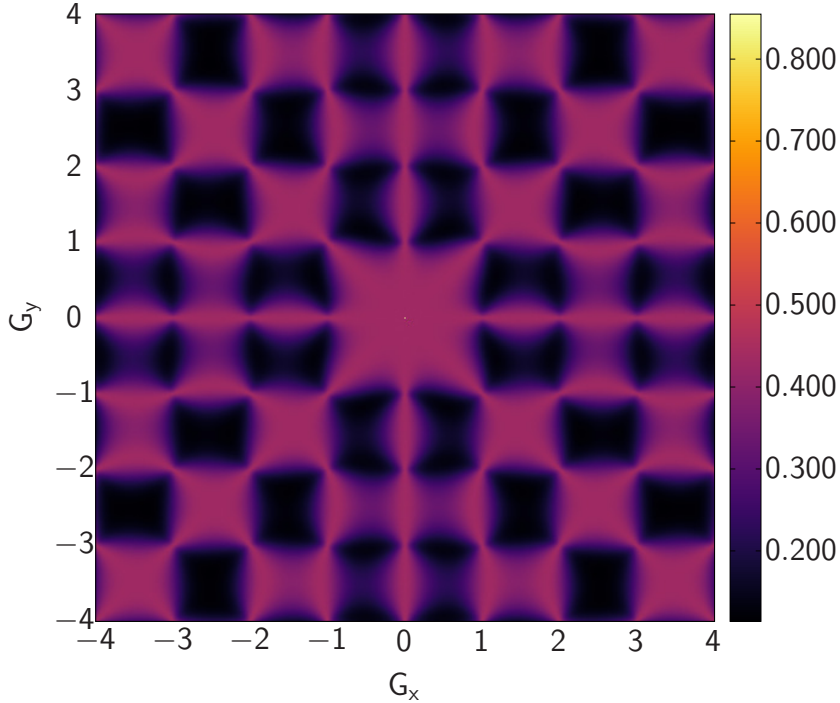


FIGURE 6.13.: ( $T = 0.275$  ;  $u = 0$ ).  $S_{\text{total}}^{\perp}(\mathbf{Q})$  above the BKT transition, displaying a finite intensity at  $\mathbf{Q} = \mathbf{0}$  and a rounded pinch point, indicating the increased intensity in the longitudinal component.

$\mathbf{Q} = \mathbf{0}$  point, which again has double the intensity of any other  $\mathbf{Q}$ , the difference in intensity is much smaller. The lowest-intensity portions of the neutron scattering function now have an intensity of around 0.7, whereas the higher intensity regions shown in Fig. 6.12 are only of magnitude 0.9.

### Lorentzian fits

We can also use the analytic expression given in Eq. 6.1 to try to reproduce the simulated results shown above [90]:

$$\mathcal{L}(\chi_1, \kappa_1, \chi_2, \kappa_2, \gamma) = \frac{\chi_1 \kappa_1^2}{\kappa_1^2 + q^2} + \frac{\chi_2 \kappa_2^2}{\kappa_2^2 + q^2} + \gamma \quad (6.1)$$

It is important to discuss the motivation for this functional form: firstly, the reasoning for the fit to a Lorentzian form with a flat background. As shown in Ref. [89], the longitudinal scattering function can be written as

$$S^L(\mathbf{q}) = \frac{\gamma}{1 + \chi/\epsilon_q} \quad (6.2)$$

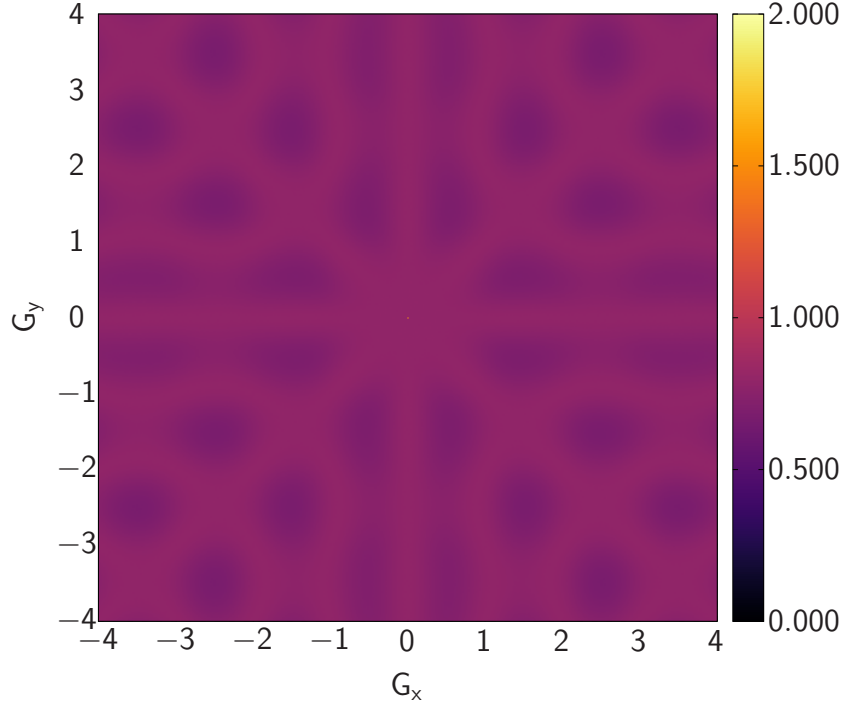


FIGURE 6.14.: ( $T = 0.500$  ;  $u = 0$ ).  $S_{\text{total}}^{\perp}(\mathbf{Q})$ . At this very high temperature, the  $\mathbf{Q} = \mathbf{0}$  point has double the intensity of any other  $\mathbf{Q}$ , and the rest of the function becomes very flat, with only a  $\approx 15\%$  difference between the highest and lowest intensities. This plot has the lower end of the scale explicitly set to zero in order to show the flatness of the function away from  $\mathbf{Q} = \mathbf{0}$ .

where  $\gamma = \chi T/C$  and  $\epsilon_q = 1 + \kappa^2/q^2$  is the Debye-Hückel dielectric constant. Eq. 6.2 can be decomposed (see Appendix B for the derivation, which is straightforward but fairly tedious) to give a sum of a Lorentzian and a flat background:

$$S^L(\mathbf{q}) = \frac{\gamma}{1 + \chi} + \frac{\chi}{1 + \chi} \frac{\gamma}{1 + q^2 \xi^2} \quad (6.3)$$

Here  $\xi = \sqrt{1 + \chi}/\kappa$  is a diffusion length, which in the case of spin ice has been shown to be closely related to the Debye length [92]; the screening length has also been shown by Minnhagen [93] to correspond to the Kosterlitz correlation length in the XY model. Henceforth I will refer to  $\xi$  as a correlation length. The equation Eq. 6.3 is then equivalent to

$$\mathcal{L} = \frac{\chi \kappa^2}{\kappa^2 + q^2} + \gamma \quad (6.4)$$

under some trivial renaming of constants.

## 6. Results for the 2D grand canonical Coulomb gas

Essentially, the flat background appears in the **longitudinal** component of the scattering because we deal with the long-range Coulomb interaction; this corresponds to the harmonic phase of Ref. [89]. Care should be taken here to note that the name “harmonic phase”, as was stated explicitly in [89], only has a specific meaning when used with respect to a given set of boundary conditions. In that work, the boundary conditions used were spherical rather than the periodic boundaries used here, and the harmonic phase corresponds to excitations out of the rotational ground state. Hence, the harmonic phase of that paper should not be confused with the harmonic mode defined here.

The motivation for using a sum of two Lorentzian functions is as follows: around the **BKT transition** the upper bound on the correlation length diverges. We expect to see a distribution of charge separations and hence of Lorentzian widths, since there is no longer any one meaningful length scale in the system, and in principle we could model this with a distribution of Lorentzians of continuously varying widths. However, this complicated distribution can be fairly well approximated by two Lorentzians with widths corresponding roughly to the upper and lower bounds of the distribution, corresponding to the Kosterlitz correlation length and the microscopic bound-pair correlation lengths respectively.

I perform the fit to the double Lorentzian form by taking a cut of the **longitudinal** scattering function (trace of the **irrotational** tensor) as shown in Fig. 6.15. This is done because attempting to use the entire trace, running over  $q_x, q_y \in [-2\pi, 2\pi]$ , results in a fit which works well at the edges of the Brillouin zone but fails to capture the behaviour at the central peak, which is the most relevant part of the function when considering **pinch point** widths. I also exclude the single point at  $\mathbf{q} = \mathbf{0}$  since it is ascribed to the harmonic mode.

Once values have been obtained for the five parameters in Eq. 6.1 I plot the resulting function over the entire Brillouin zone in order to compare with the simulation data.

Finally I use the form factor for neutron scattering, which is given by [90]

$$F_{\text{neutron}}(\mathbf{G}, \mathbf{Q}) = \frac{((G_x - Q_x)Q_x + (G_y - Q_y)Q_y)^2}{(((G_x - Q_x)^2 + (G_y - Q_y)^2)(Q_x^2 + Q_y^2))} \quad (6.5)$$

to analytically reproduce the  $S_{\text{irrot.}}^\perp(\mathbf{Q})$  and  $S_{\text{total}}^\perp(\mathbf{Q})$  functions. The **rotational** and **irrotational** components are combined via

$$S_{\text{irrot.}}^\perp = S_{\text{irrot.}}^{\text{tr.}}(1 - F_{\text{neutron}}); \quad S_{\text{total}}^\perp = S_{\text{rot.}}^{\text{tr.}}F_{\text{neutron}} + S_{\text{irrot.}}^{\text{tr.}}(1 - F_{\text{neutron}}) \quad (6.6)$$

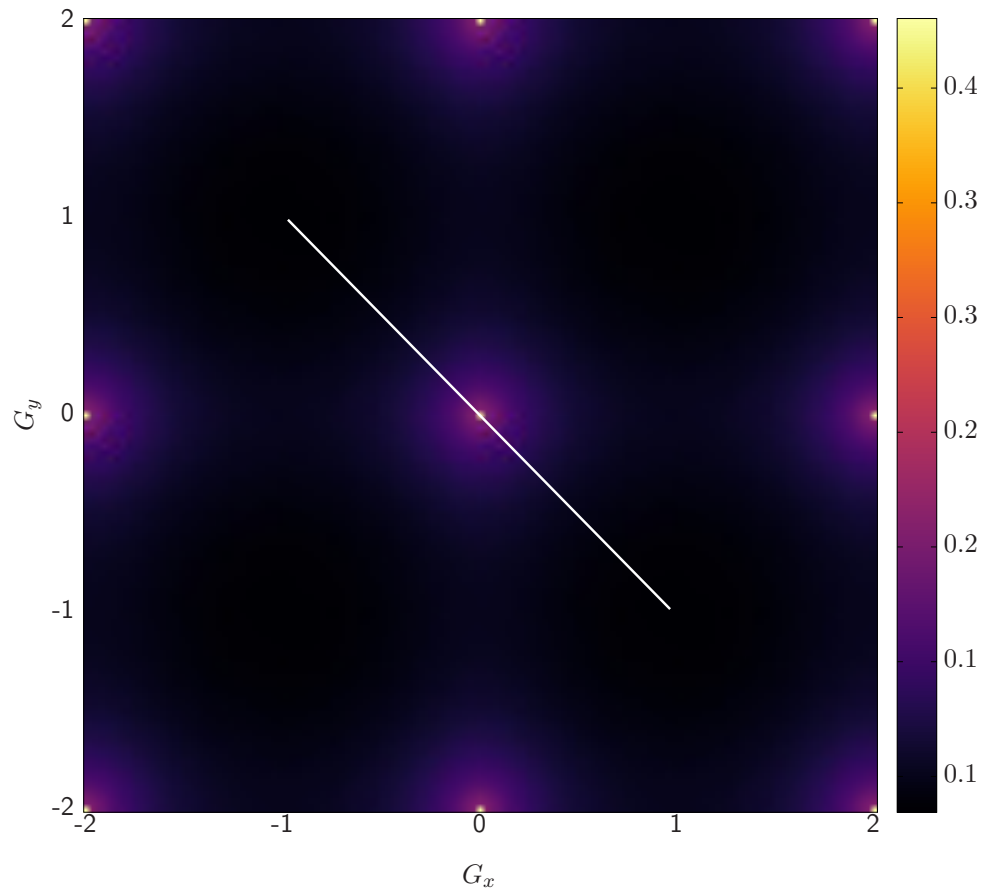


FIGURE 6.15.: ( $T = 0.223$  ;  $u = 0$ ). The trace  $S_{\text{irrot.}}^{\alpha\alpha}(\mathbf{Q})$  with the cut which I take for the Lorentzian fit shown as a white line.

## 6. Results for the 2D grand canonical Coulomb gas

where  $S_{\text{rot.}}$  is taken directly from the simulation data.

Finally I plot the results for a given choice of  $\mathbf{G}$ . In what follows I use  $\mathbf{G} = (1, 1)$ , where we expect to find a [bow tie](#) in the irrotational component and a [pinch point](#) in the total function. The choice  $\mathbf{G} = (1, 1)$  is what motivates taking the cut  $q_x + q_y = 0$  of the irrotational trace, since it is along the line  $q_x = -q_y$  that the pinch point intensity varies fastest.

The fit to the two Lorentzians at  $T = 0.223$  is shown in Fig. 6.16.

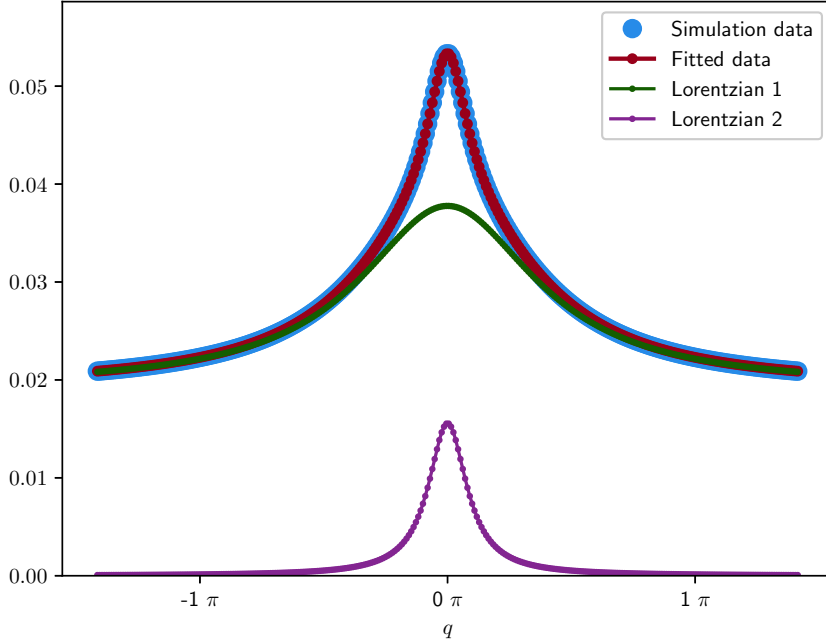


FIGURE 6.16.: ( $T = 0.223$  ;  $u = 0$ ). The fit to a cut of the trace  $S_{\text{irrot.}}^{\alpha\alpha}(\mathbf{Q})$ , showing that either Lorentzian on its own is insufficient to fit the data, and also that the flat background is required.

We see that it is necessary to add a constant background to the Lorentzians in order to accurately describe the function, and that both Lorentzians are required to reproduce the behaviour around the zone centre.

Fig. 6.17 shows the result of plotting the fitted function over the whole range  $q_x, q_y \in [-2\pi, 2\pi]$ , along with the corresponding simulated data.

We can see that the fit around the zone centre is accurate but that the simple Lorentzians fail to take into account the behaviour around the zone boundary; the function we fit to was derived under the assumption of continuous symmetry, but the lattice has a discrete translational symmetry, which manifests in the “cross” we see in the simulated data. Nonetheless, as we see from Figs. 6.18 and 6.19, the fitted  $S^\perp$  functions reproduce the simulations quite well in this case. There are slight differences towards the zone boundary as we expect, for the same reason

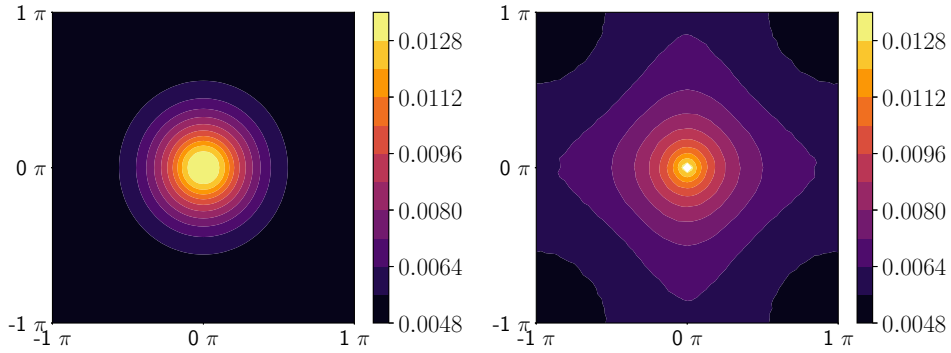


FIGURE 6.17.: ( $T = 0.223$  ;  $u = 0$ ).  $S_{\text{irrot}}^{\alpha\alpha}(\mathbf{Q})$  from fitted parameters (left), and simulation (right). The simulation result has a “cross” shape arising from the translational symmetry, whereas the fitting function has a continuous symmetry. The intensity across the chosen cut is quantitatively accurate, however.

given above: the continuous symmetry of the function we fit to does not respect the translational symmetry of the lattice.

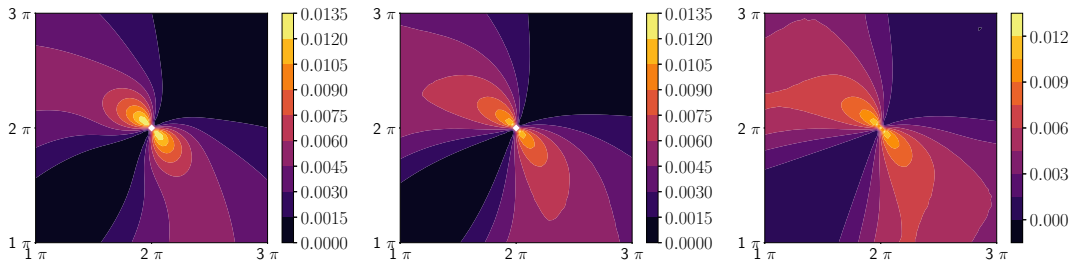


FIGURE 6.18.: ( $T = 0.223$  ;  $u = 0$ ).  $S_{\text{irrot}}^{\perp}(\mathbf{Q})$  from the fitted function using Eq. 6.6 (left), from the simulated trace  $S_{\text{irrot}}^{\alpha\alpha}(\mathbf{q})$  with Eq. 6.6 (centre), and directly from simulation (right).

There is an additional lattice-specific symmetry which produces rotated pinch points in certain Brillouin zones in the neutron scattering plot; these are not captured by the analytic expressions, and an extra  $\mathbf{G}$ -dependent factor would need to be introduced in order to reproduce this phenomenon. We see in Fig. 6.18 that the combination of the Lorentzian in the total scattering tensor and the  $(1 - F_{\text{neutron}})$  neutron scattering form factor conspire to give **bow ties** for the neutron scattering plot of the **irrotational** component. The combination of the flat **rotational** tensor and the factor of  $F_{\text{neutron}}$  gives us the expected **pinch point** pattern with a singularity at the zone centre. It is the combination of the two components which gives us a pinch point of finite width.

## 6. Results for the 2D grand canonical Coulomb gas

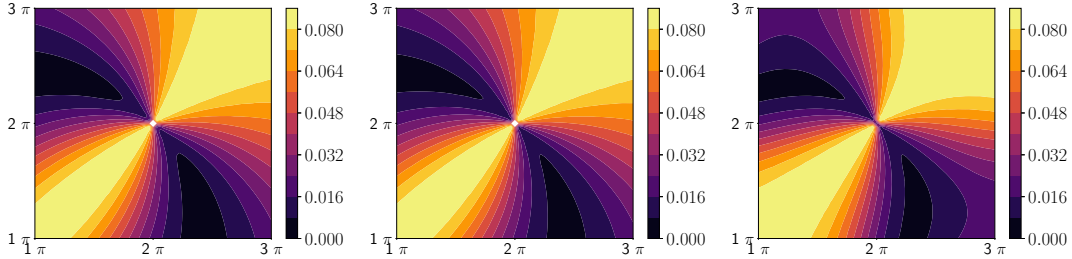


FIGURE 6.19.: ( $T = 0.223$ ;  $u = 0$ ).  $S_{\text{total}}^{\perp}(\mathbf{Q})$  from the fitted function using Eq. 6.6 (left), from the simulated trace  $S_{\text{irrot}}^{\alpha\alpha}(\mathbf{q})$  with Eq. 6.6 (centre), and directly from simulation (right). As with the irrotational component, we see that the fit reproduces the function well.

At much higher temperatures we see qualitatively different behaviour: above  $T \approx 0.35$ , the fit sets one of the Lorentzians to zero, as shown in Fig. 6.20.

We see that the fit is once again good over the cut, although at high temperature the fit slightly overestimates the width of the **pinch point** in  $S_{\text{total}}^{\perp}$ , as shown in Fig. 6.21.

The two parameters  $\kappa_1, \kappa_2$  in Eq. 6.1, as discussed above, can be related to inverse diffusion lengths. However, it has been shown [92, 94] that this diffusion length is also related to the charge-charge correlation length of the system. We can therefore use these fits to estimate the upper and lower bounds on the correlation length of the Coulomb gas across the **BKT transition**. These quantities are unaffected by the problem of rotated pinch points in the analytic neutron scattering plots, since it is calculated only from the original scattering tensor  $S_{\text{irrot}}^{\perp}(\mathbf{q})$ . Fig. 6.22 shows the results. Errors are not included on the plot since reported errors from the fits were small enough as to be invisible.

We find that the broader Lorentzian which is non-zero at all temperatures corresponds to  $\xi_1$ , a correlation length smaller than the lattice spacing, whereas the sharper Lorentzian only appearing over the range  $0.16 \leq T \leq 0.32$  gives the correlation length  $\xi_2$  larger than the lattice spacing. Both lengths have a peak just above the BKT transition temperature at  $T \approx 0.25$ .

For  $\xi_1$ , the shorter correlation length, we find a small peak followed by a gradual decrease: we attribute the increase to the unbinding of charges, and the decrease to the increased screening as the charge density becomes appreciable.  $\xi_2$  appears just below the **BKT transition** temperature and rapidly reaches a (very noisy) peak of about 5 lattice spacings; the noise would seem to suggest that better statistics or larger systems are required to make a more quantitative statement, but also

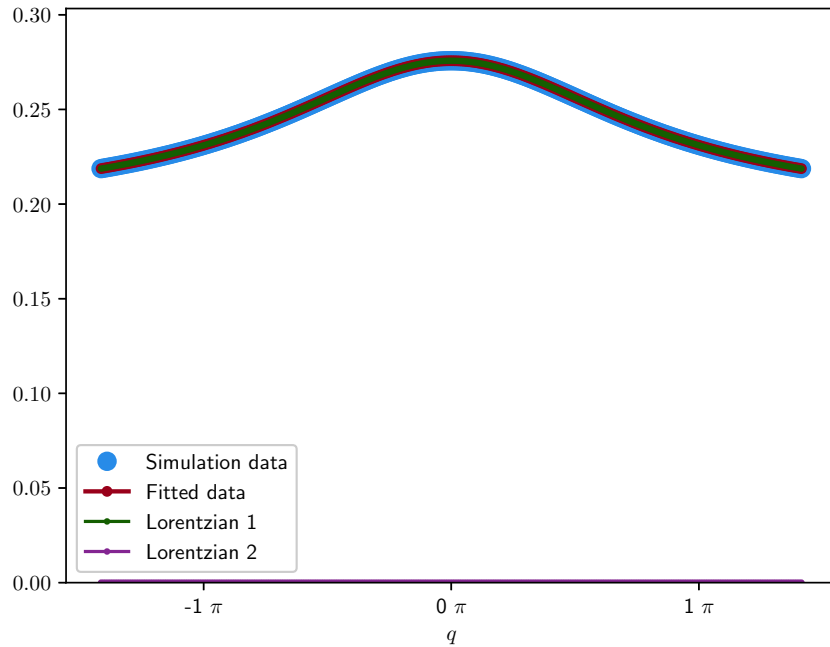


FIGURE 6.20.: ( $T = 0.700$  ;  $u = 0$ ). The fit to the cut of  $S_{\text{irrot.}}^{\alpha\alpha}(\mathbf{Q})$ . Again, the flat background is necessary, but here the data is well-described by one Lorentzian.

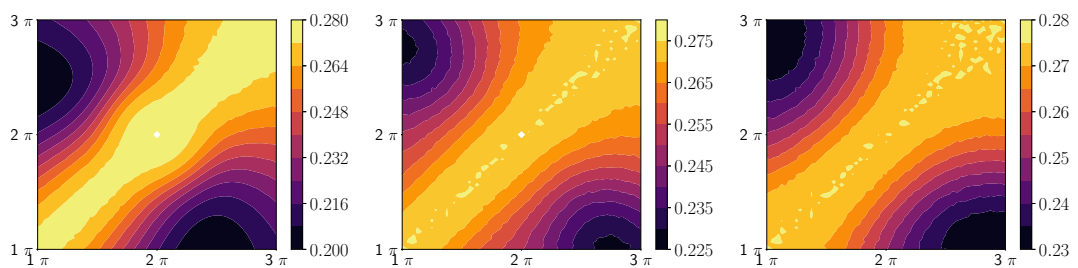


FIGURE 6.21.: ( $T = 0.700$  ;  $u = 0$ ).  $S_{\text{total}}^{\perp}(\mathbf{Q})$  from the fit (left), from the simulated trace with Eq. 6.6 (centre), and directly from simulation (right).

## 6. Results for the 2D grand canonical Coulomb gas

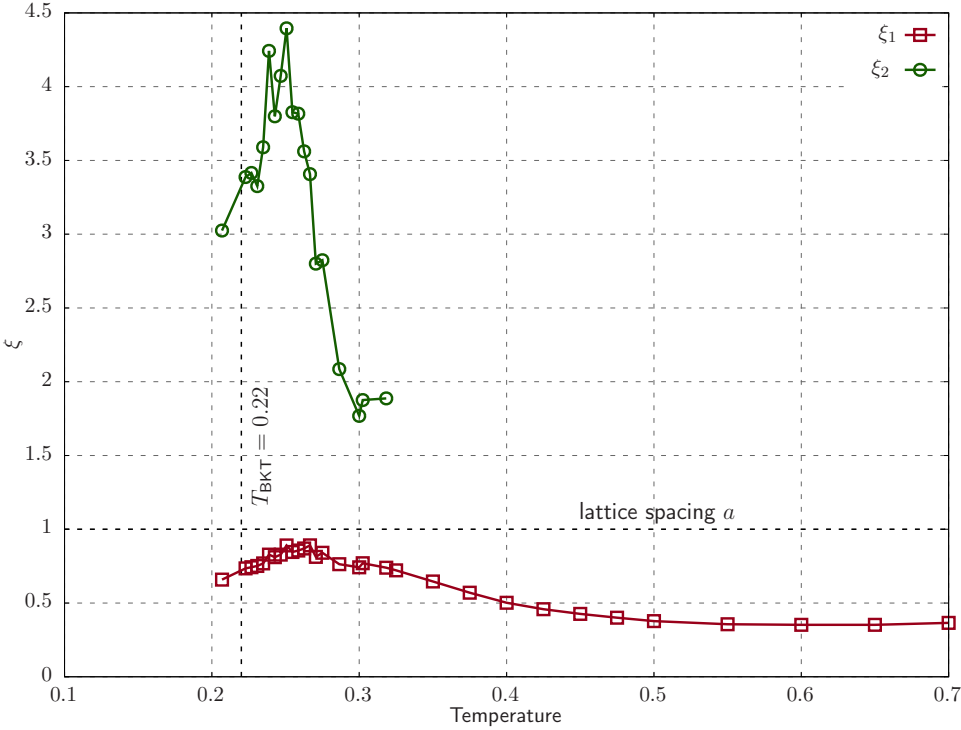


FIGURE 6.22.: The correlation lengths  $\xi_1, \xi_2$ , extracted from the fits to Eqs. 6.1, as a function of temperature. We can consider  $\xi_1$  and  $\xi_2$  as representing bound pairs and free vortices respectively.

reflects the inherent difficulty of measuring a theoretically divergent correlation length in a finite-size system. We interpret  $\xi_2$  as a measure of the length over which charges unbind across the BKT transition; as the temperature continues to increase the charge density becomes larger and the Coulomb gas becomes more strongly screened, which is indistinguishable in this case from charge pairing, and leads to the correlation length dropping off and merging with  $\xi_1$ .

Finally I plot the same quantity for  $L = 32$  on the same axis to compare the results for different system sizes: the result is shown in Fig. 6.23. Again, there is significant noise evident in the longer correlation length  $\xi_2$  in the  $L = 32$  data, but we see the same trend for both correlation lengths at both system sizes. Also, importantly, we find that the peak in  $\xi_2$  is smaller for the smaller system size, which would be expected since the largest possible correlation length is obviously smaller in a smaller system. Unfortunately, ascertaining the exact location of the peak in  $\xi_2(L = 32)$  or estimating the system-size dependence of that location is impossible from these results; it is possible that taking many more samples and

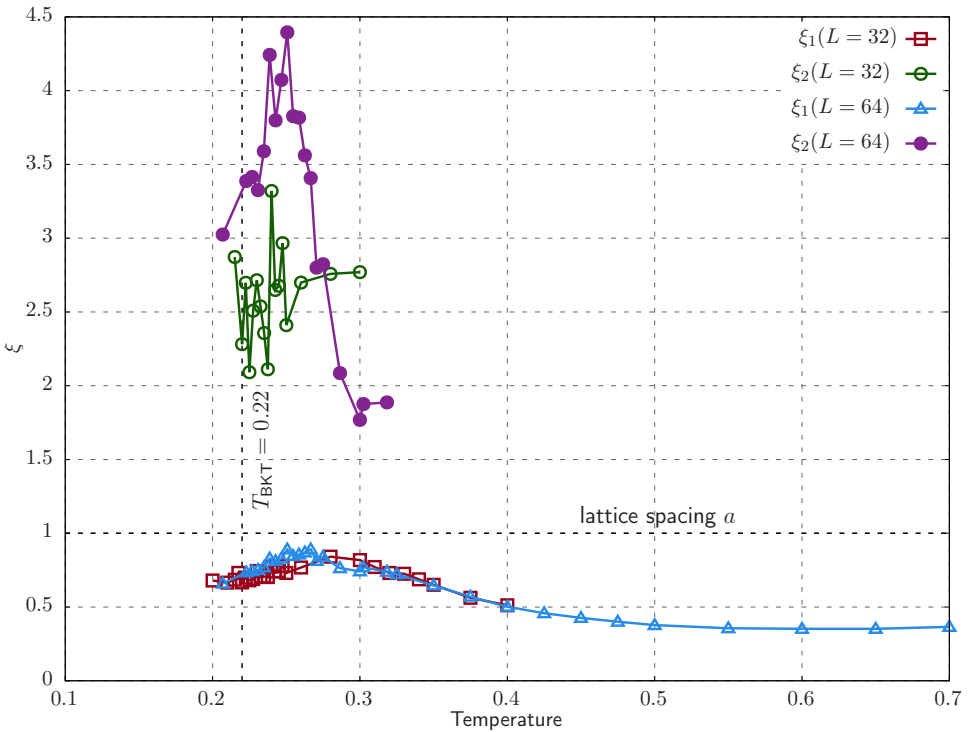


FIGURE 6.23.: The correlation lengths  $\xi_1, \xi_2$  for systems of linear size  $L = 32$  and  $64$ .  $\xi_1$  (which we interpret as a bound pair length) is shorter than the lattice spacing for all temperatures, but  $\xi_2$  (which we identify with the Kosterlitz correlation length) shows a pronounced peak just above the BKT transition.

running simulations for longer could help to smooth out the results presented here, but simulation of larger systems may also be required.

### 6.3. Pinch points and bow ties

It is useful here to summarise some of the results of the previous section in the context of pinch point and bow tie features which are familiar from neutron scattering experiments on condensed matter systems.

The central result is that pinch points and bow ties can be extracted even from a paramagnetic system: the overall neutron scattering plot for a given condensed matter system assumes a given shape based on the relative strengths of the transverse and longitudinal eigenvalues.

## 6. Results for the 2D grand canonical Coulomb gas

### 6.3.1. Correlation tensor

We recall the definition given in Chap. 5 of the correlation tensor for the field:

$$S^{\alpha\beta}(\mathbf{q}) = \langle E^\alpha(\mathbf{q})E^\beta(-\mathbf{q}) \rangle \quad (6.7)$$

As mentioned previously, this tensor is a  $d \times d$  matrix for every value of  $\mathbf{q}$ , where  $\mathbf{q}$  runs over the central Brillouin zone of the system. For a Bravais lattice, this tensor is periodic in every Brillouin zone: it respects the underlying periodicity of the system in direct space. For each  $\mathbf{q}$  the tensor has two eigenvectors and two eigenvalues, one of which can be chosen to be longitudinal to  $\mathbf{q}$  and the other transverse, giving another natural example of the Helmholtz-Hodge decomposition.

### 6.3.2. Neutron scattering

As discussed in Chap. 5, neutron scattering is a familiar technique for probing condensed matter systems. A characteristic feature of neutron scattering experiments is that a neutron only probes the “perpendicular component” of the correlation function, but in order to explain the origin of pinch point and bow tie scattering it is critical here to be clear about what exactly we refer to when we use the word perpendicular.

As stated above, the correlation tensor can be expressed in Fourier space as a function of  $\mathbf{q}$ , which runs over the central Brillouin zone *of the system*, and is periodic in every Brillouin zone. The neutron, however, has a wavevector  $\mathbf{Q}$ : outside of the central Brillouin zone, we have that

$$\mathbf{Q} = \mathbf{q} + \mathbf{G} \quad (6.8)$$

and we can see from Fig. 6.24 that for  $\mathbf{G} \neq \mathbf{0}$ ,  $\mathbf{Q}$  and  $\mathbf{q}$  are no longer parallel.

As in the previous chapter, we can write the equation for the neutron scattering function as

$$S^\perp(\mathbf{Q}) = \left( \delta_{\alpha\beta} - \hat{Q}_\alpha \hat{Q}_\beta \right) S^{\alpha\beta}(\mathbf{q}) \quad (6.9)$$

where  $\hat{Q}_\alpha$  is the normalised  $\alpha$ -component of  $\mathbf{Q}$ : the neutron “sees” the component of the correlation tensor perpendicular to *its* wavevector, which is not necessarily perpendicular to the corresponding wavevector of the correlation tensor it probes.

Inside the central Brillouin zone, it sees precisely the component of the tensor

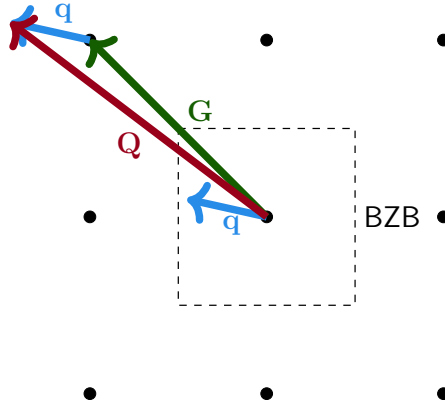


FIGURE 6.24.: Diagram showing that  $\mathbf{q}$  and  $\mathbf{Q}$  are not parallel for non-zero  $\mathbf{G}$ . BZB is the Brillouin zone boundary, shown as a dashed black line.

perpendicular to  $\mathbf{q}$ , but for non-zero  $\mathbf{G}$  some part of the parallel component will be mixed in. In the geometric language used above, the neutron scatters only from  $\lambda_t$  where  $\mathbf{G} = \mathbf{0}$ , but some mix of  $\lambda_t$  and  $\lambda_l$  elsewhere, depending on the angle between  $\mathbf{q}$  and  $\mathbf{Q}$ .

### 6.3.3. The origin of pinch point and bow tie scattering

We can now consider the cases of perfectly transverse or longitudinal fields and their resulting neutron scattering patterns. The example shown in Fig. 6.25 is taken from a simulation of the harmonic XY model below the BKT transition temperature, and will be discussed in further detail in Chap. 7. However, as shown in the previous section, the same patterns occur in simulations of the GLCG, as well as in artificial square ice arrays [36, 37].

Firstly, we take the example of a Coulomb phase in Fig. 6.25a: we see that the resulting neutron scattering pattern displays perfectly sharp pinch points with singularities at zone centres. Next, we consider a purely longitudinal field in Fig. 6.25b. In this case the neutron scattering pattern consists of sharp bow tie features, with zero intensity in the central Brillouin zone, as we expect from the above geometrical argument. The bow ties of the purely longitudinal component are seen to be conjugate to the pinch points of the transverse component.

The examples shown in Figs. 6.25a and 6.25b are taken from the exact same simulation: both sets of features can be extracted from the total correlations, which are a straight sum of the components shown here.

We can see that the relative intensities are very different in this case, where the highest intensity in the longitudinal component is over an order of magnitude

## 6. Results for the 2D grand canonical Coulomb gas

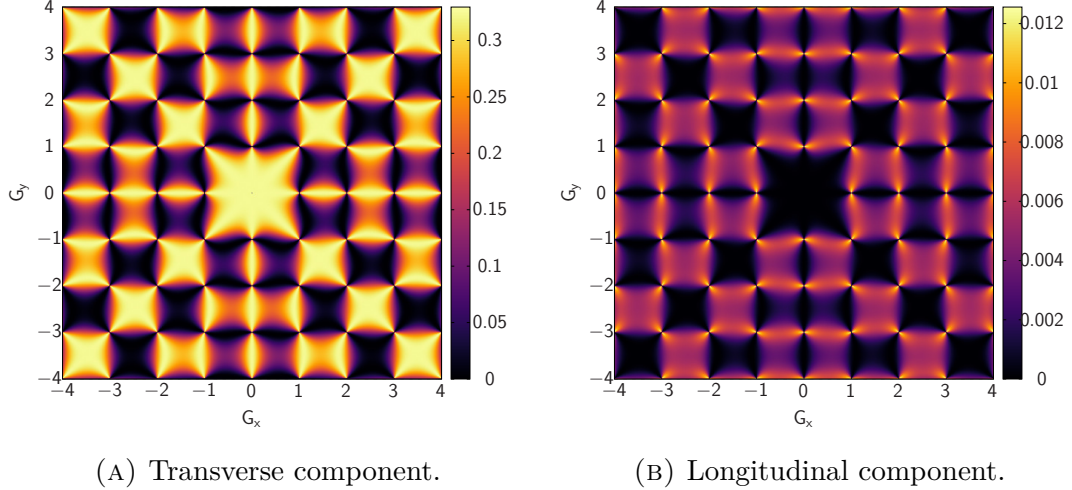


FIGURE 6.25.: Neutron scattering pattern of the transverse (a) and longitudinal (b) components of the emergent field representation of the harmonic XY model at  $T = 0.207$ , below the BKT transition temperature  $T_{\text{BKT}} \approx 0.22$ . The transverse field configuration is entirely rotational, and the resulting neutron scattering pattern shows sharp pinch point features; the longitudinal is entirely irrotational and shows sharp bow ties.

smaller than in the transverse counterpart. Hence, the total correlations are dominated by the transverse component in this case: for the GLCG or harmonic XY model below the BKT transition, we have a system approaching the Coulomb phase limit of  $\lambda_l = 0$  and a correlation tensor which is almost a perfect needle.

### 6.3.4. The harmonic mode and $\mathbf{q} = 0$

We can also explain the high-intensity scattering at the origin of the neutron scattering function and relate it to the BKT transition. As mentioned above, for my simulations which use periodic boundary conditions the harmonic mode here only enters the neutron scattering pattern at  $\mathbf{q} = \mathbf{0}$ , since we can consider it as a constant vector. In the case of my 2D GLCG simulations, the increasing intensity of the  $\mathbf{q} = \mathbf{0}$  point signals the onset of conduction [42]; part of the harmonic mode can be ascribed to topological sector fluctuations brought about by the unbinding and winding of charges around the torus.

We see a clear example of the evolution of this point in Fig. 6.26. The question is then whether to ascribe the harmonic mode to the longitudinal or transverse component. Since it is both divergence- and curl-free, it would seem we have a free choice. In actual fact, however, when we diagonalise the correlation tensor as

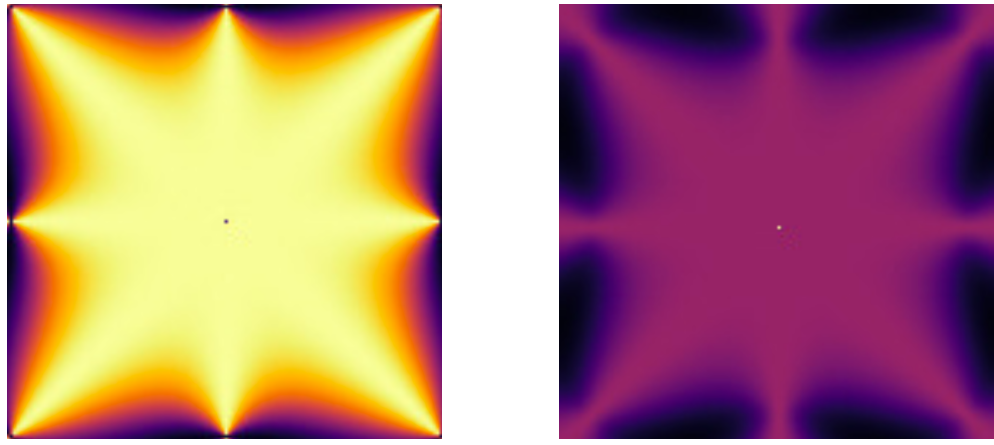


FIGURE 6.26.: The central Brillouin zone of the neutron scattering pattern for the 2D grand canonical GLCG, above and below the BKT transition. The evolution in intensity at  $\mathbf{Q} = \mathbf{0}$  is clearly visible. Colourbars are not included here, since this is a qualitative example of the chance in  $\mathbf{Q} = \mathbf{0}$ , but it is important to note that the two are not on the same scale; the intensity at  $\mathbf{Q} \neq \mathbf{0}$  remains relatively constant, while at  $\mathbf{Q} = \mathbf{0}$  it increases by an order of magnitude.

described above, we find that the eigenvalues  $\lambda_l$  and  $\lambda_t$  are always degenerate at  $\mathbf{q} = \mathbf{0}$ , i.e. the tensor is always a circle or sphere at the origin.

Hence, we find that half the intensity at  $\mathbf{q} = \mathbf{0}$  is ascribed to the longitudinal component and half to the transverse one. This carries forward to the neutron scattering pattern at  $\mathbf{Q} = \mathbf{0}$ . We then have that the pinch points and bow ties contribute to different parts of the neutron scattering function depending on  $\mathbf{Q}$  but that both contribute at  $\mathbf{Q} = \mathbf{0}$ ; this explains the result I find at high temperature, where  $\mathbf{Q} = \mathbf{0}$  reaches twice the intensity of any other point.

### 6.3.5. Pinch point rounding

Finally we show the effect of these phenomena on the neutron scattering pattern for the total field in Fig. 6.27, finding two main changes across the BKT transition and explaining the rounding of pinch point features in terms of the Helmholtz-Hodge decomposition of the field.

Firstly, the increased intensity at  $\mathbf{Q} = \mathbf{0}$  leads to a filling in of the singularities at the zone centres. This follows from the definition of  $\mathbf{Q}$ , since for every zone centre  $\mathbf{q} = \mathbf{0}$ .

Secondly, we see a rounding of the pinch point which arises from the increasing intensity in the longitudinal component of the tensor. As discussed above, the

## 6. Results for the 2D grand canonical Coulomb gas

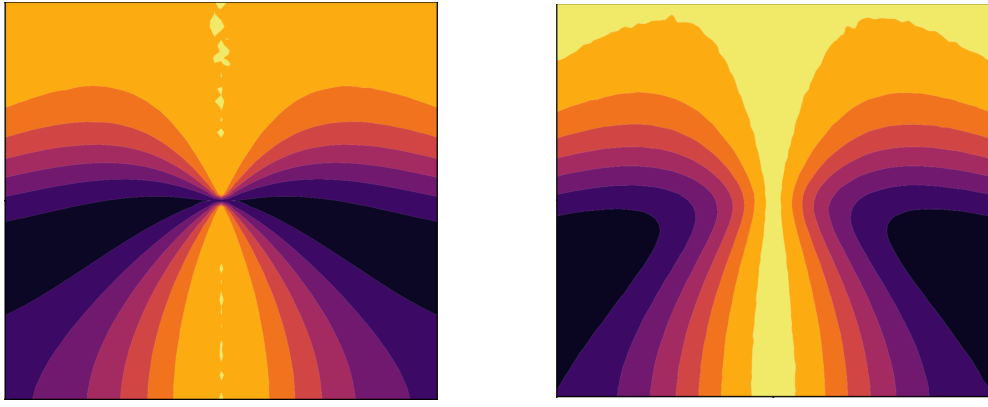


FIGURE 6.27.: Sharpness of pinch point in the total neutron scattering pattern, for the 2D GLCG across the BKT transition. We see that the sharp feature evident at  $T = 1.3$  is replaced by a rounded feature at  $T = 1.8$ . Again, colourbars are not included here since this is a qualitative example of the rounding.

bow ties which are characteristic of the longitudinal component are conjugate to the pinch points characteristic of the transverse component; as we cross the charge unbinding transition the low intensity regions around the pinch point begin to fill in. As described in Chap. 5, the limit of this is an exact degeneracy between  $\lambda_l$  and  $\lambda_t$ , at which point the two components contribute exactly the same intensity and we have the completely flat pattern of a paramagnet.

## 6.4. First-order transition

This section focuses on the behaviour of the [generalised lattice Coulomb gas](#) across the first-order transition in the [core-energy](#), where the insulating gas of paired charges in the low- $u$  limit abruptly gives way to an insulating charge crystal at critical value  $u_c$ . We find that in contrast to the infinite-order [BKT transition](#), where the field correlations change rather slowly as the temperature increases, the field correlations across the first-order transition change rapidly, as might be expected. At low core-energy constant  $u$ , below the transition, the correlations are identical to the low-temperature results shown in the previous section. Above the transition, however, we see a complex pattern of Lorentzians which almost immediately give way to Bragg peaks of varying intensities at different zone centres as the system orders. There is a brief coexistence regime where we can see both the low- $u$  rotational correlations superimposed on the Lorentzians which correspond to the ordered charge crystal. In the high- $u$  insulating solid phase we provide

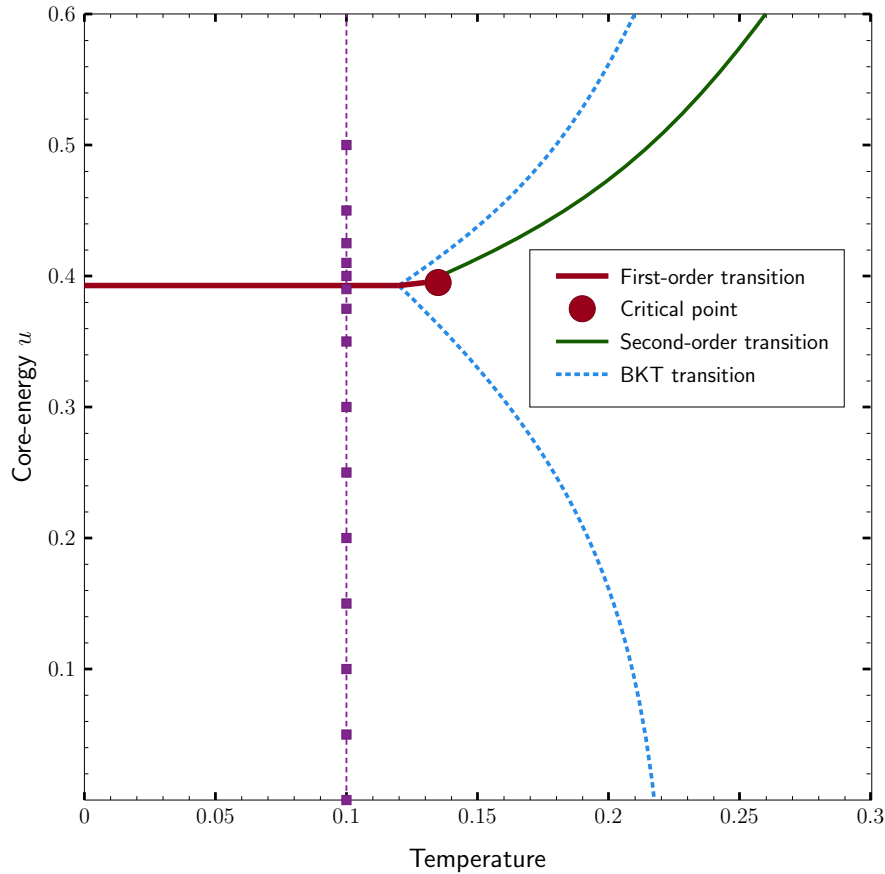


FIGURE 6.28.: Phase diagram 6.1 with the relevant  $u, T$  parameters used in my simulations of the first-order transition highlighted with purple rectangles. The dashed purple line is a guide for the eye.

a propagation vector describing the nature of the ordering and also find a surprising but phenomenologically explicable link with previously published results concerning [artificial spin ice](#).

We can easily explain the critical value  $u_c$  of the first-order transition by considering the Hamiltonian

$$H = \frac{1}{2\epsilon} \sum_{i \neq j} \rho(\mathbf{x}_i) G(\mathbf{x}_i, \mathbf{x}_j) \rho(\mathbf{x}_j) - u \sum_i \rho(\mathbf{x}_i)^2 \quad (6.10)$$

and its Fourier transform, which reads

$$H = \sum_{\mathbf{k}} \left( \frac{1}{2\epsilon} G(\mathbf{k}) - u \right) |\rho(\mathbf{k})|^2 \quad (6.11)$$

with  $G(\mathbf{k})$  given by Eq. 2.34.

We know that  $\rho(\mathbf{k})^2 = q^2 m(\mathbf{k})^2$ , and the minimum value of  $G(\mathbf{k})$  is at  $\mathbf{k} = (\pi, \pi)$

## 6. Results for the 2D grand canonical Coulomb gas

(which we will see below is also the propagation vector corresponding to the solid phase):  $G(\pi, \pi) = 1/8$ . The minimum value of the first term in Eq. 6.11 is then

$$\frac{1}{2\epsilon} G(\mathbf{k}) q^2 m(\mathbf{k})^2 \Big|_{\mathbf{k}=(\pi,\pi)} \quad (6.12)$$

$$= \frac{1}{2\epsilon} \times \frac{1}{8} \times q^2 \quad (6.13)$$

$$= \frac{q^2}{16\epsilon} \equiv u_c \quad (6.14)$$

If  $u < u_c = q^2/16\epsilon$ , the term in brackets in Eq. 6.11 ( $\frac{1}{2\epsilon}G(\mathbf{k}) - u$ )  $> 0 \forall \mathbf{k}$  and the ground state will be the vacuum, where the charge density is vanishingly small and therefore  $\rho(\mathbf{k}) = 0 \forall \mathbf{k}$ . If  $u > u_c$  the lowest energy state is one with some non-zero ordering wavevector  $\mathbf{k}_a$ , which we shall see below coincides with the minimum of  $G(\mathbf{k})$  and corresponds to alternating positive and negative charges and “antiferromagnetic” ordering in the fields. In the system of units used here, where  $q = 1$  and  $\epsilon = 1/2\pi$ , the expected critical value for the core-energy is then  $u_c = 1^2/(16/2\pi) = 2\pi/16 = \pi/8$ .

### 6.4.1. Charge density

The average charge density of the system provides a convenient characterisation of this transition and is shown here in Fig. 6.29.

The charge density is (at least technically) always finite, even below the first-order transition, since the BKT transition only corresponds to the unbinding of charges rather than the appearance of charges. We find that it begins to increase slightly below  $u_c$ , reaching a value of around 0.0148 at  $u = 0.392$  for both  $L = 64$  and 128. At around  $u = 0.4$  we see the average charge density increase more rapidly: the fastest increase in  $\rho_{\text{avg}}$  comes between  $u = 0.41$  and  $u = 0.42$ , by which point the charge density is almost 1. We also see the difference in the transition “rate” for different system sizes: as expected,  $L = 128$  reaches the charge solid phase faster than  $L = 64$  as the core-energy is increased.

### 6.4.2. Correlations

We find that the field-field correlations exhibit an interesting transition also, from a rotational-dominated low- $u$  state identical to that of the “standard” BKT transition discussed above to an irrotational-dominated high- $u$  state which consists of Bragg peaks at specific zone boundaries. Below the first order transition we have

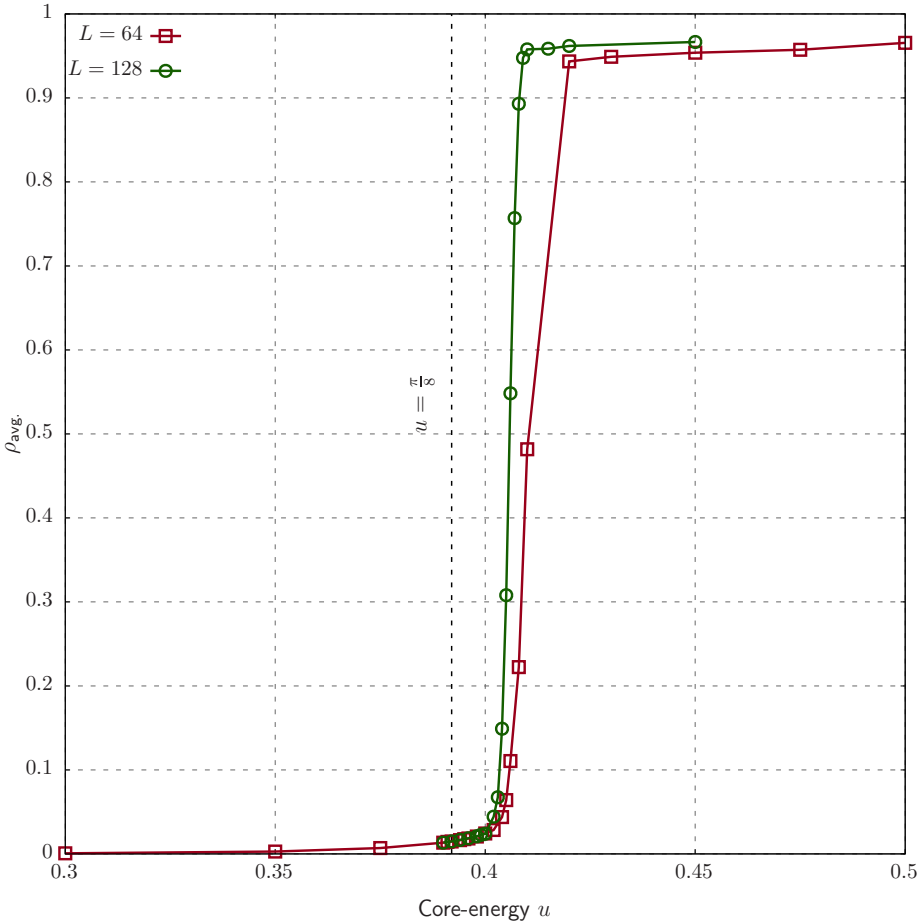


FIGURE 6.29.: The average charge density of the 2D Coulomb gas on the square lattice, as a function of core-energy constant  $u$ . The exact core-energy of the transition in the thermodynamic limit is displayed as a dashed line.

correlation tensors which are essentially identical to those of the low-temperature phase in the previous section, as shown in Fig. 6.30.

For these parameters, the **longitudinal** correlations are several orders of magnitude smaller than the **transverse**. As we cross the transition, however, we start to see a qualitative change in the tensors, with Lorentzians appearing at the corners of the Brillouin zone which come from the irrotational component of the field. Fig. 6.31, showing the correlation tensor for the irrotational component at  $T = 0.1, u = 0.392$  (the approximate location of the first-order transition), displays the crossover between the two regimes. The dark purple band across  $q_y = 0$  in  $S_{\text{irrot.}}^{xx}$ , for example, is characteristic of the low- $u$  regime (cf. Fig. 6.8b); the peak

## 6. Results for the 2D grand canonical Coulomb gas

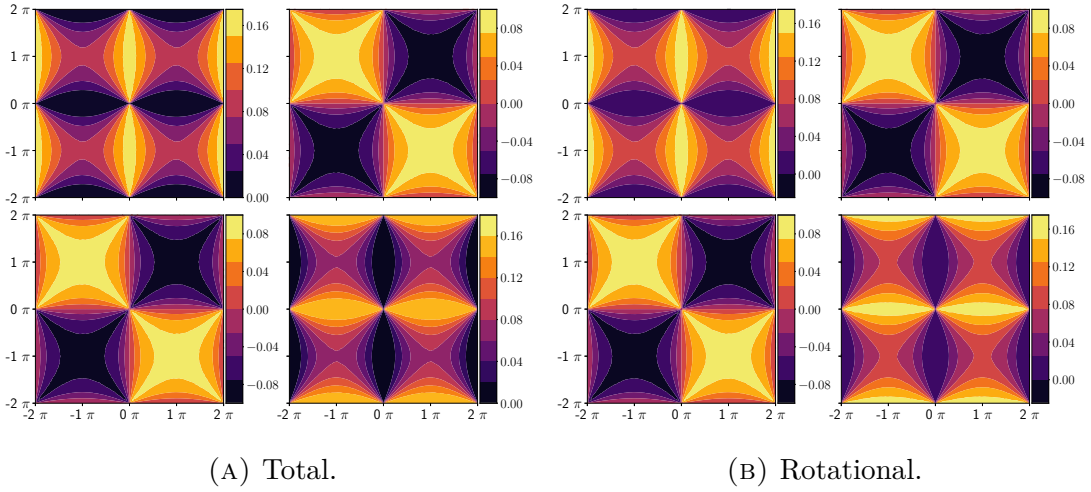


FIGURE 6.30.: ( $T = 0.100$  ;  $u = 0.200$ ). Correlation tensors  $S_{\text{total}}^{\alpha\beta}$  and  $S_{\text{rot}}^{\alpha\beta}$  respectively, below the BKT and first-order transitions. We can see that the total correlations are completely dominated by the rotational component.

appearing at  $\mathbf{q} = (\pm\pi, \pm\pi)$  is characteristic of the ordered charge solid which is the ground state of the high- $u$  regime. We see in Fig. 6.31 that the diffuse bands evident at low core-energy are still in evidence but overtaken in intensity by the peaks at  $\mathbf{q} = (\pm\pi, \pm\pi)$ .

The qualitative change is made more obvious by inspecting the trace of the tensors: as opposed to the low- $u$  regime, where the trace of the irrotational tensor is Lorentzian in character with its peak at  $\mathbf{q} = \mathbf{0}$ , as in Fig. 6.11b, here we have broader Lorentzians forming around the corners of the Brillouin zone:

We can see the broader peaks around the transition core-energy sharpening and giving way to peaks which are essentially Bragg-like by  $u = 0.410$ . By this point, the correlations in the total field are dominated by the irrotational component:

We see that the diagonal components of the correlation tensor are now essentially identical, both featuring sharp peaks at the Brillouin zone corners. The peak locations correspond essentially to antiferroelectric order in the field components; alternating positive and negative charges give fields of the same magnitude but opposite sign on neighbouring sites. Additionally, we see similar peaks in the off-diagonal term but with a negative sign when  $\text{sgn}(q_x) = -\text{sgn}(q_y)$ , reflecting the fact that each y-component “sees” fields in the x-direction of the same sign in one direction and the opposite sign in the other direction.

This is accompanied by a change in shape of the quadric of  $S_{\text{total}}^{\alpha\beta}(\mathbf{q})$ , from circular or ellipsoid to an extremely thin needle, as shown in Fig. 6.34.

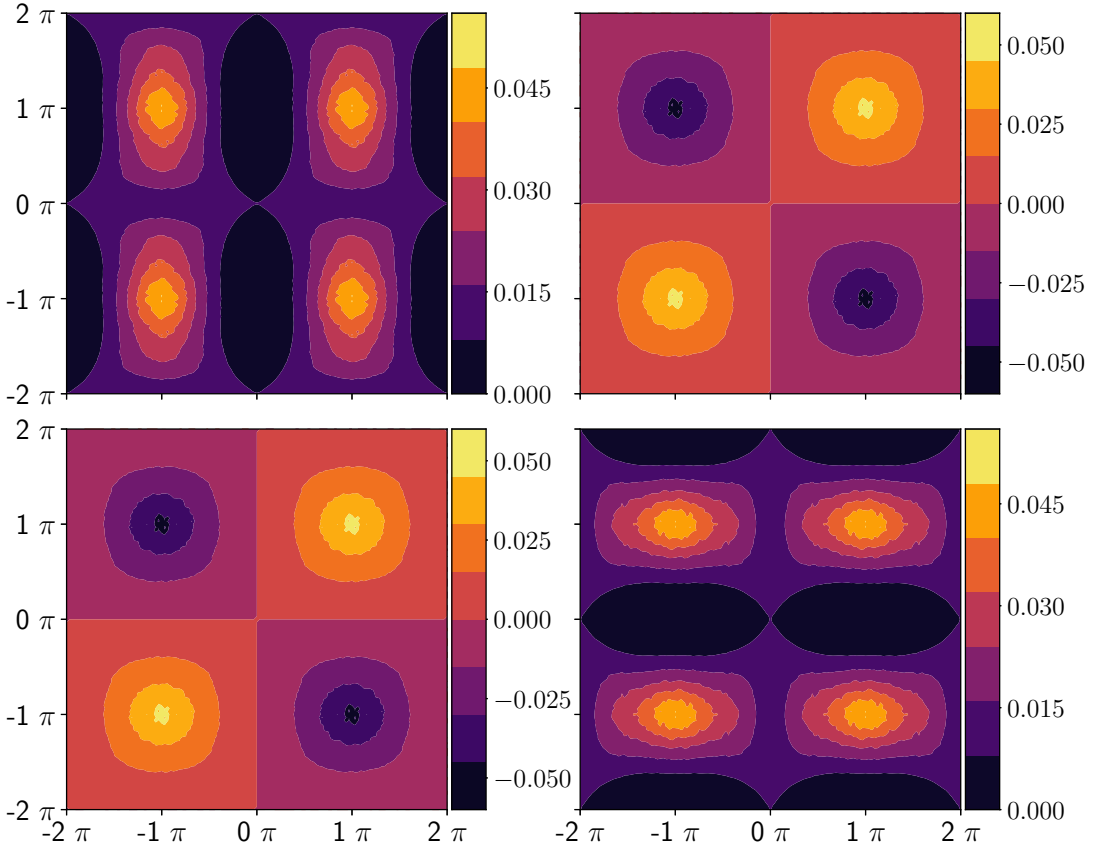


FIGURE 6.31.: ( $T = 0.100$  ;  $u = 0.392$ ). The correlation tensor for the irrotational component at  $u = 0.392$ , almost precisely at the critical core-energy value  $u_c = \pi/8 = 0.392699\dots$  in the thermodynamic limit.

### $S^\perp$ and $S^\parallel$ functions

I also calculate the perpendicular and parallel components of the tensors with respect to the scattering wavevector, as with the previous section. Here, we see the rotational-dominated low- $u$  state giving way to Bragg peaks at specific zone boundaries in the high- $u$  solid phase, as well as a brief coexistence regime around the transition. The parallel component to the wavevector is not a quantity which is normally experimentally accessible, because there is no probe in the context of a spin system which is “opposite” to a neutron in that sense; the fact that the neutron only couples to fields perpendicular to its wavevector prevents this. However, we may still calculate the projection from the correlation tensor and in the high- $u$  phase we see a striking link to experimental work on artificial spin ice arrays.

The perpendicular component for  $u < 0.392$  looks identical to those shown

## 6. Results for the 2D grand canonical Coulomb gas

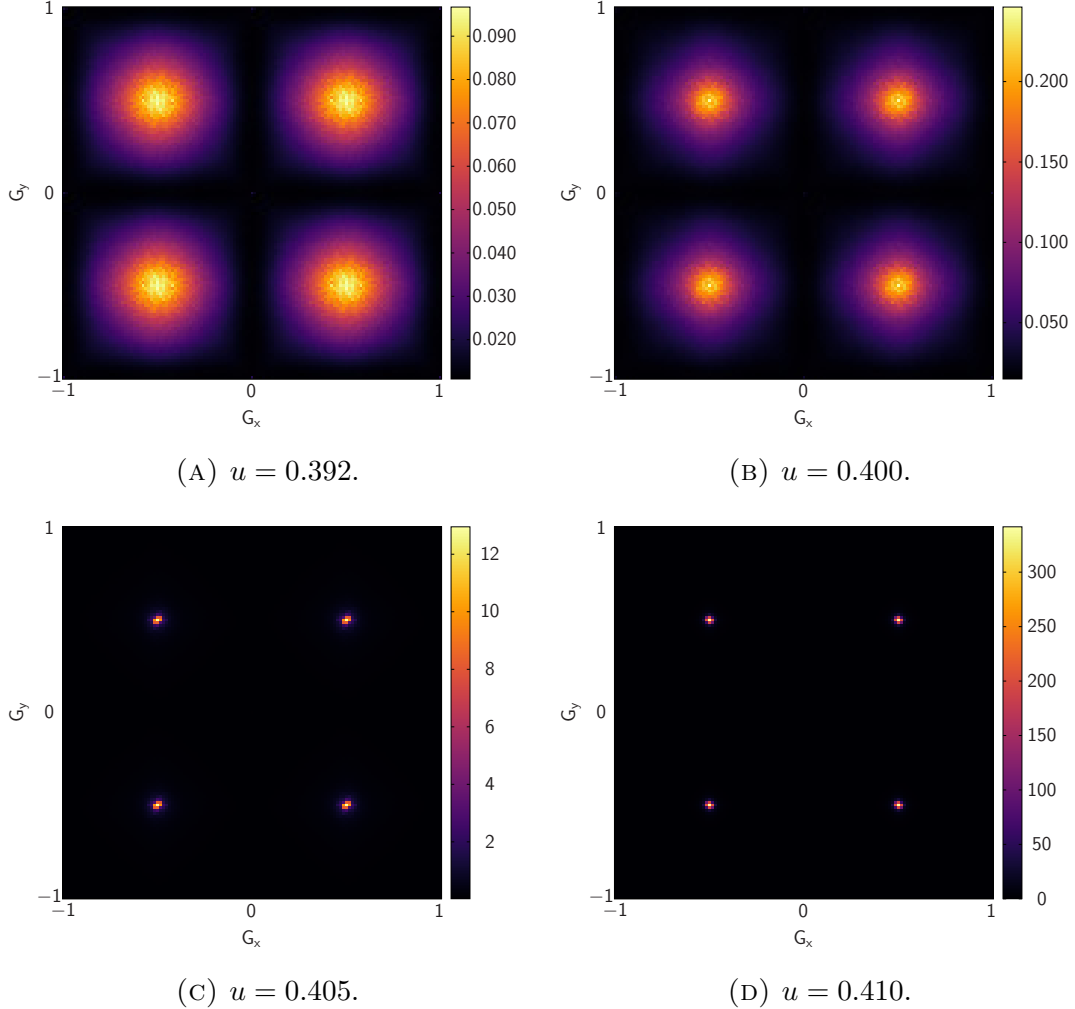


FIGURE 6.32.: ( $T = 0.100$  ;  $u = 0.392, 0.400, 0.405, 0.410$ ). The trace of the irrotational correlation tensor at  $T = 0.1$  as  $u$  increases beyond the transition, showing the growing intensity of the peaks at the Brillouin zone corners.

above, e.g. in Figs. 6.12, but is shown again here as Fig. 6.35 for completeness. We are clearly in the insulating phase here, as can be seen from the “vacancy” at  $\mathbf{q} = \mathbf{0}$ . In between the high-intensity parts of the function, at areas corresponding to Brillouin zone corners, there are areas in the Fig. 6.35 which are of higher intensity than in the zero- $u$  case, however.

As the transition to the solid phase is crossed, we start to see broad peaks appearing in the perpendicular component at these areas.

At  $u = 0.392$ , we start to see the “solid” correlations, which are the peaks arising in  $S_{\text{total}}^{\perp}$  in the areas which are of low intensity in the low- $u$  rotationally-dominated “gas” regime. For these parameters the two sets of features are of

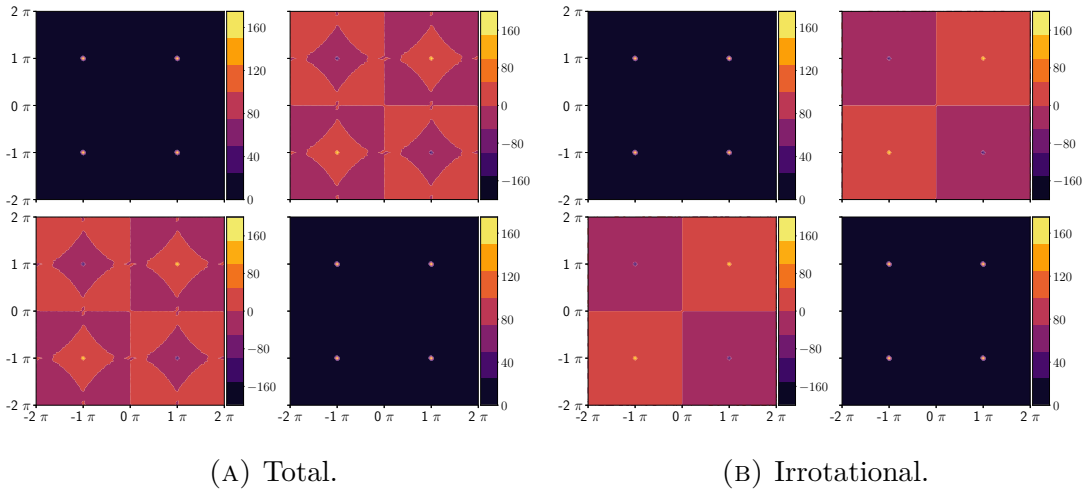


FIGURE 6.33.: ( $T = 0.100$ ;  $u = 0.410$ ). The correlation tensor for the total field (left) and irrotational component (right) at  $u = 0.410$ , showing that the total correlations are now dominated by the longitudinal component.

the same order, but the “solid” correlations have slightly lower intensity than the “gas” correlations. Referring back to Fig. 6.31 and looking at areas of Fig. 6.36, we can see how the coexistence of the two phases in the overall correlation tensor is echoed in the perpendicular component.

For a small range in  $u$ , namely  $0.392 \lesssim u \lesssim 0.402$  or thereabouts, the two phases have correlations of the same order of magnitude and we can see the gas-solid coexistence in  $S^\perp$  quite clearly, as shown below in Fig. 6.37.

At  $u = 0.404$  the system is completely in the insulating solid phase, and the peaks associated with this phase have intensities an order of magnitude larger than those of the rotational background. Correspondingly we see that  $S_{\text{total}}^\perp$  is dominated by the irrotational component, as in Fig. 6.38.

In this phase the peaks shown in Fig. 6.38 are Bragg-like; the irrotational field is ordered due to the regular charge arrangement, and the correlations reflect this. An example of an irrotational field configuration in the solid phase is given in Fig. 6.39.

The lengths of the arrows in this figure are scaled relative to the largest magnitude field link in the system, meaning that the irrotational fields shown here are all of very similar magnitude, as would be expected for a charge crystal with single-valued charges only.

The cause of the missing peaks in Fig. 6.38 follows from careful consideration of the expression for  $S^\perp(\mathbf{Q})$ . Since we normalise  $q_\alpha q_\beta$  by  $q_\alpha^2 + q_\beta^2$ , we have (at  $(\pi, \pi)$ ,

## 6. Results for the 2D grand canonical Coulomb gas

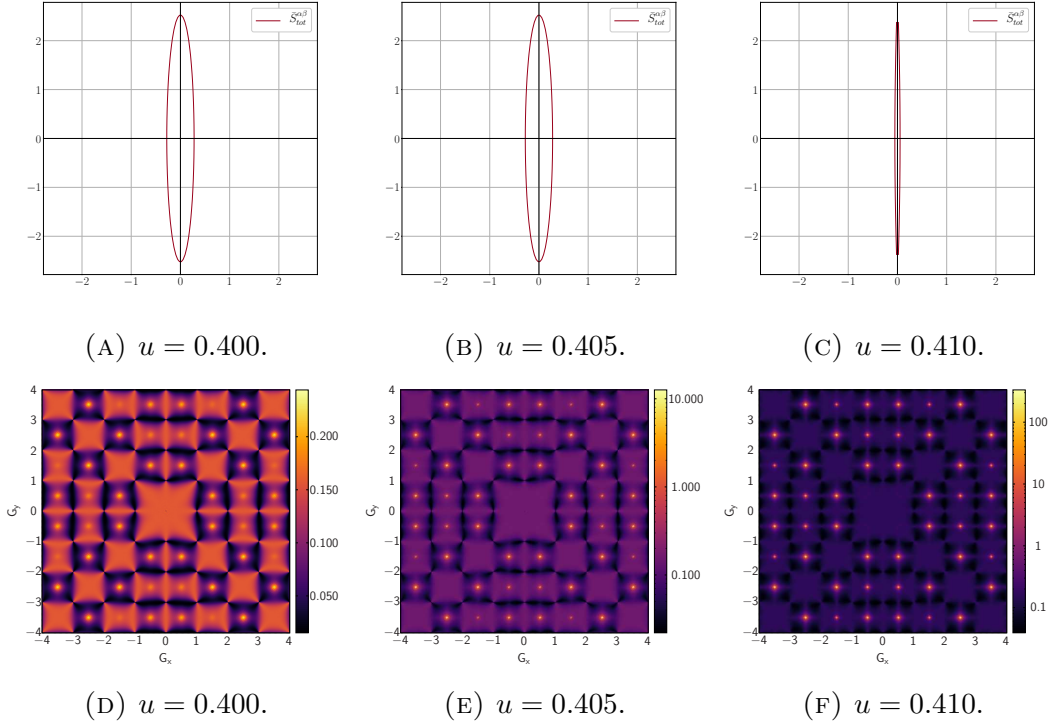


FIGURE 6.34.: ( $T = 0.100$  ;  $u = 0.400, 0.405, 0.410$ ). The quadric  $\bar{S}_{\text{total}}^{\alpha\beta}(\pi, \pi)$  as the charge solid forms (a-c), with the corresponding  $S^\perp(\mathbf{Q})$  plots (d-f). The plots for  $u = 0.405, 0.410$  use a logscale for the intensity, since otherwise the peaks become invisible against the background.

for example)

$$\left. \left( \delta_{\alpha\beta} - \frac{q_\alpha q_\beta}{q_\alpha^2 + q_\beta^2} \right) S^{\alpha\beta}(\mathbf{q}) \right|_{(q_x=\pi, q_y=\pi)} = \left( 1 - \frac{\pi^2}{2\pi^2} \right) S^{xx}(\pi, \pi) - \frac{\pi^2}{2\pi^2} S^{xy}(\pi, \pi) - \frac{\pi^2}{2\pi^2} S^{yx}(\pi, \pi) + \left( 1 - \frac{\pi^2}{2\pi^2} \right) S^{yy}(\pi, \pi) \quad (6.15)$$

$$= \frac{1}{2} S^{xx}(\pi, \pi) - S^{xy}(\pi, \pi) + \frac{1}{2} S^{yy}(\pi, \pi) \quad (6.16)$$

The vanishing of the peak can now be understood using the last line above: the total field is dominated by the irrotational field, which is the field of an ordered charge crystal. We have regular, “antiferromagnetic” fields which flow out from each positive charge into its negative neighbours and vice versa.

This field arrangement can be described by a propagation vector of  $k_a = \pm(\pi, \pi)$ ,

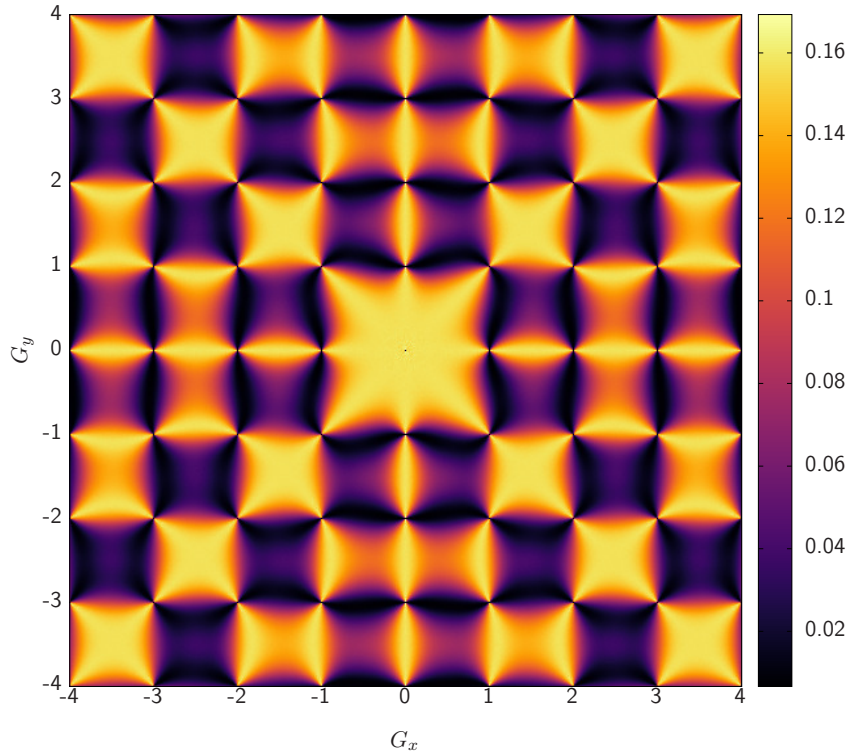


FIGURE 6.35.: ( $T = 0.100$  ;  $u = 0.375$ ).  $S^\perp(\mathbf{Q})$ . The core-energy here is below the critical value; despite its being finite, the total correlations are still those of the gas phase.

as can be shown from a consideration of a charge pair and the fields around it. Recalling Eq. 5.17, we can write

$$\boldsymbol{\mu}(\mathbf{x}) \propto \exp(-i\mathbf{k}_a \cdot \mathbf{x}) \quad (6.17)$$

and defining fields pointing up/right as positive and down/left as negative, we have

$$\boldsymbol{\mu}(0, 1/2) \propto \exp(-i(\pi, \pi) \cdot (0, 1/2)) = -i \quad (6.18)$$

$$\boldsymbol{\mu}(1/2, 0) \propto \exp(-i(\pi, \pi) \cdot (1/2, 0)) = -i \quad (6.19)$$

$$\boldsymbol{\mu}(0, -1/2) \propto \exp(-i(\pi, \pi) \cdot (0, -1/2)) = +i \quad (6.20)$$

$$\boldsymbol{\mu}(-1/2, 0) \propto \exp(-i(\pi, \pi) \cdot (-1/2, 0)) = +i \quad (6.21)$$

$$\boldsymbol{\mu}(3/2, 0) \propto \exp(-i(\pi, \pi) \cdot (3/2, 0)) = +i \quad (6.22)$$

$$\boldsymbol{\mu}(1, 1/2) \propto \exp(-i(\pi, \pi) \cdot (1, 1/2)) = +i \quad (6.23)$$

$$\boldsymbol{\mu}(1, -1/2) \propto \exp(-i(\pi, \pi) \cdot (1, -1/2)) = -i \quad (6.24)$$

## 6. Results for the 2D grand canonical Coulomb gas

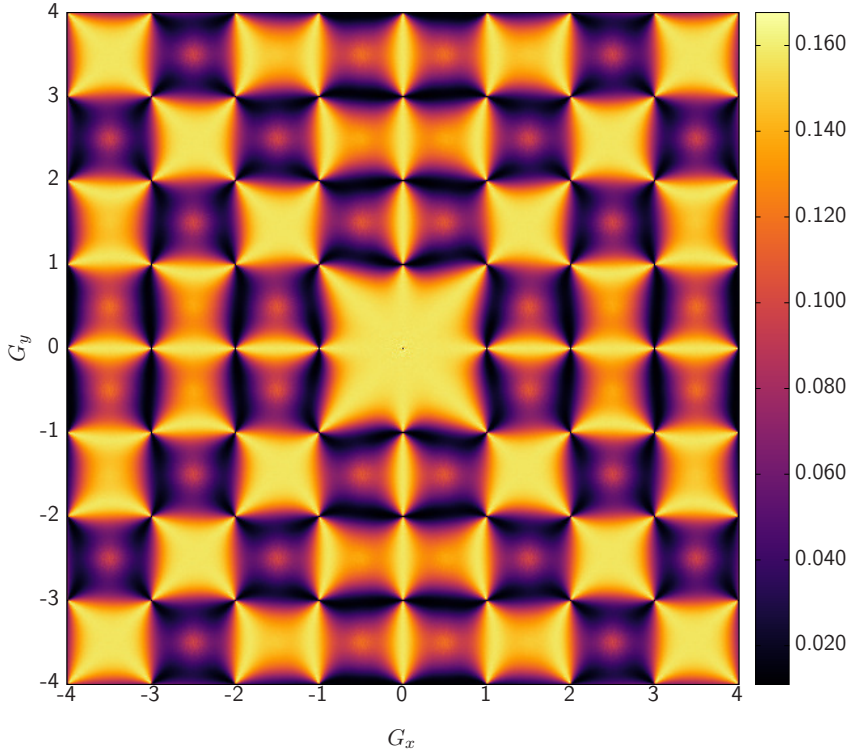


FIGURE 6.36.: ( $T = 0.100$  ;  $u = 0.392$ ).  $S^\perp(\mathbf{Q})$ . We are now essentially at  $u = u_c = \pi/8$ ; the peaks associated with the solid phase are now beginning to be visible superimposed on the diffuse correlations of the gas phase.

and so on over the entire lattice, where we see that the sign of  $\mu$  at any given point matches the direction of the field at that point.

We can check the predicted intensity of the Bragg peak in the neutron scattering plot by first taking, for some reciprocal lattice vector  $\mathbf{G}$ ,

$$\mathbf{g} = \mathbf{k}_a + \mathbf{G} \quad (6.25)$$

$$\hat{\mathbf{g}} = \frac{\mathbf{k}_a + \mathbf{G}}{\sqrt{|\mathbf{k}_a + \mathbf{G}|^2}} \quad (6.26)$$

and the basis

$$\mathbf{x}_1 = (1/2, 0), \mathbf{e}_1 = (1, 0); \quad \mathbf{x}_2 = (0, 1/2), \mathbf{e}_2 = (0, 1) \quad (6.27)$$

which corresponds to the two positive fields next to the positive charge.

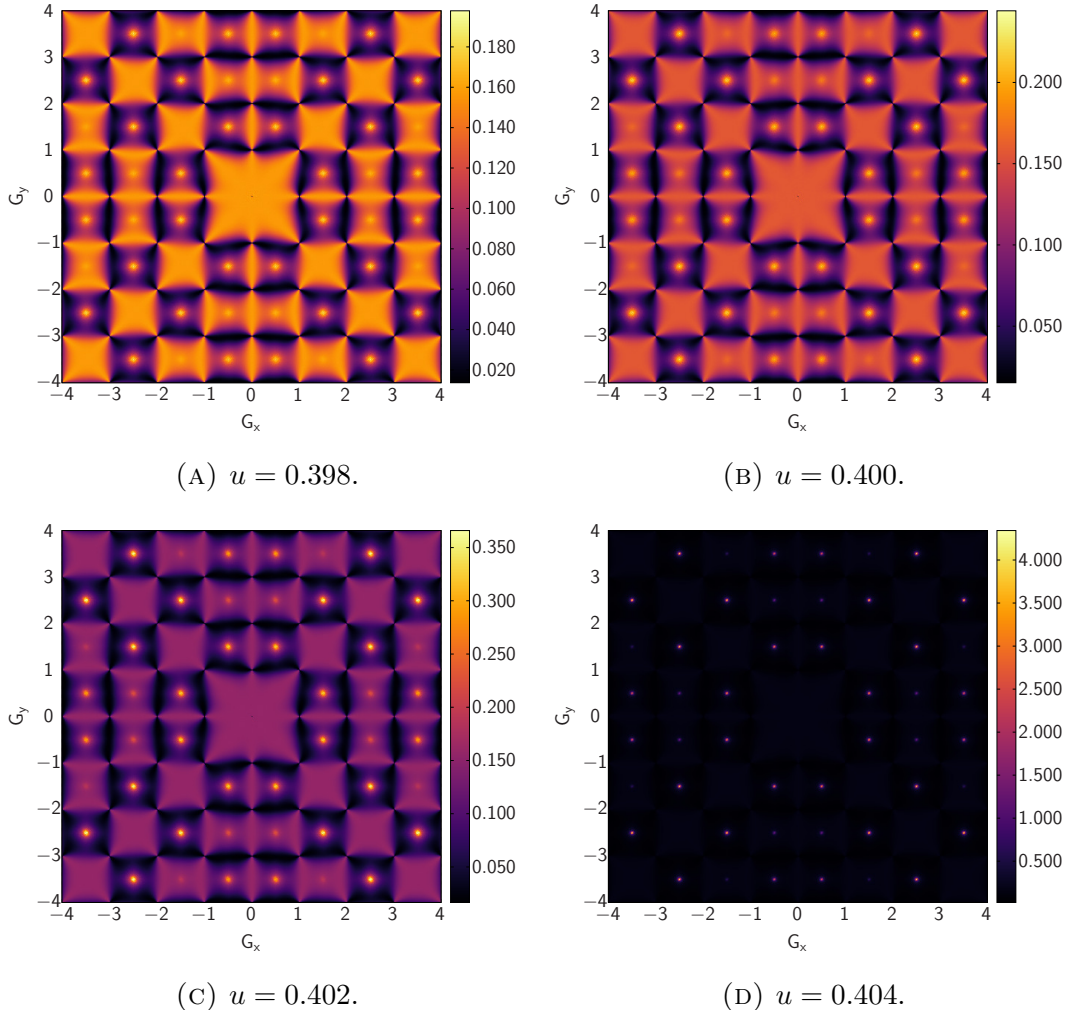


FIGURE 6.37.: ( $T = 0.100$  ;  $u = 0.398, 0.400, 0.402, 0.404$ ). Four examples of  $S_{\text{total}}^{\perp}(\mathbf{Q})$  around the critical core-energy value  $u_c$ . We can clearly see the solid-gas coexistence, with the pinch point of the gas phase and the sharpening peaks of the solid phase; by  $u = 0.404$ , the peaks are almost Bragg-like and the rotational correlations are invisible.

## 6. Results for the 2D grand canonical Coulomb gas

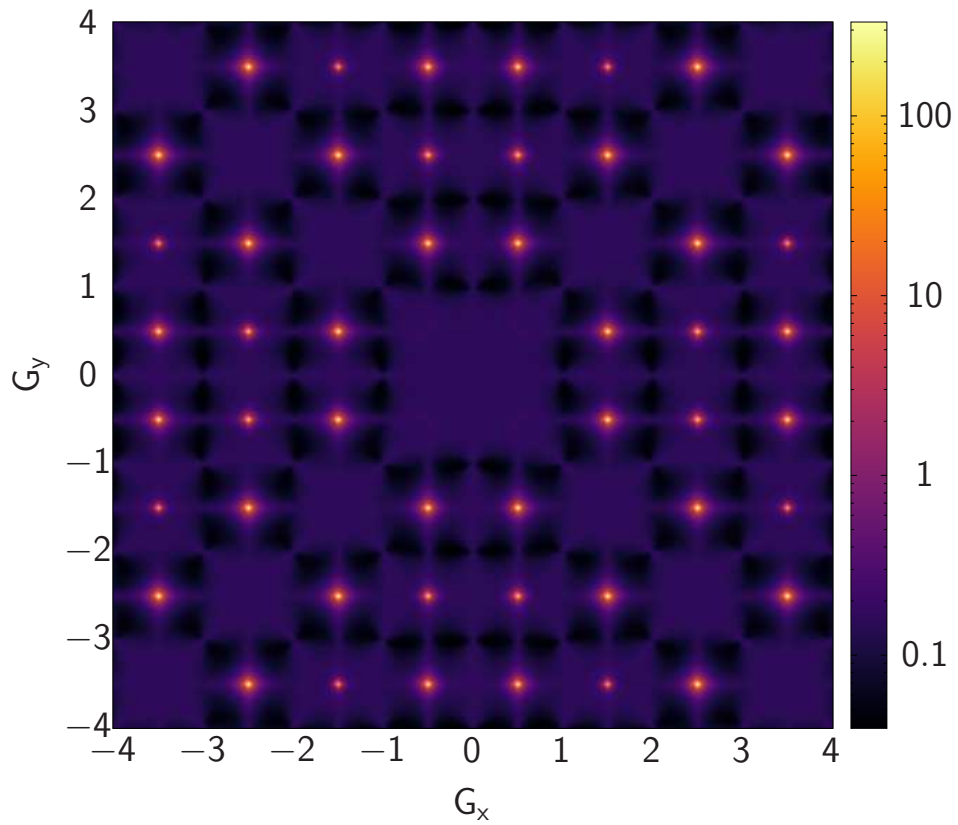


FIGURE 6.38.: ( $T = 0.100$  ;  $u = 0.410$ ).  $S^\perp(\mathbf{Q})$ . The system is now completely ordered; the neutron scattering pattern shows extremely sharp peaks. The intensities are plotted on a log scale in order to make the plot legible.

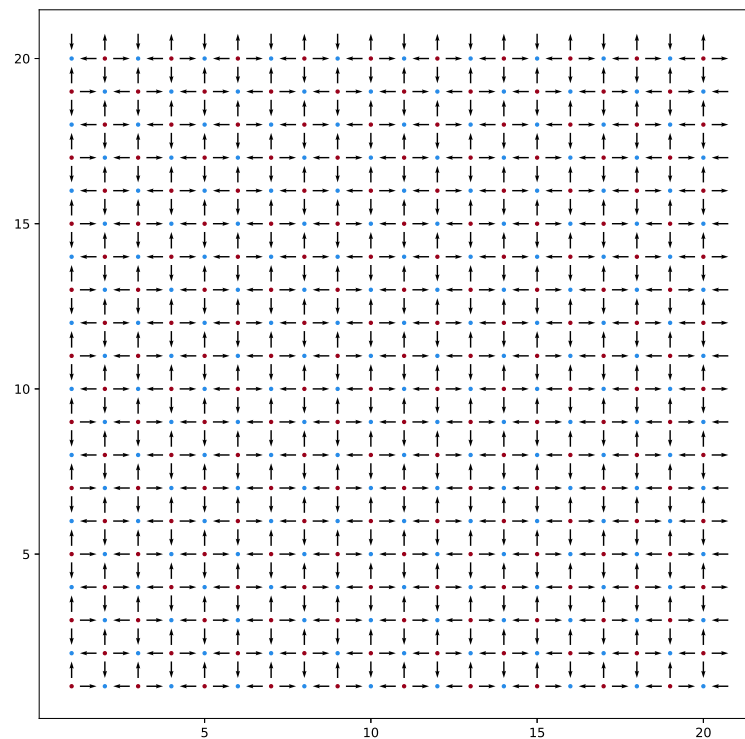


FIGURE 6.39.: ( $T = 0.100$  ;  $u = 0.420$ ). An example of an irrotational field configuration for  $L = 20$ . Here, the system is a fully ordered charge crystal; in general charge annihilations are possible, but the average charge density for these parameters is around 95%.

## 6. Results for the 2D grand canonical Coulomb gas

Then the structure factor is given by

$$f = (\mathbf{e}_1 - \hat{\mathbf{g}}(\mathbf{e}_1 \cdot \hat{\mathbf{g}})) \exp(i\mathbf{x}_1 \cdot \hat{\mathbf{g}}) + (\mathbf{e}_2 - \hat{\mathbf{g}}(\mathbf{e}_2 \cdot \hat{\mathbf{g}})) \exp(i\mathbf{x}_2 \cdot \hat{\mathbf{g}}) \quad (6.28)$$

and the intensity of the peak is given by  $|f|^2$ .

Inserting  $\mathbf{G} = (0, 0)$  we find  $\hat{\mathbf{g}} = \frac{1}{\sqrt{2}\pi}(\pi, \pi) = \frac{1}{\sqrt{2}}(1, 1)$  and that the intensity at  $(\pi, \pi)$  should be

$$\begin{aligned} f &= ((1, 0) - \frac{1}{\sqrt{2}}(1, 1)((1, 0) \cdot \frac{1}{\sqrt{2}}(1, 1))) \exp(i(1/2, 0) \cdot (\pi, \pi)) \\ &\quad + ((0, 1) - \frac{1}{\sqrt{2}}(1, 1)((0, 1) \cdot \frac{1}{\sqrt{2}}(1, 1))) \exp(i(0, 1/2) \cdot (\pi, \pi)) \end{aligned} \quad (6.29)$$

$$= (1/2, -1/2)i + (-1/2, 1/2)i \quad (6.30)$$

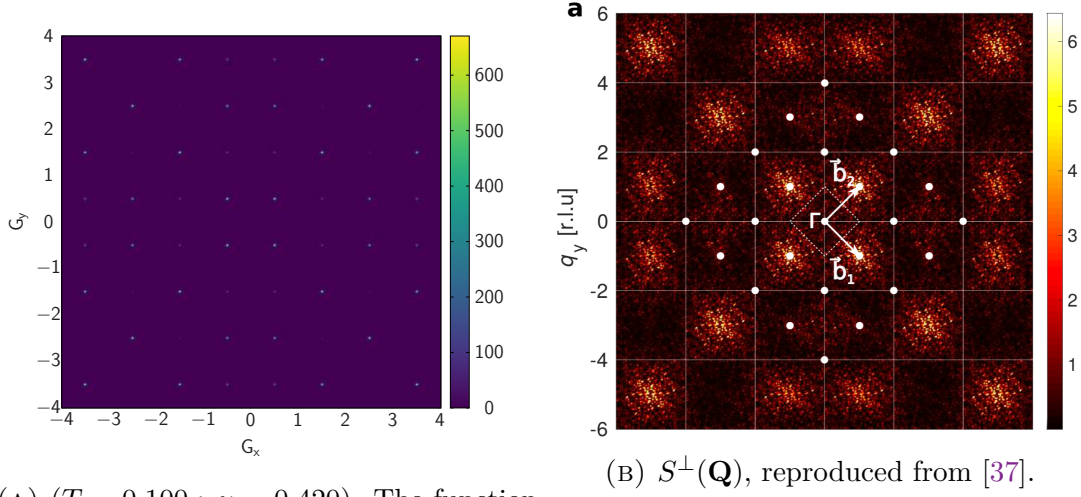
$$= 0 \quad (6.31)$$

An identical argument holds for every peak along the diagonal: the missing Bragg peaks (systematic absences) are a consequence of both the specific ordering of the **GLCG** in this phase and the specific symmetry of the lattice.

For the parallel component an analogous argument holds, but the propagation vector is now  $\pm(-\pi, \pi)$ . By the same method, this gives us the peaks along the diagonal which are missing from the perpendicular component, and the analytical consideration is again borne out by simulations. The parallel component also displays a striking resemblance to correlations obtained in [37], which are reproduced in Fig. 6.40b.

Explaining the origin of this similarity requires some knowledge of the **artificial spin ice** system used in the experiment: for the experimental parameters which produced this figure, the lattice is made up of a network of “ $T_I$ ” vertices, or equivalently vertices 5 and 6 of the 6vert as shown in Fig. 4.6. These are vertex configurations of fixed-length spins which have zero divergence (meaning the field is fully rotational) and zero overall magnetic moment: they correspond to the ground state of the **F model** of antiferroelectrics. The peaks shown in Fig. 6.40b then represent the perpendicular component of the correlations for a fully **transverse** field.

By contrast, the fields in the insulating solid regime of the Coulomb gas, especially at low temperature where the magnitude of the auxiliary field is small, are of relatively fixed length; but here, in contrast, the vertex configurations are all-in all-out, because of the arrangement of charges in the crystal, as shown in Fig. 6.39.



(A) ( $T = 0.100$ ;  $u = 0.420$ ). The function  $S_{\text{total}}^{\parallel}(\mathbf{Q})$ . Colours have been changed to make the peaks more visible.

FIGURE 6.40.: The parallel component of the scattering function of the electric field, displaying the same peaks and systematic absences as the perpendicular component of the scattering function for ASI experiments conducted in [37].

The peaks shown in Fig. 6.40a then represent the parallel component of the correlations for a fully irrotational field. This “symmetry” can be understood as reflecting the fact that in 2D, a  $\pi/2$  rotation of the field turns a rotational field into an irrotational one: we can see this by Fourier transforming the field and letting one  $q_\alpha$  be parallel (**longitudinal**) to the neutron wavevector;  $q_\beta$  is then orthogonal to  $q_\alpha$  and perpendicular (**transverse**) to the wavevector.

Lastly, we can note that the sum of the intensities in  $S^\perp$  and  $S^\parallel$  at each peak must be constant, and by plotting the sum of the two components we find regular peaks of identical intensity at  $(\pm(2n+1)\pi, \pm(2n+1)\pi)$ , as shown in Fig. 6.41.

### 6.4.3. Lorentzian fits

It is also possible to fit the peaks shown in Fig. 6.38 to a model Lorentzian and investigate the temperature dependence of the peak. For these fits I use the ansatz

$$L(\chi, \kappa, \gamma) = \frac{\chi \kappa^2}{\kappa^2 + (\mathbf{q} - \mathbf{q}_0)^2} + \gamma \quad (6.32)$$

where  $\gamma$  is a simple constant background term,  $\mathbf{q}_0$  is the Brillouin zone corner corresponding to the peak and  $\mathbf{q}$  runs for one Brillouin zone along the  $q_y$  axis.

Following the argument in the previous section, the correlation peaks in the

## 6. Results for the 2D grand canonical Coulomb gas

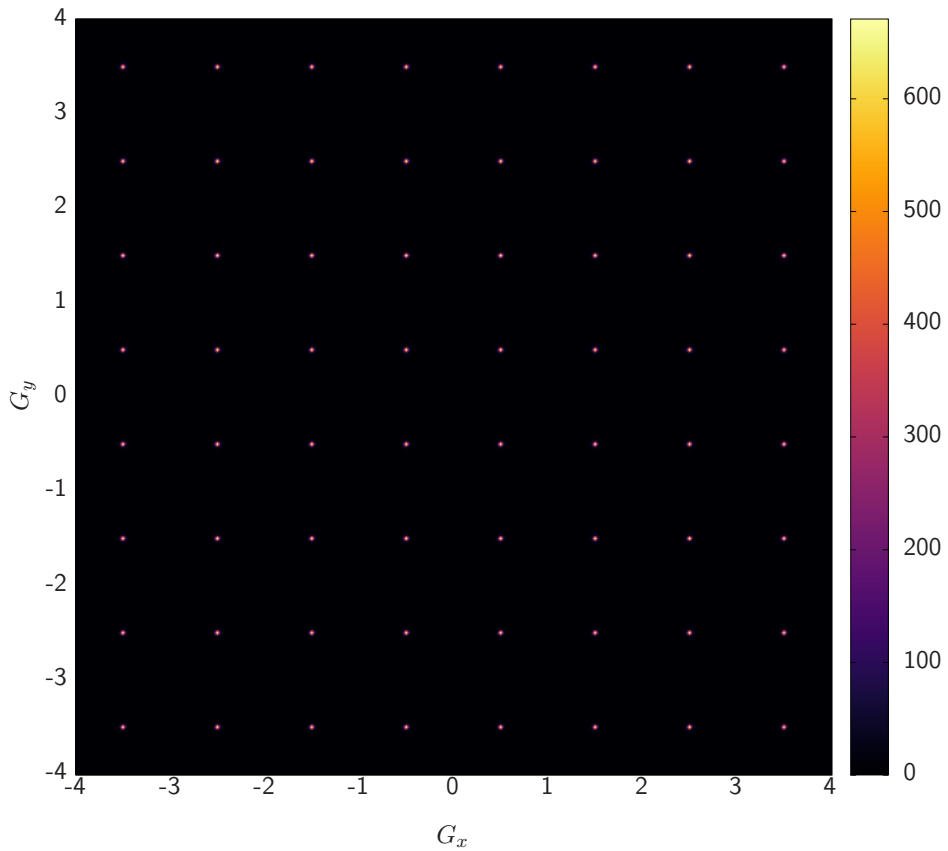


FIGURE 6.41.: ( $T = 0.100$  ;  $u = 0.420$ ).  $S_{\text{total}}^{\perp}(\mathbf{Q}) + S_{\text{total}}^{||}(\mathbf{Q})$ . We see that the function displays peaks of identical intensity at the corner of each Brillouin zone: this function essentially corresponds to taking the trace of  $S^{\alpha\beta}(\mathbf{q})$ , as shown in (for example) Fig. 6.32d.

insulating solid phase are split between the perpendicular and parallel components, so I first do  $S_{\text{total}}^{\perp} + S_{\text{total}}^{\parallel}$  and then use the line  $Q_x = \pi$ ;  $0 \leq Q_y \leq 2\pi$  to fit a Lorentzian to the peak at  $(\pi, \pi)$ .

As expected from the figures in the previous section, these fits allow us to see the evolution in the sharpness of the peak as the core-energy increases; the evolution in intensity with respect to  $u$  is shown in Fig. 6.42. At the critical core-energy  $u = 0.392$  the peak is only a small bump superimposed on the flat rotational background, but at  $u = 0.402$  the intensity at  $(\pi, \pi)$  is already three times as large as the background.

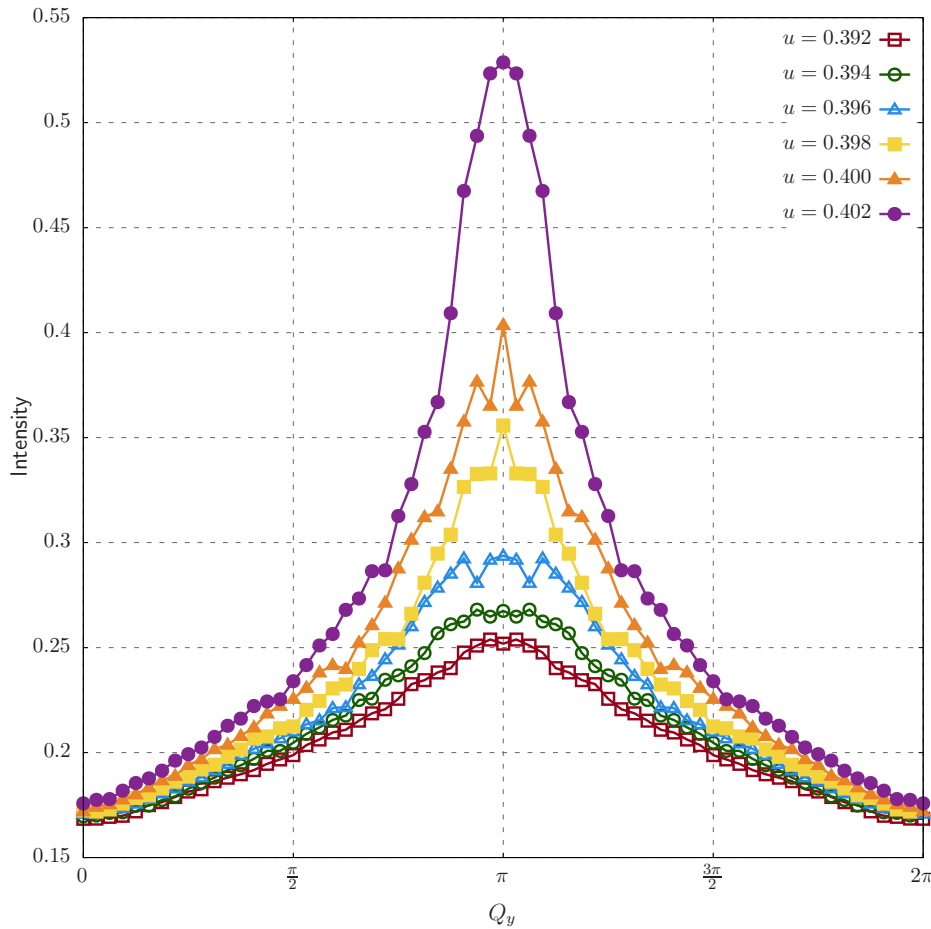


FIGURE 6.42.: The evolution of the peak in  $S_{\text{total}}^{\perp}(\mathbf{Q}) + S_{\text{total}}^{\parallel}(\mathbf{Q})$  at  $\mathbf{Q} = (\pi, \pi)$  as a function of  $u$ . At higher core-energies it becomes necessary to use a log scale and the peaks shown here become invisible.

Beyond  $u = 0.402$  it becomes necessary to use a log scale for the x axis here.

## 6. Results for the 2D grand canonical Coulomb gas

### 6.4.4. Discussion

The first-order transition of the 2D GLCG and particularly the insulating solid phase represent an idealised glimpse into the kind of magnetic-moment fragmentation discussed in [77]. The charge crystal corresponds to a monopole crystal in spin ice, and the rotational field corresponds to the background spin fluctuations. The important differences here are that double charges are forbidden in my work, and also (as previously noted) that the two components are completely uncoupled because the magnitude of the fields are not fixed.

## 6.5. High core-energy BKT and second-order transitions

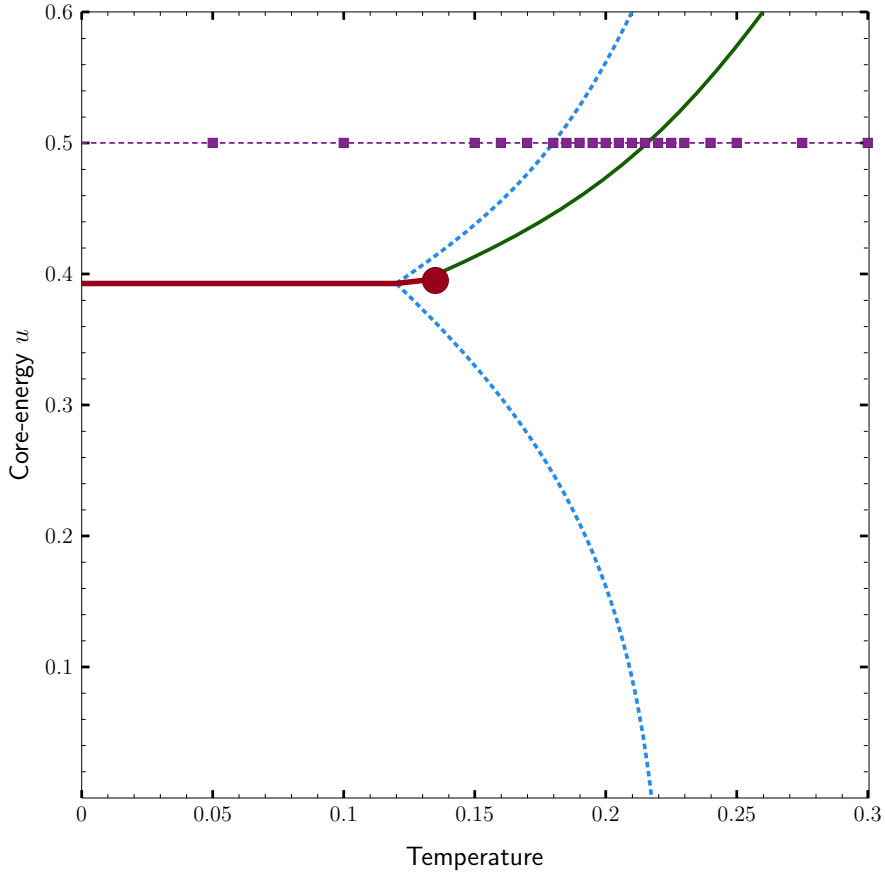


FIGURE 6.43.: Phase diagram 6.1 with the relevant  $u, T$  parameters used in my simulations of the high- $u$  transitions highlighted with purple rectangles.

The high- $u$  regime of the phase diagram corresponds to an insulating crystal

## 6.5. High core-energy BKT and second-order transitions

of alternating charges, which undergoes a BKT transition just as in the low- $u$  regime. In this case, however, the BKT transition presents as the unbinding of pairs of holes: at all temperatures lower than  $T_{\text{BKT}}^{\text{solid}}$  it is possible for charges to annihilate, but only above this temperature does entropy overcome energy and allow the vacancies to diffuse freely through the system. The BKT transition from an insulating charge solid to a conducting one is followed by a second-order transition, which corresponds to the melting of the charge solid.

I find through simulations across these transitions, holding the core-energy constant and increasing  $T$ , that the development of the  $\mathbf{Q} = \mathbf{0}$  point of the  $S^{\perp}(\mathbf{Q})$  function again gives a good signature of the BKT transition.

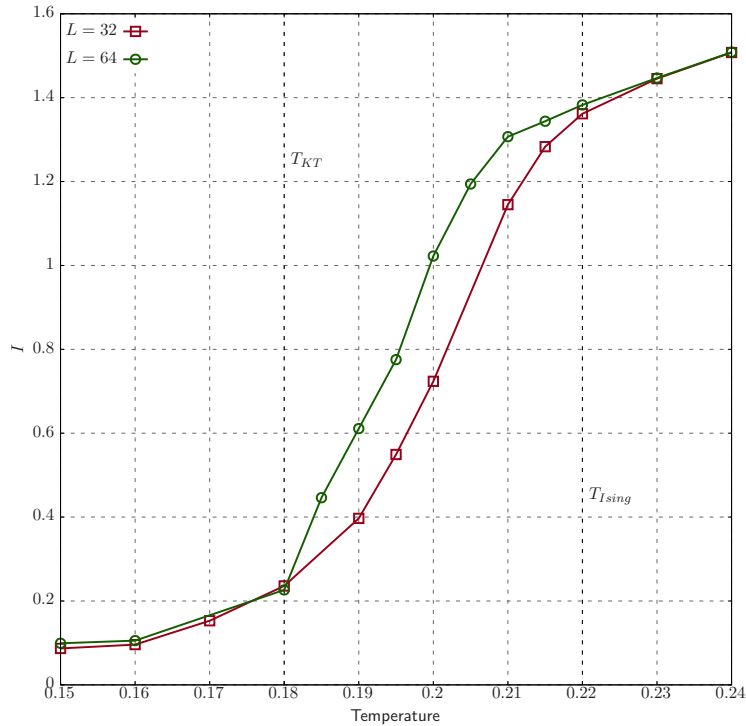


FIGURE 6.44.: The evolution of the  $\mathbf{q} = \mathbf{0}$  point of  $S_{\text{total}}^{\perp}$  across the high- $u$  BKT transition, for different system sizes. We see a sharp increase across the BKT transition followed by a slowing down above the Ising transition; the increase is sharper for the larger system size.

We can also observe the transition from the insulating solid to the conducting one in the average charge density shown in Fig. 6.45, which drops from  $\approx 95\%$  at the BKT transition temperature  $T_{\text{BKT}}^{\text{solid}} = 0.18$  to  $\approx 80\%$  at the melting temperat-

## 6. Results for the 2D grand canonical Coulomb gas

ure  $T_{Ising} = 0.22$ .

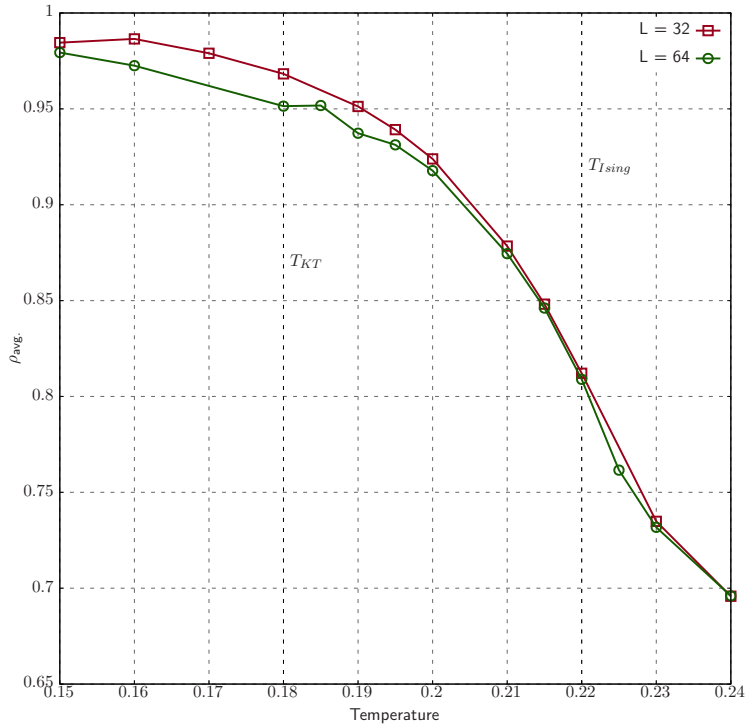


FIGURE 6.45.: Average charge density of the Coulomb solid across the insulator-conductor BKT transition, showing a drop from  $\approx 95\%$  below the BKT transition to around 0.7 at  $T = 0.24$ , just above the Ising transition.

Finite size analysis here shows essentially what we expect: the transitions occur slightly faster for larger systems.

In addition, the melting transition is shown clearly from the scattering functions: the Bragg peaks which correspond to the charge solid slowly give way to Lorentzians which broaden as the temperature increases. I fit these Lorentzians as a function of temperature to give an estimate of an inverse “Debye length” for this idealised Coulomb gas.

At very low temperature the harmonic susceptibilities are large: this is expected, since for these parameters the polarisation will be large and the temperature small; it follows then that  $\frac{L^2}{T} \left( \langle \bar{\mathbf{E}}^2 \rangle - \langle \bar{\mathbf{E}} \rangle^2 \right)$  grows large.

### 6.5.1. Correlations

In studying correlations across this BKT transition we are faced with the obvious difficulty that the system below the transition is extremely highly correlated; the Bragg peaks displayed in the correlations in the previous section persist here and lower-intensity fluctuations, such as those seen in Sec. 6.2, are invisible on the same scale. Once we move into the second-order melting transition we do see a qualitative change in the correlations, however.

#### $S^{\alpha\beta}(\mathbf{Q})$ tensors

Here I begin below the high- $u$  BKT transition, at  $T = 0.15$ ,  $u = 0.5$ . As expected, in this phase we reproduce the correlations from the previous section; the system is still in the insulating solid phase. For example,  $S_{\text{total}}^{\alpha\beta}(\mathbf{Q})$  is dominated by the longitudinal component, as shown in Fig. 6.46:

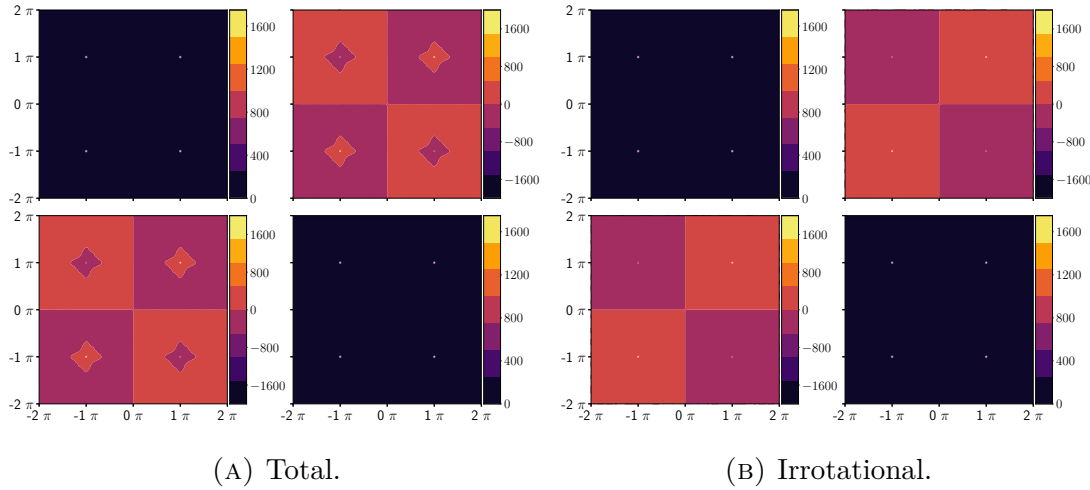


FIGURE 6.46.: ( $T = 0.150$  ;  $u = 0.500$ ). Correlation tensors  $S_{\text{total}}^{\alpha\beta}$  and  $S_{\text{irrot}}^{\alpha\beta}$ , respectively, in the insulating solid phase. As in Sec. 6.4, the correlations consist of Bragg peaks at the Brillouin zone corners consistent with the ordered charge crystal.

At this high a value of the core-energy the peaks are so sharp that they are hard to see in the contour plots, and have intensities of  $O(10^3)$ .

It is also worth explaining the origin of the diamond-shaped zone around the peaks in  $S_{\text{total}}^{xy}$ : essentially these are an artifact of the contour plots, where a very small positive number is assigned a different colour than a very small negative number. The irrotational component has a positive peak of intensity  $O(10^3)$  surrounded by low-intensity ( $O(10^{-3})$ ) positive correlations in the top-right and bottom-left quadrants of  $S^{xy}$ , where  $\text{sgn}(q_x) = \text{sgn}(q_y)$ , and a negative peak of

## 6. Results for the 2D grand canonical Coulomb gas

intensity  $O(10^3)$  small negative correlations where  $\text{sgn}(q_x) = -\text{sgn}(q_y)$ . By contrast, the rotational component features no peaks at all (as we expect from a freely-fluctuating field) but has a diffuse zone of slightly negative correlations where  $\text{sgn}(q_x) = \text{sgn}(q_y)$  and a diffuse zone of slightly positive correlations where  $\text{sgn}(q_x) = -\text{sgn}(q_y)$ . The sum of the two gives rise to the shape difference between the total and irrotational correlation tensors, but the overall difference in absolute terms is negligible.

As alluded to above, the overall correlation plots do not qualitatively change across the BKT transition; Fig. 6.47 shows the correlations in the middle of the conducting solid phase:

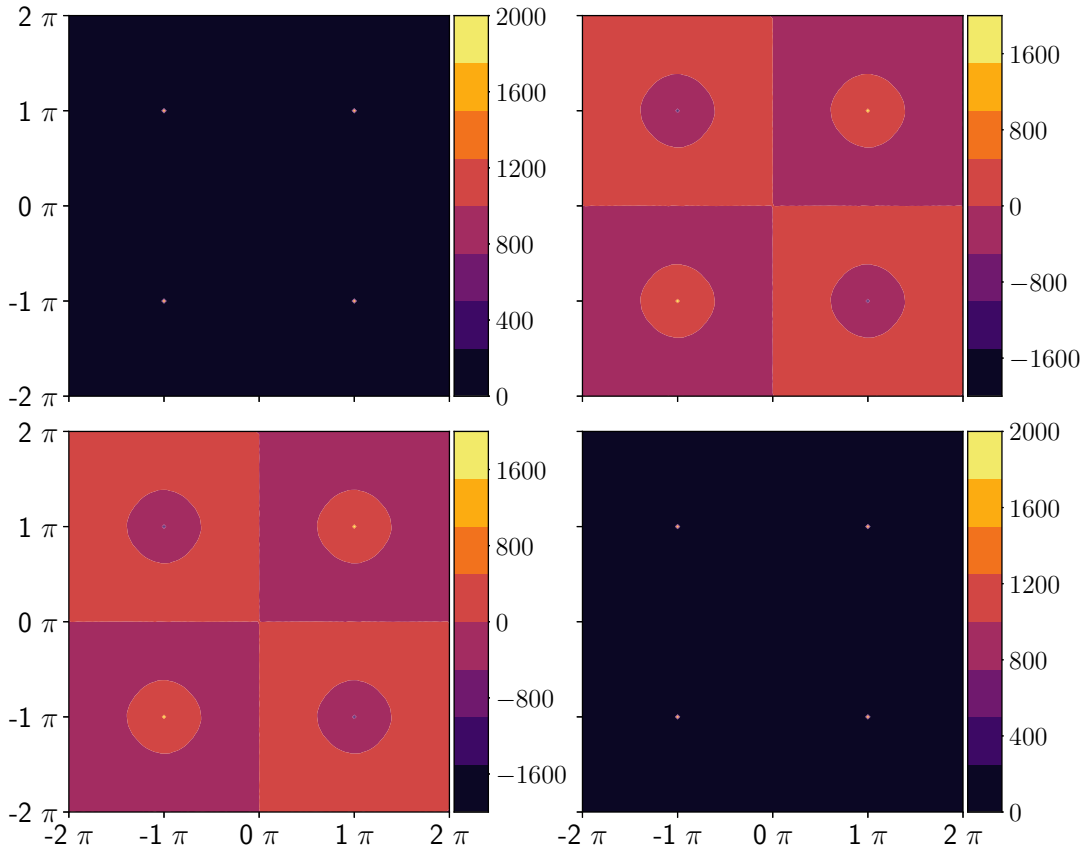


FIGURE 6.47.: ( $T = 0.200$  ;  $u = 0.500$ ).  $S_{\text{total}}^{\alpha\beta}$  in the conducting solid phase. For reference, the value of the  $\mathbf{q} = \mathbf{0}$  point here is around 0.75 – significantly higher than its value in the insulating phase, but still several orders of magnitude smaller than the peaks at the Brillouin zone corners.

The correlations at the melting transition are also virtually identical, with charge ordering still dominating the correlation tensor, as shown in Fig. 6.48.

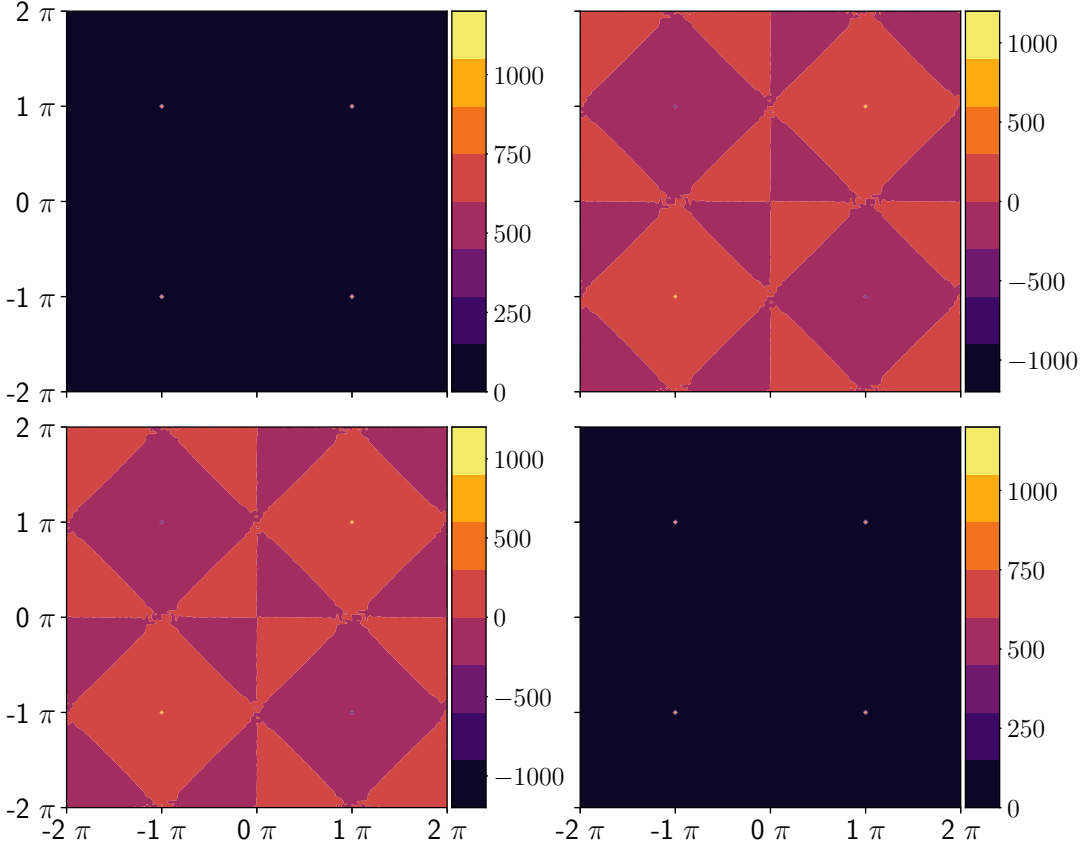


FIGURE 6.48.: ( $T = 0.220$  ;  $u = 0.500$ ), the melting transition temperature.  $S_{\text{total}}^{\alpha\beta}$ . The peaks arising from the longitudinal component are now significantly ( $\approx 50\%$ ) less intense than in Fig. 6.47, but still several orders of magnitude larger than the correlations of the transverse component, giving qualitatively similar overall correlations.

However, as we move into the conducting liquid phase, the Bragg peaks begin to diffuse outward once again, signalling the loss of strict all-in-all-out order in the system. Fig. 6.49 shows the increasing width of the peaks at  $(\pm\pi, \pm\pi)$  in  $S_{\text{total}}^{\alpha\beta}(\mathbf{q})$  as well as the decreasing intensity as the temperature increases and we move further into the conducting liquid phase.

In the liquid phase we also start to see more diffuse features around the peaks as they flatten, as in the diagonal components of Fig. 6.49b above. These come from the rotational component, which was previously invisible in plots of  $S_{\text{total}}^{\alpha\beta}(\mathbf{q})$ ; the irrotational component still displays Lorentzian peaks only.

As the temperature increases further we see the peaks in the irrotational component shifts from  $(\pm\pi, \pm\pi)$  to  $(\pm\pi, 0)$  in the  $xx$ -component and  $(0, \pm\pi)$  in the  $yy$ -component:

The comparison of (for example) the  $xx$ -component here with the  $xx$ -component

## 6. Results for the 2D grand canonical Coulomb gas

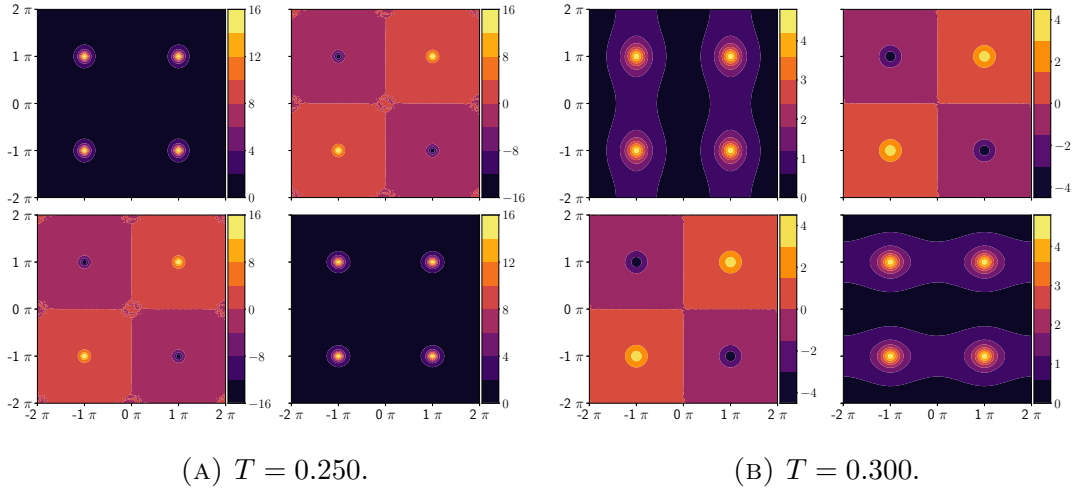


FIGURE 6.49.: ( $T = 0.220, 0.300 ; u = 0.500$ ).  $S_{\text{total}}^{\alpha\beta}$ . We can now see the peaks have a finite width instead of being Bragg-like, signifying the breakdown of crystal ordering.

for  $T = 0.600, u = 0$  is instructive:

We can then identify two trends: firstly, the decreasing intensity of the peak, and secondly the change in the location of the peak.

I interpret the small, broad peak seen in the diagonal components of the tensor as a signature of the non-zero **core-energy**: we are once again in the conducting liquid phase, which corresponds to the paramagnetic phase of the **XY model**, and so we would not expect to see another phase transition under variation of the core-energy back down to zero. However, the non-zero core-energy does favour the creation of charges, and so we do expect to see a continuous change in the charge density as  $u$  increases. The small peak in the **longitudinal** correlations is the signature of this.

A propagation vector of  $\pi \mathbf{e}_\mu$  corresponds to antiferromagnetism in the  $\mu$  direction; these two peaks in the diagonal components could then be interpreted as representing some “leftover” charge order without the strict all-in-all-out constraint of the solid phase.

### $S^\perp(\mathbf{Q})$ functions

The perpendicular components follow the total scattering tensors in the same way as discussed above: we find a gradual broadening of the Bragg peaks which corresponds to the loss of order and the decreasing of the correlation length. As we move further and further into the liquid phase we see a qualitative change in the plots of  $S^\perp$  due to the intensity of the **longitudinal** component gradually

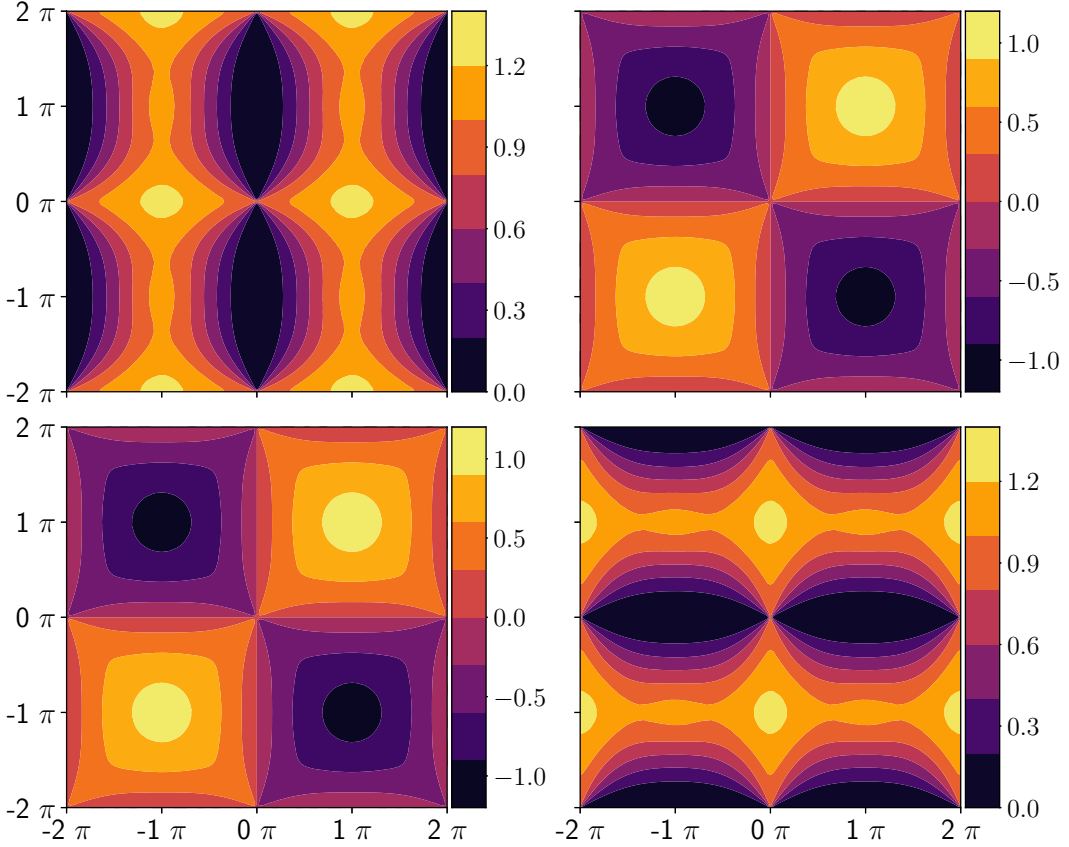


FIGURE 6.50.: ( $T = 0.600$  ;  $u = 0.500$ ). The tensor  $S_{\text{irrot}}^{\alpha\beta}(\mathbf{q})$ . We see diffuse features as in the zero- $u$  phase which are of nearly the same intensity as the peaks in the Brillouin zone corners which signal the high- $u$  phase.

relaxing to the same order of magnitude as the [transverse](#) component.

It is clear that the underlying structure is being revealed as the peaks diffuse out; in addition, at  $T = 0.6$ , we start to see the  $\mathbf{Q} = \mathbf{0}$  point appearing in the perpendicular component once again.

The final check I perform is to smoothly vary the [core-energy](#) back down to zero. For high temperature and high core-energy, we have a conducting liquid, but one where the creation of charges is energetically favourable; it is this favourability which gives us the peaks shown in Fig. 6.52. Upon decreasing the core-energy we would expect to see these peaks disappear and eventually be replaced by the correlations from, for example, Fig. 6.14, where the rotational features are in evidence but with broadened [pinch points](#) and high intensity at the origin.

## 6. Results for the 2D grand canonical Coulomb gas

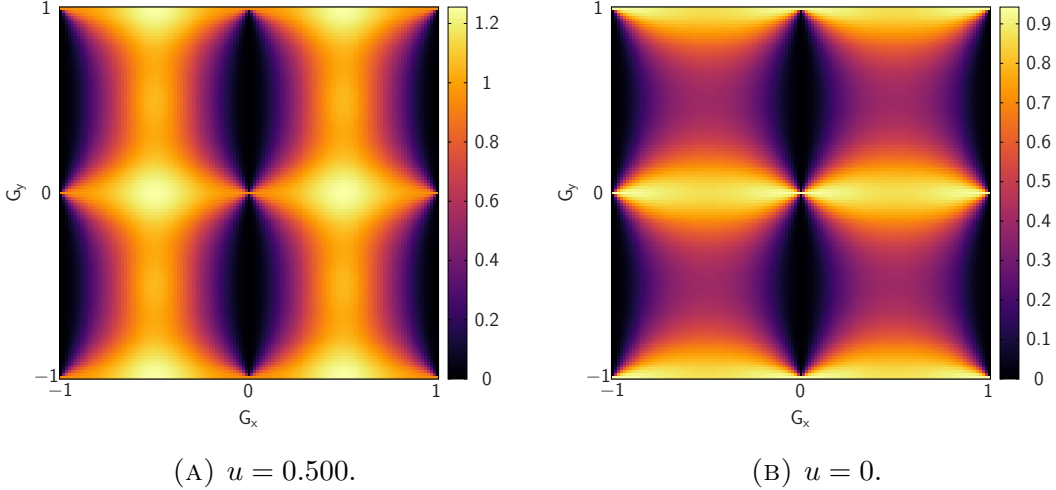


FIGURE 6.51.: ( $T = 0.600$  ;  $u = 0.500, 0.000$ ).  $S_{\text{irrot}}^{xx}$ . The diffuse features are qualitatively the same and have similar magnitudes, for example at  $\mathbf{q} = \mathbf{0}$ ; the only qualitative differences being the peak at  $(\pm\pi, 0)$  and a smaller, even less visible region of high intensity at  $(\pm\pi, \pm\pi)$ .

### 6.5.2. Lorentzian fits

I also fit the peaks in the field correlations to Lorentzians, with the ansatz identical to that given in Eq. 6.32.

Since these fits are to a Lorentzian ansatz, they do not adequately represent the correlations in the insulating or conducting solid phases; once we enter the liquid phase, at  $T \approx 0.25$ , it becomes physically reasonable to fit to a Lorentzian. I choose the peak at  $(3\pi, 5\pi)$  in  $S_{\text{total}}^{\perp}(\mathbf{Q})$  to fit to here, since it is the most prominent peak in the function. Fig. 6.53 shows examples of a cut across the  $(3\pi, 5\pi)$  peak in  $Q_y$ , with simulated data shown with blue circles and fitted data shown with joined red circles:

We can see the broadening of the peak as the temperature increases, with a concomitant reduction in the peak height  $\chi$ . In order to make this more quantitative, however, it is useful to start by inspecting the peaks on the same axis. Fig. 6.54 shows us the broadening of the peak more explicitly: The peak at  $T = 0.25$  is not shown above since it makes the higher-temperature lines impossible to distinguish. Nonetheless we see the trend: at  $T = 0.6$ , the peak is only twice the intensity of the background, and it is for this reason that we can see more and more detail in the  $S_{\text{total}}^{\perp}(\mathbf{Q})$  plots.

Next, I extract the fitted parameter  $\kappa$  as a function of temperature and fit it to a linear function; Fig. 6.55 shows the result. Once again we note that  $\kappa$  can be

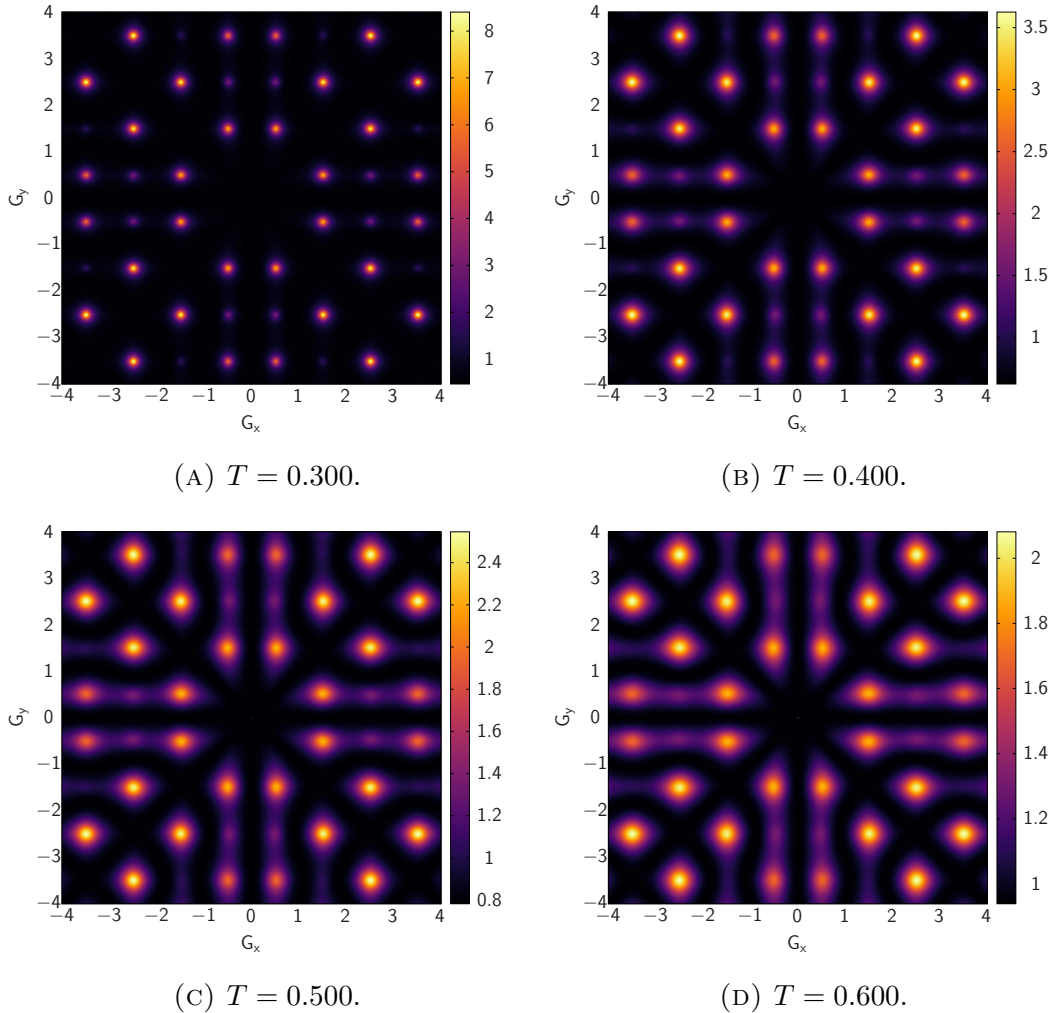


FIGURE 6.52.: ( $T = 0.300, 0.400, 0.500, 0.600$  ;  $u = 0.500$ ). Four examples of  $S_{\text{total}}^{\perp}(\mathbf{Q})$  in the conducting liquid phase as the temperature increases. We see the Bragg peaks which characterise the solid phase becoming more diffuse and Lorentzian and the intensities decreasing with temperature.

## 6. Results for the 2D grand canonical Coulomb gas

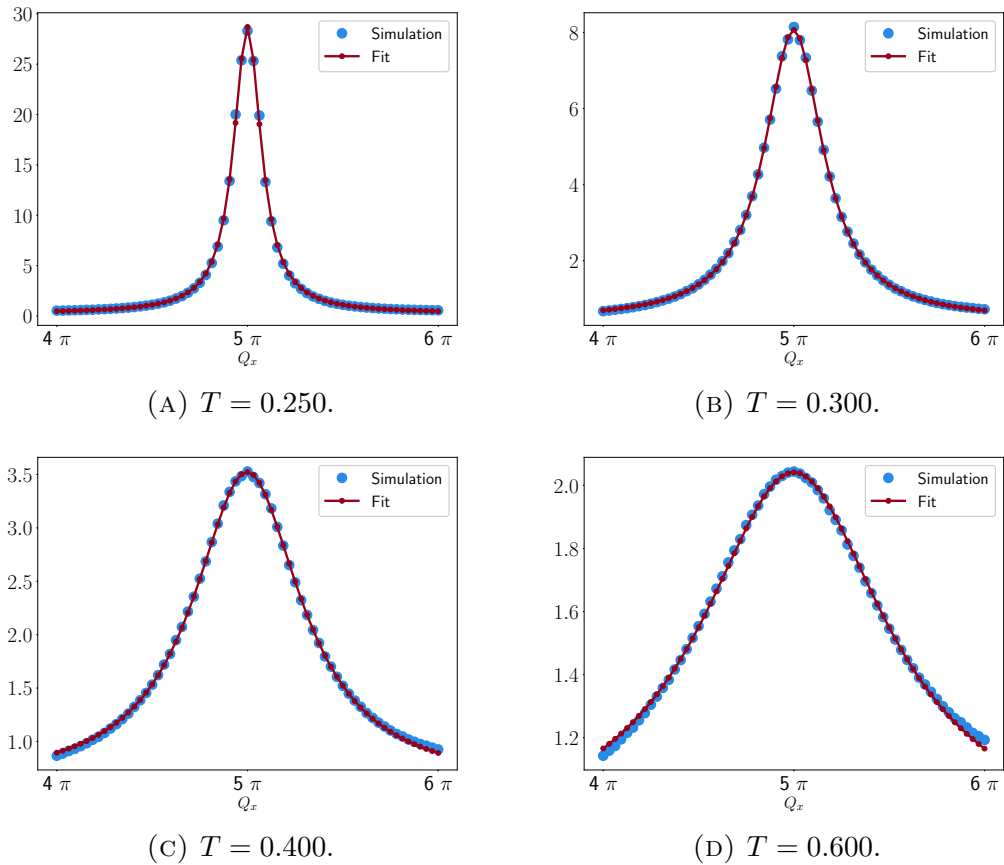


FIGURE 6.53.: ( $T = 0.250, 0.300, 0.400, 0.600$ ;  $u = 0.500$ ). Four examples of the peak at  $(3\pi, 5\pi)$  in  $S_{\text{total}}^{\perp}(\mathbf{Q})$ . We see the Lorentzians broadening and the peak height decreasing as the temperature increases.

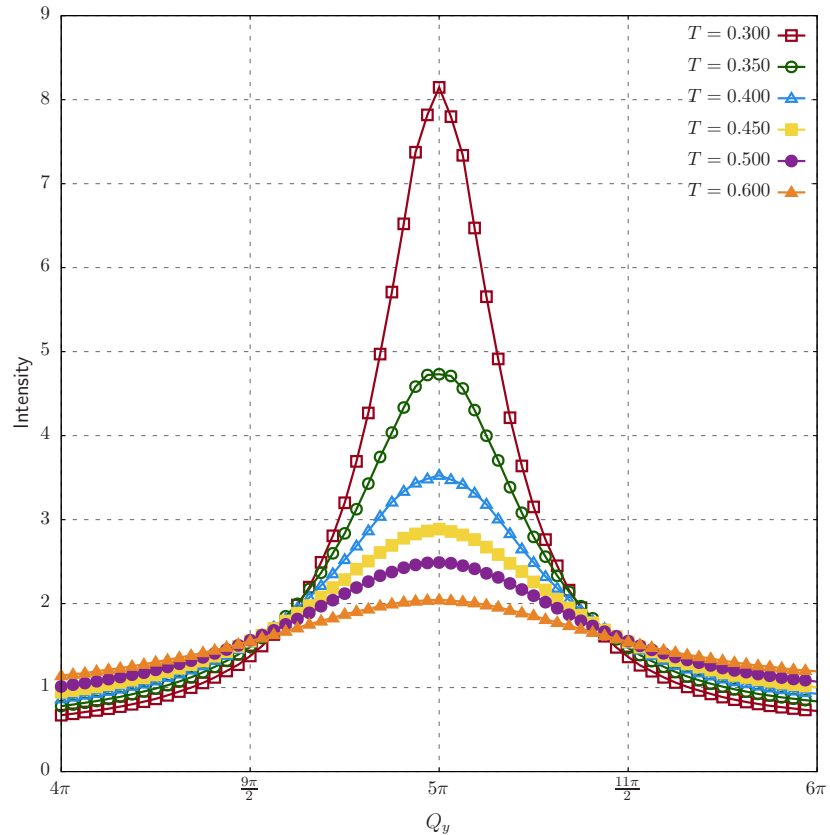


FIGURE 6.54.: The Lorentzian peak at  $(3\pi, 5\pi)$  across  $4\pi \leq Q_y \leq 6\pi$  for a range of temperatures, showing that as the temperature increases so does the width of the peak.

## 6. Results for the 2D grand canonical Coulomb gas

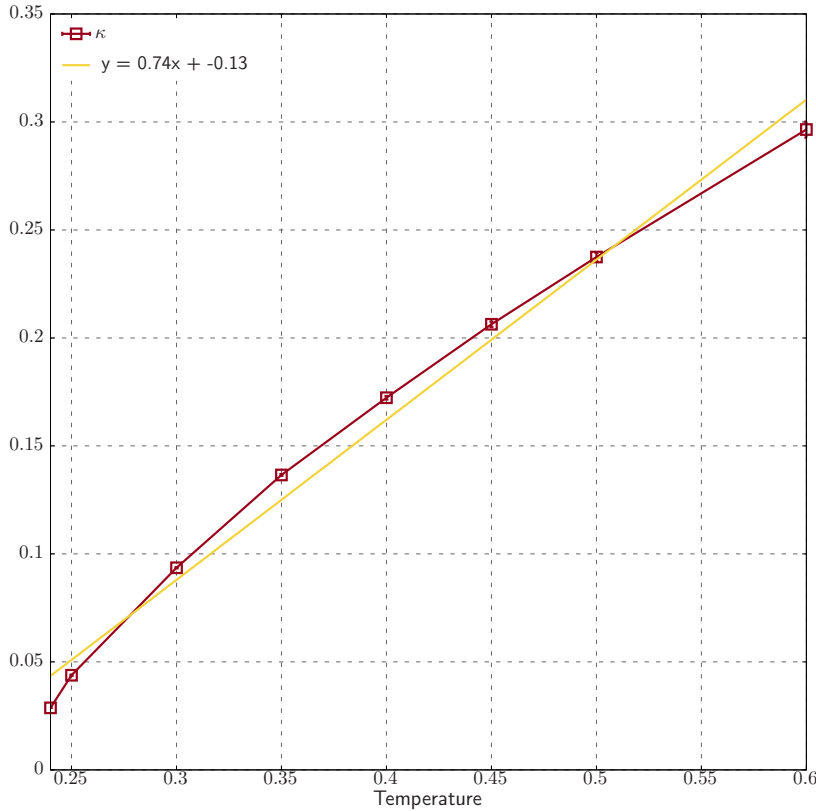


FIGURE 6.55.: Linear fit of  $\kappa(T)$ , the temperature-dependent peak width. The fitted width is fairly well approximated by a linear function, as expected due to the critical exponent for the 2D Ising transition.

interpreted as an inverse correlation length: hence, we see the correlation length decreasing as the temperature increases. In this case,  $\kappa$  does correspond to a field-field correlation length, rather than a charge-charge correlation length, since we fit to the perpendicular component of the total correlations.

We note that this result is consistent with the critical exponent for the 2D Ising transition, which is 1. Attempts to fit the data to a modified power law exponent were unsuccessful.

### 6.5.3. Decreasing core-energy

The last thing I check is that upon decreasing the [core-energy](#) back towards zero we recover the correlations of the conducting liquid phase from Sec. 6.2; four representative examples are shown in Fig. 6.56. It is important to note that there is no phase transition here: the change in the correlations is continuous as

### 6.5. High core-energy BKT and second-order transitions

the core-energy decreases. We expect to see the peaks at  $(\pi, \pi)$  diffusing out and being replaced by the flatter correlations of the high-temperature, zero core-energy phase, and this is indeed what I see.

The final plot here, Fig. 6.56d seems to be almost flat, and is dominated by the higher-intensity point at  $\mathbf{Q} = \mathbf{0}$ ; by inspecting the full tensor  $S^{\alpha\beta}(\mathbf{q})$  we can check in more detail. Fig. 6.57 shows the correlations for  $T = 0.6$  with  $u = 0$  and  $0.1$  respectively. We see from the intensities that both plots are extremely flat, with a difference of only a few percent between the highest and lowest intensity points in the Brillouin zone. The non-zero core-energy does have a clear effect on the correlation tensor, however: the remnant of the peaks at  $(\pm\pi, \pm\pi)$  from the high core-energy phase means that the region of slightly lower intensity at  $u = 0$  becomes a region of very slightly higher intensity at  $u = 0.1$ .

## 6. Results for the 2D grand canonical Coulomb gas

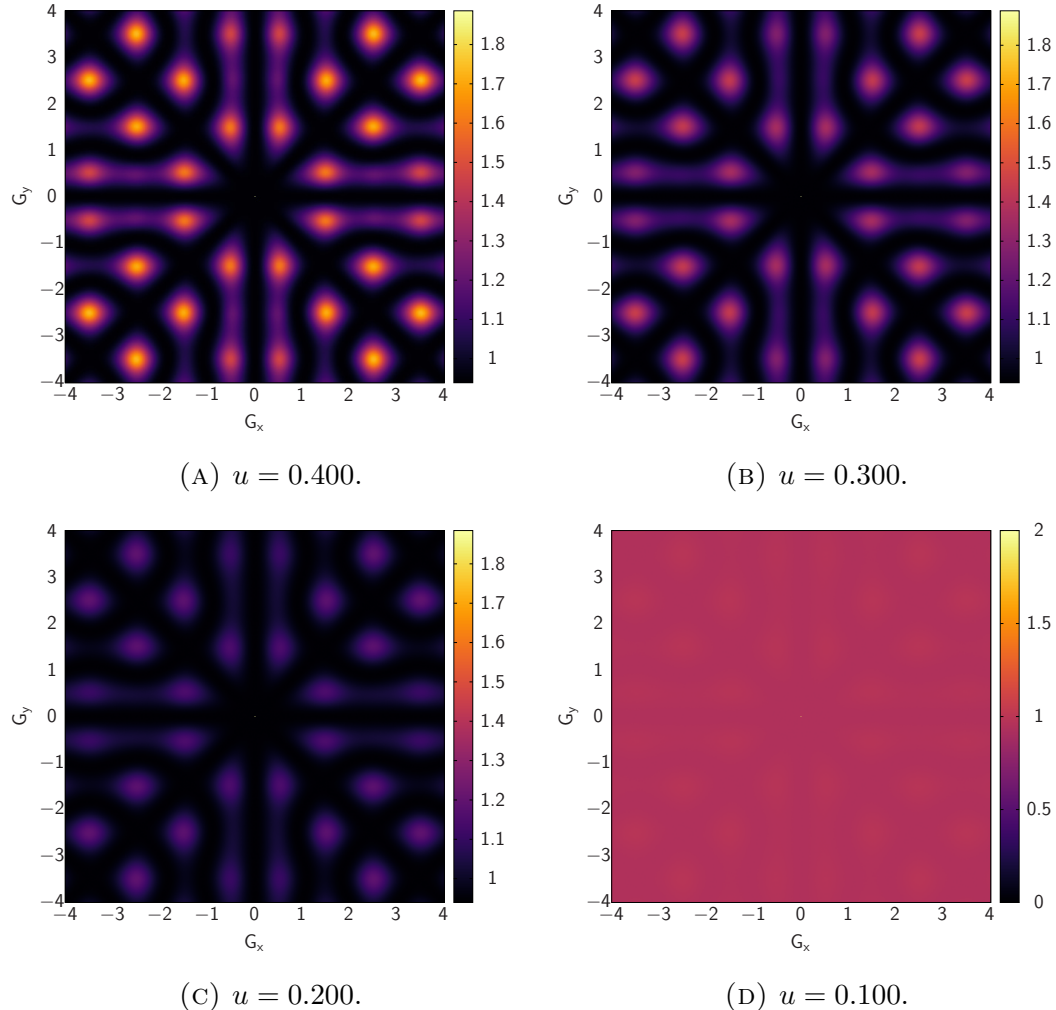


FIGURE 6.56.: ( $T = 0.600$  ;  $u = 0.400, 0.300, 0.200, 0.100$ ).  $S_{\text{total}}^{\perp}(\mathbf{Q})$  in the conducting liquid phase as the core-energy decreases, moving back towards the flatter correlations of the zero core-energy phase. At  $u = 0.1$  the function is almost completely flat; the corresponding plot has its lower bound explicitly set to zero since otherwise the function appears black everywhere.

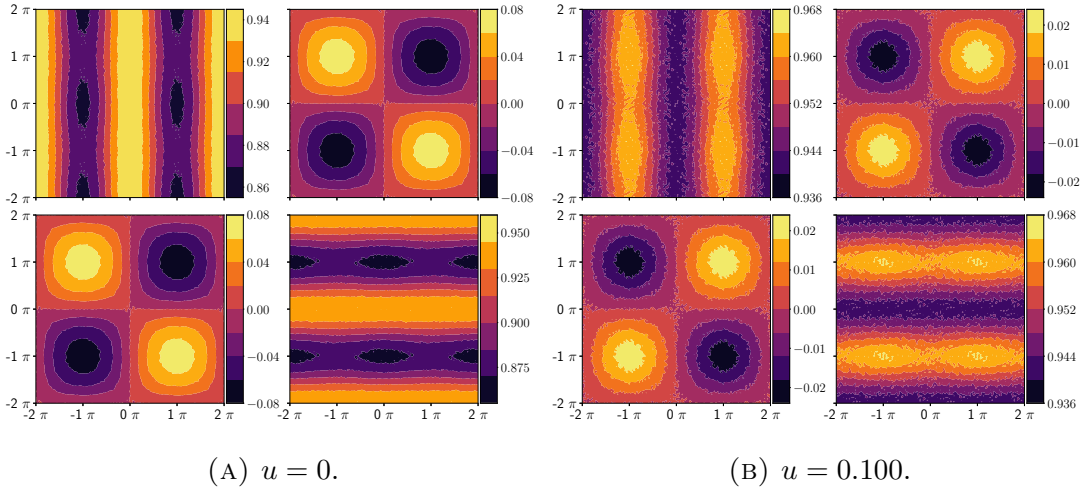


FIGURE 6.57.: ( $T = 0.600$  ;  $u = 0.000, 0.100$ ).  $S_{\text{total}}^{\alpha\beta}(\mathbf{q})$ . In both cases the diagonal components are very flat due to the high temperature, but the finite core energy has a qualitative effect: the (slightly) higher intensity band becomes the (slightly) lower intensity band and vice versa.

## 6.6. Tricritical point

Lastly there is a tricritical point in the phase diagram shown by the large red dot in Fig. 6.1, at approximately  $T = 0.15$  and  $u = 0.392$ . I have also attempted simulations around this point in order to characterise the relevant parameters and correlations. In practice it is quite hard to extract meaningful data: the order of the solid phase tends to dominate the correlations and there is the additional difficulty of the finite size system affecting the location of the critical point; further work with more simulations for multiple lattice sizes could possibly help to resolve the tricritical point in better detail. Nonetheless, there are a few combinations of parameters which suggest phase coexistence, as shown below.

For example, at  $T = 0.15$  ;  $u = 0.380$ , we see correlations which look very much like those of the high core-energy conducting liquid phase, but with much lower intensities in the correlations and a significantly lower average charge density of  $\approx 0.25$ . Additionally there is a non-zero winding susceptibility of  $\approx 0.11$ , which would ordinarily be a signature of the [BKT transition](#) at low [core-energy](#). The harmonic mode is also small but non-zero, suggesting a conducting phase, but without the overall correlations of the high-temperature liquid phase. The correlation tensor and neutron scattering plots are shown in Figs. 6.58 and 6.59.

The neutron scattering function again looks very similar to that of the system in the charge crystal phase, but with more rounded peaks and lower intensities.

## 6. Results for the 2D grand canonical Coulomb gas

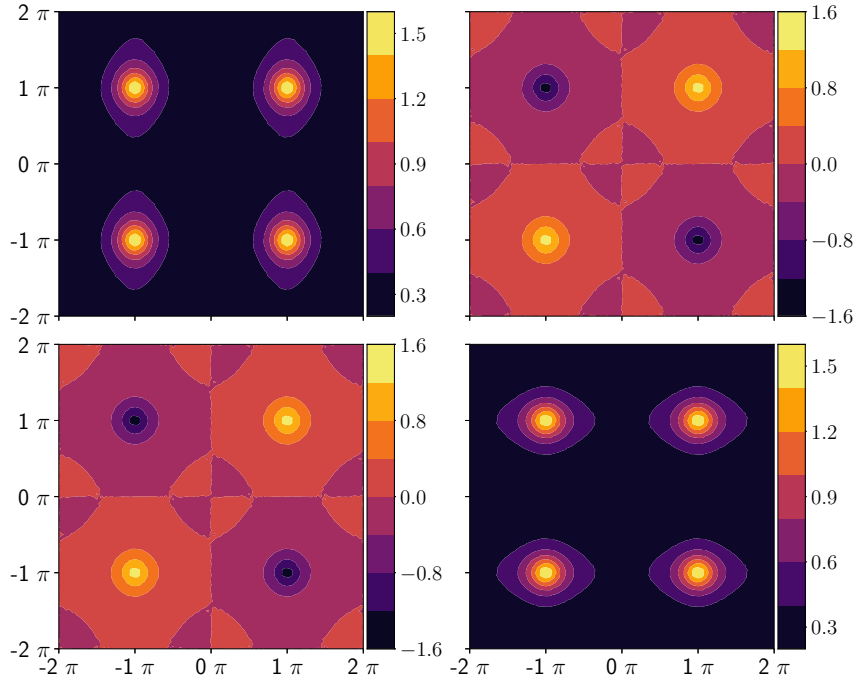


FIGURE 6.58.: ( $T = 0.150$  ;  $u = 0.380$ ).  $S_{\text{total}}^{\alpha\beta}(\mathbf{q})$ . The peaks at  $(\pm\pi, \pm\pi)$  resemble those of the crystal phase, but the intensities here are much lower, as is the charge density.

A similar picture emerges at  $T = 0.16, u = 0.360$ : Fig. 6.61 shows a similar neutron scattering function to Fig. 6.59 but with lower intensities again, presumably due to the lower core-energy. The total correlation tensor (Fig. 6.60) seems to show the diffuse correlations of the low core-energy liquid state, for example in the bands across  $q_y = 0$  in the  $xx$  component, but with broad Lorentzian peaks centred on  $(\pm\pi, \pm\pi)$  as in the high core-energy phases.

However, these features have too low an intensity to show up in the corresponding neutron scattering function, as shown in Fig. 6.61.

At  $T = 0.15$  ;  $u = 0.41$ , shown in Figs. 6.62 and 6.63, we find a charge density of 70%, rapidly approaching the solid phase, and a slightly smaller but still finite winding susceptibility of around 0.09. This is slightly above the transition value of the [core-energy](#)  $u_c$ . The correlations here, however, are qualitatively identical to those of the solid phase, with high-intensity Bragg peaks.

Overall it proves quite difficult to present clear evidence of phase coexistence from the correlations due to the ordering in the solid phase, but there are some slight differences from the results presented in the previous section which do suggest the presence of the liquid phase.

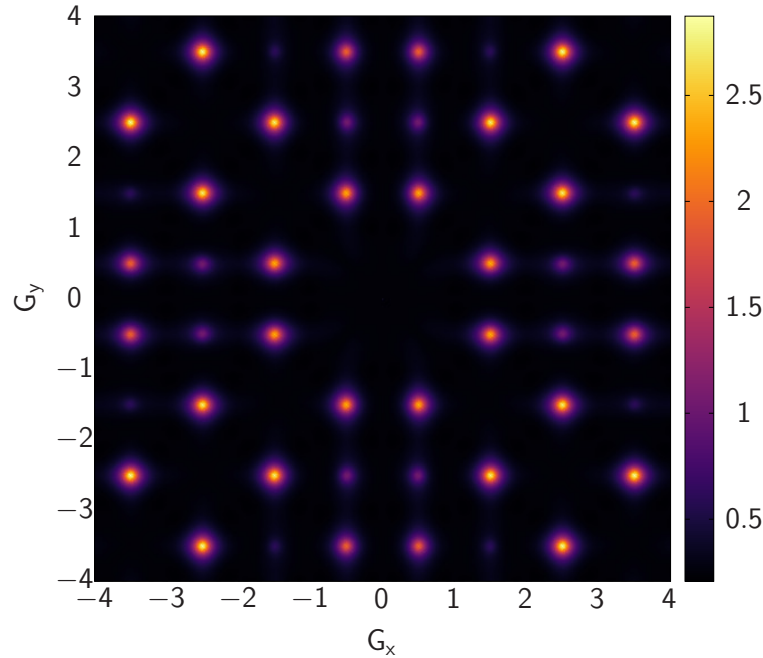


FIGURE 6.59.: ( $T = 0.150$  ;  $u = 0.380$ ).  $S_{\text{total}}^{\perp}(\mathbf{Q})$ . Again, we see peaks qualitatively similar to those of the charge crystal phase, but more rounded and with lower intensity.

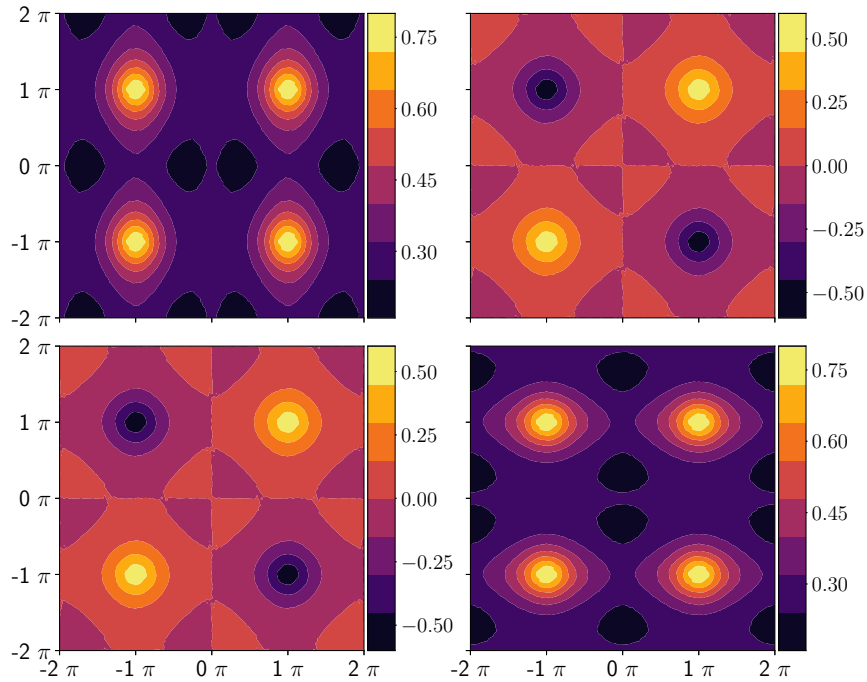


FIGURE 6.60.: ( $T = 0.160$  ;  $u = 0.360$ ).  $S_{\text{total}}^{\alpha\beta}(\mathbf{q})$ . The diffuse correlations of the transverse-dominated, low- $u$  phases can be seen in dark purple with the peaks of the high- $u$  phase superimposed.

## 6. Results for the 2D grand canonical Coulomb gas

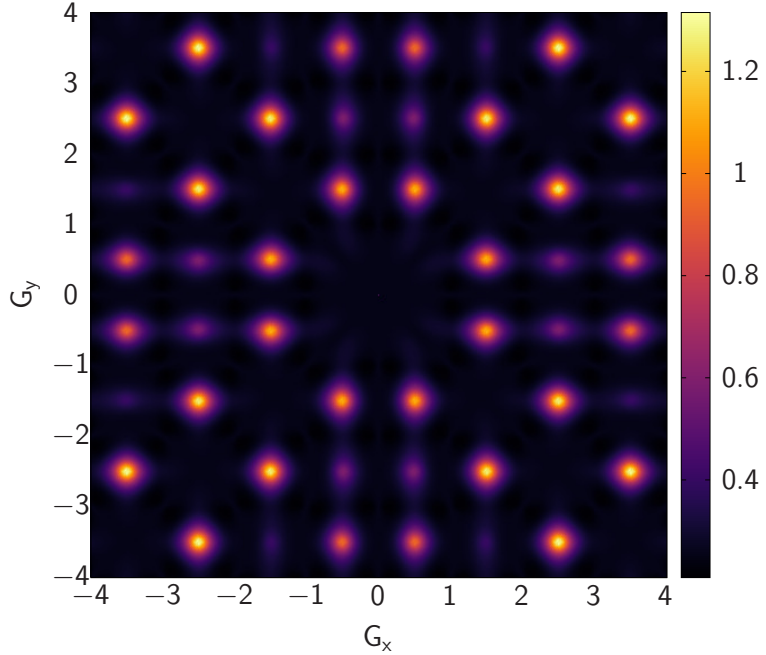


FIGURE 6.61.: ( $T = 0.160$  ;  $u = 0.360$ ).  $S_{\text{total}}^{\perp}(\mathbf{Q})$ . The lower-intensity diffuse features seen in the  $S^{\alpha\beta}(\mathbf{q})$  tensor do not survive here; the broad peaks of the high- $u$  phases dominate the neutron scattering function.

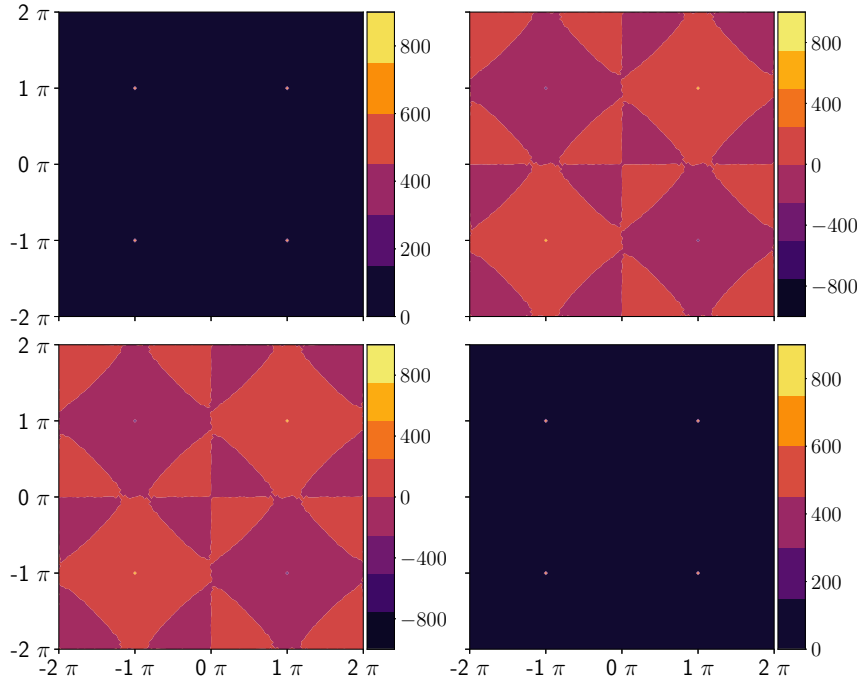


FIGURE 6.62.: ( $T = 0.150$  ;  $u = 0.410$ ).  $S_{\text{total}}^{\alpha\beta}(\mathbf{q})$ . These parameters put us very close to the critical point but in the solid phase, and the correlations of the solid phase are all that we see in the tensor.

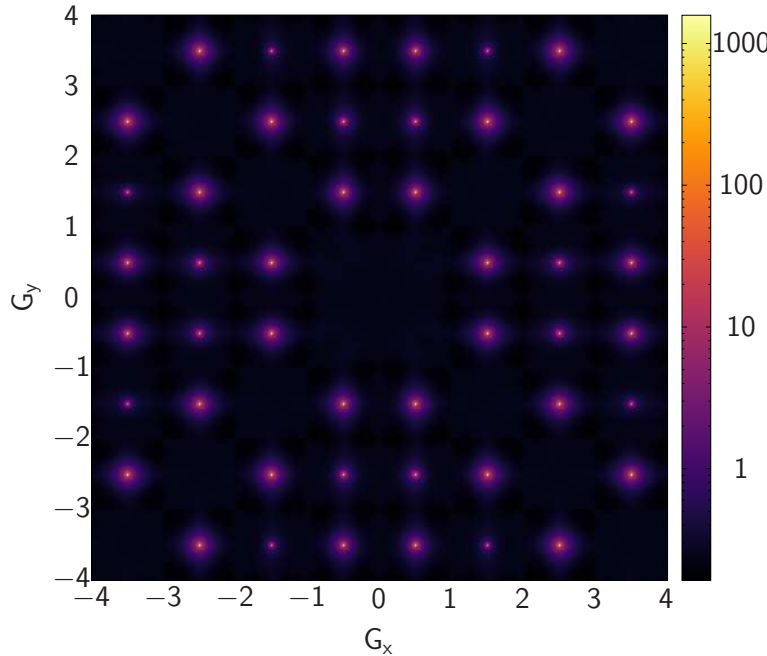


FIGURE 6.63.: ( $T = 0.150$  ;  $u = 0.410$ ).  $S_{\text{total}}^{\perp}(\mathbf{Q})$ , again showing only the correlations from the solid phase. A log scale is used to make the peaks visible against the background.

## 6.7. Discussion and conclusions

Finally, then, we characterise the phase transitions of the 2D grand canonical Coulomb gas with special regard to the Helmholtz-Hodge-decomposed field correlations in each phase.

### 6.7.1. BKT transition at zero core-energy

In the low-temperature, low-core-energy phase we find an insulating gas of tightly bound charge pairs, as we expect. The correlations are dominated by the transverse component, corresponding to a Coulomb phase as described by Henley. I plot the representation quadric of the total scattering tensor and show that it changes qualitatively from a narrow ellipse in the low-temperature phase towards a circle at high temperature, consistent with the result of Bramwell for spin ice [89]. We also see, in the simulated neutron scattering plots in Fig. 6.64, the sharp pinch points associated with dipolar correlations. At low temperature these have zero intensity at the zone centres, as shown in Fig. 6.64a due to the well-known singularity in the transverse component, which follows from the fact that  $\mathbf{q} \cdot \mathbf{E}(\mathbf{q}) = 0$  is non-analytic at the zone centre; but as the temperature increases so does the

## 6. Results for the 2D grand canonical Coulomb gas

intensity at the zone centre, and we see a pinch point of finite width in Fig. 6.64b.

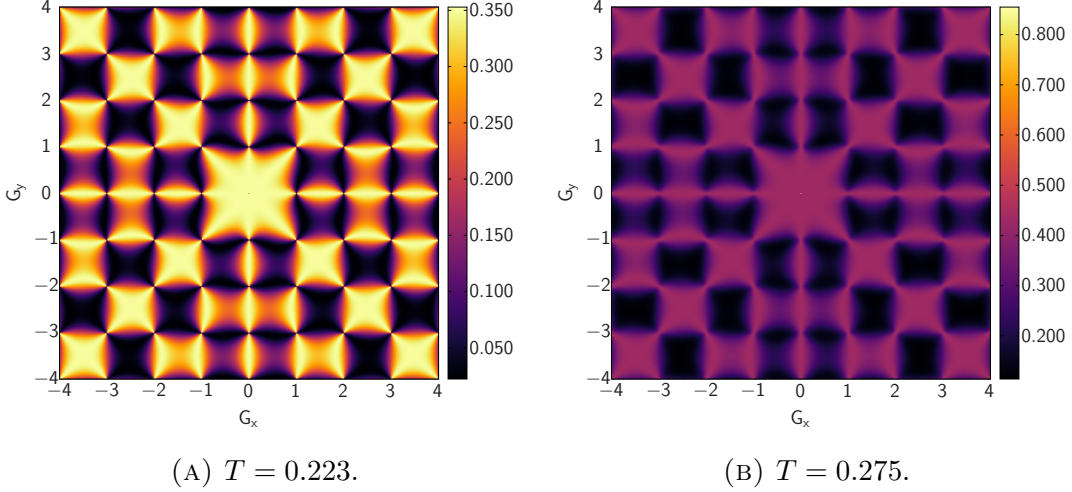


FIGURE 6.64.: Simulated neutron scattering plots of the Coulomb gas across the BKT transition, showing the increased intensity at  $\mathbf{Q} = \mathbf{0}$  and the rounding of the pinch points.

This width also increases with temperature, which can be shown to be due to the increasing intensity of the irrotational component. It is important to note the [pinch points](#) do not arise solely from the scattering tensors of the individual components; rather, the sum of the two components combine with the specific form factor which arises in a neutron scattering experiment to produce an overall pinch point, whose width varies with temperature.

As we move through the [BKT transition](#) by increasing the temperature at constant [core-energy](#) we find that in addition to the winding susceptibility used by Faulkner [31, 32] as a signature of the BKT transition, we can also see the harmonic mode of the field developing in the  $\mathbf{q} = \mathbf{0}$  point of the correlation function. The high-temperature correlations tend slowly towards those of a paramagnet via a gradual flattening out, but retain the diffuse features of the low-temperature phase with broadened pinch points and a higher background intensity.

I also fit the trace of the  $S_{\text{irrot}}^{\alpha\beta}(\mathbf{q})$  tensor to a Lorentzian, and use this to reproduce the simulated neutron scattering plots analytically; once this is done it is possible to extract a pair of effective correlation lengths for the [grand canonical GLCG](#) across the BKT transition, representing the shortest and longest correlation lengths in the system. The results show that the shorter correlation length remains below one lattice spacing, corresponding to bound pairs. The longer correlation length appears around the transition temperature and increases to several

lattice spacings before decreasing and the disappearing; we interpret this as corresponding to the unbinding of charge pairs, followed by a decrease as the charge density increases and screening becomes more important.

### 6.7.2. First-order transition

On varying the [core-energy](#) instead of the temperature, we pass through a first-order transition from the insulating gas to an insulating solid at the critical value  $u_c = \pi/8$ . This transition is obviously well characterised by the average charge density across the transition, but is also accompanied by a qualitative change in the field correlations, as shown in Figs. 6.65a below the transition and 6.65b above it.

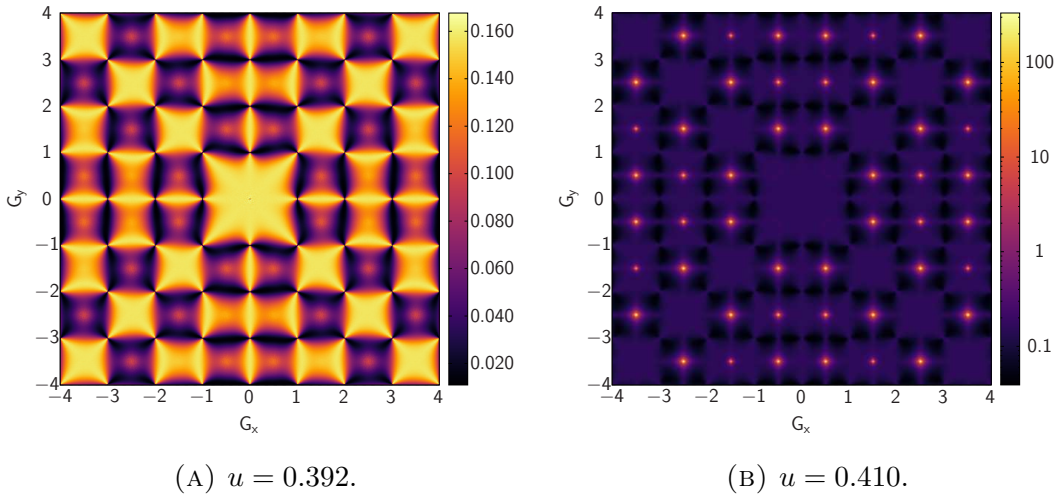


FIGURE 6.65.: Simulated neutron scattering plots of the Coulomb gas across the first-order transition, showing the emergence of sharp peaks indicating the onset of all-in-all-out order. The right-hand function is plotted to a log scale in order to make the peaks more visible.

The rotational correlations of the insulating gas phase are quickly rendered invisible: although there is still an auxiliary rotational field, the system in the insulating solid phase is dominated by all-in, all-out order in the irrotational component.

I show that this order can be compared to a kind of “antiferromagnetic” order with a propagation vector of  $\mathbf{k}_a = \pm(\pi, \pi)$ , which explains the missing Bragg peaks in the simulated neutron scattering plots. I also show that the “opposite” propagation vector  $\mathbf{k}_F = \pm(-\pi, \pi)$ , which is seen in the component of the correlations “opposite” to that of the neutron scattering plot, corresponds to the

## 6. Results for the 2D grand canonical Coulomb gas

staggered antiferroelectric order which is the [F model](#) ground state, and note that the correlations of this state can be seen in an [artificial spin ice](#) experiment.

### 6.7.3. High core-energy BKT and melting transitions

Upon increasing the temperature in the high [core-energy](#) insulating solid phase, we find another [BKT transition](#) to a conducting solid followed closely by a second-order melting transition. Once again I find that the  $\mathbf{q} = \mathbf{0}$  point of the correlation function is a useful indicator of these two transitions, corresponding as it does to the harmonic mode of the field.

I find that the intensity of this point is low in the insulating phase, increases quickly in the BKT conducting solid phase, and then saturates in the conducting liquid phase. I also show that the decreasing charge density is a good indicator of the transitions; a charge density of  $\approx 1$  in the insulating solid phase begins to decrease across the BKT transition and reaches an equilibrium value of 0.6 at high temperatures.

The field correlations in these phases are characterised by the sharp Bragg peaks of the insulating solid phase diffusing as the strict all-in-all-out order is lost, as shown in Figs. [6.66a](#) and [6.66b](#); once again, I fit these peaks to Lorentzians and plot the resulting parameters. In particular I find that the width of the peak  $\kappa$ , which corresponds to an inverse correlation length, increases fairly linearly with temperature and therefore signifies the decreasing of the correlation length and the loss of long-range order.

I then tune the core-energy back to zero and show that the peaks smoothly disappear, to be replaced by the high-temperature phase with broad pinch points displayed in Sec. [6.2](#) above the BKT transition.

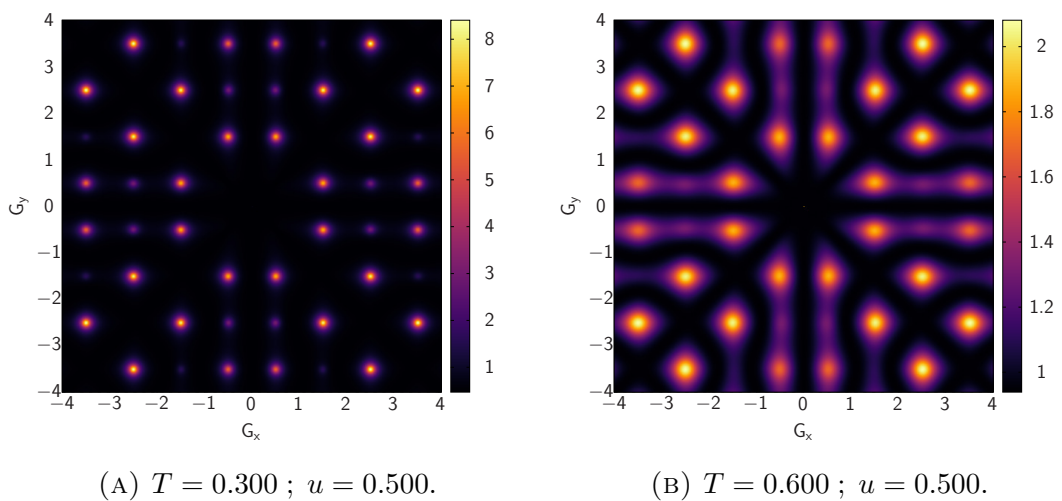


FIGURE 6.66.: Simulated neutron scattering plots of the Coulomb gas in the high core-energy conducting liquid phase. The sharp peaks of the insulating crystal phase become Lorentzian in shape with the Lorentzian width increasing linearly with temperature.



# 7. Results for the HXY model

In the previous chapter I simulated the 2d grand canonical generalised lattice Coulomb gas and characterised its phase diagram.

I have performed analogous simulations for the harmonic XY model discussed above in Sec. 4.1.5 in order to investigate its correlations.

## 7.1. Parameter choices

As previously mentioned, the energy scale of this problem goes with  $q^2/\epsilon$ ; we are in principle free to choose both. The previous chapter uses  $q = 1$  and  $\epsilon = 2\pi$  in order to reproduce exactly the transition parameters given by Lee and Teitel [44] and Gupta [45].

However, for the HXY model, it is natural to choose  $q = 2\pi$  and  $\epsilon = 1$ ; these parameters follow by construction due to the  $2\pi$  modular symmetry of the Hamiltonian. Therefore I will adopt the convention  $q = 2\pi, \epsilon = 1$  in this chapter; the overall effect is to multiply the temperatures by  $2\pi$ .

## 7.2. Specific heats, susceptibilities and effective electric permittivity

As described in Sec. 4.2, we expect the specific heat of the harmonic XY model to tail off and head towards zero at high temperature. My simulations across the BKT transition are consistent with this and with the result of Faulkner [32], as shown in Fig. 7.1.

We can define a winding susceptibility for the harmonic XY model in exactly the same way as Eq. 3.25, but replacing the permittivity with the effective HXY permittivity:

$$\chi_{\bar{\mathbf{E}}_w} = \beta \epsilon_{\text{eff}} L^2 \left( \langle \bar{\mathbf{E}}_w^2 \rangle - \langle \bar{\mathbf{E}}_w \rangle^2 \right) \quad (7.1)$$

where again I will use the notation  $\chi_w \equiv \chi_{\bar{\mathbf{E}}_w}$  for readability. Fig. 7.2 shows the winding susceptibility of the HXY model across the BKT transition.

## 7. Results for the HXY model

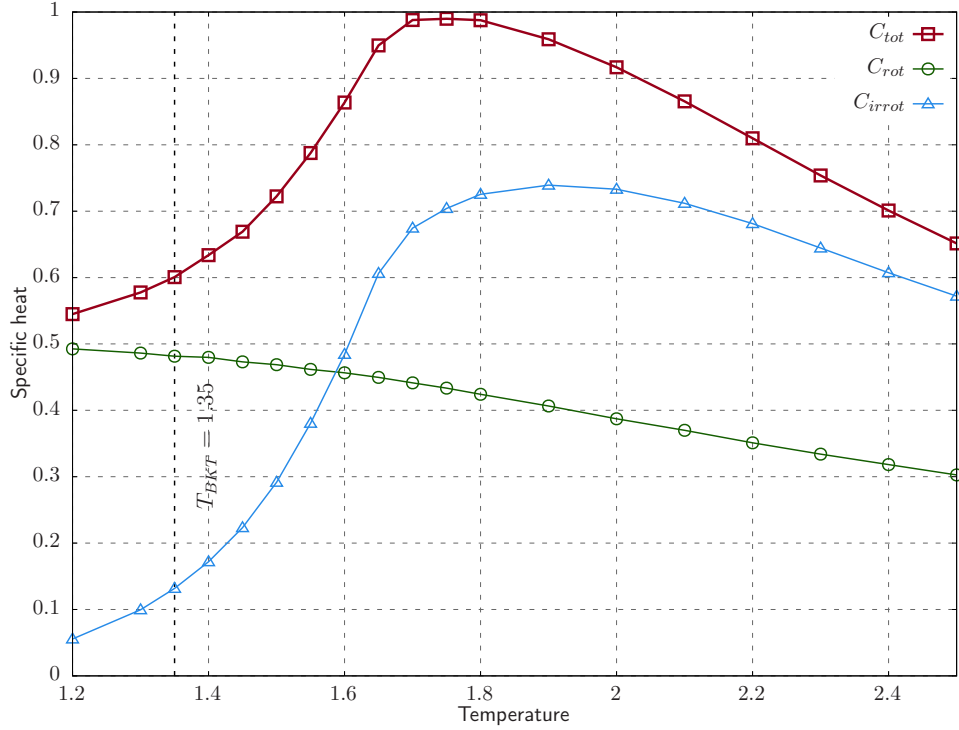


FIGURE 7.1.: The specific heats of the total and Helmholtz-decomposed components of the HXY model as a function of temperature.

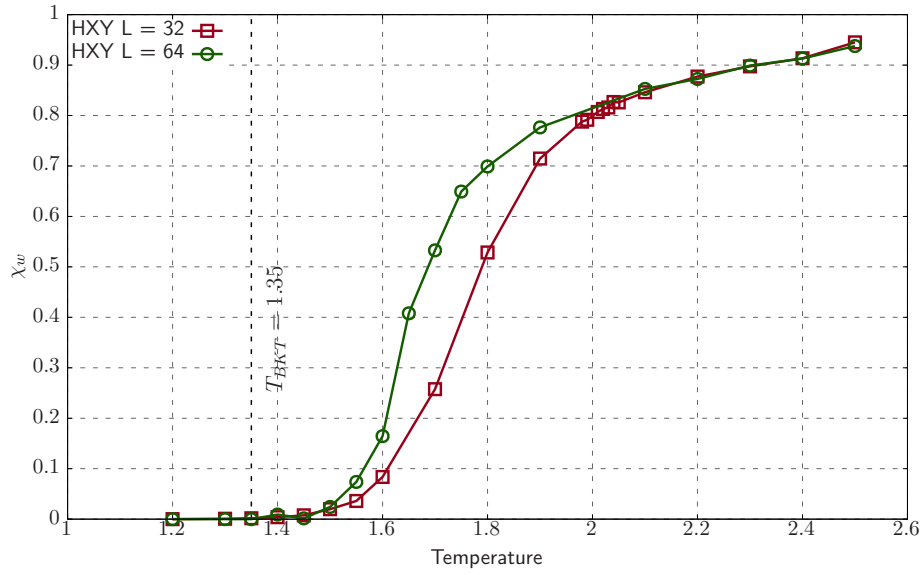


FIGURE 7.2.: The winding susceptibility  $\chi_w$  of the HXY model across the BKT transition, showing a qualitatively similar increase to that of the GLCG, but with a lower asymptotic value.

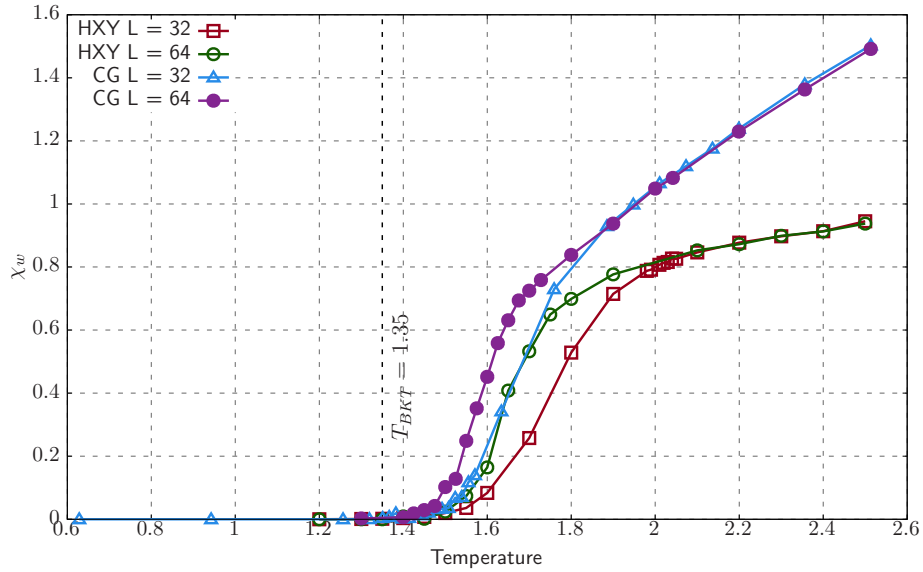


FIGURE 7.3.: Winding susceptibilities of the HXY model and Coulomb gas for  $L = 32$  and  $64$  showing that the HXY result is always smaller than the GLCG result for a given temperature and lattice size.

Finally we can compare the HXY winding susceptibility with that of the Coulomb gas and show that  $\chi_w^{\text{HXY}}(L, T) < \chi_w^{\text{CG}}(L, T)$  for a given system size and temperature, as discussed in Sec. 4.2. Fig. 7.3 shows that this is again the case.

### 7.3. Spin-spin correlations

I also calculate the spin-spin correlations using the expression

$$S_\theta^{\alpha\beta}(\mathbf{q}) = \langle \theta_\alpha(\mathbf{q})\theta_\beta(-\mathbf{q}) \rangle \quad (7.2)$$

with  $\boldsymbol{\theta}$  simply the spin direction at each lattice site: this is not the spin-difference field  $\Delta\boldsymbol{\theta}$ .

Fig. 7.4 shows correlations displaying truncated power law peaks, rather than the rotationally dominated ground state of the emergent electric field.

These peaks are difficult to see against the zero-intensity background unless a log scale is used, since they are extremely sharp and have intensity  $\approx 400$  at  $\mathbf{Q} = \mathbf{0}$  and exactly half that at every other zone centre, as explained above in Sec. 6.2. Hence, Fig. 7.4 corresponds to an essentially ferromagnetic ground state, as we would expect; the system is (quasi-)ordered with small spin-wave fluctuations.

As the temperature increases and we move towards the paramagnetic state we

## 7. Results for the HXY model

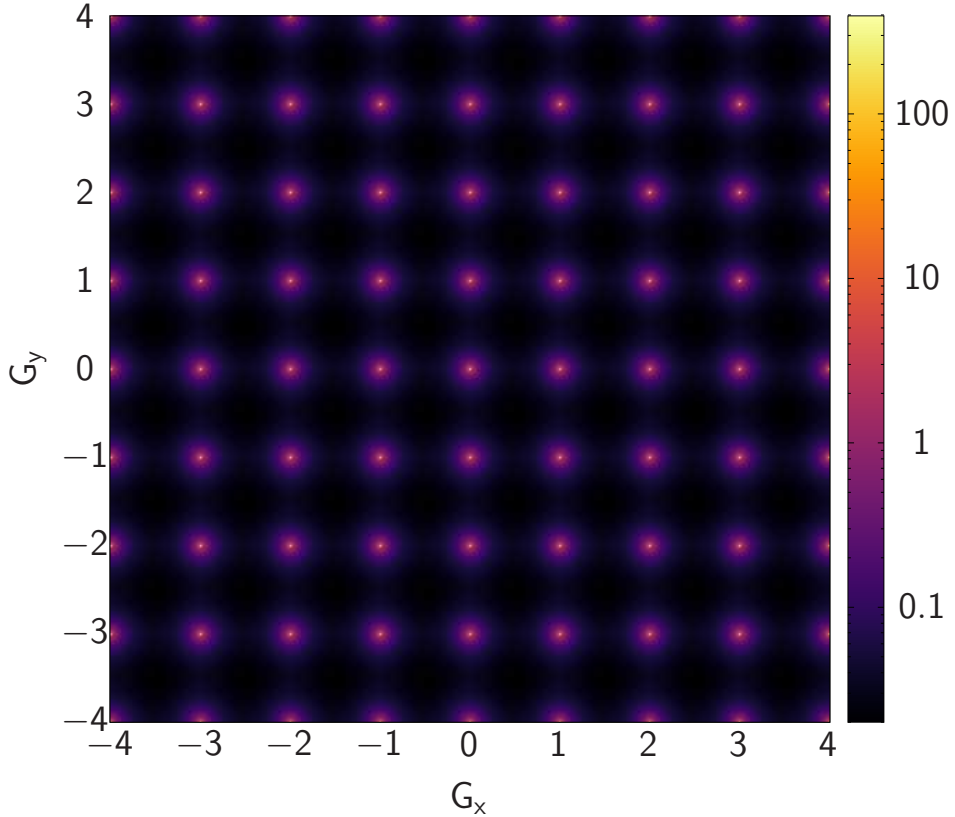


FIGURE 7.4.:  $S_\theta^\perp(\mathbf{q})$  at  $T = 1.300$ . A log scale is used in order to make the peaks visible against the background; the system is (quasi)-ordered at this low temperature.

see the same phenomenon as in Sec. 6.5: the peak broadens and therefore decreases in intensity. At  $T = 2.5$  the qualitative difference is evident, as shown in Fig. 7.5.

Again, as we expect given the finite-size scaling arguments for the XY model, the transition to a true paramagnet is very slow and we see some remaining order. Here the intensity of the  $\mathbf{Q} = \mathbf{0}$  point is only  $\approx 4$  and there are broader peaks around each zone centre, signifying the (incomplete) transition to a paramagnetic state.

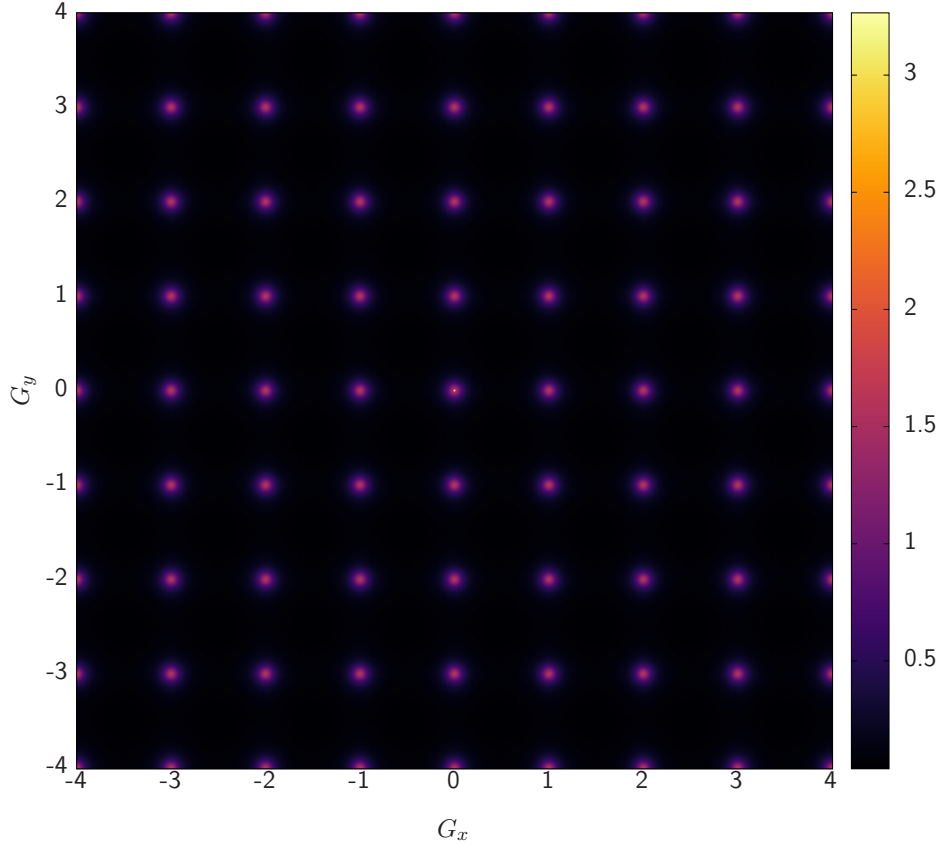


FIGURE 7.5.:  $S_\theta^\perp(\mathbf{q})$  at  $T = 2.500$ , with log scale no longer needed. The intensity of the peaks is about 1% of the intensity at  $T = 1.3$ , as was shown in Fig. 7.4.

## 7.4. Emergent field correlations

Once again I calculate the scattering tensor for the emergent electric field

$$S^{\alpha\beta}(\mathbf{q}) = \langle \mathbf{E}_\alpha(\mathbf{q}) \mathbf{E}_\beta(-\mathbf{q}) \rangle \quad (7.3)$$

and likewise for the individual Helmholtz-Hodge-decomposed components. The emergent field is again defined by Eq. 4.31.

I find correlations which are qualitatively similar to those presented in Sec. 6.2 for the zero core-energy BKT transition in the generalised lattice Coulomb gas, thereby confirming the mapping presented by Faulkner [32].

In the low-temperature phase, we see the correlations of the total field dominated by the rotational component, which corresponds to spin waves in the underlying spin network, as shown in Fig. 7.6.

Here the intensities in the irrotational correlations are two orders of magnitude

## 7. Results for the HXY model

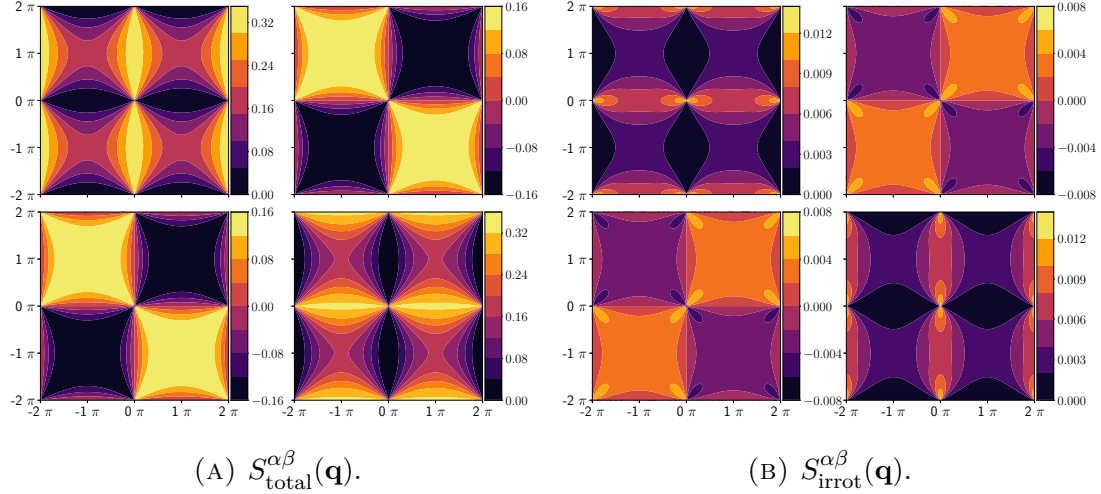


FIGURE 7.6.:  $T = 1.300$ .  $S_{\text{total}}^{\alpha\beta}(\mathbf{q})$  and  $S_{\text{irrot}}^{\alpha\beta}(\mathbf{q})$  respectively, below the BKT transition temperature  $T_{BKT} = 1.35$ . The total correlations are completely dominated by the rotational component. As in Chap. 6,  $S^{xx}, S^{xy}, S^{yx}, S^{yy}$  are shown in the top left, top right, bottom left and bottom right panels respectively.

lower than those of the rotational component and leave no trace in  $S_{\text{total}}^{\alpha\beta}$ .

Once again we see the irrotational component increasing in magnitude as we cross the transition, and the sum of the rotational and irrotational components gives a broadening of the pinch points. The high-temperature phase is again also signalled by the harmonic mode beginning to dominate the perpendicular component, but its value is lower than that for the GLCG. Fig. 7.7 shows the total correlation tensor at  $T = 1.8$  alongside the corresponding plot for the Coulomb gas.

We see in Fig. 7.7 that the correlations are qualitatively similar but that those of the HXY model are of slightly lower intensity; this is true at all temperatures  $T > T_{\text{BKT}}$ .

We can also investigate the individual components of the tensors, one example of which (again, for  $T = 1.800$ ) is shown in Fig. 7.8.

We see that the individual components as well as the total scattering tensor agree well with the Coulomb gas results from the previous chapter. There are some differences in the diffuse features which we can see, for example, in the diagonal components of the irrotational tensor, but these arise from the higher intensities of the Coulomb gas which show differently on a contour plot; the relative magnitudes of different points the scattering tensor are not substantially different.

It should also be noted here that both rotational and irrotational components of the emergent field here arise from the spin-difference field in the harmonic XY

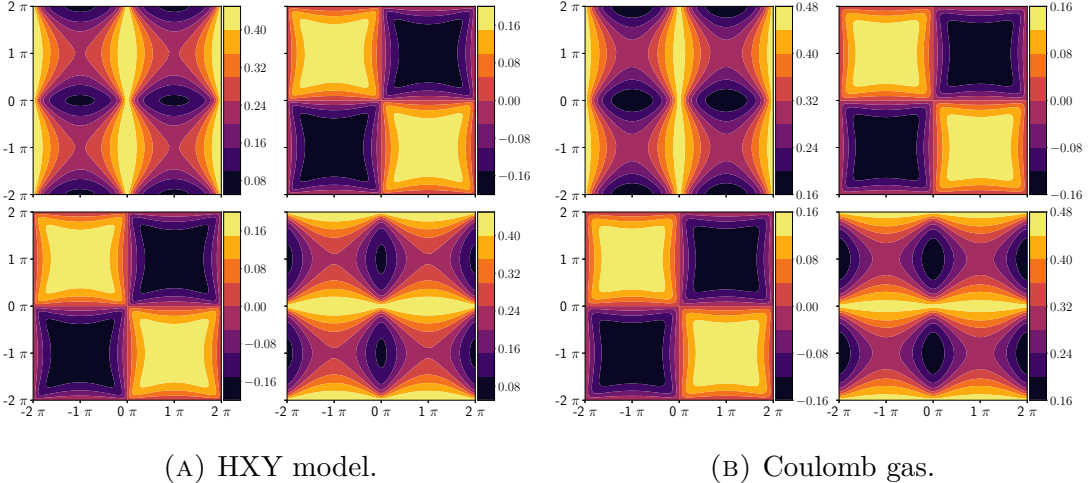


FIGURE 7.7.:  $T = 1.800$ .  $S_{\text{total}}^{\alpha\beta}(\mathbf{q})$  for the HXY model and Coulomb gas respectively, where the Coulomb gas figures were taken at  $T = 1.8/2\pi$  and with  $q = 1$ . The intensities are slightly higher for the GLCG than the HXY model; Ref. [32] attributes this difference to decreased charge mobility in the HXY model due to the constrained rotational field component.

model; the mapping from the HXY model is to a generalised Coulomb gas, not a traditional one.

## 7. Results for the HXY model

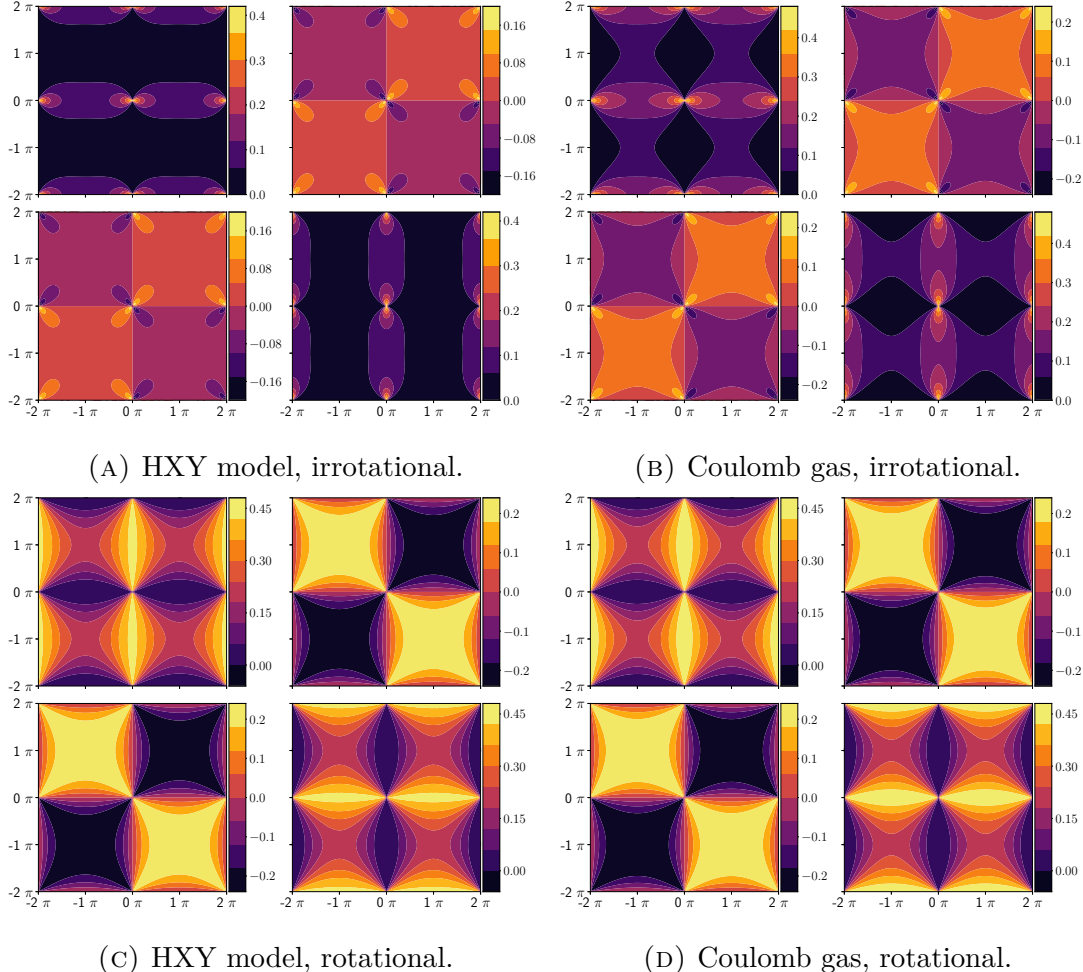


FIGURE 7.8.:  $T = 1.800$ .  $S_{\text{irrot}}^{\alpha\beta}(\mathbf{q})$  and  $S^{\alpha\beta}(\mathbf{q})$  for the HXY model and Coulomb gas respectively. We see that the irrotational component has slightly higher intensities for the GLCG than the HXY model, for the same reason as discussed in the previous figure.

### 7.4.1. $S^\perp(\mathbf{Q})$ functions

Again, we find for the harmonic XY model qualitatively similar correlations to those of the zero core-energy Coulomb gas. The simulated neutron scattering plots are dominated by the rotational component at low temperature and display pinch points which broaden as the temperature increases. Fig. 7.9 shows the evolution of the neutron scattering plot with temperature.

Again, we see that the pinch points arise from the combination of rotational and irrotational components and that the function flattens out in addition to the broadening of the pinch point. The intensities are slightly lower than those of the GLCG at the equivalent temperature, again due to the modular symmetry which constrains the phase space of the rotational component.

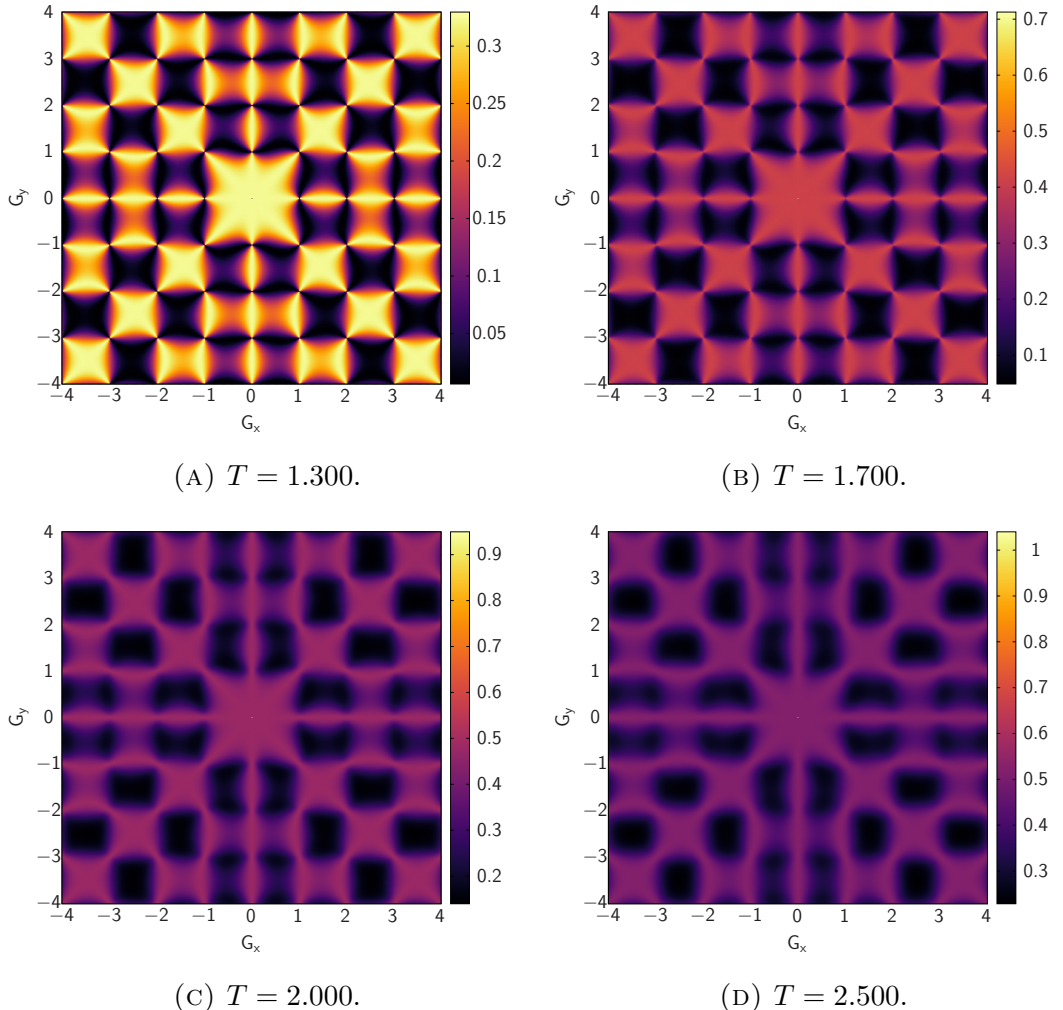


FIGURE 7.9.: The neutron scattering function  $S_{\text{total}}^{\perp}(\mathbf{Q})$  for the HXY model across the BKT transition. We see the same phenomena as for the GLCG: the harmonic mode entering at becomes the highest-intensity point in the diagram and the increased longitudinal intensity acts to round off the pinch points.

## 7. Results for the HXY model

### 7.4.2. Lorentzian fits

Once again I fit the trace of the irrotational component to a Lorentzian and use the equations Eq. 6.1 – 6.6 to plot the resulting quasi-neutron scattering function. The two resulting pairs of correlation lengths are shown together in Fig. 7.10. We see in particular that the longer length  $\xi_2$  for the HXY model seems to have a slightly shifted peak, at a higher temperature compared to that of the Coulomb gas, although it is impossible to make any quantitative statement given the noise in the GLCG results. The shorter length  $\xi_1$  also seems to have a slightly higher asymptote, although this could again be due to the lower charge mobility of the HXY model delaying the onset of charge screening somewhat.

### 7.4.3. Quadrics

Once again we see the signature of the Coulomb phase in the low-temperature regime, where the quadric tends towards a needle for every point except the origin; Fig. 7.11 shows that at  $T = 1.300$  one eigenvalue is roughly an order of magnitude larger than the other.

By contrast, Fig. 7.12 shows that the quadric at the origin is always a circle; the eigenvalues here are always virtually degenerate, and the only change is in the magnitude of the degenerate eigenvalue.

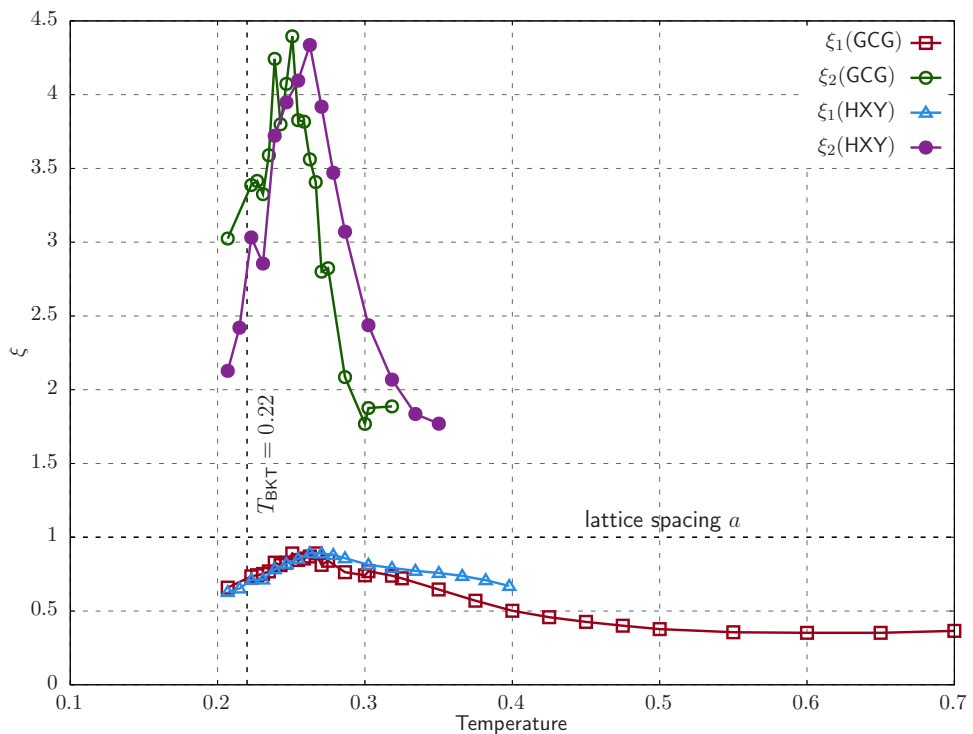


FIGURE 7.10.: The correlation lengths  $\xi_1, \xi_2$  for the HXY model and the Coulomb gas for  $L = 64$ , corrected to use the same units, showing good agreement.

## 7. Results for the HXY model

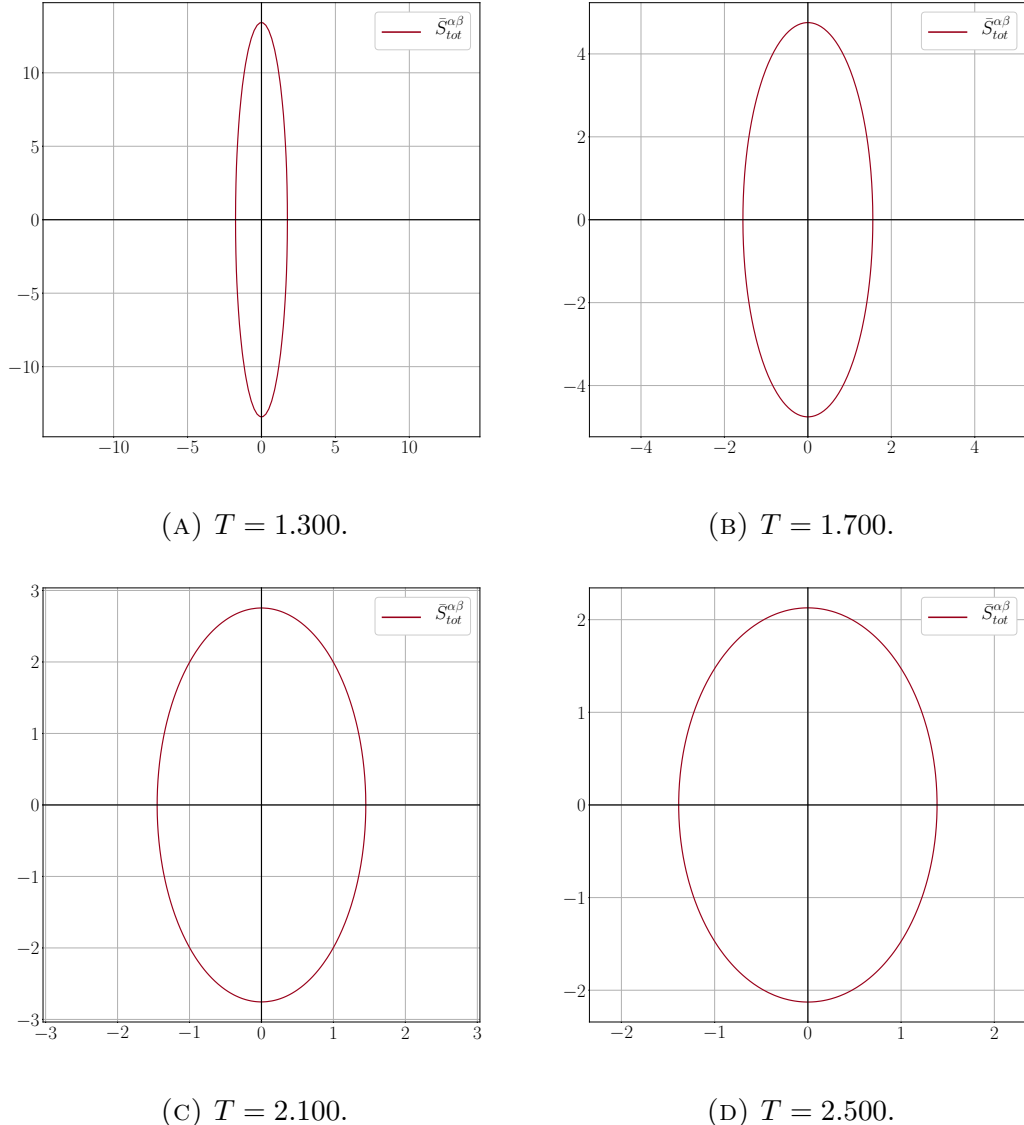


FIGURE 7.11.: The zero contour of the representation quadric at  $\mathbf{q} = (\pi, \pi)$  for  $\bar{S}_{\text{total}}^{\alpha\beta}$  as the BKT transition is crossed. We see that the eccentricity of the quadric decreases: at  $T = 1.3$  the quadric is a very thin ellipse and the transverse eigenvalue is an order of magnitude larger than the longitudinal one; at  $T = 2.5$  this is down to about 50% larger. At infinite temperature we would expect a perfect circle.

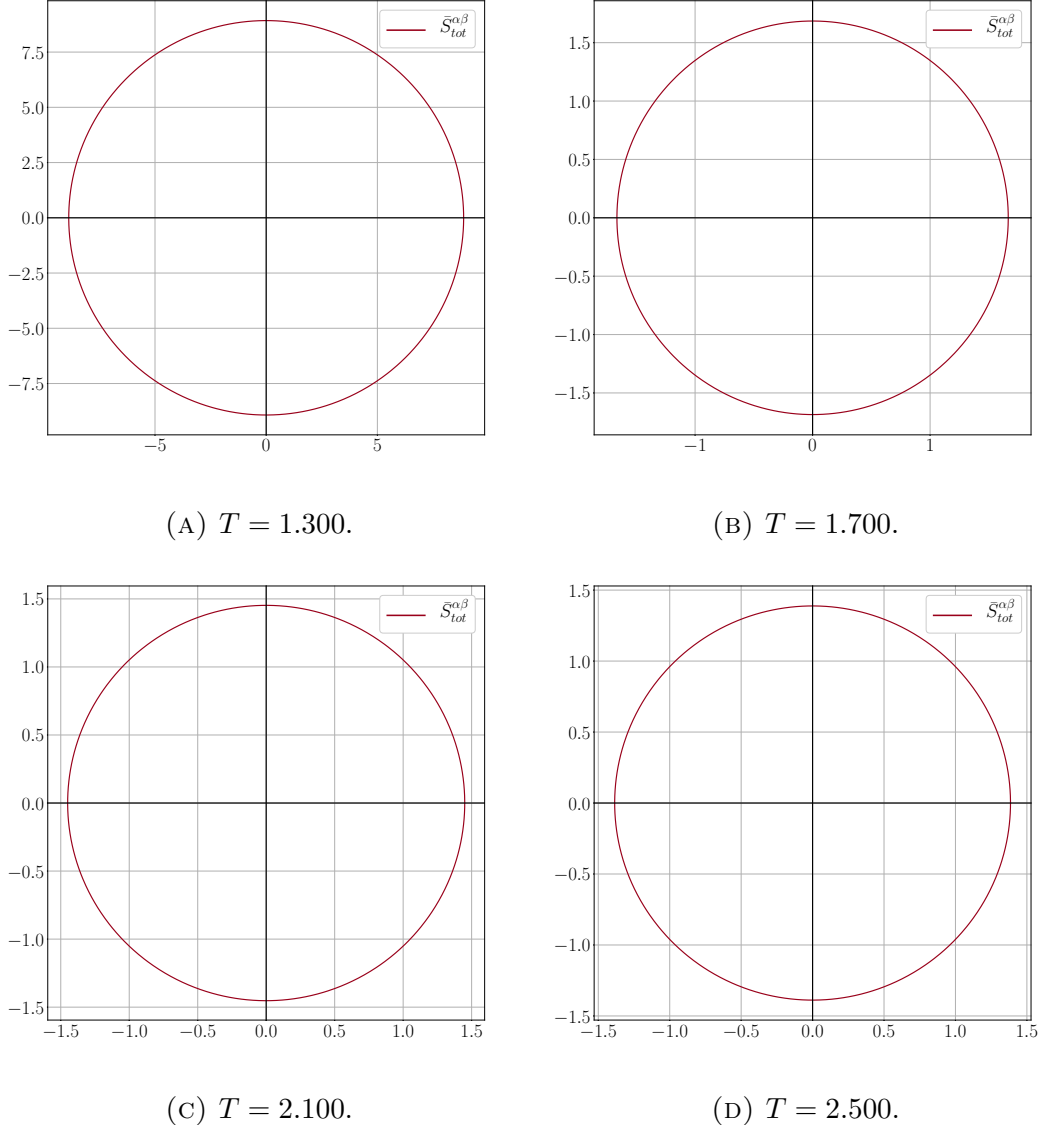


FIGURE 7.12.: The zero contour of the quadric at  $\mathbf{q} = (0, 0)$ , which is always a circle regardless of temperature. This is a reflection of the fact that the harmonic mode is both curl-free and divergence-free.

## 7.5. Discussion and conclusions

I have conducted a thorough investigation of the HXY model making use of the mapping between the HXY model and the GLCG gas, and verify various previous results concerning the susceptibilities, permittivity and specific heat of the HXY model. I focus again on the field correlations in the Coulomb gas representation and show that they are qualitatively similar to those of the generalised lattice Coulomb gas with  $q = 2\pi, \epsilon = 1$ , with lower intensities for the same temperature due to the bounded phase space of the emergent electric field.

We again see sharp pinch point patterns in the simulated neutron scattering patterns in the critical low-temperature phase which broaden as the temperature increases and the charges unbind, and fit the observed correlations to the superimposition of an analytic form factor on a Lorentzian with a flat background, finding the same qualitative behaviour for the HXY model as for the Coulomb gas, with a sharp peak just above the BKT transition temperature. The peak in the HXY Debye length is less intense for the HXY model than the Coulomb gas, which we attribute to the coupling between the vortex and spin-wave parts of the HXY Hamiltonian and which leads to decreased charge mobility in the high-temperature phase.

More generally, these results confirm the HXY  $\leftrightarrow$  Coulomb gas mapping by showing that the two have the same correlations. We also see that once again the Helmholtz-Hodge-decomposed field description provides a natural way of describing these systems.

We see that the critical low-temperature phase of the XY model, which consists of divergence-full spin-wave excitations, is transformed via the  $\pi/2$  rotation of the spin-difference field into the Coulomb gas representation, giving an entirely divergence-free Coulomb phase. Hence, the Coulomb gas representation of the XY model (arising from the gradient of the spin-difference field, not the spin field itself) displays the same Coulomb phase correlations we see in spin ice, where the Coulomb phase arises from the gradient of the magnetisation. The corollary of this is that there is no signature of the Coulomb phase correlations or the dipolar pinch points in the spin-spin correlation function of the XY model, as shown in Figs. 7.4 and 7.5.

# 8. Results for the 2d canonical and 3d grand canonical Coulomb gases

In addition to the 2d grand canonical generalised lattice Coulomb gas and the harmonic XY model I have also performed simulations of the 2d Coulomb gas in the canonical ensemble (CE) as well as a preliminary survey of the 3d grand canonical Coulomb gas.

## 8.1. 2d canonical Coulomb gas

The phase diagram of the 2d canonical Coulomb gas is shown in Fig. 8.1 was given by Gupta [45], who showed that it includes two branches of BKT transitions and an Ising transition, as in the grand canonical case, but obviously no first-order transition. There is also a phase separated region for higher densities and lower temperatures, which I will show some evidence of below.

### 8.1.1. Winding susceptibilities

Fig. 8.2 shows the winding susceptibility as a function of both temperature and number of charges. It is clear that at very low charge densities the BKT transition temperature is increased, as seen from the winding susceptibilities in Fig. 8.2 which stay very small significantly above the grand canonical BKT temperature,  $\chi_w(n=2) \approx 0.05$  even at  $T = 0.3$ . This is to be expected: the BKT transition corresponds to  $\chi_w$  becoming finite but since its magnitude is related to the number of charge windings, it follows that restricting the number of charges would reduce the magnitude of the susceptibility.

At higher densities, we start to see finite winding susceptibilities even below the grand canonical BKT transition temperature: this agrees with the prediction of Gupta [45], who predicted a reduction in the BKT transition temperature as the

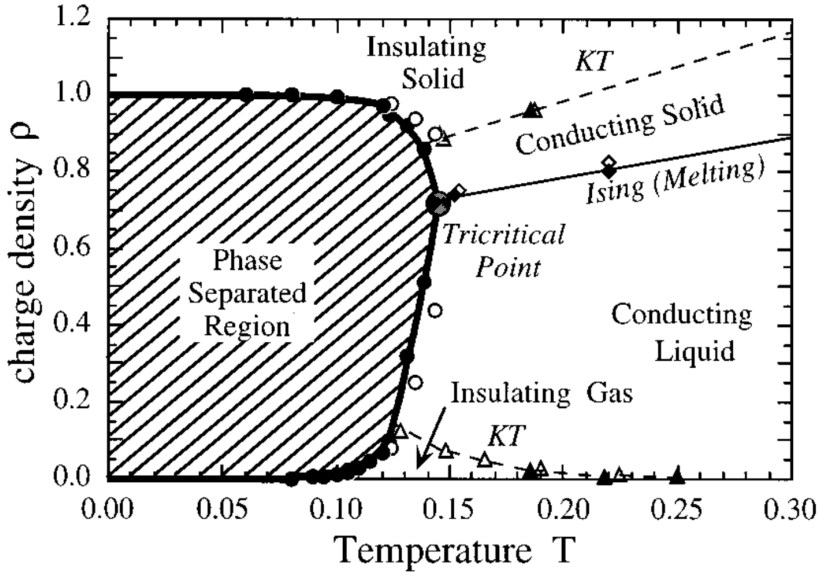


FIGURE 8.1.: The phase diagram of the 2d canonical Coulomb gas on the square lattice, probed via Monte Carlo simulation, reproduced from [45]. Open symbols are for  $L = 16$ , filled symbols for  $L = 32$ .

charge density increases up to approximately 20%, at which point there is no BKT transition and the system moves directly from phase separation to the conducting liquid phase. Fig. 8.3 shows the winding susceptibilities for higher charge densities: at the highest densities simulated,  $\chi_w$  is finite at all temperatures, consistent with the expectation of a lower BKT transition temperature.

### 8.1.2. Specific heat

I find that the specific heat for small  $n$  (i.e. low charge density) is a poor indicator of the BKT transition because the irrotational specific heat is low at all temperatures; at higher  $n$  I find that the specific heats begin to agree with the grand canonical results. This implies that the increase in specific heat is driven by the increasing charge density, rather than by the BKT transition. Fig. 8.4 shows specific heats across a range of temperatures and charge densities; at higher densities these should correspond to the relaxation of the specific heat above the BKT transition, although further simulation would be required to confirm this absolutely. Below  $n = 32$  ( $\rho = 1/128 \approx 0.008$ ) the specific heat is essentially 0.5 (corresponding to the specific heat of the rotational component) for all temperatures simulated, indicating that the irrotational component has a negligible effect on the total specific heat.

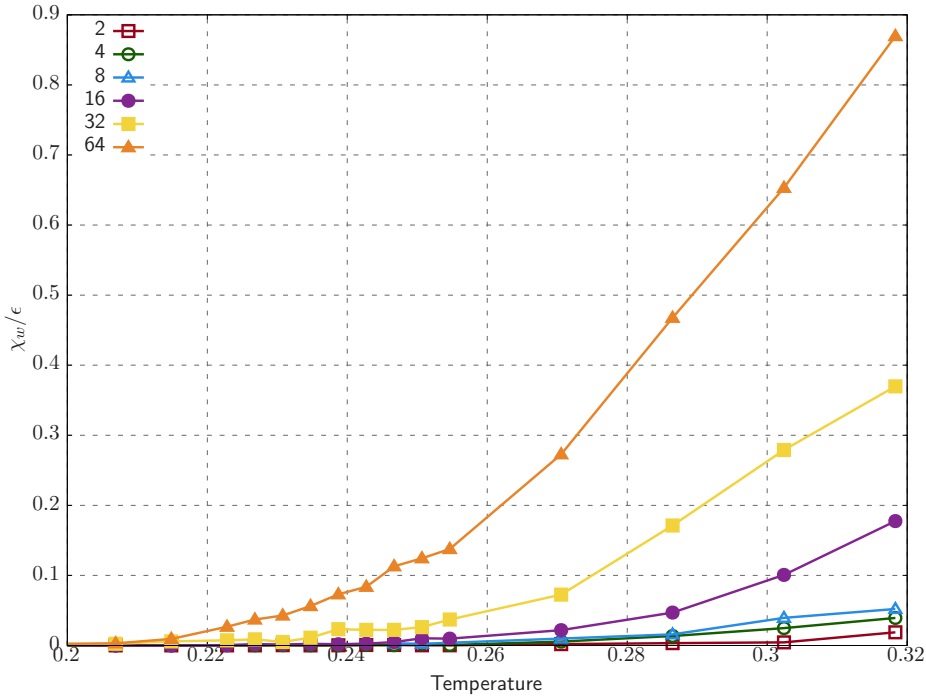


FIGURE 8.2.: The winding susceptibility  $\chi_w/\epsilon$  as a function of temperature for different values of  $n$ , for  $L = 64$ . The grand canonical BKT transition temperature in these units is  $T_{\text{BKT}}^{\text{gce}} = 0.22$ , and we see that for vanishingly low charge density  $\chi_w$  is small here well above  $T = 0.22$ , indicating that the dilute limit gives a higher BKT transition temperature.

### 8.1.3. Correlations

As expected from previous results concerning the phase diagram of the 2d canonical Coulomb gas, as well as the susceptibility and specific heat measurements shown above, we see the conducting liquid phase at a much lower temperature than in the grand canonical case as the charge density becomes appreciable.

At low charge densities, where there is a BKT transition, the temperature  $T_{\text{BKT}}(\rho)$  is predicted to increase as  $\rho$  decreases: Fig. 8.5 shows a simulation with only 2 charges at  $T = 0.25$ . We see that, despite being above the grand canonical BKT transition temperature, we still have a neutron scattering plot dominated by the divergence-free component; the  $\mathbf{Q} = \mathbf{0}$  point has an intensity of around 0.015, an order of magnitude smaller than the intensity around it.

At intermediate densities we can better see the effect of changes in  $\rho$  on the BKT transition temperature. Fig. 8.6 shows two different charge densities simulated at

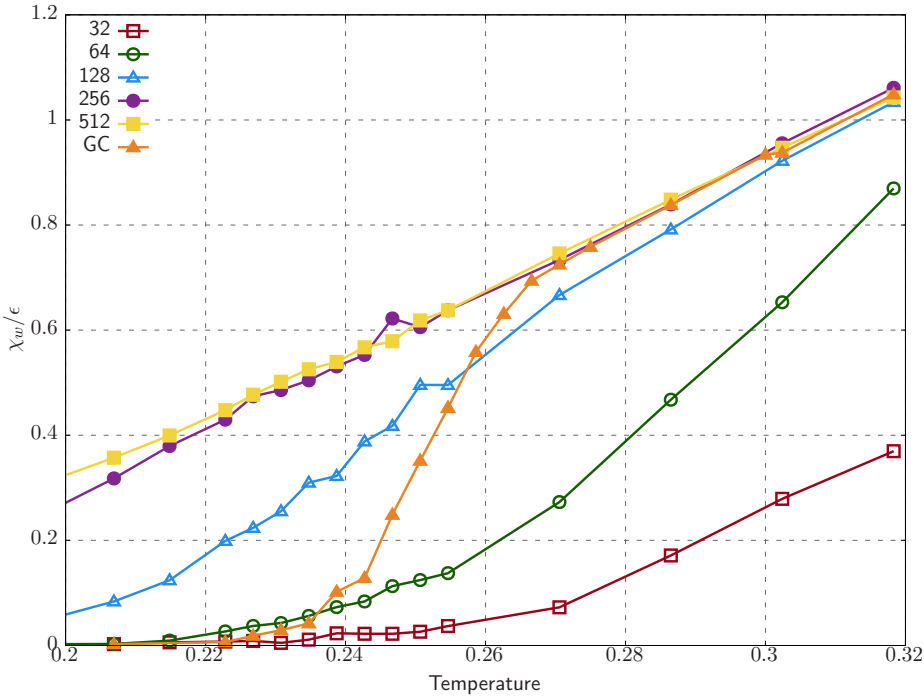


FIGURE 8.3.: The winding susceptibility  $\chi_w/\epsilon$  for higher values of  $n$  along with the grand canonical result for  $L = 64$ . We see that for higher charge densities the winding susceptibility is finite at lower temperature, consistent with a lowered BKT transition temperature.

the same temperature. Both simulations are conducted at a lower temperature than the grand canonical BKT transition  $T_{\text{BKT}}(\text{GC}) \approx 0.22$ .

Fig. 8.6a has  $n = 64$  charges, equating to  $\rho = 0.01625$ , almost at zero on Fig. 8.1.  $T = 0.207$  is at or slightly below the predicted  $T_{\text{BKT}}$  for this charge density; we see sharp pinch points and a low-intensity harmonic mode which correspond to the low-temperature insulating gas phase with  $T < T_{\text{BKT}}$ .

Fig. 8.6b, however, has  $n = 256 \rightarrow \rho = 0.0625$ , at which density we expect to see  $T_{\text{BKT}} \approx 0.16$ . We find correlations with finite pinch point widths and a high-intensity harmonic mode, characteristic of  $T > T_{\text{BKT}}$ , as expected.

At very high charge densities the behaviour is qualitatively different: at low temperature, we find correlations reminiscent of those in Sec. 6.4, with broad Lorentzian peaks arising in the same places as in the grand canonical conducting liquid phase at finite core-energy. Fig. 8.7 shows an example of this, with Lorentzians arising in the same place as for the charge crystal and with the same systematic absences, but also with a large harmonic mode at  $\mathbf{Q} = \mathbf{0}$  and pinch

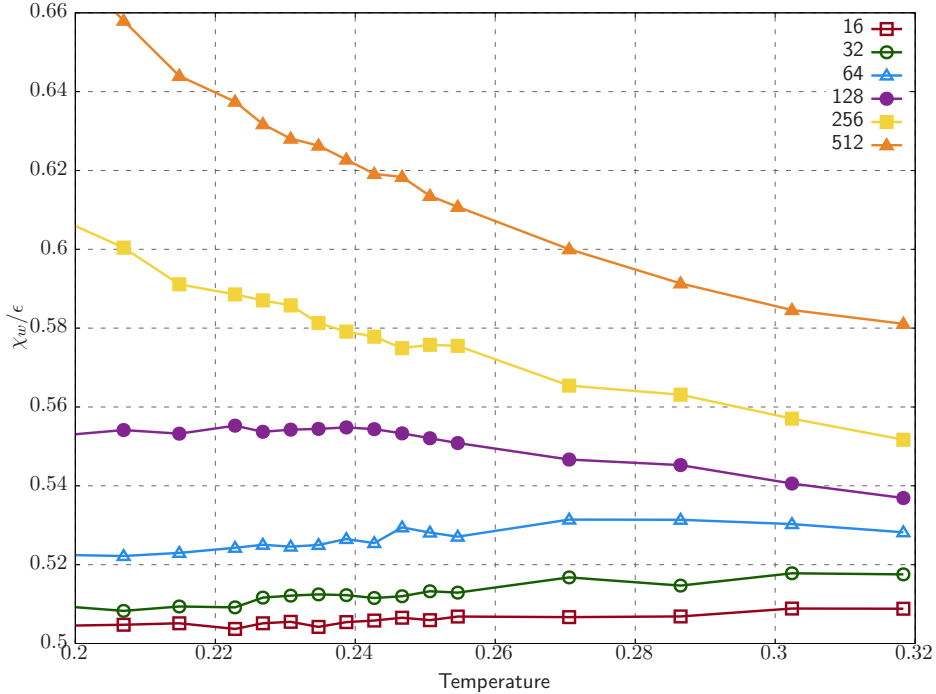


FIGURE 8.4.: Specific heat for values of  $n$  above 32. For very low charge densities the specific heat is approximately 0.5 for all temperatures, as would be the case for a purely transverse field, indicating a very small longitudinal contribution.

points of finite width which characterise the conducting liquid phase.

We interpret this as another example of phase coexistence, this time between the conducting liquid phase found at higher temperatures and the phase-separated solid-gas regime found at high  $\rho$  and low  $T$ ; although the parameters used in this simulation should put the system in the conducting liquid regime, the finite size of the system would necessarily lead to some crossover between strict phase separation and the “pure” conducting liquid phase.

At higher temperatures though we recover the correlations from the zero core-energy conducting liquid phase. Fig. 8.8 shows another example at the same charge density, but for a much higher temperature.

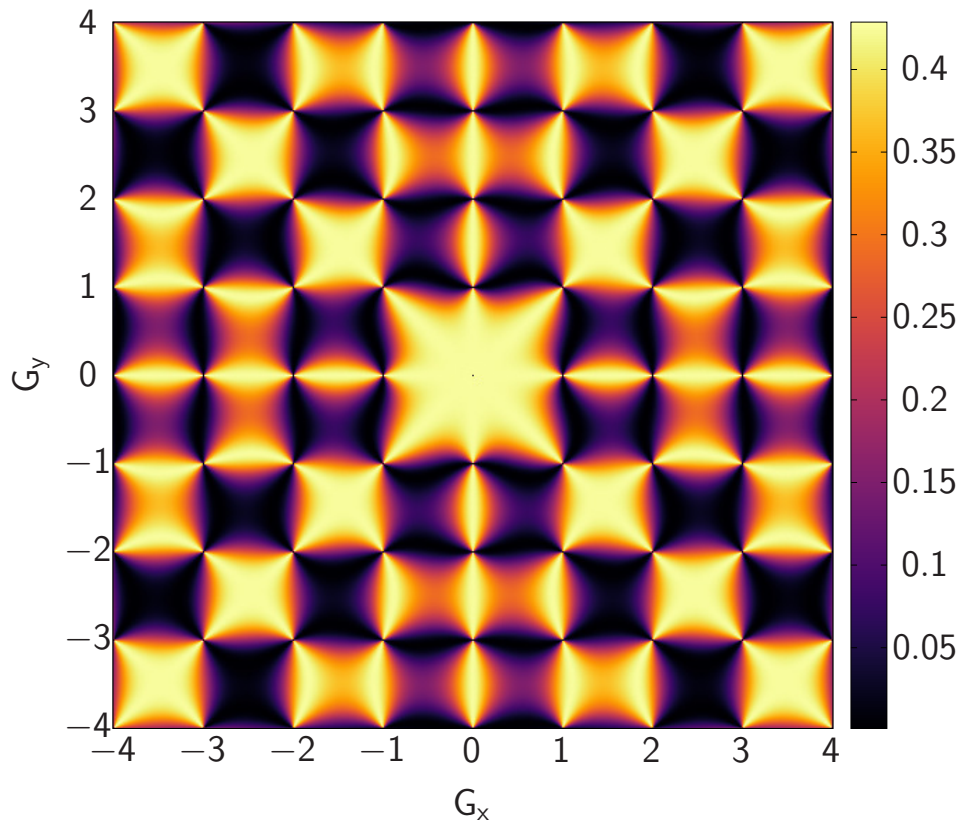


FIGURE 8.5.: ( $n = 2$ ,  $\rho = 0.0005$ ,  $T = 0.25$ ). The simulated neutron scattering function  $S_{\text{total}}^{\perp}(\mathbf{Q})$ . This temperature is significantly higher than  $T_{\text{BKT}}^{\text{gce}}$  but features sharp pinch points and zero harmonic mode, indicating the transverse-dominated phase below the transition.

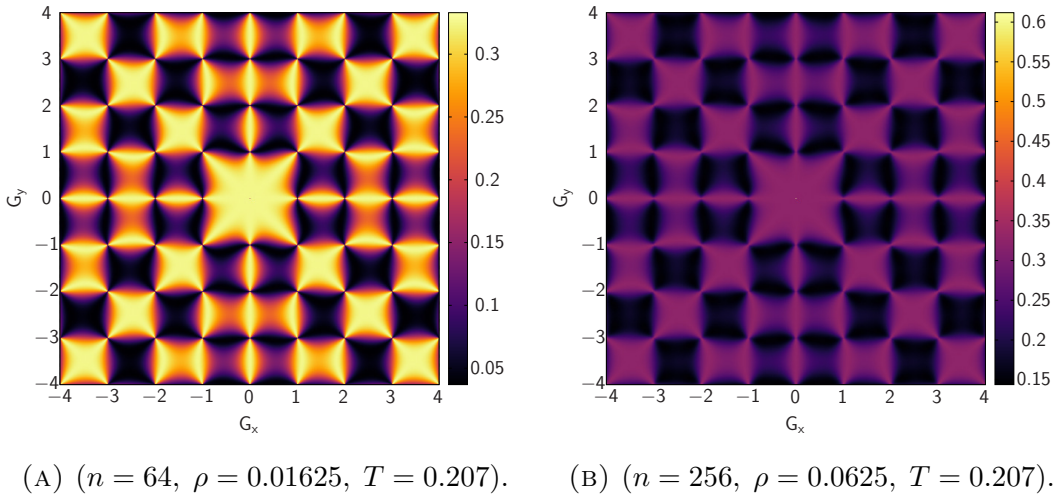


FIGURE 8.6.: The simulated neutron scattering function  $S_{\text{total}}^{\perp}(\mathbf{Q})$  for lower and higher charge densities at the same temperature. The lower density (left) shows a small harmonic mode and sharp pinch points corresponding to the insulating phase, whereas the higher density (right) shows a large harmonic mode and rounded pinch points characteristic of the conducting phase.

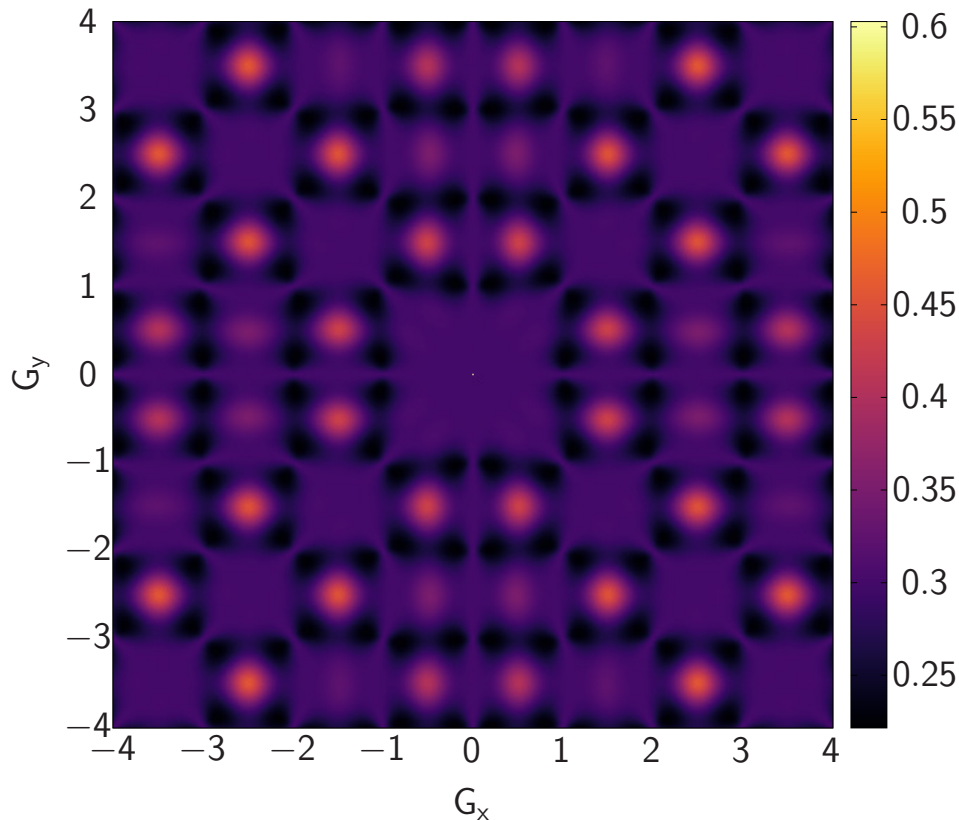


FIGURE 8.7.: ( $n = 512$ ,  $\rho = 0.125$ ,  $T = 0.191$ ). The simulated neutron scattering function  $S_{\text{total}}^{\perp}(\mathbf{Q})$ . We see the diffuse features of the transverse-dominated phase but with broad peaks superimposed which imply the presence of the solid phase: therefore, we take these correlations as suggestive of phase coexistence, as would be expected for these parameters from [45].

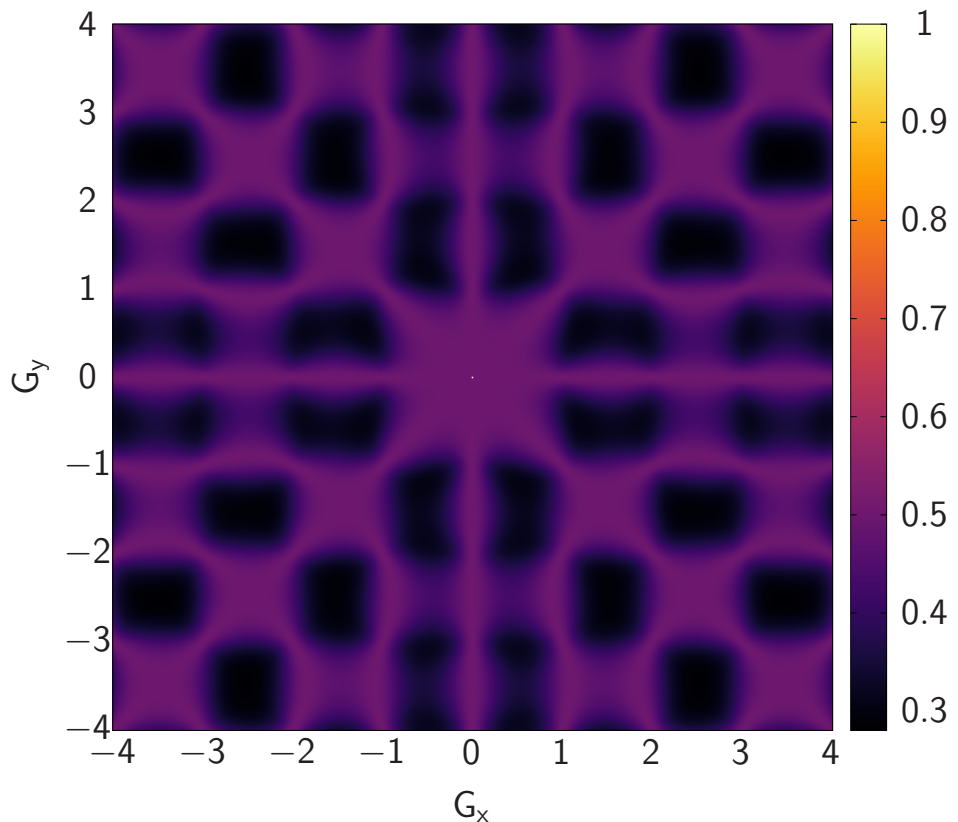


FIGURE 8.8.: ( $n = 512$ ,  $\rho = 0.125$ ,  $T = 0.318$ ). The simulated neutron scattering function  $S_{\text{total}}^{\perp}(\mathbf{Q})$ . We now see very rounded pinch points and a strong signal at  $\mathbf{Q} = \mathbf{0}$ : the system is in the conducting liquid phase, which is again consistent with the phase diagram.

### 8.1.4. Lorentzian fits

We can once again fit the trace of the irrotational correlation tensor to the form Eq. 6.1, and use this to extract higher and lower correlation lengths as a function of both temperature and charge density. Fig. 8.9 shows these results. We see that the peak in the longer length  $\xi_2$  is higher for the lowest charge densities; this could be attributed to the almost non-existent screening in a system with so few charges, but again the noise in the results makes quantitative arguments impossible. We also see that the shorter length  $\xi_1$  increases to slightly above the lattice spacing, which may also result from the very low charge densities: in the grand canonical case, as the charge density increases across the transition, we would expect to see a distribution of charge separations, but this is impossible when there are very few pairs in the system.

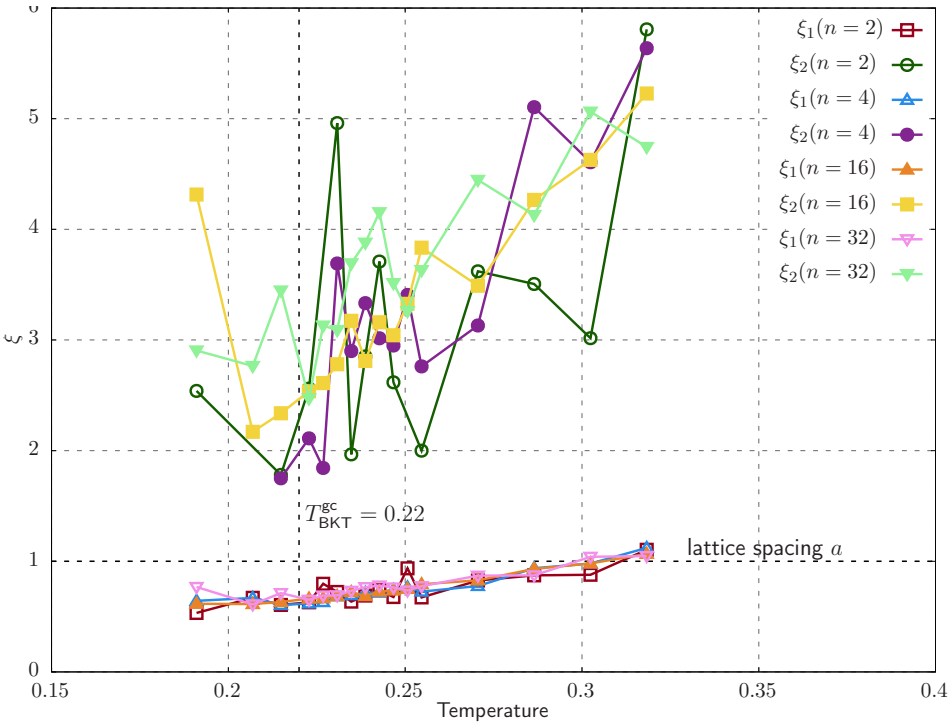


FIGURE 8.9.: The higher and lower correlation lengths of the canonical Coulomb gas as a function of temperature and charge density up to  $n = 32$  ( $\rho = 0.008$ ).

Fig. 8.10 shows the correlation lengths for higher charge densities. At these higher densities we see different behaviour again: the shorter length  $\xi_1$  is also larger than the lattice spacing at lower temperatures. The BKT transition temperature is lowered from its grand canonical value for these higher charge densities, and the winding susceptibilities are finite at all temperatures for the values shown.

Hence, one possibility is that these lengths correspond to unbound charges at all temperatures, but at temperatures low enough that screening is not very strong; this is currently just conjecture, however.

We also see the decrease in  $\xi_2$  which was observed in the canonical case. It is possible that in these slightly more charge-dense systems screening once again becomes significant at higher temperatures, resulting in  $\xi_2$  decreasing and merging with the shorter length, as was observed in Chap. 6, but further work would be needed in order to establish this with certainty.

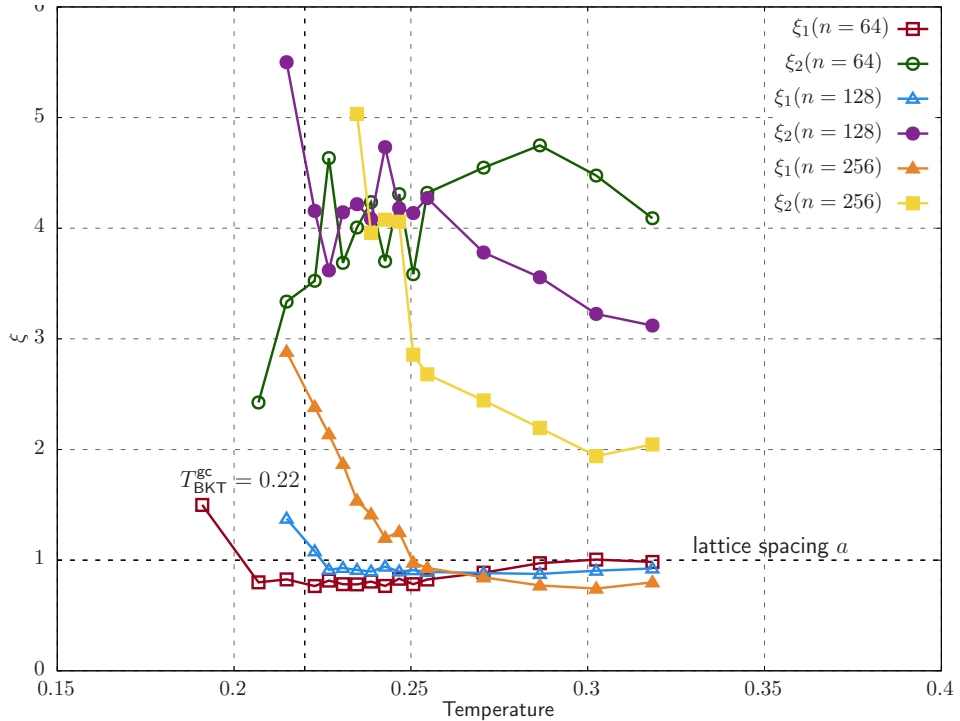


FIGURE 8.10.: The higher and lower correlation lengths of the canonical Coulomb gas as a function of temperature and charge density up to  $n = 256$  ( $\rho = 0.125$ ).

For  $n = 512$  this fit fails entirely for all temperatures. The issue with the fit can be explained by noting that we fit to a Lorentzian centred at the origin, since this is the function we expect in the zero core-energy, grand canonical case. As shown in Fig. 8.7, however, we see phase coexistence at low temperature and high charge density, which is reflected in the trace of  $S_{\text{irrot}}^{\alpha\beta}(\mathbf{q})$  as shown in Fig. 8.11. Since the peak at  $(\pm\pi, \pm\pi)$  has almost the same intensity as the origin, the fit fails. In principle it may be possible to fit to a pair of Lorentzians with different centres, with one at the origin and one at  $(\pi, \pi)$ , for example, in order to try to capture the onset of charge ordering. This would, however, beg the question of what exactly we would mean by correlation lengths in a system with gas-solid phase separation,

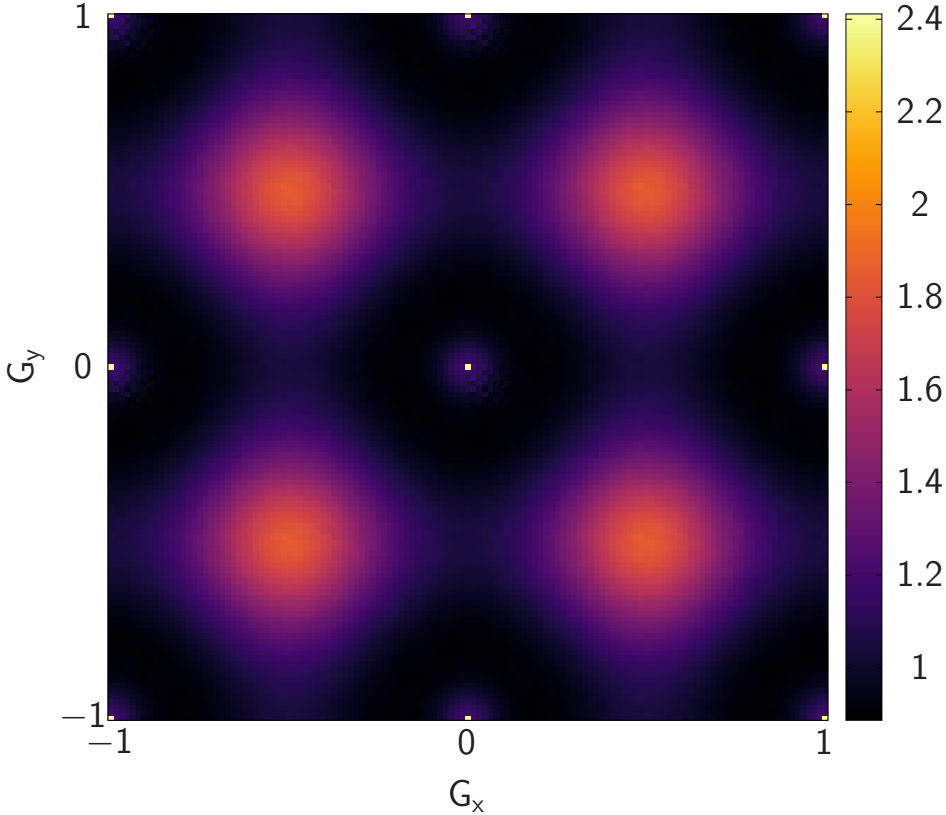


FIGURE 8.11.: ( $n = 512$  ;  $\rho = 0.125$  ;  $T = 0.191$ ). The longitudinal correlation function obtained via the trace of the scattering tensor  $S_{\text{irrot}}^{\alpha\alpha}(\mathbf{q})$ . The broad areas of high intensity at  $(\pm\pi, \pm\pi)$  are characteristic of the solid phase; the effect of this is essentially that the function can no longer be represented by a pair of Lorentzians.

since they would necessarily be different depending on which phase we inspect in direct space. For example, it is possible that similar results could be obtained to the present case, but with one correlation length corresponding to closely bound pairs in the solid phase and the other corresponding to free charges in the liquid phase.

## 8.2. 3d grand canonical Coulomb gas

I have also conducted several simulations of the 3d grand canonical Coulomb gas, varying both the charge density and temperature.

The 3D grand canonical Coulomb gas has been shown to exhibit a line of first-order transitions and a line of second-order transitions meeting at a crit-

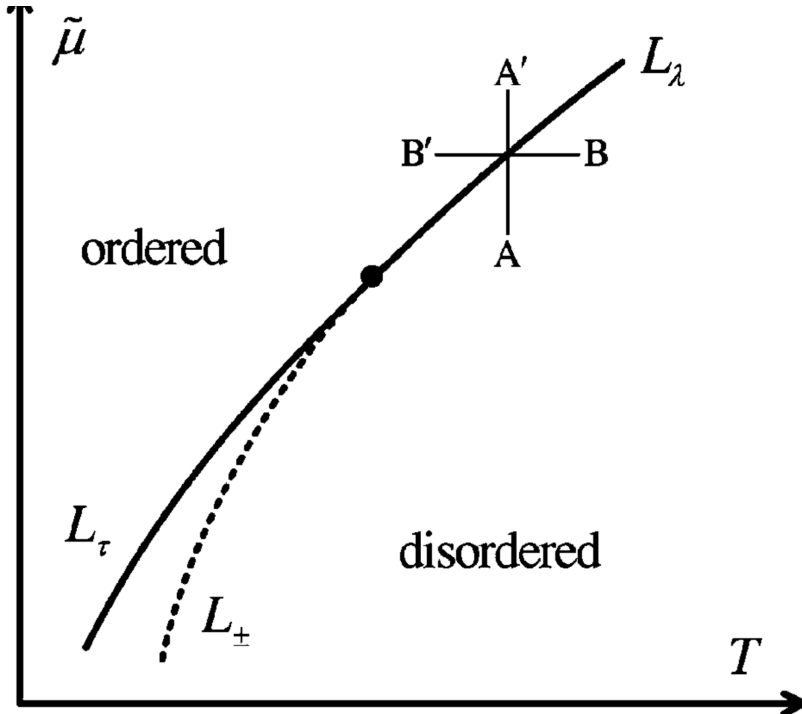


FIGURE 8.12.: Phase diagram for the 3D grand canonical restricted primitive model on the simple cubic lattice, for the zero field case, reproduced from [95].

ical point [95], as shown in Fig. 8.12; my preliminary simulations would seem to be consistent with this.

Cuts of the neutron scattering function at  $Q_z = 0$  show correlations recognisable from the 2D case and which follow a qualitatively similar pattern, although without the insulating-conducting gas BKT transition, which obviously cannot occur in 3D since the 3D Coulomb potential is non-confining. Note that the resolution of these cuts is necessarily much lower than in the 2D case, since we are inspecting only one small slice of a much larger three-dimensional function.

For example, at low temperature and zero core-energy the  $Q_z = 0$  slice of the neutron scattering function reveals the same transverse-dominated correlations of the low-temperature, low-core-energy phase in the 2D case, as shown in Fig. 8.13.

I find that as in 2D the  $Q_z = 0$  slice of the neutron scattering function is qualitatively similar to this at all temperatures and core-energies simulated.

There are also some puzzling results at intermediate temperature, where we see the correlations of the solid phase coming and going as the core-energy increases. Fig. 8.14 shows an example of this for  $T = 0.5$ , where at  $u = 0.5$  the correlations seem to be those of the low-temperature solid phase, but at  $u = 1.0$  they appear

## 8. Results for the 2d canonical and 3d grand canonical Coulomb gases

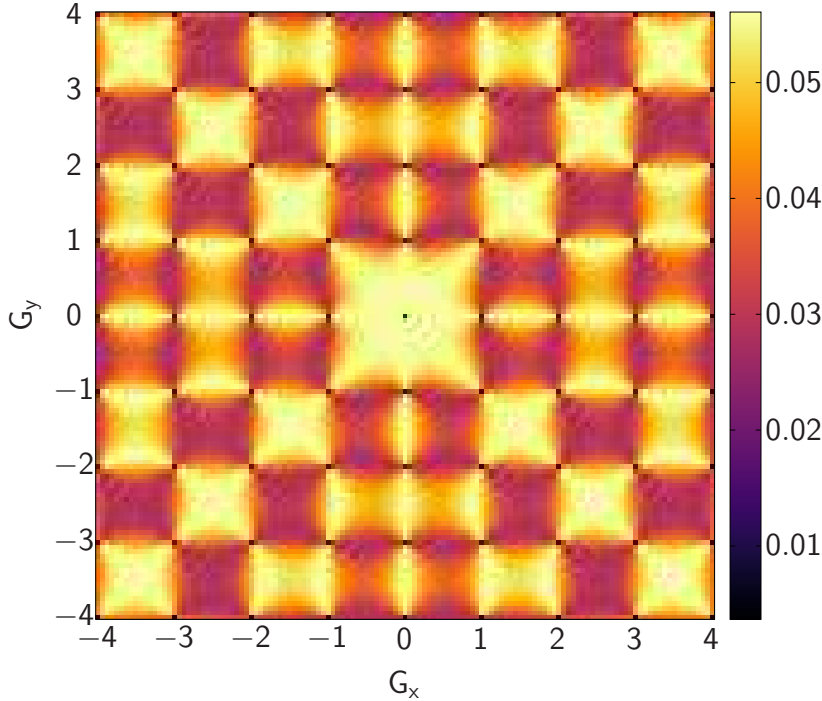


FIGURE 8.13.: ( $T = 0.25$ ,  $u = 0$ ).  $S_{\text{total}}^{\perp}(Q_z = 0)$ . At this low temperature we again see a transverse dominated state with sharp pinch points.

more like those of the high core-energy liquid above the melting transition. Again, further detailed study of the  $u - T$  phase diagram would be required to ascertain exactly what is happening here. The unit system used in [95] has  $T^* = k_B T / J(a)$  with  $J(r) = q^2 / (\epsilon r)$ , which for the parameters used in Fig. 8.14 gives  $T^* = 1/4\pi = 0.08$ . This is below the end point of the line of reported triple points  $L_\tau$  at around  $T^* \approx 0.142$ , implying that there may be no transition or triple point at this temperature.

Fig. 8.15 shows the neutron scattering plot for the irrotational component at  $Q_z = 0$ , for the higher temperature of  $T = 0.75$ , corresponding to  $T^* = 0.12$ . This is also below the reported end point of the triple point line, but here we can clearly see the evolution in the correlations; at low core-energy they are qualitatively similar to those of the conducting liquid phase in 2D, but as we increase the core-energy we start to see the peaks associated with the solid phase.

However, we also see the intensity of the correlations decreasing at the higher core-energy; whether this is due to the normalisation used or whether there is some other phenomenon would require further study to establish.

The correlations of the 3D lattice Coulomb gas in both the grand canonical and canonical cases would be a worthwhile topic of future study.

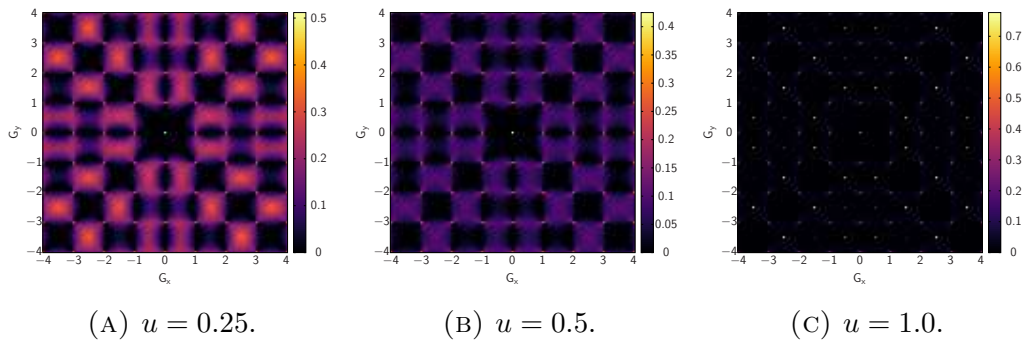


FIGURE 8.14.: ( $T = 0.500$ ;  $u = 0.250, 0.500, 1.000$ ). Three examples of  $S_{\text{total}}^{\perp}(Q_z = 0)$  with the core-energy increasing. At  $u = 0.25$  we see the onset of Lorentzians associated with the solid phase, which disappear at  $u = 0.5$  and then return at  $u = 1.0$ ; it is unclear what causes this disappearance and reappearance.

8. Results for the 2d canonical and 3d grand canonical Coulomb gases

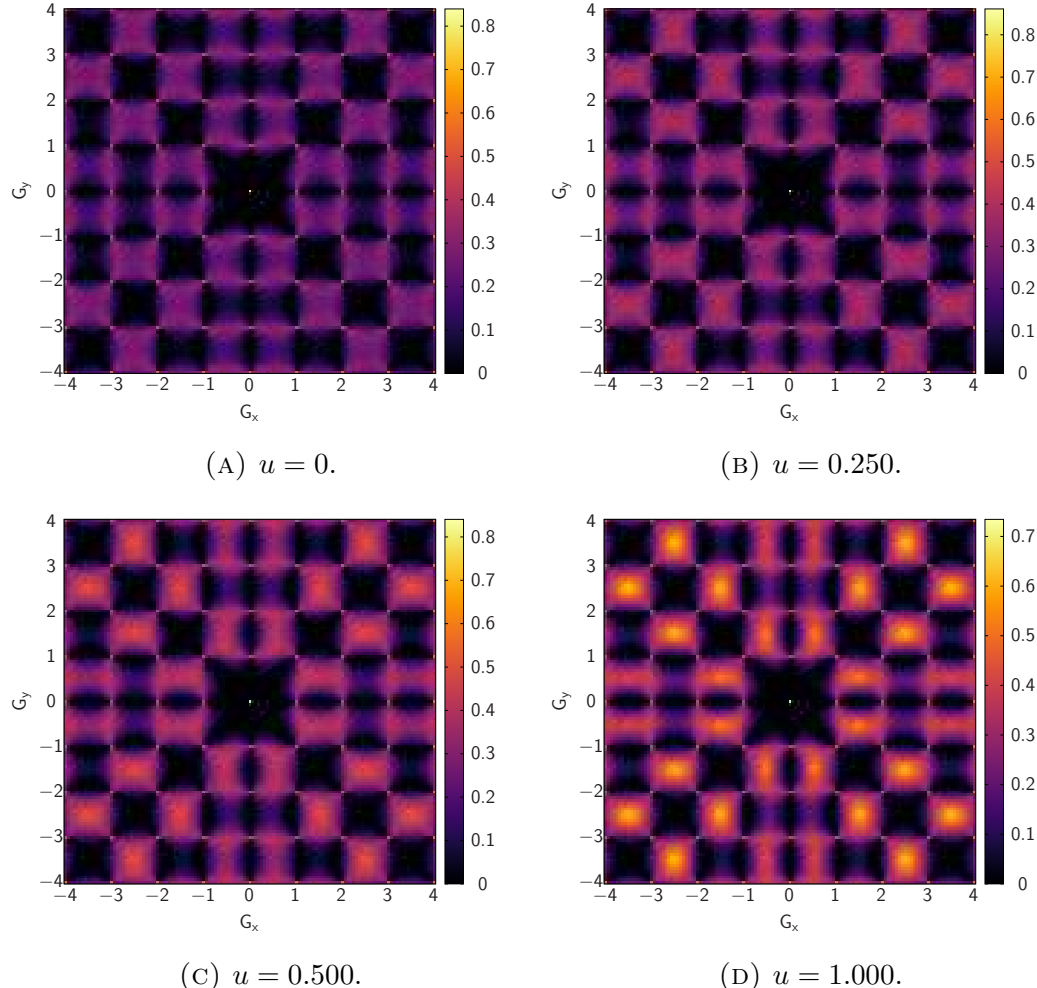


FIGURE 8.15.: ( $T = 0.750$  ;  $u = 0, 0.250, 0.500, 1.000$ ). Four examples of  $S_{\text{total}}^{\perp}(Q_z = 0)$  with the core-energy increasing. Again, we begin to see the superposition of correlations associated with the conducting liquid and solid phases.

### 8.3. Discussion and conclusions

Simulations of the 2d canonical Coulomb gas give results consistent with the phase diagram of Gupta [45] and which make sense in the context of their grand canonical counterparts. I find that the BKT transition temperature is increased from its grand canonical value for low charge densities and reduces as the charge density increases. Fig. 8.16 shows  $S_{\text{total}}^{\perp}(\mathbf{Q})$  at the same temperature  $T = 0.207$ ; we see that the low charge density has essentially rotational correlations with very sharp **pinch points** and a vanishingly small harmonic mode, indicating that the system is in the insulating gas phase where the irrotational correlations are negligible; whereas the higher charge density has a large harmonic mode and finite width pinch points indicating that we are in the conducting phase.

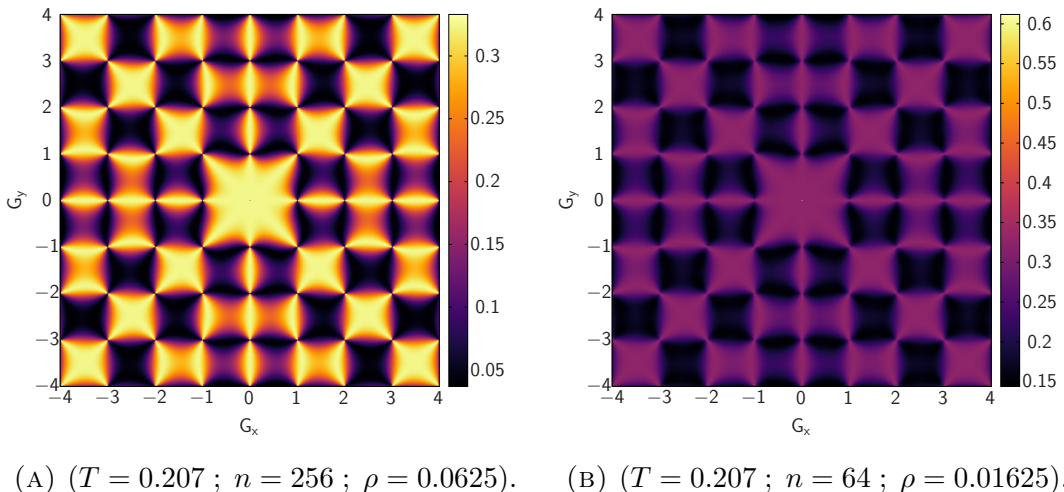


FIGURE 8.16.:  $S_{\text{total}}^{\perp}(\mathbf{Q})$  for two different charge densities at the same temperature. On the left we see correlations which correspond to the insulating phase, on the right the correlations are those of the conducting phase.

At very high charge densities and low temperatures I also find correlations suggesting solid-liquid phase separation, again as expected from the phase diagram. Fig. 8.7 shows one example. The Lorentzian peaks associated with the solid phase, which were previously seen in the high core-energy solid phase in the grand canonical case in Sec. 6.4, disappear at higher temperatures and leave only the correlations of the liquid phase, as shown in Fig. 8.8.

I also perform fits to inverse correlation lengths using Eq. 6.1 as in the grand canonical case, finding similar results at low charge densities but slightly different at higher densities, where the BKT transition is lowered in temperature.

## 8. Results for the 2d canonical and 3d grand canonical Coulomb gases

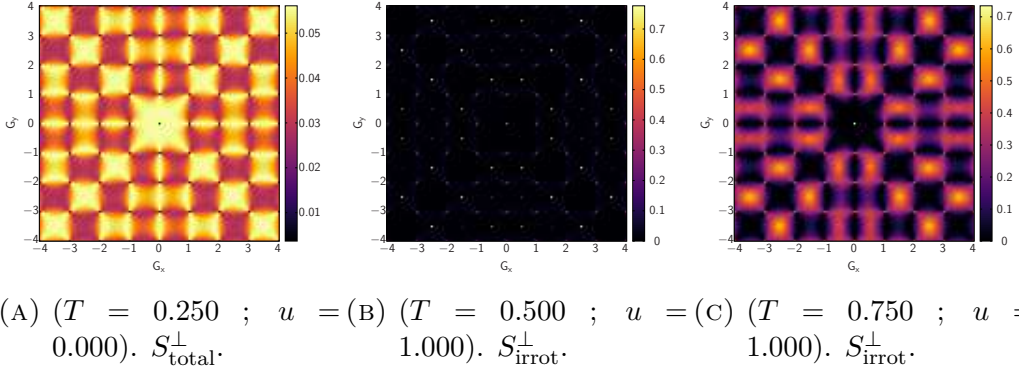


FIGURE 8.17.: Three examples of  $S^{\perp}(Q_z = 0)$  for different values of  $T$  and  $u$ . We see correlations reminiscent of the low- $T$ , low- $u$  insulating gas phase, the low- $T$ , high- $u$  insulating solid phase and the high- $T$ , high- $u$  melted phase respectively.

Further work on the 2d canonical case would focus on even higher charge densities; the densities simulated here are mostly too small to quantitatively reproduce the whole of the phase diagram.

In the 3D case I find some preliminary results showing qualitatively similar correlations to those of the 2D case, and which are broadly consistent with published results on the phase diagram of the 3D grand canonical Coulomb gas, but with several open questions which would require further study to answer, including the potential presence of a previously reported “ghost” BKT transition [96], which may be visible in the harmonic mode and hence effective permittivity. I also observe [pinch points](#) and [bow ties](#) in the [Helmholtz-Hodge](#)-decomposed components of the correlation tensor in 3D; this is to be expected, since these features are a consequence of the decomposition and the fact that the neutron only sees the part of the tensor perpendicular to  $\mathbf{Q}$ . Fig. 8.17 shows three examples.

# 9. Conclusions

## 9.1. Summary of main results

I have simulated the 2D Coulomb gas on the square lattice in both the canonical and grand canonical ensembles, as well as the harmonic XY model on the square lattice using the convenient mapping from the HXY model to the Coulomb gas, and the 3D grand canonical Coulomb gas on the simple cubic lattice. All my work has been performed using a Helmholtz-decomposed, lattice electric field description of the Coulomb system and the Maggs-Rossetto algorithm [8], which introduces an auxiliary rotational electric field in order to perform fast local simulation. This rotational field would not be present in an electrostatic system, but the thermodynamics of the field remain unchanged, and the rotational component of the field is relevant in many other Coulomb systems, for example the 2D-XY model or spin ices.

For the 2D grand canonical case, I thoroughly investigate every region of the phase diagram, including both BKT transitions, which are insulator-conductor transitions in the Coulomb picture, as well as the first-order transition between the familiar insulating gas of bound pairs and a full ordered charge crystal, and the second-order transition which corresponds to the melting of that crystal. I calculate various quantities which are relevant in characterising the phase of the system, including the specific heat, susceptibilities and charge density, but my main focus is on describing the phase of the system and the phase transitions in terms of the correlations of the electric field.

Firstly, for the BKT transition at zero core-energy, I find as expected [42] that the winding susceptibility provides a strong signature of the transition; the BKT transition signals the onset of topological sector fluctuations, which in this system arise from the winding of charges around the system, and hence are reflected in the winding susceptibility becoming finite. The correlations of the Coulomb gas across the BKT transition reveal an entirely rotational field below the transition, which corresponds to a vanishingly low density of tightly bound charge pairs, and feature sharp pinch points. Above the transition, the charge density begins to increase and

## 9. Conclusions

charge pairs are allowed to unbind; the result is that the irrotational component of the field begins to increase in intensity. A simulated neutron scattering experiment performed on the “spins” reveals that the width of the sharp pinch points of the low-temperature phase becomes finite. I fit the trace of the irrotational component of the scattering tensor to a Lorentzian and combine it with the neutron scattering form factor to fit the width of the pinch point and extract an effective shortest and longest correlation lengths for the lattice Coulomb gas across the BKT transition, which correspond to bound pairs and free charges respectively. I find that the shorter  $\xi_1$  is below the lattice constant for all temperatures, whereas the longer length  $\xi_2$  diverges from the shorter just below  $T_{\text{BKT}}$  and rises to a peak of several lattice spacings before disappearing again at  $T \approx 0.35$ , which we interpret as signalling the higher charge density and stronger screening at higher temperatures.

It is worth noting here that only by studying the entire scattering tensor and its Helmholtz-decomposed components do we arrive at these results. The perpendicular component of the tensor produces quasi-neutron scattering functions but it is not a physical property: we generate it by projecting a property of the system (the scattering tensor) onto the form factor of the scatterer. By contrast, the tensor  $S^{\alpha\beta}(\mathbf{q})$  and its trace as well as the Helmholtz-decomposed components are true physical properties of the system, and the trace of the two components summarises all the correlations of the system.

For the first order transition I find that the rotational correlations of the low core-energy phase are swept away by the charge ordering in the solid phase, with a small window around the transition where it is possible to see phase coexistence. The correlations of the solid phase are dominated by the irrotational component generated by the all-in-all-out order of the crystal. I show that the missing orders in the neutron scattering functions can be explained by a propagation vector of  $(\pi, \pi)$  which represents antiferroelectric order, and furthermore that the “opposite” component to the neutron scattering plot has peaks corresponding to a propagation vector of  $(-\pi, \pi)$ . This propagation vector is that of the F model ground state, and can also be seen in neutron scattering experiments on artificial spin ice systems, where it is possible to tune the coupling between  $x$  and  $y$  spins continuously from the F model ground state to the entirely rotational correlations of the ice-rule obeying phase.

Lastly, for the BKT and melting transitions at high core-energy, I show that the harmonic mode which enters the neutron scattering functions at  $\mathbf{Q} = \mathbf{0}$  provides a signature of the BKT transition and that the second-order melting transition is characterised by the broadening of sharp peaks into broader Lorentzians. I

fit these Lorentzians as well and show that the diffusion length in this case is a steadily decreasing function of temperature.

For the harmonic XY model I show that the mapping to the Coulomb gas established by Faulkner, Bramwell and Holdsworth [32] extends to the correlations of the emergent electric field, modulo a decrease in the intensity of the harmonic mode which we attribute to the coupling between the rotational and irrotational components of the field, causing the charge mobility to be lower than in the Coulomb gas case where the two components are independent. I perform the same Lorentzian fits as in the Coulomb gas zero core-energy BKT case and find very similar behaviour in the two correlation lengths as for the Coulomb gas, with the peak in  $\xi_2$  possibly shifted slightly upwards in temperature.

For the 2D canonical Coulomb gas I find results consistent with the phase diagram of Gupta, with an increased BKT transition temperature at very low charge densities giving way to phase separation at high charge densities. At the highest densities simulated I find solid-liquid phase coexistence characterised by the superposition of broad peaks associated with the solid phase with the high-intensity harmonic mode and finite width pinch points of the liquid phase. I find that the effective Debye length is a much less useful indicator of the transitions in this case, since the low charge densities have very small irrotational components and the highest charge densities have no BKT transition at all.

For the 3D grand canonical case I find correlations qualitatively similar to those of the 2D grand canonical case, although without the BKT transition and in fact without much evidence of the pseudo-BKT transition presented by Camp and Patey [96], although further work is required. I find evidence of the solid phases and of solid-liquid phase coexistence at different points in the  $u-T$  phase diagram, although there are some lingering questions about the low-temperature simulations and significant further work would be required to quantitatively analyse the whole phase diagram.

## 9.2. Relation to more general systems

This work also relates to many other kinds of system, including spin ices and artificial spin ices, where we find emergent Coulomb physics. These systems often have entirely rotational (transverse) fields in their ground states and longitudinal excitations out of those ground states, as was the case with the 2D grand canonical Coulomb gas. Fig. 9.1 shows a schematic of the correlations of the 2D grand canonical Coulomb gas in each part of its phase diagram.

## 9. Conclusions

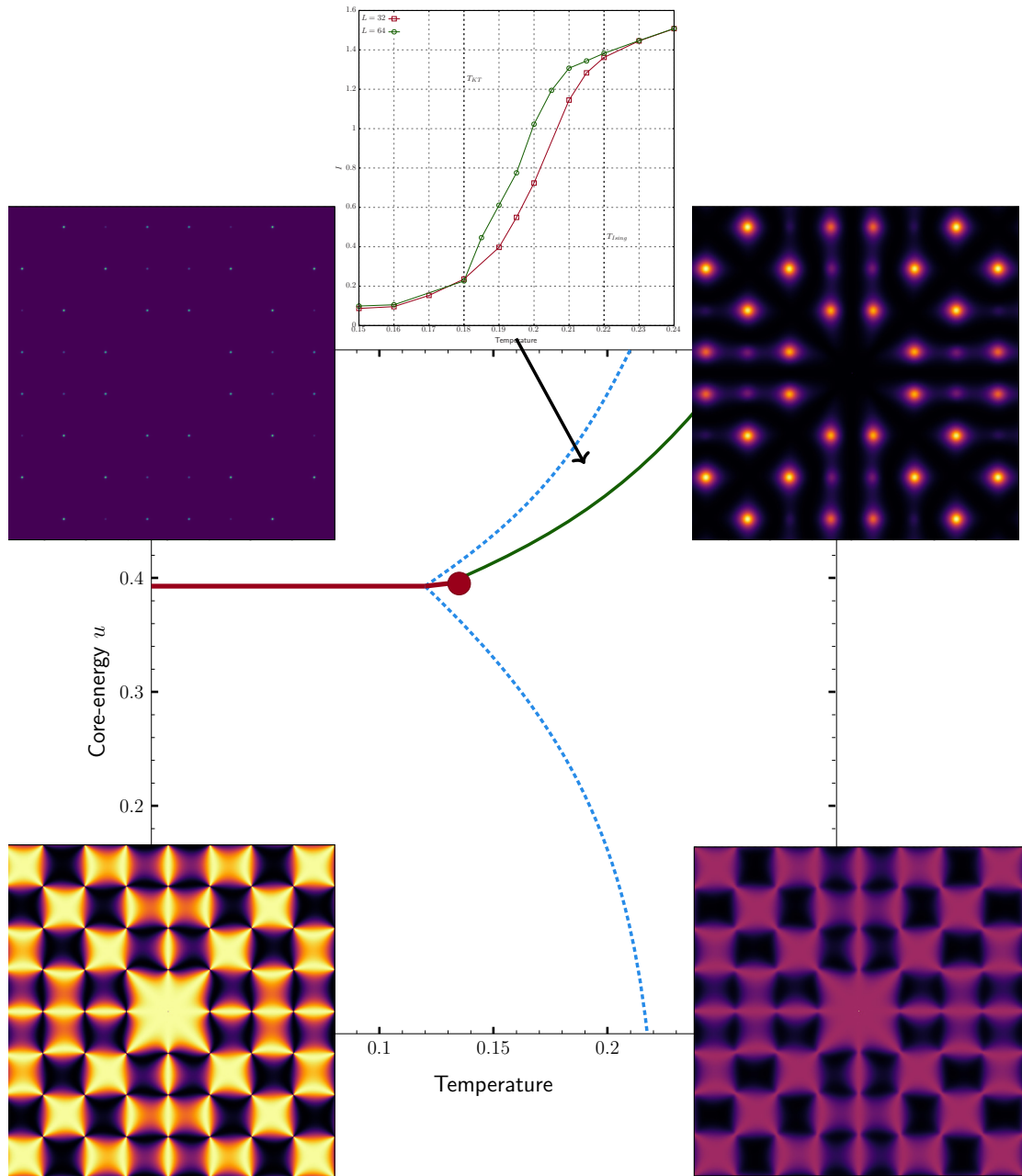


FIGURE 9.1.: The 2D grand canonical Coulomb gas phase diagram, with superimposed examples of the correlations of each phase.

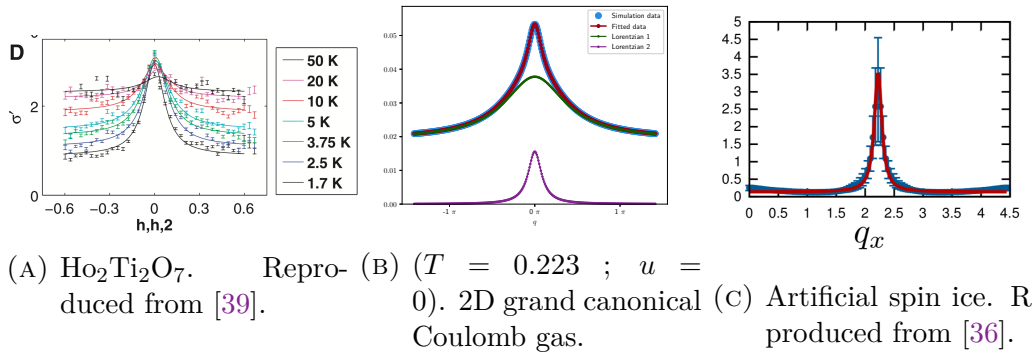


FIGURE 9.2.: Lorentzian fits to pinch points: to experimental data on the  $(h, h, 2)$  pinch point of  $\text{Ho}_2\text{Ti}_2\text{O}_7$  as a function of temperature, from [39] (left); to the longitudinal correlation function in my work (centre); and to simulations of ice-rule obeying configurations in artificial spin ice, from [36] (right).

We see that in the low-T, low- $u$  phases in the bottom left we have sharp pinch point features, which are also observed in experiment of artificial spin ice systems as shown in Figs. 1.1a, from an ASI experiment in which the two sublattices were vertically offset to tune the coupling strengths, and 1.1b, where XY-like discs were placed at the vertices of the lattice to tune the coupling strengths.

The use of a Lorentzian with flat background to fit the width of the pinch points echoes work done in Ref. [39], as shown in Fig. 9.2. Fig. 9.2c shows another fit to a Lorentzian with flat background, but in a different context: here the width of the pinch point in a simulated square ice system is measured as a function of lattice size, for perfectly ice-rule obeying configurations only. This means that there are no longitudinal excitations and no harmonic phase; the finite width of the pinch point in this case arises from the open boundary conditions used.

There are three separate factors to consider when studying the pinch point: the harmonic mode of the system controls the intensity at the zone centre, and comes from charge windings in periodic systems (as in my work) or open loops in systems with open boundaries (such as in Fig. 9.2c). The presence of defects in an ice-type system gives a Lorentzian shape across the pinch point, while the flat background can arise from true long-range interactions as in real spin ice or my work, or from finite size truncation effects as in Fig. 9.2c. We see the Lorentzian with flat background in the real spin ice system in Fig. 9.2a due to the monopole defects and their long-range interactions, and in my work because it deals with electric charges also interacting Coulombically. By contrast, a near-neighbour spin ice system would have no flat background since its interaction is short ranged, and the square ice simulation in Fig. 9.2c has a flat background due to the finite size

## 9. Conclusions

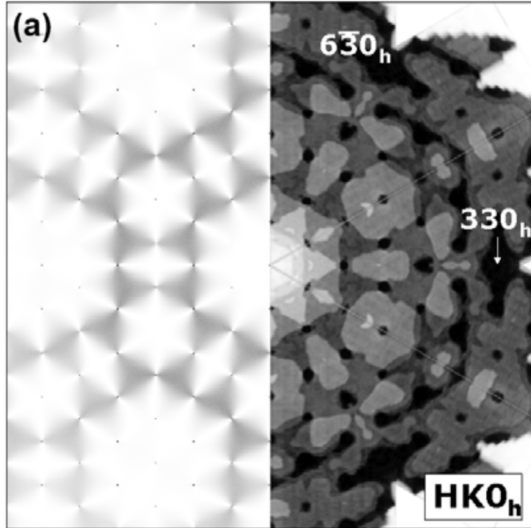


FIGURE 9.3.: Single crystal of D<sub>2</sub>O ice I<sub>h</sub> investigated via diffuse neutron scattering (right) and model calculation (left). Reproduced from [97].

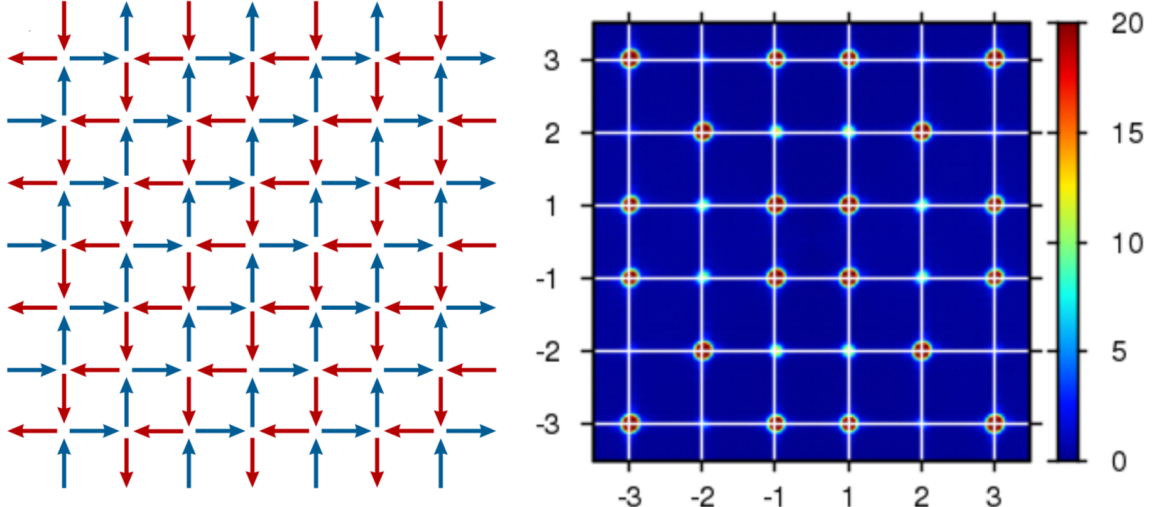
of the system; the background should go to zero as the lattice size increases.

As well as in polarised neutron scattering experiments on spin ice materials (Fig. 9.2a), finite width pinch points can be seen in scattering experiments on water ice [97], as in Fig. 9.3. We note that while water ice is composed of electric charges, which would in principle give rise to an entirely irrotational electrostatic field, a model composed entirely of dipoles would give a rotational field, in analogy with the magnetic case.

In the top left of Fig. 9.1 we see the correlations of the insulating solid phase: these can again be compared to results of experiments on artificial spin ices. In the case of a low-energy artificial spin ice with no vertical offset or mediating XY-like disc, we see a tiling of T<sub>I</sub> vertices which have two spins pointing in and two out of each vertex, and no overall magnetic moment, as shown in Fig. 9.4a. This gives an antiferromagnetic ground state with a propagation vector of  $(\pi, -\pi)$  in the resulting structure factor, and results in the correlations shown in Fig. 9.4b.

Simulation of an abstract generalised Coulomb gas then is again shown to relate to experiments on magnetic systems where emergent Coulombic behaviour can be found.

In addition, we note here that current experiments on artificial spin ices have shown that it is possible to tune the nearest-neighbour couplings in such a way that the ice-rule degeneracy is recovered, and that excitations out of the ice-rule manifold in the form of 3-in-1-out/3-out-1-in T<sub>III</sub> vertices are also possible. The interaction of these defects can be complicated [98]. However if, as in “regular”



(A) An example of an antiferromagnetic ground state for an artificial spin ice composed of Type I vertices only. Reproduced from [76].

(B) The corresponding magnetic structure factor, which has a propagation vector of  $(\pi, -\pi)$ . Reproduced from [76].

spin ice materials, the excitations can be interpreted as magnetic monopole defects which interact Coulombically, then the artificial spin ice system would form an experimentally realisable (magnetic) example of a 2D grand canonical Coulomb gas very much like the idealised one studied here, with the caveat that the dynamics of the charges are constrained by the underlying spin network. Such a scenario raises the possibility of investigating a BKT transition involving the unbinding of monopole pairs which we assume would have analogous correlations to those presented in Sec. 6.2.

### 9.3. Future work

The work presented here comprises a thorough investigation of the 2D grand canonical Coulomb gas and of the harmonic XY model, but also suggests multiple avenues for further study.

The first and most obvious subjects of interest are the 2D canonical Coulomb gas and the 3D canonical and grand canonical Coulomb gases on the simple cubic lattices, which I have not studied as closely as the 2D grand canonical case.

Another possible topic following on from this work would be a generalisation to other lattices: for example, an analogous study of the 3D grand canonical Coulomb gas on the diamond lattice would provide a close link with the physics of spin ice systems such as dysprosium and holmium titanate, among others.

## *9. Conclusions*

Finally, as has been noted in Chap. 7, for example, systems with emergent Coulomb physics are often approximately described by generalised lattice Coulomb gases; this is the case for the harmonic XY model and for artificial spin ices. The source of the approximation is often a coupling between the rotational and irrotational components of the emergent field: in spin ice materials, this coupling comes from the fact that the creation of a monopole-antimonopole pair can only happen via single spin flip excitations out of a locally ice-rule obeying configuration. Hence, the creation of the (irrotational) defect pairs necessarily changes the (rotational) field of the underlying spin network. Analogously in the harmonic XY model, the rotational component of the emergent field is constrained by the  $2\pi$ -modularity of the Hamiltonian, which is what gives rise to vortex excitations, and results in the inseparability of the two components in the partition function [32]. An algorithm much like the Maggs-Rossetto algorithm but which included some form of coupling between the irrotational and rotational components of the field could in principle study this in more detail to provide a new perspective on emergent Coulomb systems.

# Bibliography

1. Berezinskii, V. *Sov. Phys. JETP* **32**, 493 (1971).
2. Kosterlitz, J. M. & Thouless, D. J. Ordering, metastability and phase transitions in two-dimensional systems. *Journal of Physics C: Solid State Physics* **6**, 1181 (1973).
3. Henley, C. L. The “Coulomb Phase” in Frustrated Systems. *Annual Review of Condensed Matter Physics* **1**, 179–210 (2010).
4. Rys, F. Magnetic relaxation in rare-earth oxide pyrochlores. *Helv. Phys. Acta* **36**, 537–560 (1963).
5. Lieb, E. H. Exact Solution of the  $F$  Model of An Antiferroelectric. *Phys. Rev. Lett.* **18**, 1046–1048 (24 June 1967).
6. Bramwell, S. T. & Holdsworth, P. C. W. Magnetization: A characteristic of the Kosterlitz-Thouless-Berezinskii transition. *Phys. Rev. B* **49**, 8811–8814 (13 Apr. 1994).
7. Vallat, A. & Beck, H. Coulomb-gas representation of the two-dimensional XY model on a torus. *Phys. Rev. B* **50**, 4015–4029 (6 Aug. 1994).
8. Maggs, A. C. & Rossetto, V. Local simulation algorithms for Coulomb interactions. *Physical Review Letters* **88**, 196402. ISSN: 0031-9007 (2002).
9. Bernal, J. D. & Fowler, R. H. A Theory of Water and Ionic Solution, with Particular Reference to Hydrogen and Hydroxyl Ions. *The Journal of Chemical Physics* **1**, 515–548 (1933).
10. Pauling, L. The Structure and Entropy of Ice and of Other Crystals with Some Randomness of Atomic Arrangement. *Journal of the American Chemical Society* **57**, 2680–2684 (1935).
11. Lieb, E. H. Exact Solution of the Problem of the Entropy of Two-Dimensional Ice. *Phys. Rev. Lett.* **18**, 692–694 (17 Apr. 1967).

## Bibliography

12. Villain, J. Theory of one- and two-dimensional magnets with an easy magnetization plane. II. The planar, classical, two-dimensional magnet. *J. Phys. France* **36**, 581–590 (1975).
13. *Electrostatic Effects in Soft Matter and Biophysics* (eds Holm, C., Kékicheff, P. & Podgornik, R.) (Springer, 2001).
14. Naji, A., Jungblut, S., Moreira, A. G. & Netz, R. R. Electrostatic interactions in strongly coupled soft matter. *Physica A: Statistical Mechanics and its Applications* **352**, 131–170. ISSN: 0378-4371 (2005).
15. Baus, M. & Hansen, J. Statistical mechanics of simple coulomb systems. *Physics Reports* **59**, 1–94. ISSN: 0370-1573 (1980).
16. Levin, Y. Electrostatic correlations: from plasma to biology. *Reports on Progress in Physics* **65**, 1577–1632. ISSN: 0034-4885 (Nov. 2002).
17. Arrhenius, S. Über die Dissociation der in Wasser gelösten Stoffe. *Zeitschrift für Physikalische Chemie* **1U**, 631–648 (1 1887).
18. Debye, P. & Hückel, E. De la theorie des electrolytes. I. abaissement du point de congelation et phenomenes associes. *Physikalische Zeitschrift* **24**, 185–206 (1923).
19. Debye, P. The theory of electrolytes. I. *Z. Phys.* **24**, 305–324 (1923).
20. Bjerrum, N. J. Untersuchungen über Ionenassoziation. *Mathematisk-fysiske meddelelser, bd. 7, nr. 9* **7** (1926).
21. Fisher, M. E. & Levin, Y. Criticality in ionic fluids: Debye-Hückel theory, Bjerrum, and beyond. *Phys. Rev. Lett.* **71**, 3826–3829 (23 Dec. 1993).
22. Levin, Y. & Fisher, M. E. Criticality in the hard-sphere ionic fluid. *Physica A* **225**, 164–200 (1996).
23. *Theory of Simple Liquids* (eds Hansen, J.-P. & McDonald, I. R.) ISBN: 978-0-12-387032-2 (Academic Press, 2013).
24. Kosterlitz, J. M. The critical properties of the two-dimensional xy model. *Journal of Physics C: Solid State Physics* **7**, 1046 (1974).
25. José, J. V., Kadanoff, L. P., Kirkpatrick, S. & Nelson, D. R. Renormalization, vortices, and symmetry-breaking perturbations in the two-dimensional planar model. *Physical Review B* **16**, 1217–1241. ISSN: 01631829 (1977).
26. Salzberg, A. M. & Prager, S. Equation of State for a Two-Dimensional Electrolyte. *The Journal of Chemical Physics* **38**, 2587–2587 (1963).

27. Nelson, D. R. & Kosterlitz, J. M. Universal Jump in the Superfluid Density of Two-Dimensional Superfluids. *Phys. Rev. Lett.* **39**, 1201–1205 (19 Nov. 1977).
28. Ambegaokar, V., Halperin, B. I., Nelson, D. R. & Siggia, E. D. Dissipation in Two-Dimensional Superfluids. *Phys. Rev. Lett.* **40**, 783–786 (12 Mar. 1978).
29. Trombettoni, A., Smerzi, A. & Sodano, P. Observable signature of the Berezinskii–Kosterlitz–Thouless transition in a planar lattice of Bose–Einstein condensates. *New Journal of Physics* **7**, 57 (2005).
30. Beasley, M. R., Mooij, J. E. & Orlando, T. P. Possibility of Vortex-Antivortex Pair Dissociation in Two-Dimensional Superconductors. *Phys. Rev. Lett.* **42**, 1165–1168 (17 Apr. 1979).
31. Faulkner, M. F. *Topological and Emergent Phenomena in Lattice BKT Systems* PhD thesis (University College London, 2015).
32. Faulkner, M. F., Bramwell, S. T. & Holdsworth, P. C. W. An electric-field representation of the harmonic XY model. *Journal of Physics: Condensed Matter* **29**, 085402 (2017).
33. Harris, M. J., Bramwell, S. T., McMorrow, D. F., Zeiske, T. & Godfrey, K. W. Geometrical frustration in the ferromagnetic pyrochlore  $\text{Ho}_2\text{Ti}_2\text{O}_7$ . *Phys. Rev. Lett.* **79**, 3–6. ISSN: 0031-9007 (13 1997).
34. Bramwell, S. T. & Gingras, M. J. Spin ice state in frustrated magnetic pyrochlore materials. *Science* **294**, 1495–501 (Nov. 2001).
35. Castelnovo, C., Moessner, R. & Sondhi, S. L. Magnetic monopoles in spin ice. *Nature* **451**, 42–5. ISSN: 1476-4687 (2008).
36. Perrin, Y., Canals, B. & Rougemaille, N. Extensive degeneracy, Coulomb phase and magnetic monopoles in artificial square ice. *Nature* **540**, 410 (Nov. 2016).
37. Östman, E. *et al.* Interaction modifiers in artificial spin ices. *Nature Physics* **14**, 375–379 (2018).
38. Lao, Y. *et al.* Classical topological order in the kinetics of artificial spin ice. *Nature Physics*. ISSN: 1745-2481 (2018).
39. Fennell, T. *et al.* Magnetic Coulomb Phase in the Spin Ice  $\text{Ho}_2\text{Ti}_2\text{O}_7$ . *Science* **326**, 415–417. ISSN: 0036-8075 (2009).
40. Chew, W. C. Electromagnetic theory on a lattice. *Journal of Applied Physics* **75**, 4843–4850. ISSN: 00218979 (1994).

## Bibliography

41. Guttmann, A. J. Lattice Green's functions in all dimensions. *Journal of Physics A: Mathematical and Theoretical* **43**, 305205 (2010).
42. Faulkner, M. F., Bramwell, S. T. & Holdsworth, P. C. W. Topological-sector fluctuations and ergodicity breaking at the Berezinskii-Kosterlitz-Thouless transition. *Phys. Rev. B* **91**, 155412 (15 Apr. 2015).
43. De Leeuw, S. W., Perram, J. W. & Smith, E. R. Simulation of Electrostatic Systems in Periodic Boundary Conditions. *Proceedings of the Royal Society of London A: Mathematical, Physical and Engineering Sciences* **373**, 27–56. ISSN: 0080-4630 (1980).
44. Lee, J.-R. & Teitel, S. Phase transitions in classical two-dimensional lattice Coulomb gases. *Phys. Rev. B* **46**, 3247–3262 (6 Aug. 1992).
45. Gupta, P. & Teitel, S. Phase diagram of the two-dimensional lattice Coulomb gas. *Phys. Rev. B* **55**, 2756–2759 (5 Feb. 1997).
46. Mermin, N. D. & Wagner, H. Absence of Ferromagnetism or Antiferromagnetism in One- or Two-Dimensional Isotropic Heisenberg Models. *Phys. Rev. Lett.* **17**, 1133–1136 (22 Nov. 1966).
47. Tobochnik, J. & Chester, G. V. Monte Carlo study of the planar spin model. *Phys. Rev. B* **20**, 3761–3769 (9 Nov. 1979).
48. Minnhagen, P. & Kim, B. J. Direct evidence of the discontinuous character of the Kosterlitz-Thouless jump. *Phys. Rev. B* **67**, 172509 (17 May 2003).
49. Foini, L., Levis, D., Tarzia, M. & Cugliandolo, L. F. Static properties of 2D spin-ice as a sixteen-vertex model. *Journal of Statistical Mechanics: Theory and Experiment* **02**, P02026. ISSN: 1742-5468 (Feb. 2013).
50. Lieb, E. H. Residual Entropy of Square Ice. *Physical Review* **162**, 162–172. ISSN: 0031899X (1967).
51. Baxter, R. J. *Exactly solved models in statistical mechanics* ISBN: 9780486462714 (1982).
52. Savit, R. Duality in field theory and statistical systems. *Rev. Mod. Phys.* **52**, 453–487 (2 Apr. 1980).
53. Nienhuis, B. Critical behavior of two-dimensional spin models and charge asymmetry in the Coulomb gas. *Journal of Statistical Physics* **34**, 731–761. ISSN: 1572-9613 (Mar. 1984).

54. Weigel, M. & Janke, W. The square-lattice F model revisited: a loop-cluster update scaling study. *Journal of Physics A: Mathematical and General* **38**, 7067 (2005).
55. Van Beijeren, H. Exactly Solvable Model for the Roughening Transition of a Crystal Surface. *Phys. Rev. Lett.* **38**, 993–996 (18 May 1977).
56. Rosenkranz, S. *et al.* Crystal-field interaction in the pyrochlore magnet  $\text{Ho}_2\text{Ti}_2\text{O}_7$ . *Journal of Applied Physics* **87**, 5914–5916 (2000).
57. Harris, M., Bramwell, S., Holdsworth, P. & Champion, J. Liquid-Gas Critical Behavior in a Frustrated Pyrochlore Ferromagnet. *Physical Review Letters* **81**, 4496–4499. ISSN: 0031-9007 (1998).
58. Zhou, H. D. *et al.* Chemical Pressure Effects on Pyrochlore Spin Ice. *Phys. Rev. Lett.* **108**, 207206 (20 May 2012).
59. Isakov, S. V., Gregor, K., Moessner, R. & Sondhi, S. L. Dipolar spin correlations in classical pyrochlore magnets. *Physical Review Letters* **93**, 1–4. ISSN: 00319007 (2004).
60. Den Hertog, B. C. & Gingras, M. J. P. Dipolar Interactions and Origin of Spin Ice in Ising Pyrochlore Magnets. ISSN: 0031-9007 (2000).
61. Kaiser, V. *The Wien Effect in Electric and Magnetic Coulomb systems - from Electrolytes to Spin Ice* PhD thesis (MPIPKS Dresden, 2015).
62. Castelnovo, C., Moessner, R. & Sondhi, S. L. Debye-Hückel theory for spin ice at low temperature. *Phys. Rev. B* **84**, 144435 (14 Oct. 2011).
63. Kaiser, V., Bramwell, S. T., Holdsworth, P. C. W. & Moessner, R. AC Wien Effect in Spin Ice, Manifest in Nonlinear, Nonequilibrium Susceptibility. *Physical Review Letters* **115**, 037201. ISSN: 0031-9007 (Dec. 2015).
64. Castelnovo, C., Moessner, R. & Sondhi, S. L. Spin Ice, Fractionalization, and Topological Order. *Annual Review of Condensed Matter Physics* **3**, 35–55 (2012).
65. Jaubert, L. D. C. & Holdsworth, P. C. W. Magnetic monopole dynamics in spin ice. *Journal of physics. Condensed matter : an Institute of Physics journal* **23**, 164222. ISSN: 1361-648X (Apr. 2011).
66. Anderson, P. W. Ordering and Antiferromagnetism in Ferrites. *Phys. Rev.* **102**, 1008–1013 (4 May 1956).
67. Nagle, J. F. Lattice Statistics of Hydrogen Bonded Crystals. *Journal of Mathematical Physics* **7**, 1484–1491 (1966).

## Bibliography

68. Bramwell, S. T. *et al.* Spin correlations in  $\text{Ho}_2\text{Ti}_2\text{O}_7$ : a dipolar spin ice system. *Physical Review Letters* **87**, 047205. ISSN: 0031-9007 (2001).
69. Melko, R. G. & Gingras, M. J. P. Monte Carlo studies of the dipolar spin ice model. *Journal of Physics: Condensed Matter* **16**, R1277–R1319. ISSN: 0953-8984 (Nov. 2004).
70. Isakov, S., Moessner, R. & Sondhi, S. Why Spin Ice Obeys the Ice Rules. *Physical Review Letters* **95**, 217201. ISSN: 0031-9007 (Nov. 2005).
71. Ryzhkin, I. A. Magnetic relaxation in rare-earth oxide pyrochlores. *Journal of Experimental and Theoretical Physics* **101**, 481–486. ISSN: 1063-7761 (Sept. 2005).
72. Stormer, H. L., Tsui, D. C. & Gossard, A. C. The fractional quantum Hall effect. *Rev. Mod. Phys.* **71**, S298–S305 (2 Mar. 1999).
73. Hou, C.-Y., Chamon, C. & Mudry, C. Electron Fractionalization in Two-Dimensional Graphenelike Structures. *Phys. Rev. Lett.* **98**, 186809 (18 May 2007).
74. Nisoli, C., Moessner, R. & Schiffer, P. Colloquium: Artificial spin ice: Designing and imaging magnetic frustration. *Rev. Mod. Phys.* **85**, 1473–1490 (4 Oct. 2013).
75. Cugliandolo, L. F. Artificial Spin-Ice and Vertex Models. *Journal of Statistical Physics* **167**, 499–514. ISSN: 1572-9613 (May 2017).
76. Perrin, Y. *Réseaux artificiels à frustration géométrique*. PhD thesis (Université Grenoble Alpes, 2016).
77. Brooks-Bartlett, M., Banks, S., Jaubert, L., Harman-Clarke, A. & Holdsworth, P. Magnetic-Moment Fragmentation and Monopole Crystallization. *Physical Review X* **4**, 011007. ISSN: 2160-3308 (Jan. 2014).
78. Chern, G.-W., Morrison, M. J. & Nisoli, C. Degeneracy and Criticality from Emergent Frustration in Artificial Spin Ice. *Phys. Rev. Lett.* **111**, 177201 (17 Oct. 2013).
79. Gilbert, I. *et al.* Emergent ice rule and magnetic charge screening from vertex frustration in artificial spin ice. *Nature Physics* **10**, 670 (Aug. 2014).
80. Marshall, W. & Lovesey, S. *Theory of thermal neutron scattering* (Oxford Press, 1971).
81. White, R. M. *Quantum Theory of Magnetism: Magnetic Properties of Materials* ISBN: 9783540690252 (Springer Berlin Heidelberg, 2007).

82. Bramwell, S. T. in *Introduction to Frustrated Magnetism: Materials, Experiments, Theory* (eds Lacroix, C., Mendels, P. & Mila, F.) 45–78 (Springer Berlin Heidelberg, 2011).
83. Moon, R. M., Riste, T. & Koehler, W. C. Polarization Analysis of Thermal-Neutron Scattering. *Phys. Rev.* **181**, 920–931 (2 May 1969).
84. Squires, G. L. *Introduction to the Theory of Thermal Neutron Scattering* 3rd ed. (Cambridge University Press, 2012).
85. Ressouche, E. Reminder: Magnetic structures description and determination by neutron diffraction. *JDN* **13**, 02001 (2014).
86. Wills, A. Magnetic structures and their determination using group theory. *J. Phys. IV France* **11** (2001).
87. Nye, J. F. *Physical Properties of Crystals: Their Representation by Tensors and Matrices* ISBN: 9780198511656 (Clarendon Press, 1985).
88. Eisenhart, L. *Coordinate Geometry* (Dover Publications, 1939).
89. Bramwell, S. T. Harmonic phase in polar liquids and spin ice. *Nature Communications* **8**, 2088–. ISSN: 2041-1723 (2017).
90. Bramwell, S. T. *Private communication*.
91. Youngblood, R. W. & Axe, J. D. Polarization fluctuations in ferroelectric models. *Phys. Rev. B* **23**, 232–238 (1 Jan. 1981).
92. Ryzhkin, M. I., Ryzhkin, I. A. & Bramwell, S. T. Dynamic susceptibility and dynamic correlations in spin ice. *EPL (Europhysics Letters)* **104**, 37005. ISSN: 0295-5075 (Nov. 2013).
93. Minnhagen, P. The two-dimensional Coulomb gas, vortex unbinding, and superfluid-superconducting films. *Rev. Mod. Phys.* **59**, 1001–1066 (4 Oct. 1987).
94. Bramwell, S. T. Generalised Longitudinal Susceptibility for Magnetic Monopoles in Spin Ice. *Proceedings of the Royal Society A: Mathematical, Physical and Engineering Sciences*, 5738–5766. ISSN: 1364-503X (2011).
95. Ren, R., O’Keeffe, C. J. & Orkoulas, G. Simulation of symmetric tricritical behavior in electrolytes. *The Journal of Chemical Physics* **125**, 124504 (2006).
96. Camp, P. J. & Patey, G. N. Ion association in model ionic fluids. *Phys. Rev. E* **60**, 1063–1066 (1 July 1999).

## Bibliography

97. Wehinger, B. *et al.* Diffuse scattering in Ih ice. *Journal of Physics: Condensed Matter* **26**, 265401 (2014).
98. Vedmedenko, E. Y., Mikuszeit, N., Oepen, H. P. & Wiesendanger, R. Multipolar Ordering and Magnetization Reversal in Two-Dimensional Nanomagnet Arrays. *Phys. Rev. Lett.* **95**, 207202 (20 Nov. 2005).

## A. Simulation details

The simulations presented in this thesis of both the Coulomb gas and the HXY model use a program of my own development. The program is written in Fortran 2003 and uses OpenMPI with OpenMP for parallel simulation on high-performance computing (HPC) clusters. The simulations were run on the LCN HPC cluster. Each sample consisted of 500,000 thermalisation Monte Carlo sweeps where no measurements of any quantity were performed, and then a further 250,000 sweeps with measurement of relevant quantities performed every 10 sweeps. One Monte Carlo sweep corresponds to proposing  $N = L^d$  field link updates,  $dN$  rotational updates and  $N$  harmonic updates and using the Metropolis algorithm on the relevant energy changes to accept or reject each proposed update. One simulation corresponds to 32 or 40 samples, run in parallel using OpenMPI with different random number seeds and then averaged.

The code is not reproduced here since it would run to several hundred extra pages, but is available upon request or from <http://github.com/cuamll/mr>.



## B. Equivalence of Lorentzian forms

Ref. [89] introduces a Lorentzian form for the longitudinal scattering function

$$S^L(\mathbf{q}) = \frac{\gamma}{1 + \chi/\epsilon_q} \quad (\text{B.1})$$

where  $\gamma = \chi T/C$  and  $\epsilon_q = 1 + \kappa^2/q^2$  is the Debye-Hückel dielectric constant.

As stated in the text, this decomposes to a standard Lorentzian with flat background of the form

$$\mathcal{L}(x) = \frac{AB^2}{B^2 + x^2} + C \quad (\text{B.2})$$

The full derivation is reproduced here.

Firstly, we define  $\xi = \frac{\sqrt{1+\chi}}{\kappa}$ , so that

$$\epsilon_q = 1 + \kappa^2/q^2 \quad (\text{B.3})$$

$$= 1 + \frac{1}{\frac{q^2\xi^2}{1+\chi}} \quad (\text{B.4})$$

$$= 1 + \frac{1+\chi}{q^2\xi^2} \quad (\text{B.5})$$

$$= \frac{q^2\xi^2 + (1+\chi)}{q^2\xi^2} . \quad (\text{B.6})$$

Substituting this into the denominator of Eq. B.1 we find

$$1 + \frac{\chi}{\epsilon_q} = 1 + \chi \frac{(q^2\xi^2)}{q^2\xi^2 + (1+\chi)} \quad (\text{B.7})$$

$$= \frac{q^2\xi^2 + (1+\chi) + \chi q^2\xi^2}{q^2\xi^2 + (1+\chi)} \quad (\text{B.8})$$

$$= \frac{(1+\chi)(1+q^2\xi^2)}{q^2\xi^2 + (1+\chi)} \quad (\text{B.9})$$

which we then insert back into Eq. B.1:

### B. Equivalence of Lorentzian forms

$$S^L(\mathbf{q}) = \frac{\gamma}{\frac{(1+\chi)(1+q^2\xi^2)}{q^2\xi^2+(1+\chi)}} \quad (\text{B.10})$$

$$= \frac{\gamma(q^2\xi^2 + (1+\chi))}{(1+\chi)(1+q^2\xi^2)} \quad (\text{B.11})$$

$$= \frac{\gamma}{1+\chi} \left( \frac{q^2\xi^2 + (1+\chi)}{1+q^2\xi^2} \right) \quad (\text{B.12})$$

Lastly, we split up the right hand fraction and separate the two components:

$$S^L(\mathbf{q}) = \frac{\gamma}{1+\chi} \left( 1 + \frac{\chi}{1+q^2\xi^2} \right) \quad (\text{B.13})$$

$$= \frac{\gamma}{1+\chi} + \frac{\gamma}{1+\chi} \left( \frac{\chi}{1+q^2\xi^2} \right) \quad (\text{B.14})$$

$$= \frac{\gamma}{1+\chi} + \frac{\chi}{1+\chi} \left( \frac{\gamma}{1+q^2\xi^2} \right) \quad (\text{B.15})$$

which by inspection is the sum of a Lorentzian and a flat background.